Single Photon Detection with Semiconductor Pixel Arrays for Medical Imaging Applications

Bettina Mikulec

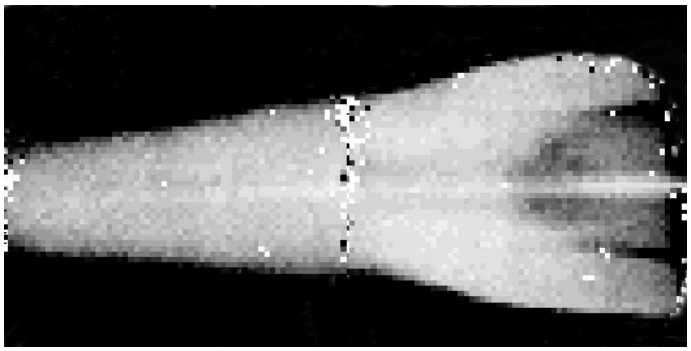

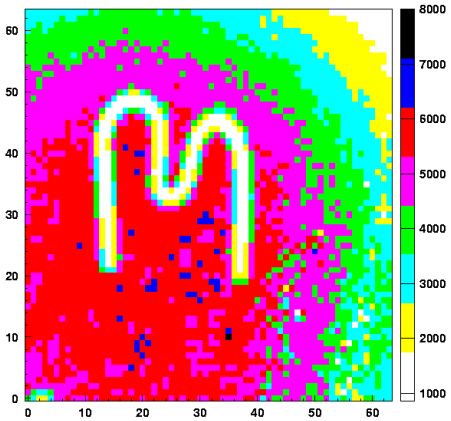

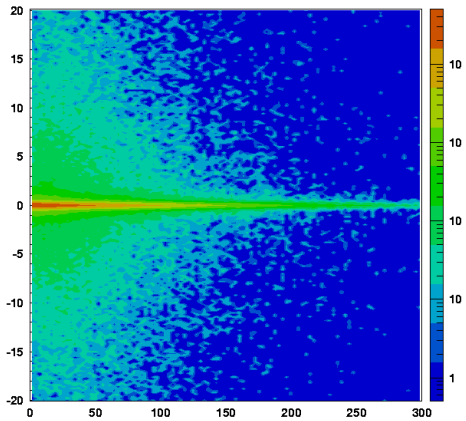

PhD Thesis, University of Vienna, Austria June 2000

CERN-THESIS-2000-021

Single Photon Detection with Semiconductor Pixel Arrays for Medical Imaging Applications

Bettina Mikulec

Dissertation
zur Erlangung
des akademischen Grades
Doktor der Naturwissenschaften

Supervisors:

Prof. Dr. W. Kutschera, Institut für Isotopenforschung und Kernphysik der Universität Wien, Vienna, Austria
Dr. E.H.M. Heijne, CERN/EP, Geneva, Switzerland

CERN, Geneva, Switzerland, June 2000

In memory of my grandfather
who instilled in me his fascination for research
and his love for medecine.

Contents

Abstract

This thesis explores the functioning of a single photon counting pixel detector for X-ray imaging. It considers different applications for such a device, but focuses mainly on the field of medical imaging.

The new detector comprises a CMOS[1] read-out chip called PCC[2] containing 4096 identical channels each of which counts X-ray hits. The conversion of the X-rays to electric charge takes place in a semiconductor sensor which is segmented into 4096 matching square diodes of side length 170 μm, the 'pixels'. The photon counting concept is based on setting a threshold in energy above which a hit is registered. The immediate advantages are the elimination of background and the in principle unlimited dynamic range. Moreover, this approach allows the use of an electronic shutter for arbitrary measurement periods.

As the device was intended for operation in the energy range of ∼10-70 keV, gallium arsenide was selected as the preferred sensor material.

The development of this detector followed on from about 10 years of research aimed at developing hybrid silicon pixel detectors for the future Large Hadron Collider at CERN.

A general overview of the requirements for medical imaging is presented. Semiconductor detectors and in particular GaAs detectors are discussed. Charge deposition and charge collection simulations were carried out. Minimum threshold, threshold spread, noise and spatial resolution measurements are presented and finally some images are shown. The combination of the detector simulations and the measurements of the device give important information about the limits of single photon counting devices and indicators for future developments.

[1]Complementary Metal Oxide Semiconductor

[2]Photon Counting Chip developed in the framework of the Medipix collaboration.

Zusammenfassung

In der vorliegenden Dissertation werden die Eigenschaften eines Pixeldetektors, der im 'single photon counting mode' arbeitet, der Zählmethode einzelner Photonen, im Hinblick auf eine Anwendung in der Röntgendiagnostik untersucht. Andere Anwendungsgebiete werden ebenfalls berücksichtigt, das Hauptaugenmerk liegt jedoch auf dem Gebiet der medizinischen Bildgebung.

Der neuartige Detektor beinhaltet einen CMOS[3] Auslesechip genannt PCC[4], welcher aus einer Matrix von 4096 identischen Kanälen aufgebaut ist, von denen jeder separat Röntgenstrahlen zählt. Die Konvertierung der Röntgenstrahlen in elektrische Ladung findet in einem Halbleiter-Sensor statt. Dieser ist in eine dem Chip entsprechende Matrix von 4096 quadratischen Dioden mit Seitenlänge 170 μm unterteilt, den 'Pixeln'. Die Zählmethode basiert auf der Festlegung eines Energie-Schwellwertes oberhalb dessen ein Photon registriert wird. Sofort ersichtliche Vorteile sind die Unterdrückung störenden Untergrundes sowie der prinzipiell unbeschränkte dynamische Bereich. Außerdem ermöglicht dieses Konzept die Verwendung eines elektronischen Shutters[5] für frei wählbare Meßperioden.

Gallium Arsenid wurde als Sensormaterial ausgewählt, da der Detektor für einen Betrieb im Energiebereich von ∼10-70 keV optimiert ist.

Die Entwicklung des PCC baut auf 10-jähriger Forschungsarbeit auf dem Gebiet von hybriden Silizium Pixeldetektoren für den zukünftigen 'Large Hadron Collider' am CERN auf.

In der Arbeit wird ein Überblick über die Anforderungen der medizinischen Röntgendiagnostik gegeben. Halbleiter-Detektoren und im speziellen GaAs Detektoren werden behandelt. Simulationen betreffend Ladungsdeponierung und Ladungssammlung werden vorgestellt. Experimentell bestimmt wurden Systemparameter wie minimaler Schwellwert, Variation der Schwellwerte, elektronisches Rauschen und Ortsauflösung. Aufnahmen veranschaulichen das Potential des PCC Systems. Die Kombination von Messungen und Simulationen liefert wichtige Informationen über die Grenzen von Pixeldetektoren, welche im 'single photon counting mode' arbeiten, sowie Anhaltspunkte für zukünftige Entwicklungen.

[3]Complementary Metal Oxide Semiconductor

[4]Photon Counting Chip. Der PCC wurde im Rahmen der Medipix Kollaboration entwickelt.

[5]=aktive Meßzeit.

Introduction

Nowadays the populations of industrialised countries enjoy a high standard of living. Life expectancy has been steadily increasing in large part due to improved medical provision and treatment. On the other hand, cancer affects an increasing proportion of the population. Breast cancer for example is estimated to affect up to one out of every nine women and will claim the lives of 30% of those affected [Fre97]. X-ray mammography is considered to be the only current diagnostic imaging modality with long-term proved efficacy in the early detection of breast cancer [Bur95], but is clinically and technically extremely demanding. The early diagnosis of breast cancer is essential for a successful treatment to preserve quality of life and life expectancy of the female patients [Pat93]. Preventive screening programs attempt to address this issue. However, these programs are still controversial as the accumulated X-ray dose over a woman's lifetime increases the risk of radiation induced cancer.

In this thesis I try to understand the performance and potential benefits of a new kind of X-ray imaging detector which may lead in time to lower administered dose due to an improved radiological image quality. I would be honoured if the work described in this thesis and consecutive developments could contribute to reduce physical and psychological suffering.

The origins of the development of the new detector lie in the domain of High Energy Physics. In the early 1990's researchers at CERN[6] began to face up to the challenges of the future Large Hadron Collider (LHC). The steady increase in energy and luminosity of the colliders and especially the change to hadronic interactions will result in a huge amount of close particle tracks (see for example the simulation of a Higgs decay into four muons in fig. 1) which can only be disentangled by 2-dimensional detectors with very high spatial resolution.

At that time a small group of physicists and engineers were working in the framework of a research and development project at CERN, the RD19 project, on a new type of vertex detector, hybrid and monolithic silicon 'micro-pattern' pixel tracking detectors. *Active pixel detectors* are 2-dimensional devices which consist of a sensor part converting the X-rays into detectable charge and CMOS read-out electronics.

[6]European Organization for Nuclear Research near Geneva, Switzerland. The name 'CERN' comes from the name of the original council from 1951, the 'Conseil Européen pour la Recherche Nucléaire'.

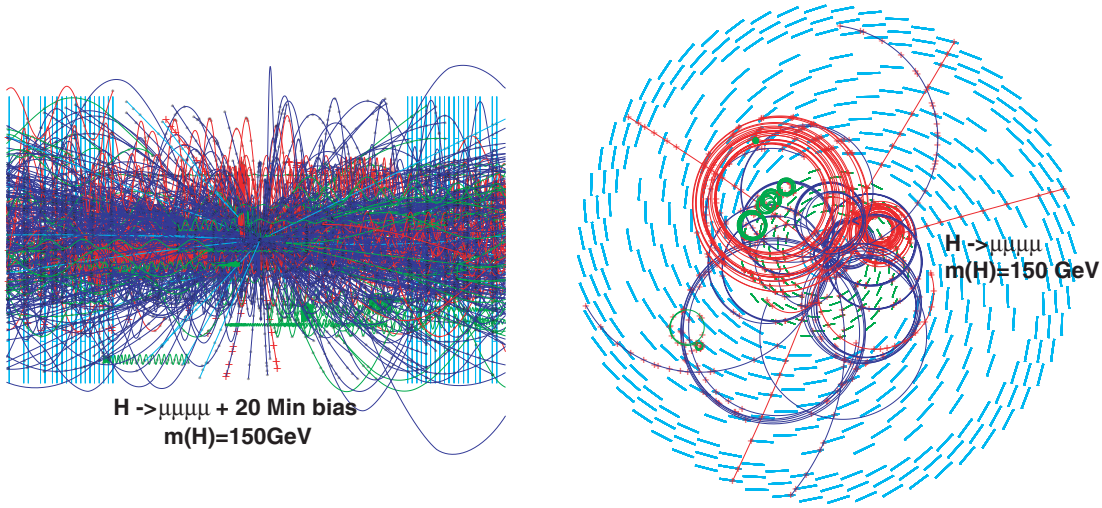

a) b)

Figure 1: *Simulation of one Higgs event with the Higgs decaying into four muons. a) includes all the background tracks and b) shows only the reconstructed Higgs event [CMS].*

The detector is segmented into a large number of tiny channels with integrated signal processing and logic. They are able to record and process patterns arising from the energy loss of ionising particles in the sensor part of the system.
As a means of characterising the quality of the contacts between the sensor and electronics chips (in the case of a hybrid system), X-ray sources were used. These also provided the only exact means of making an absolute calibration of the pixel thresholds. These tests proved that such pixel devices could provide a new way of imaging with X-rays. To optimise the pixel chip for imaging applications, the read-out electronics had to be redesigned to work in counting mode instead of selecting and reading out only triggered events. Also the pixel shape had to be adapted - square pixels were chosen.

The PCC (**P**hoton **C**ounting **C**hip) is the first active CMOS pixel chip designed at CERN in the framework of the Medipix collaboration that was aimed at imaging applications. Its design is especially well adapted for medical X-ray diagnosis. The PCC is a typical example of a spin-off product from the experience and abilities gained during the pixel detector development process for high energy physics experiments.

This thesis summarises the characterisation, first measurements and experiments with the PCC photon counting chip connected to GaAs detectors. Measurements were chosen mainly in view of medical X-ray imaging applications, but the aptitude of the PCC for some other applications is also investigated.

The field of medical X-ray imaging is introduced in chapter 1. A short overview of traditional medical imaging systems is presented and parameters that determine the quality of an image are explained. Emphasis is placed on the distinction between

direct and indirect detection systems and the integrating and counting method. PCC detectors combine the advantages of direct photon detection and the photon counting principle.

Chapter 2 focuses on the energy loss of photons in matter as a basis for choosing the appropriate photon detection material and to be able to interpret simulation results from chapter 7.

The fundamentals of semiconductor detectors are presented in chapter 3. A short introduction to charge carrier transport processes and their mathematical description is given.

Chapter 4 is devoted to GaAs, a semiconductor material which is used as sensor material to convert the photons. This material has a complicated band-gap structure which has much impact on its intrinsic and charge carrier transport properties and therefore its properties as a particle detector. Different material growth processes are briefly introduced and it will be seen that due to the defect content and its compensation GaAs detectors fabricated from differently grown material can show large differences in performance.

The development of the PCC will be reported in chapter 5. The design and functionality of the photon counting chip are explained. The different steps from chip design to a working hybrid detector assembly are illustrated. Characterisation measurements of the electronics chip with electrical test pulses are shown.

Chapter 6 summarises measurements with radioactive alpha, beta, gamma and X-ray sources of the PCC connected to GaAs sensors. The assemblies are first of all characterised in terms of functionality, threshold, noise and uniformity with electrical test pulses. The electrical measurement results have to be converted into absolute values of charge. Such an absolute calibration performed with a radioactive X-ray source is presented. With IV-curves and an alpha source it is possible to determine the optimum detector bias voltage.
After this thorough characterisation, images of various samples taken with different radioactive sources are shown. They all indicate that the PCC together with a highly efficient detector material is a very promising way to produce images with high contrast, high spatial resolution and low dose.
The chapter ends with a description of experiments performed at a synchrotron X-ray powder diffraction test beam and of the evaluation of the PCC system for the use as a gamma camera.

Further miniaturisation, made possible by the steady technological progress of micro-electronics, would further improve the PCC. In particular future developments will lead to a much reduced pixel size. Charge sharing between pixels working in photon counting mode will therefore become an issue. Investigations were undertaken

to estimate the relative importance of the energy loss and the charge collection processes. The energy loss of photons is simulated with the 'Fluka' Monte Carlo code with emphasis on the lateral dimension of the deposited charge for different semiconductor materials. In the second part the collection of the deposited charge through an applied electric field is simulated for a GaAs pixel detector with 'Davinci', a 3D semiconductor device simulator. The simulation results are presented in chapter 7.

This thesis describes the first steps in photon counting undertaken at CERN. This new kind of device which comprises an efficient direct photon conversion sensor and a pixel chip with complete integrated functionality is a very promising approach for a lot of applications. It will probably still need a number of years to get accepted by the end users and established as a basis of a system.

Chapter 1

Medical X-ray Imaging

Contents

Attempts to image inside parts of the human body date back to the 19th century, but only with the discovery of the X-rays on Nov. 8th 1895 by Wilhelm Conrad Röntgen [Roe95] the basis was made for 20th century medical diagnosis. Figure 1.1 shows the famous image of the hand of Mrs. Bertha Röntgen, one of the first images

Figure 1.1: *One of the first X-ray images showing the hand of Mrs. Röntgen [han].*

made with X-rays.

Nowadays medical diagnostic imaging is not only restricted to X-ray radiology, but a huge field of various examination methods exist. Depending on the part of the body to be imaged, on the imaging task and on the available equipment different imaging methods can be chosen. In general, images are based on the physics of the interactions between energy and matter. X-rays interact with the inner and outer shells of atoms, gamma rays are good probes for atomic nuclei. Visible and infrared radiation as well as microwaves can only give information connected to the outer electron shells and hence the surface of the body. Ultrasonic examinations are based on reflections and refractions of sound waves on matter of different densities. Therefore it is understandable that medical imaging has to be multifaceted.
Medical imaging has grown into a major and important specialised field. Examples for different medical imaging applications are *X-ray diagnostic radiology, radio-isotope imaging* including **C**omputed **T**omography (CT), **P**ositron **E**mission **T**omography (PET), **S**ingle **P**hoton **E**mission **C**omputed **T**omography (SPECT) and auto-radiography, *ultrasound,* **N***uclear* **M***agnetic* **R***esonance (NMR)* or *infrared imaging*, just to note the most common methods. These can again be subdivided into 2-dimensional imaging methods and 3-dimensional reconstruction computed tomography which has implications on detector size, image processing and mathematical complexity.

This chapter will limit itself to the physical principles of diagnostic X-ray projection radiology. Nevertheless, the ideas behind many of these concepts can be taken over to other medical imaging techniques.

In general, an X-ray image of a sample is formed through the interaction with the detector of the X-rays which passed through the sample. The image represents the

photon attenuation properties of the sample and its details.
In medical X-ray diagnosis the X-rays are mainly provided by X-ray tubes. In an X-ray tube electrons emerge from a heated filament and are accelerated under an electric potential difference onto a target which is fixed at a steep angle with respect to the incoming electron beam. The reaction with the target material results in an emission of bremsstrahlung X-rays and fluorescence X-rays. The different parameters of the tube such as electron beam dimensions, acceleration voltage, target material, target angle, collimator shape, focal spot size and used filters have to be chosen depending on the part of the body to be imaged. For the choice of the tube voltage, the target material and the filter material a compromise has to be made between the highest possible contrast between the details to be separated in the image and the lowest possible dose to the patient. For most examinations a tungsten target is used. A high atomic number of the anode material is important for a better bremsstrahlung yield. The resulting spectrum is well adapted to imaging of thicker body sections and provides sufficient contrast between bones and soft tissue.
For applications such as *mammography*, the difference in photon attenuation coefficient between tumours and normal breast tissue is much smaller[1]. So-called microcalcifications may be the only sign of a precancerous stage [Pat93]. A plot of the contrast to normal breast tissue between such a calcification and glandular tissue as a function of photon energy makes clear that low energies should be used (fig. 1.2 [Dan81]). A compromise between sufficiently high contrast and reasonably low dose to the patient has to be made. The photon transmission through varying tissue thickness for five different photon beam energies is shown in fig. 1.3 [Web98]. A reduction of breast thickness by compression represents a large improvement.

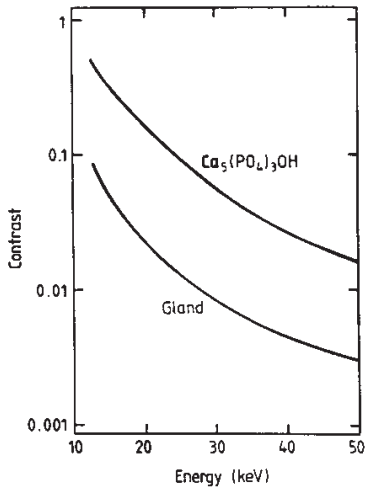

Figure 1.2: *Logarithmic variation of contrast with photon energy [keV] for a 100 μm calcification (calcium hydroxyapatite) and 1 mm of glandular tissue with respect to normal breast tissue [Dan81].*

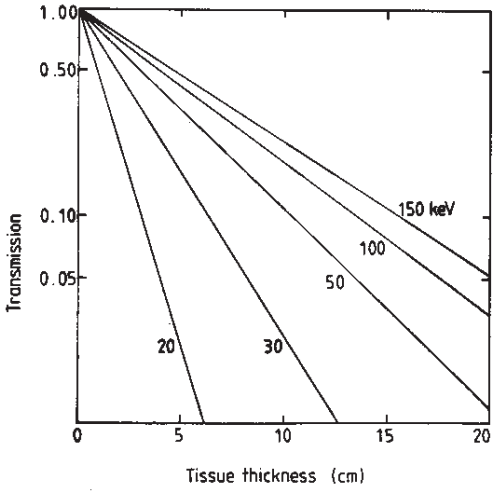

Figure 1.3: *Transmission of monoenergetic photons with energies 20, 30, 50, 100 and 150 keV as a function of soft tissue thickness [Web98].*

[1]Malignant regions can often only be detected due to the related change in breast architecture.

A molybdenum target is used in X-ray tubes for mammography. A spectrum of such a tube with 30 kV potential is shown in fig. 1.4(a) [Web98]. It is common practice to use also a molybdenum filter to cut off a large fraction of the bremsstrahlung photons above 20 keV. Fig. 1.4(b) shows the (normalised) spectrum after passage through 5 cm of soft tissue. A *hardening* of the spectrum is evident and is due to the dependence of the attenuation coefficient on the photon energy (see section 2.4). The bremsstrahlung photons with energy higher than the Mo absorption edge produce more likely diffuse radiation due to Compton interaction in the breast tissue than the lower energy photons which smears out image details. The missing photons with respect to the incident photon beam correspond principally to dose delivered to the patient.
Although the dose for one mammographic image is relatively low (in the order of 1 mGy) national mammographic screening programs are still a very controversial subject. Dose integration over several years increases the risk of associated carcinogenesis. Investigations to weigh risks and benefits still yield conflicting results. One critical point is the starting age of such programs. Young women have denser breasts which reduces strongly the contrast to cancerous spots. Therefore higher exposures have to be used going along with higher delivered dose. Unfortunately, breast cancer is most dangerous in young women as it tends to develop faster than in older patients.
Besides the breast composition the optimum photon energy varies with breast thickness. If cost would not play a role monochromatic synchrotron radiation which is adjustable in energy would represent a major benefit[2]. On one hand the energy could be optimised to the patient anatomy and on the other hand X-ray energy ranges which rather deteriorate the image could be avoided.

Another way to reduce dose is to increase significantly the image quality. This direction was taken by the Medipix collaboration by developing the PCC, the Photon Counting Chip.

The PCC has to prove that it fulfills the requirements for a medical X-ray imaging system. The aim for the future is to improve image quality or - formulated in a different way - to maintain image quality at a much reduced dose. To evaluate the performance of an imaging system for radiography there are many parameters placed at the disposal, each of them focusing on a different criterion. These image quality parameters are described in the following sections.
X-ray imaging systems can be divided up (see section 1.2) into systems detecting directly the incoming X-rays and systems which have to convert the X-rays first into visible light and detect this light subsequently (indirect detection).
Another important distinction between different imaging systems is between analog and digital systems (section 1.3).
Section 1.4 compares the charge integration method with the counting method which are two different ways of treating signals in digital radiology.

[2]Alternative approaches to produce narrow energy-band tunable X-ray beams exist as well. One example for such a proposal is described in [Gam95].

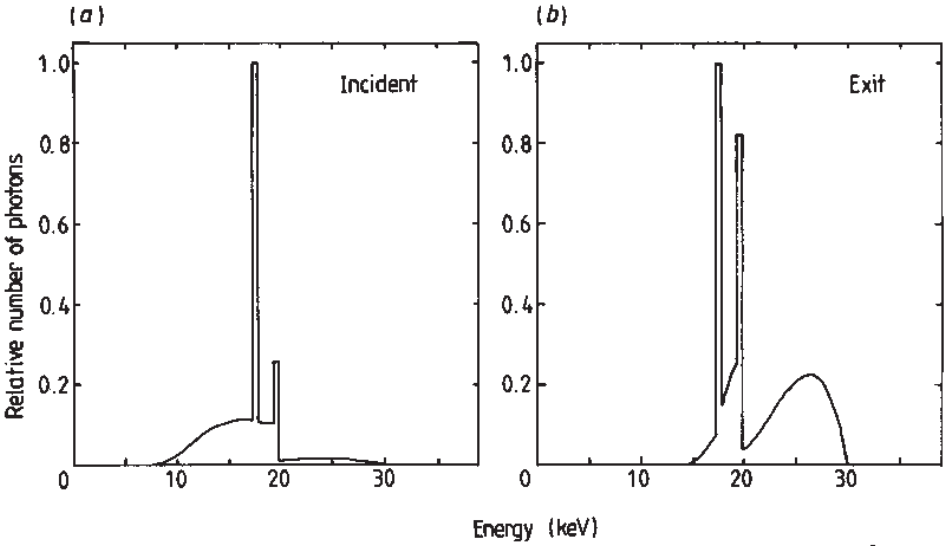

Figure 1.4: *Normalised X-ray spectra before (a) and after (b) attenuation by 5 cm of soft tissue [Web98]. The setup of the X-ray tube consists of a molybdenum target, 30 kV potential and a 30 μm thick molybdenum filter.*

A brief overview over various existing systems for X-ray imaging will be given in section 1.5.

1.1 Image quality assessment

Each new imaging system on the market has to go through a detailed assessment of its imaging quality. Image quality is expressed in terms of a number of parameters. These parameters will be described in the following sections, although the list is not exhaustive. Moreover, image formation does not by itself determine whether an object is detected or not. Image processing or optimum image display are extremely important as well, and the last decision is made by the ability of a human observer based on his/her experience. To treat the complete decision process is far beyond the scope of this thesis. Therefore only a brief introduction into the physical image quality parameters will be given.

1.1.1 Contrast

One criterion for determining radiographic quality is *radiographic contrast*. It describes mainly the density difference between two adjacent areas in a radiograph. The contrast C of the signal may be defined as

$$C = \frac{\Delta I}{I}$$

with I as the mean intensity of the background signal and ΔI a small difference in intensity compared to this level. For a counting system ΔI can be replaced by ΔN,

the difference in the number of counted hits between the signal- and the background area, and I by the number N of background counts which yields $C = \Delta N/N$.
Basically C depends only on the difference in attenuation coefficients of the viewed detail and the surrounding material, but scattering should be considered as well as it contributes to the measured intensity [Web98].
The contrast remains unchanged for an increasing number of incident photons, i.e. increasing dose. Therefore it is not the ideal term to evaluate image quality for radiography.
On the other hand, it is very useful to determine the minimum threshold which the system is just able to visualise. This *threshold contrast* is inversely proportional to the square root of the object area and the number of photons [Wor97]. To measure the threshold contrast detail detectability so-called *phantoms* are commercially available. They consist of a block of some kind of tissue substitute with small calibrated objects embedded which simulate clinical image features. There exist many varieties; one sort of phantom uses objects which change their size at a fixed contrast value in one direction, and in the other direction the size is fixed but the contrast varies. With such a phantom the minimum detectable contrast for a specific object size at a certain value of exposure can be determined and graphically represented in a *contrast-detail diagram*.

1.1.2 Signal-to-noise ratio

Contrary to the contrast the *signal-to-noise ratio* (SNR) is a good indicator for radiographic image quality. In a radiographic system the quality of an image is determined not only by the quality of the recorded signal, but also by the noise level. Noise fluctuations can mask real fluctuations and care should be taken of reducing noise as much as possible. For a real signal to be detectable, the signal has to be higher than the noise; published threshold values for the SNR range between 3 [Wor97] and 5 [Web98] above which a human observer can recognise a detail.

Photonic noise is the fundamental noise limit for any system and corresponds to the lowest limit for patient irradiation in diagnostic radiology. It is due to fluctuations in the number of X-rays absorbed per unit area of the detector and is also called 'quantum mottle'. Other noise sources are fixed pattern noise which is related to inhomogeneities in the detector and electronic noise from the connected read-out chain. Fixed pattern noise is directly proportional to the signal and can be diminished through proper calibration. Electronic noise in integrating systems is proportional to the exposure time [Fro98].
Photonic noise obeys Poisson statistics. For a mean number of N absorbed X-rays per unit area, the actual number absorbed in other identical areas will result in a statistical distribution with N as mean value and $\sqrt{N}$ as its standard deviation[3]. For a linear radiographic imaging system where photonic noise dominates and single quanta can

[3]Semiconductors with a Fano factor much smaller than 1 deviate from Poisson statistics (section 4.1.1).

be counted the SNR is given by

$$\mathrm{SNR} = \frac{\Delta N}{\sqrt{N}} = C\sqrt{N} \tag{1.1}$$

using the defined parameters from section 1.1.1. More generally this equation can be written as

$$\mathrm{SNR} = \frac{\Delta I}{\sigma_I} = \frac{CI}{\sigma_I}$$

where σ_I denotes the standard deviation of the intensity distribution. The higher the number of absorbed X-rays, the better the SNR and the image quality, but evidently the dose increases as well. The SNR doubles for a linear system when the exposure time is quadruplicated.
Besides the absorption efficiency of the detector the SNR depends on the operation mode of the system; counting or integrating mode. It was shown that the 'ideal' detector which yields maximum SNR disregards energy information in the beam and simply counts the photons [San92]. Energy integrating systems can only reach maximum SNR with a monoenergetic photon beam.

In reality, the noise is not fully described by its amplitude value. Fluctuations of the integrated noise with spatial frequency have to be taken into account. From a uniform X-ray exposure the variance of the resulting distribution can be analysed in view of the the spatial frequency components. This gives the *Noise Power Spectrum* (NPS) also referred to as the *Wiener spectrum* [Wel95]. The intensity of the noise sources usually decreases with increasing spatial frequency [Wor97] (like for real signal sources) because they get more blurred by the imaging system.

1.1.3 Detective quantum efficiency

The *detective quantum efficiency* (DQE) describes how a SNR at the input of an imaging system SNR_{in} is transferred to the output (SNR_{out}).

$$\mathrm{DQE} = \frac{\mathrm{SNR}_{out}^2}{\mathrm{SNR}_{in}^2}$$

An ideal detector extracts all the information from the incident beam which means SNR_{out}=SNR_{in} and DQE=1.
The DQE for a complex imaging system is the product of the DQE for each stage in the imaging chain. Therefore, the DQE for a complete system is never better than the DQE of its weakest component. In a direct detection system (see section 1.2) the efficiency equals essentially the absorption efficiency of the sensor.

1.1.4 Modulation transfer function, contrast transfer function and line spread function

Spatial frequency in radiographic images is an important concept already mentioned in section 1.1.2. It leads to the formulation of the *modulation transfer function* (MTF) whose measurement is widely used to evaluate the performance of an imaging system.
Signals which change often over a given distance have a high spatial frequency and are more difficult to detect than signals which change slowly over the same distance. Therefore the MTF has its maximum of 1 at a spatial frequency of 0. It decreases with spatial frequency more slowly for highly granular systems than for systems which have less granularity.
The basis of the MTF are sinusoidal intensity profiles with different frequencies in space. Using Fourier transformations each image detail can be decomposed to be the sum of such profiles of different spatial frequencies with varying amplitude and phase relationships. With this concept information about the size of an object (spatial domain) can be related to the spatial frequency domain. Large structures contain mainly low spatial frequencies whereas small details with sharp edges have to be described including mostly high spatial frequencies.
The MTF is the ratio of the amplitude of spatial frequency at the output of the imaging system to the amplitude of the same spatial frequency at the input and describes therefore the ability of an imaging system to reproduce signals of a range of spatial frequencies [Wor97]. Sharp images can be produced with an imaging system which is able of well reproducing high spatial frequencies. Considering a pixel system the pixel size should be at least as small as twice the highest spatial frequency to detect. This requirement is called the 'Nyquist sampling criterion'[4]. If the pixel size is larger this will lead to image distortions called 'aliasing'.

The *contrast transfer function* (CTF) is very similar to the MTF. It concerns the modulation of a signal passing through a *test grating* or *bar pattern*. Test gratings are made from a series of groups of lead bars and spaces with bars and spaces being of equal width and are used to determine spatial resolution of imaging systems. Spatial resolution is then given in units of lp/mm (*line pairs per mm*). If the system is capable of visualising a pattern with bars and spaces of a width of 100 μm, its spatial resolution is 1/(0.1+0.1)=5 lp/mm.
The CTF is measured by exposing a number of bar patterns with known spatial frequencies ν_i [Fro98]. It can be determined by calculating the modulation of the resulting signal:

$$\mathrm{CTF}(\nu) = \frac{I_{max}(\nu) - I_{min}(\nu)}{I_{max}(\nu) + I_{min}(\nu)}$$

[4]The Nyquist frequency is defined as 1/(2×pixel size [mm]) and is therefore ∼3 mm^{-1} in the case of the PCC.

The same method is often used to measure the MTF. This is not strictly correct as a series of line pairs corresponds to a square wave pattern and not to a sine wave pattern, but the resulting difference seems to be small [Wel94].

The most common method for calculating the MTF is to measure the *line spread function* (LSF) [Fro98]. One makes use of the fact that a square function can be expressed as a Fourier series of sine functions. The LSF is a measure of the blurring of the image from a very thin line[5]. The broader the LSF the worse is the blurring. The result of the measurement depends on the orientation of the line mask for digital systems. The slit should be inclined approximately 45^o with respect to the pixel side for square pixels [Wel94] with the peak of the LSF at the centre of a pixel. To determine the LSF one has to calculate the distance between the slit and the centre of the respective pixel for a large number of pixels. The signal of these pixels is then plotted as a function of distance [Fro98]. The MTF is obtained subsequently by Fourier transformation of the LSF and is valid in the direction perpendicular to the slit.
The image of a sharp edge can be used as well. The underlying principle is the same; the normalised MTF is calculated making again use of a Fourier transformation, but this time of the measured *edge spread function* (ESF) [Gep98].
A 2-dimensional representation of the system transfer function in the spatial frequency domain can be obtained through a 2-dimensional Fourier transformation (with normalisation of MTF(0)=1) of a measured *point spread function* (PSF).

To be complete, the *optical transfer function* (OTF) should be mentioned as well. It is defined as the (2-dimensional) Fourier transform of the output of a (2-dimensional) system which has a delta function as its input. For linear and uniform systems an image may be thought of as a superposition of many delta functions [Dob95]. The 1-dimensional OTF is the same as the Fourier transform of the LSF and the MTF is nothing else as the amplitude of the complex OTF.

1.1.5 Noise equivalent quanta

The *noise equivalent quanta* (NEQ) is also an important parameter and signifies the maximum $(\mathrm{SNR})^2$ of a system at a specific spatial frequency ν. As the MTF describes the transferred amplitude of a system at a given ν and the noise power spectrum the amplitude variance at ν, then the (properly normalised) ratio of these quantities gives information about the maximum available SNR as a function of ν [Dob95].

$$\mathrm{NEQ}(\nu) = \frac{(\text{large area signal})^2\ \mathrm{MTF}^2(\nu)}{\mathrm{NPS}(\nu)}$$

This equation is valid if the measured large area signal (also referred to as intensity transfer function) is linearly related to the input signal.
The name 'noise equivalent quanta' is explained considering equation 1.1 as the NEQ

[5] much thinner than the pixel size.

is equal to the apparent number of X-ray quanta per unit area used in image formation $=(\mathrm{SNR})^2$. This apparent number is always less than the actual number of incident X-rays due to noise processes and inefficiencies in detection, conversion and collection. The DQE for a given spatial frequency and an incident quantum fluence Q can therefore be derived [Wor97]:

$$\mathrm{DQE}(\nu) = \frac{\mathrm{NEQ}(\nu)}{Q}$$

From this description of the various image quality parameters it is already possible to recognise the properties which should be optimised. Low noise, high absorption and conversion efficiency in each imaging stage, high spatial resolution, uniformity, low scattering etc. The following sections will discuss different concepts applied to obtain good images at minimum patient exposure.

1.2 Indirect and direct X-ray detection systems

An important distinction between different imaging systems can already be made at the photon detection level. In *direct* photon detection systems the X-rays convert in the detector itself whereas in *indirect* systems use is made of an intermediate layer to convert the X-rays into visible light which is subsequently detected in the sensor. In the latter case the spatial resolution is deteriorated because of the lateral spread of the light photons which is a function of the distance of the light emission point to the detector. This suggests that direct photon detection is preferable for spatial and contrast resolution.
In radiology most of the systems are indirect photon detection systems (screen-film, image intensifier, CCD systems,...). A lower spatial resolution is accepted as a trade-off with improved sensitivity. For a direct exposure X-ray film the energy absorption efficiency for 20 keV photons ranges only around 7% whereas with screen-film systems $\sim$95% can be reached for the same energy [Web98]. The fluorescent screens consist of special phosphors with high energy absorption coefficients and high fluorescence yields.

1.3 Analog and digital systems

Although most of the images in radiology are still only available on film which means in analog form, there is no question that the future will be digital. There are too many advantages related to data in digital form (a report of clinical experiences with digital systems is given in [Kra93]). First of all it is possible to perform *image processing*. Selecting different ranges in brightness or information density in the image display enables the doctor to focus on different details of the image. The use of specific mathematical algorithms and software filters can enhance barely visible structures or

structure edges[6]. A second major advantage is that digitised images are produced instantaneously and *transferred easily*. Thus images can be evaluated by specialists in different locations. *Data storage and archiving* is much facilitated compared to film[7]. Moreover it requires less space and no development procedures. Film development is not only time consuming, but requires also chemicals and represents one more critical step in the image formation.

Besides these points *dose reduction* is certainly one of the strongest arguments for digital systems. Films have a very limited margin of exposure defined by their characteristic curves (see section 1.5). With digital systems the dose can be optimised to the required signal-to-noise level for a specific setup, task and patient anatomy.

Image processing is a powerful tool which requires digital systems. One basic technique is *subtraction imaging*. The principle of subtraction imaging is to enhance the part of the body to be examined by subtracting the surrounding body environment. For this purpose a contrast medium is given to the patient which accumulates in the region of interest and which attenuates strongly the X-rays. Images are taken before and after the contrast agent is injected and they are subtracted from one another.
Digital subtraction angiography (DSA) makes use of this method to visualise blood vessels. In conventional coronary arteriography a contrast agent, mostly containing iodine, is injected by means of a catheter directly into the orifice of the coronary artery [Rub84]. The catheter is needed in order to inject the contrast agent close to the imaging region providing maximum image contrast through minimal dilution of the iodine. Unfortunately, this arterial invasion represents quite some risks to the patient; there are complications in about 2.2% of cases with 0.5% severe complications and ∼0.23% mortality [Lew97]. Therefore the use of coronary arteriography is limited to patients suspected of having a far advanced disease.
With DSA the image contrast can be dramatically improved (contrast resolutions as low as 1% can be achieved [Web98]) which avoids arterial invasion. Still it stays an invasive method introducing a catheter into the central venous circulation. There the contrast agent is injected under high pressure. For time subtraction one image without the contrast agent is made and is logarithmically subtracted from the one taken after injection of the contrast agent. To get dynamic information in time several images with a certain frame rate are taken (pulsed or continuous (!) X-ray exposure depending on the speed of the contrast agent dilution). Anatomic motion prevents that this method can be applied to image small vessels and coronary arteries.
An improvement can be obtained by adding energy subtraction. *Dual-energy radiology* is another image subtraction technique and consists of subtracting two images at two different X-ray energies. Each material in the body has its own attenuation curve which is a function of the photon energy (compare chapter 2). If two materials are considered (e.g. bone and tissue) it is possible to calculate with the information of the

[6]Offline image treatment and especially 3-dimensional image reconstruction has grown to one of the most important fields within medical imaging.

[7]although image compression and high disc storage capacitance seem necessary.

two images the thickness of the materials at each point of the projection. Therefore attenuation maps can be produced and the image corrected in a way that only one material, e.g. bone, is selected. The problem of this technique is the need for rather monoenergetic X-ray beams. X-ray tubes with appropriate filtering were proposed, but then the X-ray flux is insufficient.
K-edge dichromography is certainly the most efficient technique for DSA. The major limitation of the technique is that it requires precise and intensive monoenergetic X-ray beams which can only be provided by synchrotrons. As contrast agent a suitable high Z medium has to be chosen with a K-edge at a convenient energy. Again iodine is a very good candidate with its K-edge at $\sim$33.17 keV [Nis]. The idea is to make one image just above and another image just below the K-edge. The difference in photon attenuation between these two energies amounts to a factor of $\sim$6 whereas the attenuation almost doesn't change for normal body materials. The image created by logarithmic subtraction of the two images is therefore primarily composed of the iodine signal. The resulting improvement of the image is sufficient to allow for a reduction in the amount of contrast agent which in turn allows for a safe intravenous injection[8]. Synchrotron based K-edge subtraction imaging can also be applied to the imaging of lungs and respiratory passages using inhaled xenon as a contrast agent [Rub95].

1.4 Counting versus integrating method

There are two different principles for recording the signals from particles or photons; the counting or the integrating method. In the *photon counting method* the signal height from a photon is compared to a threshold set in a comparator. If the signal exceeds this threshold the value of a counter is incremented. Each photon with an energy above threshold has the same weight of one. The possibility to set a threshold implies that background can be eliminated which increases the signal-to-noise ratio and the dynamic range.

The *integrating method* does not comprise a threshold. All the incoming signals including noise are added up. This reduces the signal-to-noise ratio and the dynamic range. Moreover, a weighting of photons with different energies takes place. Photons of higher energy deposit more charge in the detector or produce more blackening which results in a higher signal. Compared to photon counting this could be a disadvantage. If one considers again mammography the higher part of the energy spectrum of fig. 1.4(b) after having passed through the patient carries much less useful information than the lower energy part, but has more weight in the image formation of an integrating system.
Examples for integrating systems are all kinds of film systems, amorphous semicon-

[8]The iodine gets diluted during transit to the coronary arteries by a factor of approximately 50 [Lew97].

ductor arrays or CCDs.

Advantages of photon counting detectors include

- Noise suppression. This leads to ↪
  - *Higher SNR* [Gep98]. The elimination of different noise sources results in a higher signal above noise. This goes along with *dose reduction* and a *higher dynamic range*.
  - Long data acquisition periods for *low dose rate imaging* become possible. Applications like autoradiography[9] could profit from this fact.
    No intermediate read-out or refresh signals are necessary if an active shutter and static logic are chosen in the design. This reduces dead time to negligible values on the single pixel level[10].

- *Linear and theoretically unlimited dynamic range.* Film systems suffer from a very restricted linear range. In CCDs the linearity is much extended, but as mentioned already higher energy photons are weighted greater than low energy ones. Moreover, the dynamic range has a practical limit given by the technology[11] which has to be compared with the noise level.
  The limitation in dynamic range of counting devices consists only of the space needed to implement the transistors for the counters in a certain area of the pixel cell.

- A very precise threshold setting opens the *possibility to cut off strongly Compton scattered events* [Ped97]. This is mainly valid for monoenergetic X-ray sources. Scattering in the patient is a serious problem which leads to image blurring. Ratios of scattered to primary radiation can attain 80% after passage through a 6 cm thick breast [Dan81, Jon82]. Scattered radiation is one cause why small details and low contrast objects are often undetectable. Usually this problem is addressed with anti-scatter grids, airgaps or scanning slits (the related increase in dose is in the order of a factor 2 [Sae96] for mammography).

1.5 Systems used for X-ray imaging

In this section a brief overview over a selection of systems for medical X-ray imaging will be given. This should help in better understanding the difficulties related to this field and the advantages a PCC-like system could bring.

[9] In autoradiography quantitative 2D-imaging of the distribution of radioactive tracers in thin biological samples is performed. The available photon intensity is very low which usually requires exposure times in the order of several hours or even days.

[10] Dead time is reduced to the reset time of the amplifier after a pixel received a hit above threshold.

[11] The voltage which can be applied to the transistors has to stay below breakdown values.

1.5.1 Film based systems

Film based systems still represent the biggest fraction on the market of medical X-ray imaging systems. Their main advantage is an excellent spatial resolution which is mainly limited by the thickness of the sensitive emulsion ($\sim$20 μm [Web98]). The film emulsion is composed of gelatin containing a silver compound and is deposited on a flexible support, the film base. The silver halide[12] grains are about 1 μm in diameter. When energy from X-rays or from light is absorbed by the grains, one or more electrons are released from the halogen atoms. These electrons slow down through ionisation and are eventually captured at trapping centres within the grains. So-called development centres arise which attract more and more electrons. These development centres contain the *latent image*. Film development amplifies the conversion of the illuminated grains into black metallic silver. The unexposed silver is removed as part of the fixing process.

The film blackening is expressed in terms of *optical density* D. It is defined over the transmission of light through the film by the relation

$$D = \log_{10}(I_0/I)$$

where I_0 and I are the intensities of a light beam before and after passage through the emulsion.
Each film+processing is characterised by a *characteristic curve* or *H&D curve* (named after Hurter and Driffield who first used the curve with photographic films in 1890). Film characteristic curves plot the relationship between optical density and the logarithm of relative film exposure. An example for two different characteristic curves of two screen-film combinations (A and B) are shown in fig. 1.5 [Piz93]. The *film contrast* relates the differences in optical density on the radiograph to the differences in exposure. It is expressed through the Γ-*factor* of the film and corresponds to the slope in the linear part of the characteristic curve. The steeper the curve the better the contrast between small differences in X-ray fluence. Since exposure conditions were the same for the two radiographs in fig. 1.5, film B has a higher film contrast.
Film *latitude* is related reciprocally to film contrast. It corresponds to the exposure range which can be applied to produce a satisfactory radiograph. Wide latitude films have lower film contrast than low latitude films. The choice of latitude depends on the application. In general, wide latitude films are used if the inherent subject contrast is high (like for chest radiography).
A considerable disadvantage of film systems is their limited range of exposure. Over- or underexposure results in a loss of contrast. The region for insufficient exposure is called the 'toe'-region of the film. The toe-region is dominated by the *fog level* (compare fig. 1.5. The fog level is a certain optical density arising from factors other than the radiation used for imaging like heat, humidity, background radioactivity or spontaneous conversion of the silver halide grains into metallic silver. The other end of the characteristic curve corresponding to an overexposure of the film is called the

[12]Bromide is the most commonly used element of the halide family.

'shoulder'-region. The optical density reaches saturation, and increased exposure does not improve the contrast anymore.

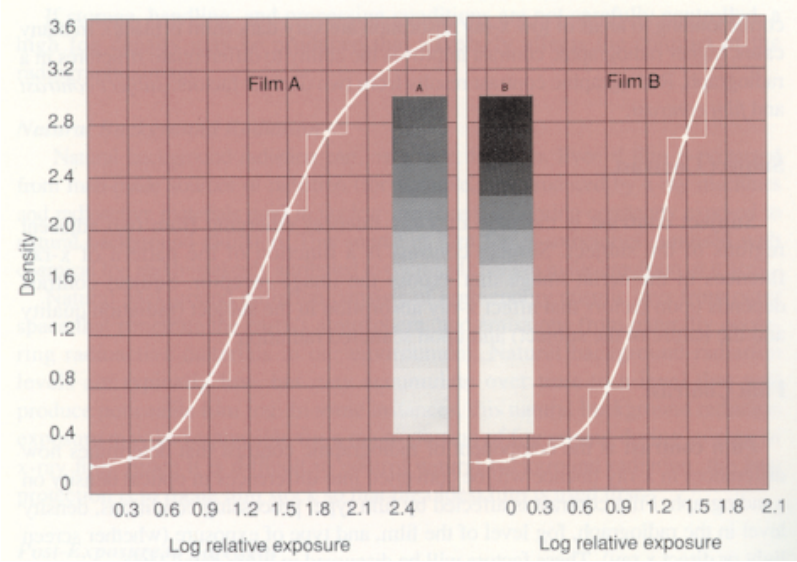

Figure 1.5: *Radiographs of a stepped-wedge taken under identical exposure conditions with two screen-film combinations A and B and their associated characteristic curves [Piz93]. The density differences between steps in the middle density range of curve B are larger than those for curve A which is a result of the higher film contrast of curve B.*

It was already mentioned (section 1.2) that a sheet of film has only a very poor absorption efficiency for X-rays. In spite of their high spatial resolution this is the reason why such *direct exposure films* are practically not in use.
Nevertheless they are widely used as receptors in *screen-film combinations*. An intensifying screen absorbs part of the X-rays. A fraction of their energy is then re-emitted as light fluorescence photons which are subsequently detected in the emulsion. A screen consists of a 70-350 μm thick layer of active phosphor crystals embedded in a binder together with other optimising components. They are fast devices, but screen-film combinations tend to lead to blurred images as a result of the lateral spread of the fluorescence photons in the screen. A good contact between screen and emulsion is essential and often absorptive dyes are used which favour the light produced close to the emulsion. To increase the absorption efficiency two screens with two emulsions on either side of the film base can be employed. Mammography is an example for a single-screen application. There a good spatial resolution is more important than some dose reduction.
Examples for phosphors used in intensifying screens are calcium tungstate, barium sulfate, oxybromides and especially oxysulfides of the rare-earth elements (gadolinium, lanthanum and yttrium). These phosphors should possess among other requirements high X-ray absorption efficiency, high conversion efficiency and a good spectral matching with the light-sensitive film. X-ray conversion efficiencies are below 20% and the prob-

ability for the light photons to reach the emulsion about 50% [Web98]. The losses of quanta during the various stages of image formation combined with the absorption efficiency result in a relatively low DQE for screen-film systems, a typical good value being of the order of 0.2 at a spatial frequency of 0 cycles/mm [Yaf97].

1.5.2 Xeroradiography

Xeroradiography is a non-silver photographic system and produces images on paper which are viewed by reflected light. The receptor consists of a 125 μm layer of amorphous selenium deposited on a 2 mm thick aluminium backing plate [Web98]. Prior to radiographic exposure, a uniform positive charge is produced on the surface of the selenium. The X-rays which are absorbed during the examination produce electron-hole pairs in the semiconductor. The electrons that reach the top surface due to the internal electric field recombine with the positive charges which results in the formation of a latent image.
An aerosol of blue powder is sprayed on the surface; a matching powder pattern builds up. After the development process positive or negative images on paper are obtained.

The system is slower than screen-film systems and the charge collection efficiency (CCE) of the receptor is quite low (only $\sim$16% of the created electron-hole pairs reach the Se surface). Moreover, the radiation dose is 2-4 times higher than for a screen-film combination with a molybdenum X-ray tube [Web98]. Therefore the only justification to use xeroradiography is its excellent image quality in terms of resolution and edge-enhancement.

1.5.3 Phosphor/CCD systems

Imagers based on charge coupled devices (CCDs) have obtained a steadily increasing importance. In many fields they replace film as the image receptor due to the advantages a digital system implies. Their development could profit from the technology push from the camcorder market.

A CCD imager consists of a pixellated silicon detector which is segmented into a matrix of square potential wells. The photons which penetrate in the semiconductor substrate produce electron-hole pairs which are separated through an applied electric field. The charge accumulates in the potential wells $\Rightarrow$ signals from several events are integrated in the pixel(s) closest to the interaction point. Different read-out architectures exist. Usually, for an imaging array one row of data is first transferred to a read-out register which is clocked out. Subsequent rows are transferred to the read-out register sequentially. When the integrated charge of each pixel reaches the output node at the end of the read-out register, it is measured by a charge sensitive amplifier and subsequently digitised by an analog-to-digital converter. The output of a CCD results in a serial train of pulses which is well adapted for display on a video monitor. Often correlated double sampling is used to correct for the zero level of the

charge integrating capacitance in the output node to minimise correlated noise.

In medical X-ray imaging the conversion of the X-rays takes place in phosphor screens. Because the size of CCDs is limited, it is necessary to employ some means of demagnification between screen and CCD. This can be achieved either by optical lens coupling or by using a fibre optic taper. Fibre optic taper is preferred due to smaller light losses [Yaf97].

CCDs with pixel sizes around 10 μm are already available, but spatial resolution is deteriorated mainly by the lateral spread of the light photons produced in the phosphor screen. The dynamic range of CCDs is determined by the depth of the potential wells minus the integrated noise. With low noise a dynamic range of about 10^5 can be achieved [Far95]. Read-out times are in the order of a few seconds; faster read-out increases the noise [Far00]. Care has to be taken to prevent the overfilling of the wells at regions of high exposure and to achieve practically perfect charge transport efficiencies from pixel to pixel.

A *scanning system* has been proposed for mammography [Yaf97]. It consists of a series of long and narrow CCDs. This 'slot' detector is connected with fibre optic tapers to three phosphor strips of 3.2 mm $\times$ 240 mm which are butted together. In order to avoid an inefficient utilisation of the X-ray tube in the case that only collimators would be used, the X-ray beam is narrow by itself, but extends across the full image field. The X-ray beam works continuously during acquisition and a time delay integration mode is employed as read-out mode of the CCDs. In time delay integration mode charge is shifted down the CCD columns; at the same time the X-ray beam plus the detector moves upwards. Therefore the charge packets remain in principle stationary with respect to a given projection path through the breast. The CCD arrays are read out at the end of the scanning procedure.
Scanning systems have the advantage of reducing significantly scattering, but they require longer examination times. This tends to wear out the X-ray tubes and incurs the risk of patient movement which distorts the image.

1.5.4 Storage phosphors

Storage phosphors are frequently used detectors for digital radiography. They make use of *photostimulable luminescence*. Electrons which are generated by ionisation are trapped at an intermediate energy level between valence and conduction band and can be released by exposure to red or near-infrared light. Suitable phosphors are commonly found in the barium fluorohalide family and contain europium which introduces an energy level below the conduction band. When X-rays interact with the material a large fraction of the generated electrons are trapped at this level producing a latent image in the phosphor plate [Yaf97]. After exposure the plate is raster scanned with an appropriate laser beam which releases the trapped electrons and raises them to the conduction band. Subsequently, shorter wavelength light is emitted and measured

with a photomultiplier tube via a linear light guide. The output of the photomultiplier can be digitised.
Storage phosphor plates can be used as a replacement of film cassettes in a conventional X-ray machine setup. Large area detectors are conveniently produced and the plates are reusable after erasure of any residual latent image. Spatial resolution is limited by the spreading out of the stimulating light beam as well as of the released stimulated light (which is a function of the phosphor thickness) and depends also on the laser power. It is comparable to the spatial resolution of film-screen systems. Administered doses tend to be slightly higher than for screen-film systems (lower X-ray conversion efficiency), but the big advantage of storage phosphors compared to screen-film systems is their broad and linear dynamic range up to approximately 10^5 [Har88]. This allows for a wide choice of exposure conditions. Over- or underexposure and repeat exposures can be avoided. Therefore storage phosphors are widely used for emergency and in mobile radiography.

1.5.5 Image intensifier tubes

Image intensifiers are high-gain devices with a low associated radiation dose. They can operate in *fluoroscopy* mode where the X-ray tube runs continuously, but at a very low current [Web98]. Image intensified fluoroscopy is at the moment essentially the only dose-efficient X-ray detection technique that allows *real-time imaging* [Yaf97].

In image intensifier tubes the X-rays enter the entrance window of the evacuated tube and are converted into light in the large input phosphor screen. The photons from the fluorescence then liberate electrons from the directly coupled photocathode. The ejected photoelectrons are accelerated through a potential difference of 20-30 kV and electrostatically focused onto a small ($\sim$2.5 cm diameter) output phosphor screen. The image produced at the exit window is generally viewed by a video camera, but other systems like CCDs can be used as well.

Image intensifier tubes are used to study processes that involve some kind of movement like control during surgery, insertion of catheters or investigations with contrast media. Mainly because of its high gain and demagnification an image intensifier tube is a *quantum limited device* [Yaf97]. Disadvantages are non-uniformities, unsharpness and image distortion as well as its still bulky construction.

1.5.6 Flat-panel systems

Flat-panel systems are relatively new digital devices which offer the possibility of instantaneous read-out besides the traditional radiographs. This advantage together with the rapid improvement in terms of spatial resolution, compactness and the possibility of large area coverage explains the interest of the medical community. This approach benefits from the developments made for flat-panel systems from the already well known technology of large area active matrix arrays for liquid crystal displays and

solar cells.
Two general approaches for flat-panel digital X-ray detectors exist and will be explained briefly: the indirect method where a phosphor layer is used in combination with the photodiode array and the direct method which can do without phosphors because of a high-Z X-ray detection material.

1.5.6.1 Phosphor based flat-panel systems

In this type of flat-panel detector the X-ray conversion takes place in a phosphor layer such as gadolinium oxysulfide or thallium-doped cesium iodide[13]. The large area photodetector consists of a matrix of individual photodiodes made of hydrogenated amorphous silicon (a-Si:H)[14]. The charge created by the light photons is stored on the pixel capacitances. During read-out one row after the other is activated and the signals are amplified at the end of the column, multiplexed and digitised. Large area a-Si imagers with a pitch of $\sim$100 μm are already available [Rah99].
One disadvantage which becomes more pronounced for small pixel sizes is the fill factor of the device which is less than 100%. The fill factor denotes the active detection area. The insensitive pixel area is due to the switching logic, control and signal lines. Attempts have been made to increase this fill factor with optimised pixel layouts [Rah99]. Besides the problem of the fill factor the X-ray conversion layer leads to some lateral spread of light. In spite of this the reported image quality seems to surpass screen-film systems [Cow97].

1.5.6.2 Direct X-ray conversion flat-panel systems

Lateral spread of light or charge which deteriorates the spatial resolution can be minimised with direct X-ray conversion detectors. Amorphous selenium (a-Se) is well suited for this purpose. It is a photoconductive material with high stopping power for X-rays in the diagnostic energy range and is uniform over large areas (no grain boundaries).
In an a-Se imager the absorbed X-rays create electron-hole pairs in a Se layer which is evaporated onto a matrix of pixel electrodes and control logic. An electric field guides the charge to the pixel electrodes where it accumulates on the pixel capacitance ($\Rightarrow$ charge integrating system). A similar read-out scheme as already described for the a-Si imager can be used as well as laser-induced discharge of the surface charge distribution.
Amorphous selenium imagers offer the same advantages as indirect (a-Si:H) flat-panel systems including real-time imaging, but they avoid the fill factor problem and possess excellent intrinsic spatial resolution [Cow97].

[13] Higher spatial resolutions can be achieved with (CsI:Tl) as it can be produced in a special column structure with cracks in between resulting in a sort of photon channelling [Cow97].

[14] Amorphous silicon differs significantly from single crystal silicon material. Electron and hole lifetimes for example are orders of magnitude less than those of silicon which limits the thickness of a-Si detectors [Squ95].

One disadvantage is the relatively large amount of energy needed to create an electron-hole pair (in the order of 44 eV [Web98]). Moreover, charge carrier lifetimes in amorphous materials are orders of magnitude below the ones of pure crystalline material. Therefore high voltages have to be applied to the detector.

In principle, other easy producible high-Z materials with sufficient homogeneity could be used instead of a-Se. For example mercuric iodide, cadmium-zinc telluride or thallium bromide are being investigated as detector materials in imaging devices. Silicon as the best known and cheapest semiconductor material is not very well suited as a direct detection material in medical imaging due to its poor photon attenuation. Nevertheless, a layer of 1.5 mm thickness would be sufficiently efficient in the diagnostic X-ray energy range (1.5 mm Si have an absorption efficiency of ∼91% at 70 keV X-ray energy). On the other hand, spatial resolution would decrease, especially if the X-rays do not enter the material with an angle of 90^o. This problem can be avoided if the detector array is arranged along a curved surface with the radius of curvature equal to the source to image plane distance [Yaf97].

1.5.7 CMOS imagers with direct photon detection

The next step in the development of a direct conversion flat-panel imager is certainly a direct conversion CMOS imager. A high-Z material converts the X-rays with high efficiency and an electric field collects the created electron-hole pairs leading to an optimum intrinsic spatial resolution. A CMOS pixel chip which is either integrated in the sensor material (monolithic approach) or closely connected to the segmented sensor (hybrid approach) offers a steadily increasing amount of functionality and signal processing on chip [Cam89, Fos97]. This functionality can be adapted to a specific imaging task, and fundamental limits are only set by the CMOS component size which decreases steadily and by the performance of the sensor material. Dynamic range as an example has in principle no upper limit. A large area coverage is the only important issue of CMOS imagers which has to be solved in the coming years[15].

The photon counting chip system (PCC) is such a novel detector which comprises a high-Z semiconductor sensor bump-bonded to a CMOS pixel chip (the chip will be described in detail in chapter 5). The sensor of the PCC system converts the X-rays directly into electric charge which is collected under the influence of an applied electric field at the pixel electrodes (square pixels with 170 μm pitch). A semiconductor material with high atomic number, GaAs, was selected to assure a high photon detection efficiency in the photon energy range used for radiology (see chapter 7). A 300 μm thick GaAs detector is theoretically ∼100% efficient in the detection of photons produced by a mammographic X-ray tube.

[15]Tiling of the single detectors is the simplest solution, 3-side buttable chips can produce long linear arrays and large 2-dimensional arrays could be achieved with multi-chip modules (MCMs) if the technology can prove its reliability.

The special features of the chip design are the integrated pulse height comparator which discriminates events with charge deposition above the set threshold from those below the threshold which includes noise signals. The selected hits are counted in a 15 bit counter. Therefore, the PCC is a digital imaging system and comprises all the mentioned advantages of digital systems. To be more precise, its basic principle is binary. A photon is either counted as one if the collected charge which it created in the detector material is above threshold or it is ignored. The threshold can be set corresponding to different values of deposited charge. Noise suppression should certainly lead to some dose reduction, and the variable threshold could also be used to optimise some of the imaging techniques. Threshold uniformity over the pixel matrix is improved through the availability of 3 bits per pixel for fine tuning. A compensation circuitry for the detector leakage current is integrated as well.

There are also other groups which have chosen the photon counting approach. The efforts can be divided up in groups that have been developed CMOS pixel chips [Roe96, Col97b, Fis99, Bro99, Sel99] or read-out chips for strip detectors working in photon counting mode [Beu98, Col97b]. These strip detectors are made of silicon, but are oriented edge-on with respect to the X-ray beam to assure a high X-ray absorption efficiency. They are used as a linear scanning system. Such a configuration simulates a pixel system; 2-dimensional resolution is defined in one direction by the strip pitch and in the second direction by the scanning step [Arf96, Mal00].

1.6 Summary

This introductory chapter into the physics of medical imaging is intended to point out the challenges detector systems have to face in X-ray projection radiology. This defines the tasks detectors have to comply with. Mammography is used as an example as it is one of the most technically challenging medical applications. First stages of breast cancer can occur in different forms; either as rather large objects, but with extremely low contrast compared to the surrounding breast tissue, or as microcalcifications with higher contrast, but of very small size. Therefore detectors should possess high spatial resolution as well as low noise and high dynamic range.
The assessment of image quality for different systems is a standard procedure to follow before a system is allowed to be sold on the market. Objective criteria were defined which concern different image parameters. An image in X-ray projection radiology should represent an attenuation map of the irradiated sample. Therefore objects can only be distinguished from each other if they have different photon attenuation properties which equals different contrast. Contrast is also one criterion in the image itself, but it does not imply the dose given to the patient. Good contrast can almost always be reached with sufficiently long exposure. The most important image quality parameters are related to dose and are the signal-to-noise ratio and the detective quantum efficiency. The system behaviour concerning the reproduction of different spatial frequencies and the limiting spatial resolution are best described with the modulation

transfer function.
Different imaging techniques have different limitations. Direct X-ray detection without prior conversion into light photons is better due to smaller image blurring. Counting the photons compared to an integration of the generated signal should also improve the image quality especially because it does not give a higher weight to higher energetic X-rays and requires a threshold which minimises noise.
Finally, an overview over existing systems for X-ray diagnosis is given. The largest fraction of the systems in use is still film based, but this will change steadily towards much more flexible digital systems.

The following chapters will describe the different parts of the PCC; the next chapter introduces the X-ray conversion processes in the detector material.

Chapter 2

Interactions of Low Energy Photons in Matter

Contents

In this chapter different energy loss processes for photons will be explained. As this thesis focuses on medical X-ray imaging applications only the energy loss of low energy photons (<200 keV) and of the subsequently produced secondary electrons (section 2.5) will be treated.
The energy loss of low energy photons is quite different from the energy loss of charged particles. Charged particles lose their original energy usually throughout many sequential interactions. Mainly ionisation of the orbital electrons within the target atoms makes them slow down gradually. Contrary to that photons are either completely removed from the incident photon beam or scattered after an interaction. They might also pass through the absorber without any deterioration of their energy and angle.
The main energy loss processes for photons are the following:

① Photo-electric absorption

② Compton scattering

③ Pair production

④ Nuclear reactions

In addition a pure scattering interaction can take place where the energy of the photon stays unchanged:

⑤ Rayleigh scattering

Only processes where the photons lose at least some of their energy contribute to the signal formation in an imaging system. Nevertheless in a segmented imaging detector scattering without energy loss can play a role. Photons which are scattered in such a way and later on produce a signal by undergoing some energy loss process falsify the spatial information of the irradiated sample. This problem will be discussed in chapter 7.

Pair production is the generation of a pair of an electron and a positron mainly in the Coulomb-field of a nucleus, but much less probably also in the Coulomb field of an electron. To create an electron-positron pair the energy of the interacting photon has to be at least 2 times the rest energy of the electron[1] and in the case where the pair is created in the Coulomb-field of an electron 4 times (due to the recoil energy which can be neglected for a nucleus). In medical X-ray diagnostics where X-ray energies are below 100 keV pair production does not occur inside the detectors. Also process ④ will not be described further in this thesis as nuclear reactions like photo-nuclear absorption are only relevant for photon energies in the MeV-region (see e.g. [Ful76]).

The different relative importance of energy loss processes ①-③ depending on the photon energy and the atomic number of the absorber is illustrated in Fig. 2.1. It can be seen that for X-ray imaging energies the photo-electric effect clearly dominates.

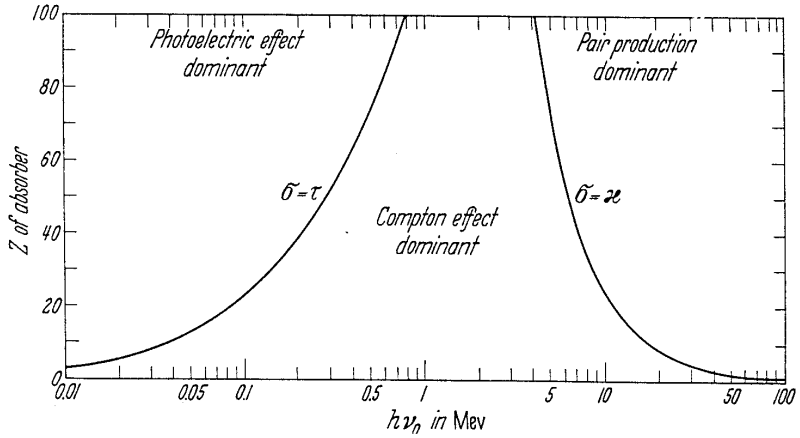

Figure 2.1: *Regions of the relative dominance of the photo-electric effect, Compton effect and pair production depending on the photon energy $h\nu_0$ and the atomic number Z of the target material [Eva55]. The left curve represents the location for equal atomic cross-section of the photo-electric reaction (τ) and the Compton effect (σ), the right curve of Compton effect and pair production (χ).*

[1]Rest energy of the electron: $m_e c^2 = 511$ keV.

2.1 Photo-electric effect

The photo-electric effect is one of the energy loss processes where the photon disappears after the interaction. A complete absorption of the photon energy is only possible with the bound electrons of an atom. The nucleus will take over the recoil momentum and a so-called *photo-electron* from one of the atomic shells is ejected. Therefore the energy of the interacting photon has to be greater than the binding energy E_b of the photo-electron plus the recoil energy (which is negligible). The probability of absorption of the photon is highest for K-shell electrons due to their proximity to the nucleus. After ejection of the photo-electron the atom is ionised. The vacancy in the bound shell will be refilled with an electron from the surrounding medium or from an upper shell. This may lead either to the emission of one or more *characteristic fluorescence X-rays* with an energy equal to the energy difference between the binding energies in the corresponding shells or to the ejection of an electron from one of the outer shells called an *Auger electron*. The Auger electron might originate from the L-shell ejected with an energy of $E_K - 2E_L$ as well as from the M-shell having an energy of $E_K - E_L - E_M$ and so on. The ratio of the two competing processes of fluorescence radiation emission and the Auger processes define the *fluorescence yield* (see table 2.1) which is an increasing function with Z [Seg77].

The emitted photo-electron forms an angle θ with respect to the direction of the incoming photon. With $\beta = v/c$ (v=speed of the photo-electron, c=speed of light) the angular distribution $d\tau/d\Omega$ (Ω as the solid angle) of the photo-electrons can be described for lower atomic numbers by the following formula [Sta71] with τ denoting the photo-electric cross-section:

$$\frac{d\tau}{d\Omega} \propto j(\theta) = \frac{\sin^2\theta}{(1-\beta\cos\theta)^4} + \frac{1}{2}\frac{3\left(1-\sqrt{1-\beta^2}\right)-2\beta^2}{\left(1-\beta^2\right)^{3/2}}\frac{\sin^2\theta}{(1-\beta\cos\theta)^3}$$

The first term treats the non-relativistic situation whereas the second term corrects for the relativistic case. It is now straightforward to transform the angular distribution in the solid angle to a distribution depending on the photo-electron emission angle θ with the following relation:

$$d\Omega = 2\pi \sin\theta \, d\theta \tag{2.1}$$

The resulting distribution $d\tau/d\theta$ normalised to 1 is shown in Fig. 2.2 in polar coordinates. The lower the photon energy the closer the maximum of the distribution gets to 90 degrees of θ. For 20 keV photons most of the photoelectrons are emitted at an angle of about 70 degrees.

The photo-electric cross-section per atom can be approximated for photons with non-relativistic energies above the K-edge:

$$\tau = 4\sqrt{2}\alpha^4\epsilon^{-7/2}Z^5\sigma_{Th}$$

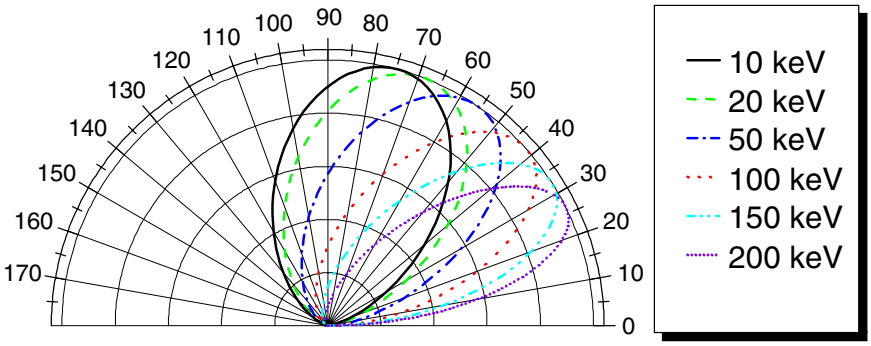

Figure 2.2: *Normalised angular distribution of the emitted photo-electron as a function of the incident photon energy.*

α corresponds to the fine-structure constant ($\approx 1/137$), ϵ is the reduced photon energy $h\nu/m_e c^2$ and σ_{Th} the Thomson cross-section (see equation 2.2). Correction factors have to be used when coming close to the different edges K, L, M,... [Leo87] (see Fig. 2.3). The photo-electric cross-section grows with falling photon energy which makes the photo-electric effect the dominant interaction for low energy photons (Fig. 2.1). Also there is a strong dependence on the atomic number Z which is very important when choosing an appropriate material for photon detection. The Z-exponent is found to vary between 4 and 5 in the energy range 0.1 MeV $\leq h\nu \leq$ 5 MeV [Eva55]. Fig. 2.3 shows the photo-electric absorption in GaAs depending on the photon energy. Clearly visible are the different L-edges close to 1 keV and the K-edges above 10 keV for gallium and arsenic. As soon as the incoming photon has enough energy to free e.g. an electron from the K-shell the cross-section rises strongly which results in the already mentioned *edges* in the absorption curve. Table 2.1 summarises the different values for K-, L- and M-edges above 1 keV for some chosen elements used in semiconductor photon detectors [Boo96].

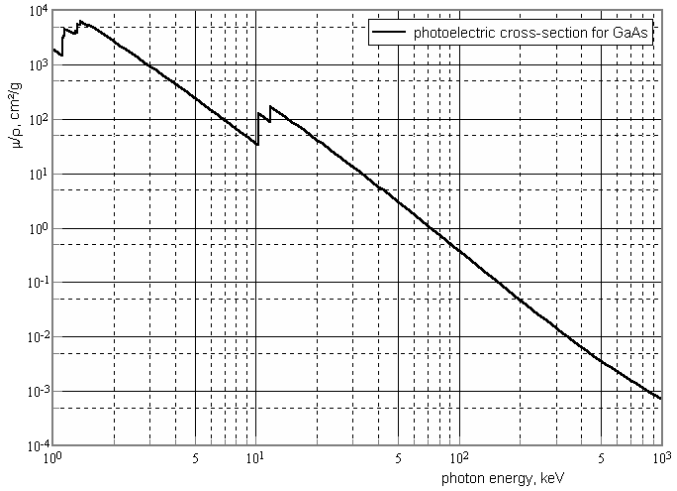

Figure 2.3: *Photo-electric absorption in GaAs as a function of the photon energy in the range 1 keV to 1 MeV ([Xmu] with data from [Boo96]). Above 1 keV the cross-section increases due to the different L-edges of Ga and As; the K-edges are responsible for the sudden increases above 10 keV.*

element	Z	K-edge	L1-edge	L2-edge	L3-edge	M1-edge	α_1	α_2	K-yield
Si	14	1.839	0.150	0.100	0.100		1.739	1.739	0.041
Zn	30	9.659	1.194	1.043	1.020	0.140	8.639	8.616	0.473
Ga	31	10.367	1.298	1.142	1.115	0.160	9.252	9.225	0.505
As	33	11.867	1.527	1.359	1.323	0.205	10.544	10.508	0.566
Se	34	12.658	1.654	1.476	1.436	0.230	11.222	11.182	0.593
Cd	48	26.711	4.018	3.727	3.538	0.772	23.173	22.984	0.836
Te	52	31.814	4.939	4.612	4.341	1.006	27.473	27.202	0.873

Table 2.1: *Summary of the K-, L- and M-edges above 0.1 keV for different elements used in photon detectors [Boo96, Ebi]. α_1=K-L3 and α_2=K-L2 are the energies of the most probable emitted fluorescence photons (all energies given in keV). The K-yield defines the probability for the emission of fluorescence radiation after refilling of the K-level.*

2.2 Compton effect

Experimental results from A.H. Compton in 1922 showed that scattered radiation was lower in energy than the primary. This could only be explained by the quantum character of radiation contrary to the wave model used until then and describing the elastic scattering of photons on electrons through the Thomson cross-section. Thomson started his calculations from the assumption that a free electron can oscillate in the electro-magnetic field of a photon and act like a dipole with the scattered radiation as its radiation field. With these assumptions including the prediction that the scattered radiation would have the same frequency as the incident radiation the *Thomson scattering cross-section* can be expressed as

$$\sigma_{Th} = \frac{8\pi}{3} r_0^2 = 0.6652 \times 10^{-24} \text{ cm}^2 = 6.652 \text{ barn per electron} \tag{2.2}$$

with $r_0 = \frac{e^2}{m_e c^2} = 2.8179 \times 10^{-13}$ cm as the classical electron radius.
Later experiments proved that the prediction of no energy change during the scattering process was incorrect, but still the Thomson formula is useful to describe some effects and is valid in the classical limit $h\nu \ll m_e c^2$.

For higher energies one has to consider the quantum nature of light which permits the mathematical description of the *Compton effect*. The Compton effect deals with photons which are scattered by free electrons[2] and lose some of their primary energy. The change in wavelength of the photon increases with increasing scattering angle θ. The energy and momentum lost by the photon is transferred to one electron, the *recoil electron* which is emitted in an angle ϕ with respect to the direction of the incoming photon and can have a maximum kinetic energy defining the so-called *Compton edge*. Since the electron subsequently loses its energy in the material the Compton cross-section σ is a sum of the scattering cross-section σ_s and the absorption cross-section σ_a: $\sigma = \sigma_s + \sigma_a$ (see e.g. [Eva58] for details).

[2]The electrons in an atom are considered as free due to the high photon energy compared to the binding energy of the atomic electrons.

Applying Dirac's relativistic quantum theory Klein and Nishina calculated a formula for the differential collision cross-section for the energy scattered from unpolarised incident radiation by stationary and unbound electrons [Kle29], the *Klein-Nishina formula*:

$$\frac{d\sigma}{d\Omega} = \frac{r_0^2}{2}\left(\frac{1}{1+\epsilon(1-\cos\theta)}\right)^2\left\{1+\cos^2\theta+\frac{\epsilon^2(1-\cos\theta)^2}{1+\epsilon(1-\cos\theta)}\right\} \tag{2.3}$$

ϵ is again the reduced photon energy of section 2.1. Transforming the dependence on the solid angle with equation 2.1 to units of the scattering angle θ one can plot the angular distribution of the scattered photons (see left plot of Fig. 2.4) which is given by

$$\frac{d\sigma}{d\theta} = 2\pi\sin\theta\frac{d\sigma}{d\Omega}$$

The angle θ of the scattered photon is related to the angle ϕ of the recoil electron through the formula

$$\cot\phi = (1+\epsilon)\tan\frac{\theta}{2}$$

derived considering momentum and energy conservation [Eva58]. Using this formula together with equation 2.3 one can also write down the angular distribution of the recoil electrons visualised in Fig. 2.4 in the right plot:

$$\frac{d\sigma}{d\phi} = \frac{d\sigma}{d\Omega}\left[\frac{2\pi(1+\cos\theta)\sin\theta}{(1+\epsilon)\sin^2\phi}\right]$$

All scattering cross-sections refer to the scattering on one electron. They have to be multiplied by the atomic number Z to obtain the scattering cross-section per atom[3].

2.3 Rayleigh scattering

Contrary to Thomson scattering (scattering of photons by free electrons) Rayleigh scattering describes photon scattering by atoms as a whole. It is also called *coherent scattering* as the electrons of the atom contribute to the interaction in a coherent manner and because there is no change in the wavelength λ. *No energy is transferred to the material.* The elastic scattering process changes only the direction of the incoming photon. The Rayleigh scattering cross-section per atom σ_R is given by

$$\sigma_R = \frac{3}{8}\sigma_{Th}\int_{-1}^{+1}(1+\cos^2\theta)[F(x,Z)]^2 d(\cos\theta) \qquad \text{with} \qquad x = \frac{\sin(\theta/2)}{\lambda}$$

[3]This is only valid for the approximation of free electrons. In reality the cross-section for the scattering on an atom is lower than calculated with this assumption.

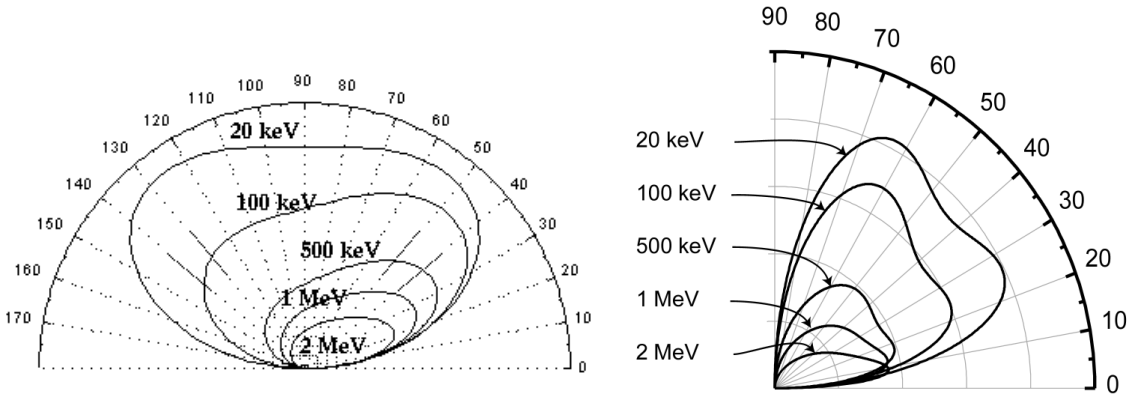

Figure 2.4: *Angular distribution of Compton scattered photons (left) and recoil electrons (right) for primary photon energies of 20 keV, 100 keV, 500 keV, 1 MeV and 2 MeV.*

$F(x, Z)$ are atomic form factors determined after various theoretical models. The relativistic Hartree-Fock form factors are used quite frequently and the tabulated values can be found in [Hub79]. Especially for high Z-values they differ quite significantly from the non-relativistic form factors.

Fig. 2.5 demonstrates that Rayleigh scattering plays a non negligible role for photons up to an energy of ∼100 keV in the attenuation of a photon beam in Gallium Arsenide material.

2.4 Photon interaction coefficients

After description of the different photon interactions with matter this section will give an overview over different coefficients used to understand better the overall transport behaviour of both primary and secondary particles resulting from these interactions. The photon attenuation coefficient makes it possible to estimate the number of photons surviving the passage through a certain material thickness without interaction. Knowledge of the energy absorption coefficient gives a good idea about the energy lost inside the material crossed by a photon beam.

2.4.1 Photon attenuation coefficients

A narrow photon beam composed of N_0 photons of energy E passing through material with thickness t will be attenuated following an exponential law which enables calculating the number N of photons which survived the passage without interaction:

$$\frac{N}{N_0} = e^{-\mu(E)t}$$

Each interaction of the photons will remove them from the beam either by absorption or by scattering away from the detection direction[4]. μ is called the *linear attenuation*

[4]Experimentally the detector has just a small opening corresponding to the photon beam diameter.

coefficient representing the fraction of incident photons interacting with the material per unit length[5]. It is the sum of the different interaction probabilities mentioned in the previous sections:

$$\mu = \tau + \sigma + \chi + \sigma_R + \sigma_{photonuclear}$$

As the linear attenuation coefficient depends on the density of the absorber one uses much more frequently the *mass attenuation coefficient* μ/ρ (in [cm^2/g]) with ρ as the absorber density. This changes the attenuation law into the form

$$\frac{N}{N_0} = \exp\{-[\mu(E)/\rho]\ \rho\ t\} \tag{2.4}$$

with $\rho\ t$ known as the *mass thickness* of the absorber which determines its degree of attenuation and μ/ρ as a fundamental material constant also independent of the phase state of the absorber. The reciprocal of μ/ρ is λ, the *mean free path* of the photons defined as the average distance photons travel in the absorber without an interaction. For compounds (c) and mixtures (m) the mass attenuation coefficient is simply the sum of μ/ρ of the different elements multiplied with the corresponding weight fractions w_i.

$$\left(\frac{\mu}{\rho}\right)_{c,m} = \sum_i w_i \left(\frac{\mu}{\rho}\right)_i$$

Fig. 2.5 represents the total mass attenuation coefficient as a function of the incident photon energy for GaAs and fig. 2.6 for CdTe showing the contributions of the different energy loss and scattering processes [Boo96].

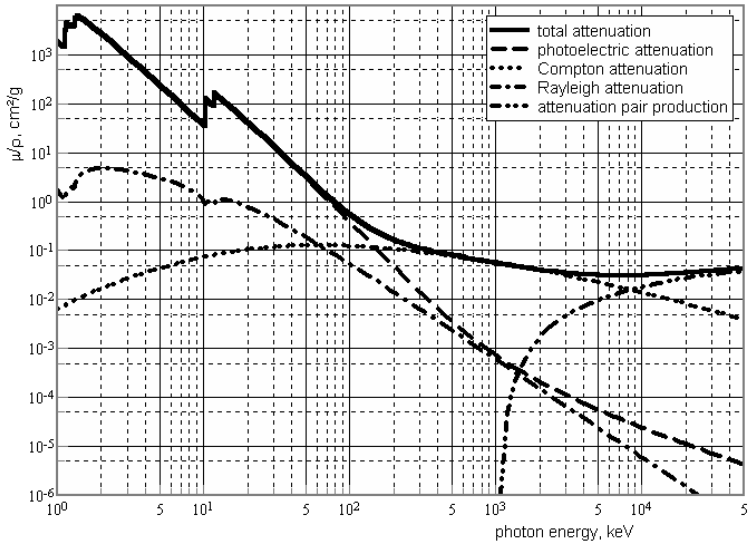

Figure 2.5: *Total mass attenuation coefficient (solid line) for GaAs and incident photon energies from 1 keV to 5 MeV. Shown are the different contributions to the total mass attenuation coefficient arising from the photo-electric effect (dashed line), Compton scattering (dotted line), Rayleigh scattering (dashed-dotted line) and pair production (dashed-dotted-dotted line) [Xmu, Boo96].*

[5]It should not be confused with the mobility.

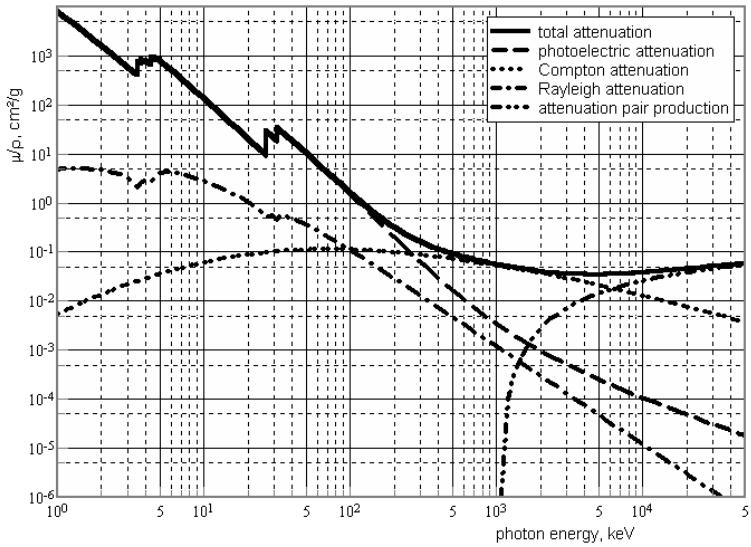

Figure 2.6: *Total mass attenuation coefficient (solid line) for CdTe and incident photon energies from 1 keV to 5 MeV divided up in its different contributions [Xmu, Boo96].*

2.4.2 Mass energy absorption coefficient

Considering again a mono-energetic photon beam of energy E one can derive an equivalent formula for the energy attenuation in a material of thickness t and density ρ as for the photon attenuation (equation 2.4):

$$\frac{\psi}{\psi_0} = \exp\{-[\mu_{en}(E)/\rho]\ \rho\ t\}$$

This equation is called the *energy absorption coefficient attenuation law* with μ_{en}/ρ (in $[\mathrm{cm}^2/\mathrm{g}]$) as the *mass energy absorption coefficient*. ψ_0 is the initial photon energy flux[6] and ψ the photon energy flux after a material thickness of t. This formula describes the transferred photon energy flux at material depth t which is the sum of the fluxes of energy from the photons without interaction and of the fraction of kinetic energy of the produced secondary charged particles which could reach t.

This is easier to understand starting from the so-called *mass energy transfer coefficient*, $\mu_{tr}(E)/\rho$ (also in $[\mathrm{cm}^2/\mathrm{g}]$). The mass energy transfer coefficient takes into account the fraction of incident photon energy which is transferred to kinetic energy of secondary charged particles. $\mu_{tr}(E)/\rho$ multiplied by the photon energy flux gives the dosimetric quantity K called *kerma* (transferred energy per unit mass $[\mathrm{J/kg}]\equiv[\mathrm{Gy}]$)[7]. The secondary charged particles may again lose a fraction of their kinetic energy, g, in radiative energy-loss processes (like bremsstrahlungs losses) during their slowing

[6] $\psi_0 = \phi_0 E$, ϕ_0 being the incident photon flux.

[7] This illustrates the significance of these parameters for the calculation of absorbed dose.

down. With this information one can define the mass energy absorption coefficient

$$\left(\frac{\mu_{en}}{\rho}\right) = (1-g)\left(\frac{\mu_{tr}}{\rho}\right) \tag{2.5}$$

The error in the determination of μ_{en}/ρ is mainly related to the insufficient knowledge of the conversion factors g for the different energy loss processes and was estimated to be in the order of 3-5% [Ber61].

2.5 Energy loss of secondary electrons

The energy loss of electrons will be treated in this section as it is the electrons which transfer in secondary interactions the energy of the photons to matter. First, the photons have to be converted - the different processes for soft photons have already been described - transmitting all or part of their energy to kinetic energy of electrons[8]. These secondary electrons dissipate the kinetic energy along their tracks in multiple collisions producing excitation and ionisation of the atoms of the medium. Only at high energies radiative energy loss of the electrons due to scattering in the electric field of a nucleus ('bremsstrahlung') becomes dominant[9].

In general, the energy loss of charged particles with masses much heavier than the electron mass is described by the Bethe-Bloch formula

$$-\frac{dE}{dx} = 2\pi N_A r_e^2 m_e c^2 \rho \frac{Z}{A}\frac{q^2}{\beta^2}\left[\ln\left(\frac{2m_e\gamma^2 v^2 W_{max}}{I^2}\right) - 2\beta^2\right] \tag{2.6}$$

		$2\pi N_A r_e^2 m_e c^2 = 0.1535$ [MeV/(g/cm^2)]
N_A	...	Avogadro's number = 6.022×10^{23} mol^{-1}
r_e	...	classical electron radius = 2.8179×10^{-13} cm
m_e	...	electron mass
c	...	speed of light
ρ	...	density of the absorber
Z	...	atomic number of the absorber
A	...	atomic weight of the absorber
q	...	charge of the incident particle in units of e
β	...	v/c of the incident particle
γ	...	$1/\sqrt{1-\beta^2}$
W_{max}	...	maximum energy transfer in a single collision
I	...	mean excitation potential

with the maximum energy transfer originating from knock-on collisions and given by [Leo87]

$$W_{max} = \frac{2m_e c^2 \eta^2}{1 + 2s\sqrt{1+\eta^2} + s^2}$$

[8]For X-ray diagnostic applications secondary electrons are produced in the course of photo-electric absorption and Compton scattering processes.

[9]Bremsstrahlung equals radiative losses at about $EZ = 800$ [Leo87, Seg77] with E in units of MeV, e.g. at ≈25 MeV in GaAs.

with $\eta = \beta\gamma$ and $s = m_e/M$, M being the mass of the incident particle.
For low particle energies the energy loss is high and dominated by the factor $1/\beta^2$ decreasing steadily. It reaches a minimum[10] at about $\beta \approx 0.96$. As the energy increases the logarithmic term becomes dominant leading to the relativistic rise of the energy loss, but not in all media as explained below.

Several corrections exist to the Bethe Bloch formula, the most important being the density correction δ and the shell correction C. The density correction compensates the relativistic rise taking into account the fact that the particles polarise the atoms along their tracks. It gets more important for higher particle velocities and denser materials.
On the other hand the shell correction plays a role for low particle velocities comparable or smaller than the orbital velocity of the electrons in the atomic shell. In this case the Bethe Bloch formula breaks down as the assumption that the shell electrons are stationary with respect to the incident particle is no longer valid.
By adding $(\delta + 2C/Z)$ to the term in the square brackets of the Bethe Bloch formula these two main corrections will be accounted for and give accurate results down to particle velocities $\beta \approx 0.1$. Values for the different correction parameters can be found in [Ste84]. There exist also various other corrections, but they are usually negligible [Leo87].

For *electrons and positrons* the Bethe Bloch formula has to be changed quite radically. First, one has to include as already mentioned radiative energy losses (negligible for low electron energies) due to their small masses. Second, the electrons are deflected in the collisions from their incident trajectories and the collisions are now happening between identical particles. Therefore equation 2.6 has to be modified[11]. Including these effects the Bethe Bloch formula changes to [Leo87]

$$-\frac{dE}{dx} = 2\pi N_A r_e^2 m_e c^2 \rho \frac{Z}{A}\frac{1}{\beta^2}\left[\ln\frac{\tau^2(\tau+2)}{2(I/m_e c^2)^2} + F(\tau) - \delta - 2\frac{C}{Z}\right]$$

τ being the kinetic energy of the electron/positron in units of $m_e c^2$. For electrons the function $F(\tau)$ is given by

$$F(\tau) = 1 - \beta^2 + \frac{\tau^2/8 - (2r_e + 1)\ln 2}{(\tau+1)^2}$$

and for completeness for positrons by

$$F(\tau) = 2\ln 2 - \frac{\beta^2}{12}\left(23 + \frac{14}{\tau+2} + \frac{10}{(\tau+2)^2} + \frac{4}{(\tau+2)^3}\right)$$

[10] Particles around and above this energy are called *minimum ionising particles*, often indicated with m.i.p. or MIP.

[11] For example the maximum energy transfer becomes $W_{max} = E_{kin}/2$ where E_{kin} is the kinetic energy of the incident electron or positron.

2.6 Summary

This chapter reviews the various processes involved in the interactions of low energy photons with matter. Photo-electric conversion and Compton scattering are the dominant effects.
In the case of the PCC system, the conversion of the X-rays in a high-Z semiconductor detector into measurable charge represents the first stage in the detection process of the X-rays which were beforehand attenuated by a sample and which form the radiographic image. Suitable materials have to be chosen with respect to a maximum X-ray absorption. Losses in absorption efficiency correspond to useless dose given to the patient.
There is a strong energy dependence of the different energy loss processes. The position of the absorption edges dominates the behaviour of such high-Z semiconductor materials in the diagnostic energy range and has to match the default configuration of X-ray tubes resulting in different X-ray spectra depending on the examination. Small shifts in the position of the K-edge can influence the detector response and therefore the DQE of the system. This will be investigated in chapter 7 where simulations of the energy loss processes of X-rays in Si, GaAs and CdTe for different X-ray energies are presented.
The following chapter will make the transition from a piece of pure semiconductor material to a semiconductor detector. This includes charge transport and represents the second critical phase in image formation and system efficiency after the X-ray conversion.

Chapter 3

Basic Concepts of Semiconductor Detectors

Contents

Semiconductors owe their widespread use as detector materials to the small amount of energy (few eV) needed to create an electron-hole pair which is at the same time high enough to avoid thermally generated charge carriers which give rise to a continuous 'dark' current. This property makes semiconductor detectors also very attractive as low energy (in the keV region) X-ray detectors. Despite the small energy deposition it is possible to distinguish clearly each X-ray from the dark current background due to the sufficiently high number of electron-hole pairs produced by the X-ray.
Subsequent to the creation of the electron-hole pair the electron is excited into the conduction band where it contributes to the signal current as well as the hole in the valence band which acts like an independent positive charge carrier. Other particle detector materials like gaseous detectors or scintillators need a considerably larger amount of energy for the creation of a signal.

3.1 Crystal structure and energy bands of semiconductors

Most semiconductor materials occur in a crystalline structure[1]. The individual atoms form a three-dimensional periodic lattice. Semiconductors can consist of single elements like silicon (Si) or germanium (Ge) or of compounds of two or more elements like gallium arsenide (GaAs), cadmium telluride (CdTe) or cadmium zinc telluride ($Cd_{1-x}Zn_xTe$). Si atoms form a diamond lattice whereas GaAs has a zincblende lattice (see table 3.1).

semiconductor	**Si**	**GaAs**	**CdTe**	**InP**	**Ge**	**C**
atomic number	14	31/33	48/52	49/15	32	6
density [g/cm^3]	2.33	5.31	6.20		5.32	3.52^a
crystal structure	diamond	zincblende	zincblende	zincblende	diamond	diamond
band-gap [eV] at 300 K	1.12	1.42	1.56	1.35	0.66	5.47
at 0 K	1.17	1.52		1.42	0.74	5.48
mobility at 300 K [cm^2/Vs]						
of electrons	1500	8500	1050	4600	3900	1800
of holes	450	400	100	150	1900	1200
direct/indirect	I	D	D	D	I	I
ϵ_s/ϵ_0	11.9	13.1	10.2	12.4	16.0	5.7

Table 3.1: *Properties of some semiconductor materials (ideally pure and perfect) used or potentially suitable for medical X-ray diagnostics. The data was taken from [Sze81] except the values for the density which are from [Ste84] and ^{a} from [Mei99].*

A crystal can be approximated by a periodic array of potential wells. A charge carrier travelling through the crystal will therefore either be accelerated or decelerated according to its position relative to the crystal atoms. Making use of the particle-wave duality principle the energy levels of such a particle can be calculated using the Schrödinger equation. Under periodic boundary conditions the wave function can be written as a travelling wave with a certain amplitude and the *wave vector* $\mathbf{k}$ which can be positive or negative representing opposite travelling directions. For certain regions of the resulting energy eigenvalues $\mathbf{k}$ is complex. These regions correspond to forbidden energy bands and arise from the discontinuities in energy at the boundaries.

In the same way the *band structure* of semiconductors can be treated. It is a result of the N-fold degenerate levels of N free atoms in a crystal structure. Linear combinations of the atomic wave functions describing attraction and repulsion of the atoms lead to the formation of energy bands when the number of participating atoms is high. Depending on the crystal structure and the number of valence electrons a semiconductor is characterised by an empty[2] *conduction band* separated by a gap from the filled *valence band*. Conduction and valence band themselves have a substructure given by the overlap of the valence electron energy bands (see fig. 3.1).

[1]Exceptions are e.g. amorphous materials or polymeric semiconductors.
[2]at 0 K

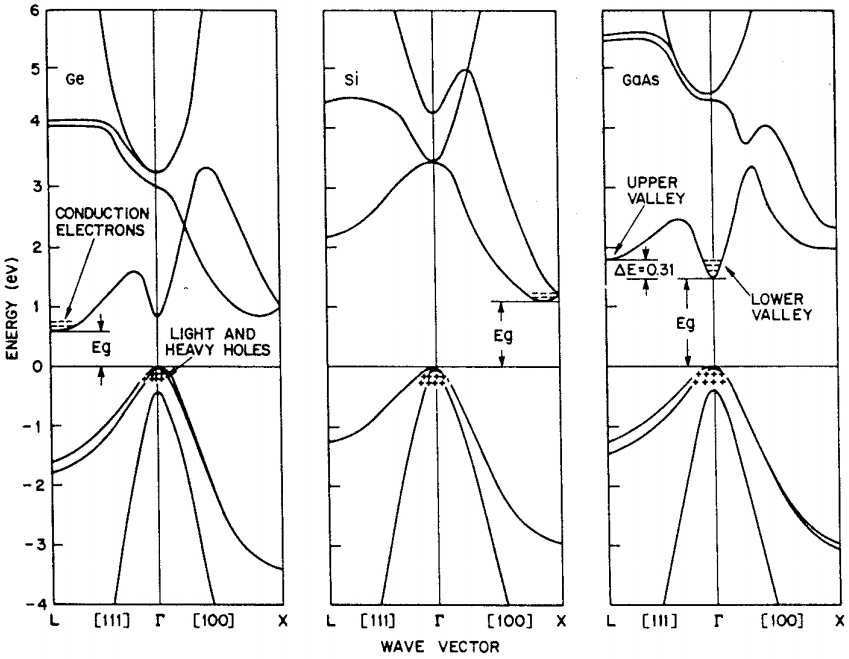

Figure 3.1: *Energy-band structures of Ge, Si and GaAs (from [Sze81] after calculations from Chelikowsky and Cohen [Che76]). The value of the band-gap is increasing from 0.66 eV (Ge) to 1.12 eV (Si) and 1.42 eV (GaAs) at room temperature and its location within the Brillouin zone changes. Different valence bands are shown below 0 eV and conduction bands above.*

The region between the lowest conduction band and the highest valence band representing the forbidden energy region is called the **band-gap**, E_g. For Si or Ge the extreme values of the valence and conduction bands appear at zone boundaries, significant points being the X and L points at the centres of the {002} and {111} faces of the reciprocal lattice respectively. In this case a transition of an electron from the valence to the conduction band does not only require a minimum energy $\geq E_g$, but also some extra thermal energy or momentum provided by crystal vibrations. Such semiconductors are called *indirect* semiconductors. The need for extra momentum reduces severely the probability of a transition. Another way for a transition of an electron to the conduction band consists of using 'steps' which are energy levels within the band-gap (see next section).
On the other hand *direct* semiconductors exist like GaAs. For example for light-emitting diodes or semiconductor lasers this property is a requirement (compare table 3.1). In such materials the extremes of the band edges point in the same direction in the momentum space. For GaAs the location of the minimum of the conduction band and the maximum of the valence band lies on the Γ point (centre of the Brillouin zone[3] corresponding to a wave vector of 0; E_g=1.42 eV at 300 K, see Fig. 3.1). The band-gap structure of GaAs and its influence on detector properties will be explained in more

[3]The first Brillouin zone corresponds to the Wigner-Seitz cell which is the unit cell of the reciprocal lattice. Brillouin zones are used to describe the propagation of waves in a periodic lattice. Any wave vector **k** in the reciprocal space can be reduced to a point in the Brillouin zone.

detail in the next chapter.

The band-gap depends on the impurity concentration, the temperature and the pressure. For highly doped materials the band-gaps become smaller. Temperature and pressure coefficients (dE_g/dT and dE_g/dP) depend on the material (even their sign can change; see empirical equations 4.1 and 4.2 for GaAs).

Another description of semiconductor properties and the band-gap can be obtained using a thermodynamic approach where the band-gap is known to be the standard Gibbs energy $G = H - TS$ with H as the enthalpy and S as the entropy of the formation of electrons and holes. Therefore the equilibrium condition can be calculated by minimising G. It can be shown [Thu75] that the band-gap corresponds to the sum of the standard chemical potentials of electrons and holes at a certain temperature T and constant external pressure.

For the temperature dependence of the band-gap Varshni [Var67] proposed following empirical relation

$$E_g(T) = E_g(0) - \frac{\alpha T^2}{T + \beta} \tag{3.1}$$

with α and β as constants (see Fig. 3.2) being in very good agreement with measurements. The major contribution to the temperature dependence of the band-gap besides a dilatation of the lattice (linear with T at high temperatures) arises from a temperature-dependent electron-lattice interaction. This results in a shift in the relative position of the conduction and valence bands which is proportional to T below the Debye temperature[4] θ and proportional to T^2 above θ [Var67]. Therefore in equation 3.1 β is reasonably close to θ.

Choosing the appropriate material (see table 3.1) for particle detection involves consideration of many parameters like atomic number (high Z means better stopping power for higher X-ray energy), carrier lifetime and mobility, trapping, mechanical properties, availability, cost etc. Concerning the intrinsic semiconductor properties a trade-off between high detection sensitivity (small band-gap to detect clearly low energetic particles and to profit from high statistics) and low thermal current (large band-gap; using e.g. Ge imposes mostly cooling facilities) has to be made.

3.2 Intrinsic carrier concentration and doping

Due to the band-gap between the filled electron levels in the valence band and the vacant ones in the conduction band semiconductors have ideally a conductivity of

[4]The Debye temperature can be deduced from the Debye model where atoms vibrate independently, but form at the same time a system of coupled oscillators contrary to the Einstein model where all atoms vibrate with a fixed frequency ω. The Debye temperature is defined as $\theta = \frac{\hbar\omega_{max}}{k_B}$ with $\omega_{max} = 2\sqrt{\text{const}/M}$ (M denotes the atomic mass).

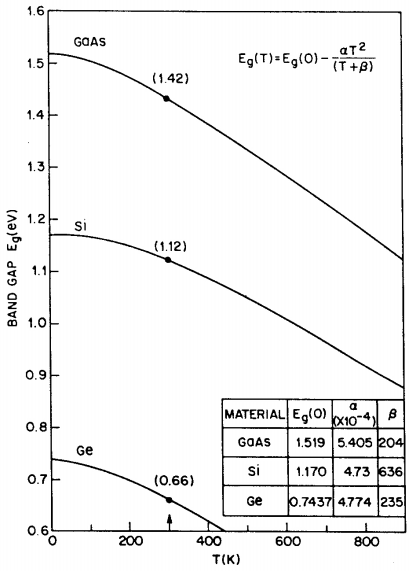

Figure 3.2: *Energy band-gaps of Ge, Si and GaAs as a function of temperature for high-purity materials and under normal atmosphere [Sze81]. The curves represent equation 3.1 proposed by Varshni [Var67] with constants α and β published by Thurmond [Thu75]. The values for the band-gaps at 300 K are pointed out.*

zero at 0 K. At higher temperatures it is possible for electrons in the valence band to reach the conduction band through thermal excitation. This process is in equilibrium with the recombination process between the electrons in the conduction bands and the holes in the valence bands.

Carrier concentration and material properties can be changed with the introduction of *impurities*. Impurities are either foreign atoms or defects in the crystal structure. They lead to a disturbance of the crystal periodicity which results in extra energy levels inside the forbidden band-gap. As explained later, foreign atoms are often added deliberately for doping reasons leading to very shallow energy levels. Defects on the other hand are mostly unwanted imperfections frequently with energy levels deep inside the band-gap acting as very efficient charge traps (see next section). For GaAs these defects play an important role in the detector performance and will be treated in section 4.2.2.

It is possible to calculate the electron density n in the conduction band (see e.g. [Sze81]) using the Fermi-Dirac distribution function[5] describing the probability that an electronic state with energy E is occupied by an electron:

$$n = N_C \exp\left(-\frac{E_C - E_F}{kT}\right) \qquad \text{with} \qquad N_C = 2\left(\frac{2\pi m_n^* kT}{h^2}\right)^{3/2} \tag{3.2}$$

[5] $F(E) = \frac{1}{1+\exp[(E-E_F)/(kT)]}$

N_C ... effective density of states in the conduction band
N_C (Si, 300 K)= 2.8×10^{19} cm^{-3} [Sze85]
N_C (GaAs, 300 K)= 4.7×10^{17} cm^{-3} [Sze85]
E_C ... energy of the bottom of the conduction band
E_F ... Fermi energy level[6]
k ... Boltzmann constant
m_n^* ... electron effective mass[7]
h ... Planck constant

The corresponding formula can be derived for p, the hole density in the valence band:

$$p = N_V \exp\left(-\frac{E_F - E_V}{kT}\right) \qquad \text{with} \qquad N_V = 2\left(\frac{2\pi m_p^* kT}{h^2}\right)^{3/2} \tag{3.3}$$

N_V ... effective density of states in the valence band
N_V (Si, 300 K)= 1.04×10^{19} cm^{-3} [Sze85]
N_V (GaAs, 300 K)= 7.0×10^{18} cm^{-3} [Sze85]
E_V ... energy of the top of the valence band
m_p^* ... hole effective mass[8]

The product of n and p is always constant and allows to determine the intrinsic carrier density n_i

$$np = n_i^2 = N_C N_V \exp\left(-\frac{E_g}{kT}\right) \tag{3.4}$$

with the band-gap energy $E_g \equiv (E_C - E_V)$. Contrary to *extrinsic* semiconductors *intrinsic* semiconductors have equal concentration of electrons and holes under equilibrium conditions ($n = p \simeq 10^{19}$ cm^{-3} for pure Si). Equation 3.4 is also valid after an introduction of impurity atoms and is called the **mass-action law**. The product of n times p will always stay constant at constant temperature whereas the sum $|n| + |p|$ will increase.
Doping with atoms which leave an excess of electrons (=*donors*) renders the semiconductor material *n-type*, a material with an excess of holes (introducing *acceptors*) is called *p-type* material. Doping introduces extra energy levels in the band-gap of the semiconductor which should lie close to the conduction or respectively to the valence band. At the same time the Fermi energy level will move closer to one or the other band edge depending on the doping concentration. With increasing doping concentration the band-gap will also become smaller.
Doping with appropriate atoms ($\approx 10^{12}$-10^{19} atoms/cm^3 for Si) reduces the total net carrier concentration and increases the resistivity of a semiconductor material. This procedure is called *compensation*.

[6]The Fermi level is the energy at which the probability that an electronic state is occupied by an electron is exactly one half. For intrinsic semiconductors E_F lies very close to the middle of the band-gap.
[7]indirectly proportional to the curvature of the corresponding conduction band
[8]indirectly proportional to the curvature of the corresponding valence band

3.3 Charge carrier generation and recombination processes

A semiconductor can be provoked momentarily out of its equilibrium condition, but equilibrium will be again restored afterwards. Non-equilibrium can occur following thermal changes, doping or a current flow.
Electrical equilibrium can be disturbed through illumination or irradiation with external particles ($\Rightarrow np > n_i^2$). These processes fall under the term *carrier generation* which is represented by the generation rate, G.
To restore the equilibrium condition ($np = n_i^2$) *carrier recombination* processes will take place at a certain recombination rate R. Recombination means that an electron-hole pair gets annihilated due to the transition of an electron from the conduction band downwards to the valence band.
Other forced instantaneous non-equilibrium conditions can occur in a semiconductor device when it is connected to an external circuit. For example *carrier extraction* ($np < n_i^2$) for a reverse biased p-n junction (section 3.5.1) with carrier re-generation restoring electrical equilibrium. *Charge injection* is the inverse process where charge carriers are injected at the device contacts.
In the case of charge introduction the excess carriers will recombine either through *direct (≡band-to-band) recombination* or *indirect recombination*[9]. The rate of direct recombination is orders of magnitude higher for direct band-gap semiconductors than for indirect ones as no extra phonons are needed. Indirect recombination has to make use of recombination centres located inside the band-gap and is dominant for indirect band-gap semiconductors.

Recombination in band-to-band processes releases energy either by emission of photons (=*radiative recombination*) or by energy-transfer to another free electron or hole (=*Auger process*) as illustrated in Fig. 3.3. Illuminating the semiconductor with photons of appropriate energy is the inverse process of radiative recombination and impact ionisation the inverse of the Auger process, both generating charge carriers.

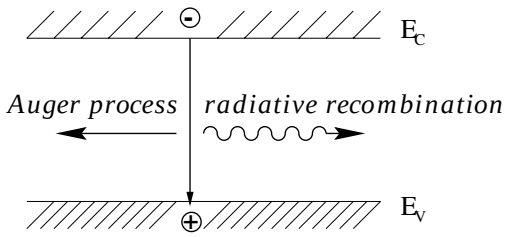

Figure 3.3: *Direct carrier recombination processes; in the case of radiative recombination the annihilation of the electron from the conduction band with a hole in the valence band is accompanied by an emission of a photon whereas in the Auger process the gained energy is transferred to a third free carrier.*

Indirect recombination is possible due to intermediate band-gap levels. Single transitions that can occur are illustrated in Fig. 3.4 (after [Sho52]), squares indicating

[9]Not to be confused with direct and indirect band-gap transitions (see section 3.1).

the recombination centres[10].
In process a) an electron from the conduction band gets captured by the centre. Because of the Pauli exclusion principle this centre cannot capture another electron. Therefore, the electron capture rate is proportional to the number of centres not occupied by an electron (as well as it is proportional to the number of electrons evaluated for the energy range dE). The probability that a centre is empty and thus capable of capturing an electron is given by $F(E_{pt}) = 1 - F(E_t)$ where $F(E_t)$ denotes the Fermi-Dirac function of the centre[11]. With N_t as the total number of centres, $F(E)$ as the Fermi distribution function describing that a quantum state of energy E is occupied by the electrons, $N(E)dE$ as the total number of electron states in the energy range dE and c_n as the proportionality factor called the *electron capture coefficient*, the electron capture rate, R_a, is determined by

$$R_a = F(E_{pt})N_t c_n(E)F(E)N(E)dE \qquad \text{with} \qquad c_n(E) = v_{th}\sigma_n(E)$$

v_{th} is the thermal velocity of the carriers[12] and $\sigma_n(E)$ the electron capture cross-section of the centre for states of energy E.

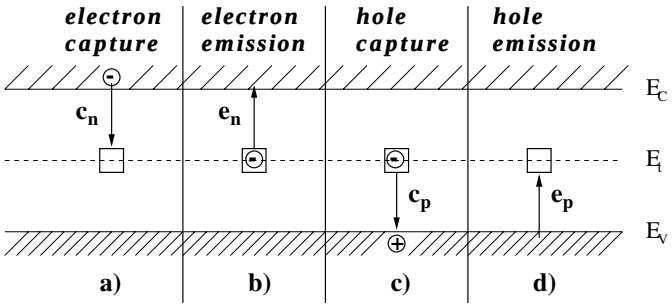

Figure 3.4: *Basic indirect carrier recombination processes: process a) describes the capture of an electron from the conduction band by a recombination centre symbolised by a square. In b) the electron gets emitted by the centre. c) is called hole capture - the electron captures a hole from the valence band - and d) is the hole emission process leading to a negatively charged centre and a free hole in the valence band. The arrows are always indicating the direction of the electron motion.*

Process b) where a captured electron gets emitted by the centre into the energy range dE is the inverse of process a), therefore the electron emission rate is proportional to the concentration of centres occupied by electrons, $N_t F(E_t)$, and the probability that the states in the energy range dE are empty. Analogous with an electron emission coefficient e_n one can derive the formula for the electron emission rate R_b:

$$R_b = F(E_t)N_t e_n[1 - F(E)]N(E)dE$$

[10]Recombination centres are at the same time generation centres as they behave symmetrically for carrier recombination and carrier generation.
[11]$F(E_t) = \frac{1}{1+\exp[(E_t - E_{Ft})/(kT)]}$ with E_{Ft} as the quasi-Fermi level of the centre. Therefore $F(E_{pt})$ is determined by $F(E_{pt}) = F(E_t)\exp[(E_t - E_{Ft})/(kT)]$.
[12]$v_{th} = \sqrt{(3kT)/m_n^*}$

In thermal equilibrium one can set E_F equal to E_{Ft} and the condition $R_a = R_b$ has to be fulfilled yielding

$$\frac{e_n}{c_n} = \exp\left[-\frac{(E - E_t)}{kT}\right]$$

As the emission and capture coefficients are directly related to the emission and capture cross-sections it is evident that the emission of an electron from a centre is much more effective for centres lying close to the conduction band ($\hat{=}(E - E_t)$ small). Inversely centres situated around mid-gap (like gold in Si or the so-called EL2-defect in GaAs which will be treated in chapter 4) are extremely efficient capture centres. Therefore minority carrier lifetimes[13] decrease strongly with the introduction of mid-gap centres (arising from certain impurity atoms or from irradiation with high energy particles causing damage to the crystal lattice). For a p-type semiconductor the electron lifetime is given by [Sze85]

$$\tau_n = \frac{1}{\sigma_n v_{th} N_t}$$

For completeness the corresponding formulas for the hole capture rate R_c (process c) in Fig. 3.4) where an electron situated in a recombination centre annihilates with a hole from the valence band, and for the hole emission rate R_d (process d)) describing the excitation of an electron from the valence band to an unoccupied centre should be noted

$$R_c = F(E_t) N_t c_p(E)[1 - F(E)]N(E)dE$$

and

$$R_d = F(E_{pt}) N_t e_p(E) F(E) N(E) dE$$

with the corresponding hole capture coefficient $c_p(E)$ and hole emission coefficient $e_p(E)$ being again proportional to the hole capture and hole emission cross-sections. The net capture respectively emission rates can be calculated integrating over dE for all possible energy states in the conduction and valence band. Analogous to the electron case the hole lifetime in an n-type semiconductor is given by

$$\tau_p = \frac{1}{\sigma_p v_{th} N_t}$$

Usually one finds multiple level generation-recombination centres in a semiconductor, shallow and deep-level centres. There are also combinations of different processes possible, an example being Shockley-Read-Hall recombination which involves an electron capture followed by a hole capture and accompanied by the emission of several phonons. More precisely the Shockley-Read-Hall process is a trap assisted recombination

[13] For an n-type semiconductor the minority carriers are holes, for p-type material they are electrons.

making use of a single set of traps which act as intermediate step for the electrons between conduction and valence band.
Centres located inside the band-gap are referred to as **traps** when the probability of re-emission of the charge carriers from the centre to a free state is greater than of re-combination with a carrier of opposite sign at the same centre [Ove69]. Inversely such centres are called recombination centres if the captured carrier has a greater probability of recombining with a carrier of opposite sign at the imperfection than of being re-excited to the free state. This distinction is only based on the relative probability of thermal ejection versus recombination which changes obviously with different temperature conditions, photon illumination etc. This might explain why in common practice there is made no distinction between the two terms.

Traps play a very important role in semiconductor detectors. When charge carriers get captured they are re-emitted by the trap after an average *de-trapping time*. If this de-trapping time is too long (longer than the shaping time of the read-out electronics) part of the charge gets lost. Apart from this time dependence this signal loss is proportional to the number of traps and their trapping cross-section. GaAs is an example of a semiconductor material whose charge collection efficiency often is reduced because of the presence of mid-gap centres.

In addition to the various carrier generation processes mentioned briefly free charge can be generated by the energy loss of particles or electro-magnetic rays passing through the semiconductor (see chapter 2). Without electric field the created electrons and holes will recombine. For particle detector applications the use of an electric field is therefore required to separate the generated electron-hole pairs and to guide them towards the collecting electrodes.

3.4 Charge carrier transport in semiconductors

Once free charge is generated in a semiconductor charge recombination starts. But charge will also be transported due to the carrier concentration gradient. This process is called diffusion and will be described in the next section.
Using semiconductors as particle detectors the generated charge has to be collected on the detector electrodes which is provoked by applying an external voltage to the detector. The resulting electric field inside the semiconductor is responsible for the motion of the charge towards the electrodes, called the charge drift.
A mathematical description of all these processes is necessary to calculate the signal obtained from particles impinging on the semiconductor detector.

3.4.1 Diffusion

Diffusion occurs when there are local differences of carrier concentration in the semiconductor. Then a *diffusion current* will flow from the region of high carrier

concentration to the region of low carrier concentration. This diffusion current is proportional to the gradient of the electron density and the diffusivity D_n.

$$J_{n,diff} = qD_n \frac{dn}{dx} \qquad \text{with} \qquad D_n \equiv v_{th}\lambda_C \tag{3.5}$$

λ_C is the *mean free path* (= the average distance between collisions) of the electron and v_{th} its thermal velocity. Using the thermal energy of the electron (Boltzmann statistics) and assuming $n \ll N_C$ one obtains the *Einstein relation*

$$D_n = \left(\frac{kT}{q}\right)\mu_n \tag{3.6}$$

where μ_n is the electron *mobility*. Evidently equations 3.5 and 3.6 are also valid for the diffusion of holes. Fig. 3.5 shows the dependence of mobilities and diffusivities in Si and GaAs at 300 K from the impurity concentration. The carrier mobilities are strongly reduced with increasing impurity concentration. One will notice that electron mobilities are bigger compared to hole mobilities due to their lower effective mass[14]; the upper limitation of the mobilities is given by lattice scattering (temperature-dependent!).

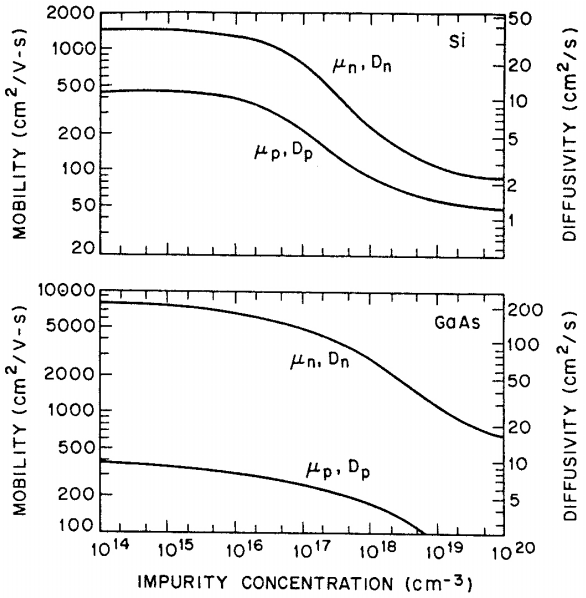

Figure 3.5: *Mobilities and diffusivities for electrons (subscript n) and holes (subscript p) in Si (top) and GaAs (bottom) as a function of impurity concentration [Sze85].*

3.4.2 Charge carrier drift

Applying an electric field ($\mathcal{E}$ denoting the magnitude of the electric field) in a semiconductor will superimpose a so-called drift motion on top of the statistical thermal

[14]The higher effective mass of holes is a result of the degeneracy of the valence bands which gives rise to inter-band scattering (see section 4.1.1).

motion of the electrons. Each electron will experience a force $-q\mathcal{E}$ in the opposite direction to the electric field and therefore a momentum $-q\mathcal{E}\tau_C$ with τ_C as mean free time between two collisions of the electron. This gives the relation

$$v_n = -\left(\frac{q\tau_C}{m_n^*}\right)\mathcal{E} = -\mu_n\mathcal{E} \tag{3.7}$$

for the *drift velocity* v_n with the electron *mobility* μ_n as proportionality factor[15]. This formula enables to calculate the *drift current*. The electron drift current density $J_{n,drift}$ is given by

$$J_{n,drift} = \sum_{i=0}^{n}(-qv_i) = -qnv_n = qn\mu_n\mathcal{E} \tag{3.8}$$

It is important to point out that like the diffusion current also the drift current is linearly dependent on the mobility (if Boltzmann statistics can be used).
It is now easy to write down the total current J_{drift} in a semiconductor resulting from the application of an electric field:

$$J_{drift} = J_{n,drift} + J_{p,drift} = (qn\mu_n + qp\mu_p)\mathcal{E} = \sigma\mathcal{E}$$

σ is called the *conductivity* and its reciprocal is known as the *resistivity* ρ of the semiconductor:

$$\rho = \frac{1}{\sigma} = \frac{1}{(qn\mu_n + qp\mu_p)} \tag{3.9}$$

3.4.3 Continuity equations and Poisson's equation

The *continuity equations* for electrons and holes govern the electrical behaviour of semiconductor devices. They combine drift, diffusion, charge generation and recombination. For the one-dimensional case the electron continuity equation can be derived considering the net in- and outflow of electrons in an area through the mentioned processes and is given by (see e.g. [Sze85])

$$\frac{\partial n}{\partial t} = \frac{1}{q}\frac{\partial J_n}{\partial x} + (G_n - R_n) \tag{3.10}$$

with G_n as the charge generation rate, R_n as the charge recombination rate and J_n as the total *current density* resulting from drift and diffusion

$$J_n = q\mu_n n\mathcal{E} + qD_n\frac{dn}{dx}$$

The corresponding (one-dimensional) continuity equation for holes is the following:

$$\frac{\partial p}{\partial t} = -\frac{1}{q}\frac{\partial J_p}{\partial x} + (G_p - R_p) \tag{3.11}$$

[15]Equation 3.7 changes to $v_p = \mu_p\mathcal{E}$ for holes in the valence band.

with

$$J_p = q\mu_p p\mathcal{E} - qD_p\frac{dp}{dx}$$

For a full description of the semiconductor device *Poisson's equation* has to be solved in addition to the continuity equations[16]. With the electrostatic potential ψ, ϵ_s as the permittivity of the semiconductor, ρ_s as the space charge density (see section 3.5), N_D as the donor concentration and N_A as the concentration of acceptors Poisson's equation (for static conditions[17]) is given by

$$\frac{d^2\psi}{dx^2} = -\frac{d\mathcal{E}}{dx} = -\frac{\rho_s}{\epsilon_s} = -\frac{q}{\epsilon_s}(p - n + N_D^+ - N_A^-) \tag{3.12}$$

A unique solution exists for Poisson's equation plus continuity and current-density equations, but is due to the complexity of the equations very time-consuming to calculate. It is therefore common practice to use approximations for finding the solution.

3.5 Semiconductor detectors

For efficient particle detection in a semiconductor it is necessary that the created electron-hole pairs be separated as fast as possible in order to avoid recombination and therefore charge loss. Moreover, the whole detector volume should be free of other charge carriers again to reduce the probability of recombination. This is reached through a *reverse biased junction* which means that a positive voltage has to be applied on the n-side with respect to the p-side of the junction. Recombination will be minimised and the generated charge will drift to and be collected on the corresponding electrodes.

3.5.1 Junction diodes

A p-n junction is formed by putting a p-type region in contact with an n-type region (fig. 3.6a)). The carrier concentration gradient leads to diffusion of holes to the n-side and electrons to the p-side leaving fixed negative acceptor ions on the p-side and positive donor ions on the n-side close to the junction. This means that a negative space charge gets formed at the p-side of the junction and a positive space charge at the n-side. This *space charge region* creates an electric field which is in the opposite direction to the diffusion current for both carriers. At thermal equilibrium, the resulting drift current has to cancel the diffusion current (see fig. 3.6b)). Using equations 3.5, 3.6 and 3.8 and expressing the electron and hole densities in terms of the intrinsic carrier concentration n_i and the intrinsic Fermi level E_i (at mid-gap)[18]

[16] In the presence of a magnetic field the remaining Maxwell equations have to be solved as well.

[17] For static or very low frequency conditions $\mathcal{E} = \mathcal{D}/\epsilon_s$ with $\mathcal{D}$ known as the displacement vector defined in the Maxwell equations

[18] $n = n_i \exp[(E_F - E_i)/(kT)]$ and $p = n_i \exp[(E_i - E_F)/(kT)]$

it can be seen that the Fermi level E_F must be constant across the entire device (in absence of externally applied voltages). This leads to a space charge distribution shown schematically in fig. 3.6c) given by the Poisson's equation 3.12. The regions far away from the junction are essentially neutral ($\frac{d^2\psi_n}{dx^2} = \frac{d^2\psi_p}{dx^2} = 0$) which enables us to calculate the electrostatic potential difference at thermal equilibrium between these regions, called the *built-in potential* V_{bi}:

$$V_{bi} = \psi_n - \psi_p = \frac{kT}{q} \ln \frac{N_A N_D}{n_i^2}$$

Moving from the neutral regions beyond the transition region the mobile carrier densities are zero. This region is called the **depletion region**. Semiconductor detectors are based on the principle of extending the depletion region to the entire detector volume by applying a reverse bias voltage[19]. If the energy from a particle is deposited there and the created electron-hole pairs are immediately separated by an externally applied electric field the collected charge is an absolute measure for the deposited energy provided there is no charge trapping. The width W of the depletion layer is given by [Sze85]

$$W = \sqrt{\frac{2\epsilon_s}{q} \left(\frac{N_A + N_D}{N_A N_D} \right) V_{bi}}$$

For an abrupt junction[20] ($\hat{=}$ abrupt change of doping concentrations between the n- and p-type regions) and a reverse bias voltage V the depletion layer width can be transformed to

$$W = \sqrt{\frac{2\epsilon_s}{q} \frac{(V_{bi} + V)}{N_B}} \tag{3.13}$$

with N_B denominating the lightly doped bulk carrier concentration. Inserting the resistivity (equation 3.9) makes it clear that a high bulk resistivity helps in creating a large depletion width at reasonable levels of bias voltage.

Current-voltage characteristics for a p-n junction can be deduced from this formula, in particular the dependence of W on the square root of the reverse bias voltage. Reverse bias increases the electrostatic potential across the depletion region which reduces the diffusion current giving rise to a small reverse current. Increasing the reverse bias voltage reaching electric field values of about 10^6 V/cm or more, tunnelling and avalanche multiplication occur leading to junction breakdown and to a very large current flow. This regime is usually avoided in semiconductor detectors.
On the other hand increasing the detector bias voltage in forward direction reduces the electrostatic potential across the depletion region enhancing diffusion and resulting in an exponentially increasing forward current. As can be seen a p-n junction represents a *rectifying* contact allowing current to flow mainly only in one direction.

[19] = positive voltage on the n-side with respect to the p-side

[20] Detectors are frequently designed as one-sided abrupt junctions, e.g. if $N_A \gg N_D$ the junction is called a p^+-n junction. The depletion layer develops mainly in the low-doped region.

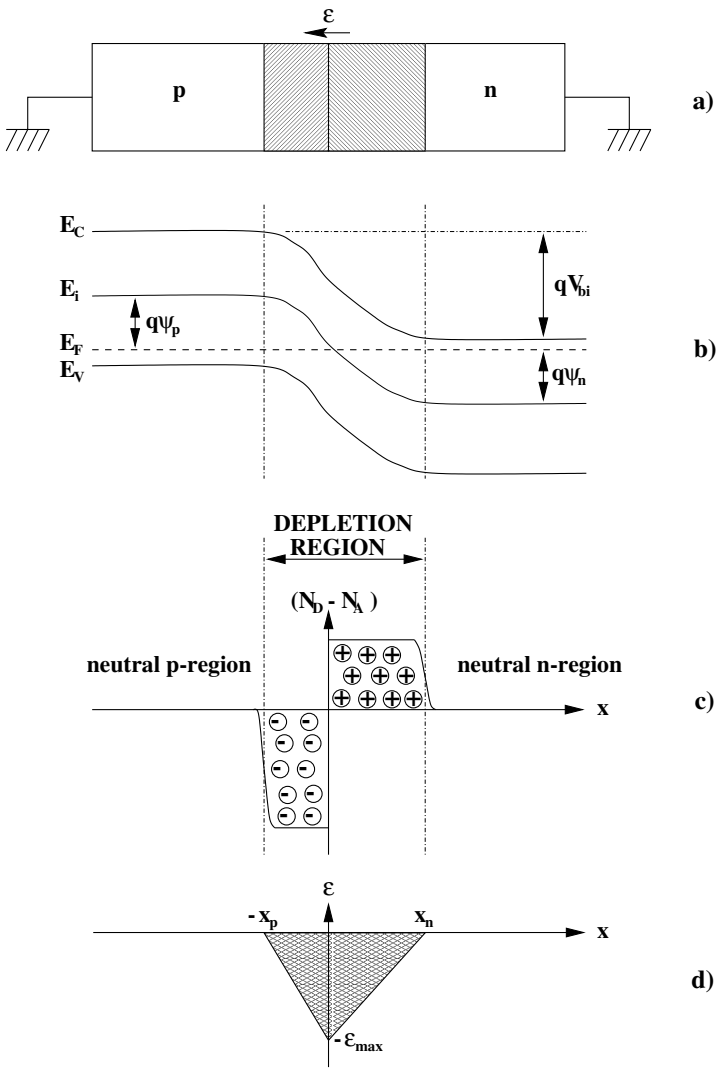

Figure 3.6: *a) Abrupt p-n junction. b) Energy band diagram showing the built-in potential V_{bi}. The Fermi level of the junction remains constant. c) Space charge distributions and depletion region formed by the junction. d) Electric field distribution.*

3.5.2 Metal-semiconductor contacts

The deposition of metallic electrodes on a semiconductor detector can lead to different sorts of contacts. The contacts can be either rectifying or ohmic. Walter Schottky explained in 1938 the rectifying nature of a metal-semiconductor contact through the formation of a barrier at the interface leading to the name **Schottky diode** for such a device [Sch39].
Like for the p-n diode the Fermi levels of the metal and the semiconductor have to line up at the contact at thermal equilibrium which results in bending of the conduction and valence bands and a potential barrier. The barrier height $q\phi_{Bn}$ for a contact metal to n-type semiconductor is given by the difference between the metal work function[21]

[21]Energy difference between the Fermi level of the metal and the vacuum level.

and the electron affinity[22] of the semiconductor. For n-type GaAs this barrier height has been measured to lie around 0.8-0.9 V at room temperature depending on the metal contact [Sze81]. For the ideal metal to p-type semiconductor contact the barrier height is then given by $E_g - q\phi_{Bn}$, the sum of the two barrier heights being equal to the band-gap. Identical charge distribution and electric field distribution for the metal to n-type semiconductor contact are obtained in a similar way as for a p^+-n junction. Reverse biasing such a contact yields a depletion width W (similar to equation 3.13), which increases with increasing reverse detector bias:

$$W = \sqrt{\frac{2\epsilon_s}{qN_D}(V_{bi} + V)} \qquad \text{with} \qquad V_{bi} = \phi_{Bn} - (E_C - E_F) = \phi_m - \phi_s$$

The built-in potential V_{bi} is the difference between the work function of the metal, ϕ_m (in the order of 3.5-6 V [Sze85]), and the work function of the semiconductor, ϕ_s (in the order of 2-6 V [Sze81]).

Current-voltage curves of Schottky junctions are very similar to I-V curves of p-n junctions, only that exponential current increase under forward bias occurs faster for Schottky diodes. The main difference between the two junctions is that current transport in Schottky diodes is mostly due to majority carriers in contrast to p-n junctions. The dominant charge transport process (for moderately doped semiconductors) is the flow of majority carriers from the semiconductor over the potential barrier into the metal, called thermionic process. A current flow due to minority carriers is also possible through hole injection from the metal to the semiconductor, but is orders of magnitude smaller than the majority carrier current. Therefore, Schottky diodes are *unipolar* devices.

In practice studying surface barrier detectors Schottky's model cannot explain all phenomena. Surface barrier characteristics are changed due to the high resistivity of the semiconductor material employed. Influencing factors are the charge being present at the metal-semiconductor interface, oxidation of the evaporated metal layer and heat treatments [Hei83].

For highly doped semiconductors the barrier width at the contact becomes very narrow. Quantum-mechanical tunnelling of electrons through the barrier becomes the dominant charge transport process. This decreases strongly the contact resistance leading to an **ohmic** contact which is useful when device performance should not be degraded by a high voltage drop across the contact. Most p-n junction devices have regions of high doping which are used as ohmic contacts to provide the link to external electronics.

[22] In the case of a large density of surface states on the semiconductor surface occupying energy levels inside the band-gap the barrier height is not anymore determined by the metal work function, but by the property of the semiconductor surface.

3.6 Summary

The X-ray detection process with the PCC system takes place in a high-Z, high resistivity semiconductor detector. In this chapter the energy band structure of semiconductors was explained. It is the underlying mechanism which results in the production of free charge carriers during the X-ray conversion stage. These free charge carriers have to be separated immediately after their formation and transported to the corresponding electrodes in order to generate a measurable current signal. This task is accomplished through an externally applied electric field. A high resistivity material is preferred as this allows the full depletion of the detector with a reasonable bias voltage. For a high efficiency it is essential that there is as little charge recombination and charge trapping as possible during charge transport and charge collection on the electrodes. Contact fabrication is also one critical parameter for the behaviour of the semiconductor detector. Contacts have to be able to withstand the detector bias voltages which have to be applied without breakdown or charge injection. Moreover, they have to collect the charge without losses and to enable a good electrical connection to the pixel electrodes of the matching electronics chip.
The following chapter uses this introduction into semiconductor physics and detector concepts to explain in detail GaAs, the material which was used as X-ray sensor in the PCC system. Almost all of the measurements which will be presented in chapter 6 were performed with GaAs detectors.
Charge carrier transport characteristics and equations will be the foundation for discussions of measurement results in chapter 6 and for the charge transport simulations of chapter 7.

Chapter 4

Semi-Insulating (SI) Gallium Arsenide Detectors

Contents

In the early 60's different groups started to investigate the use of GaAs as a radiation detection material and more specifically as room temperature gamma spectrometer (overview in [McG95]). Several material characteristics of GaAs are well suited for this application, especially the value of its band-gap and its high atomic number. General requirements for a good detection material are listed below:

- an appropriate band-gap: large enough for low leakage current at room temperature yet small enough to provide a detectable signal
- high atomic number Z for efficient radiation interactions (high stopping power)
- high charge carrier mobilities combined with long charge carrier lifetimes (big product $\mu\tau$)
- homogeneous material
- few defects
- easy deposition of electrodes without introduction of impurities

- possibility to produce larger area detectors
- possibility to produce sufficiently thick detectors
- easy mechanical handling
- availability of economical, commercial production facilities

The main limitation at present with GaAs detectors is the defect content which will be discussed in section 4.2.2. The other sections describe the intrinsic properties of GaAs material and semi-insulating GaAs. Emphasis will be placed on those properties which are important for the use of GaAs as a radiation detector. All the measurements with the PCC hybrid pixel system presented in this thesis were performed with SI GaAs as detector material. As will be explained later in detail (chapter 6), it is indispensable for a correct interpretation of the measurement results to understand the detector behaviour.

4.1 Major properties of GaAs

GaAs is a III-V semiconductor compound formed by Gallium (atomic number 31) and Arsenic (atomic number 33), the bonding being partly ionic and partly covalent. Its high Z, large band-gap and high electron mobility can explain the interest of researchers who planned to use it as a material for making fast electronic devices or directly as a radiation detector. The link with VLSI[1] industry led to extensive material studies for the last 40 years, but it seems that the crystal growth process is still not fully optimised. Nowadays, GaAs is mainly present in the laser and LED market or in microwave circuits.

There is an abundance of literature about different intrinsic properties of GaAs, but data do not always agree between authors. An attempt will be made in this section to present a coherent summary of the most important ones in view of a radiation detector application. A list of the main properties of GaAs at room temperature is given in table 4.1.

GaAs crystallises into the zincblende structure with face-centred cubic symmetry. One unit cube consists of 4 GaAs molecules; each Ga atom has four As neighbours and inversely. The side length of the unit cube measures ∼5.653 Å at 298 K which yields a density of ∼5.318 g/cm^3 [Str65].
GaAs is grey in colour and is relatively fragile. The crystal cleaves most easily in the {110} family planes. Most planes can be chemically etched; poor etching results are only obtained for the (111A) plane. From the eight planes of the {111} family there are four (111A) planes comprising only Ga atoms, whereas the four (111B) planes consist of only As atoms, a situation explaining the different chemical behaviour.

[1] **v**ery **l**arge **s**cale **i**ntegration

The melting point of GaAs is 1511 K, higher than for Ge, but lower than for Si[2]. The thermal conductivity of GaAs is lower than of Si and Ge whereas the linear thermal expansion coefficient is higher [Sze81]. The higher thermal expansion coefficient combined with the lower thermal conductivity could lead to mechanical stress in delicate GaAs/Si hybrid flip-chip bonded pixel assemblies (see next chapter).

The exact determination of the **energy band structure** of GaAs is of great importance for its use as a radiation detector material. In particular, it affects the electron and hole transport characteristics and therefore the speed and efficiency of a detector. The band structure, effective masses and effective carrier densities of GaAs will be explained in some detail now.

As already mentioned, GaAs has a direct band-gap located at the Brillouin zone centre $\Gamma(000)$. The band-gap can be obtained through analysis of absorption or reflectance data. In [Sel74] a high precision double-beam reflectance study was performed comparing the reflectance of GaAs samples to a mirror of known reflectance in the photon energy range between 1.2 and 1.8 eV. With high purity samples the room temperature band-gap could be assigned as 1.424±0.001 eV. It was also shown that the refractive index is strongly dependent on the carrier concentration with the peak value of the refractive index versus photon energy curve shifting to higher energy with increasing carrier concentration. The temperature dependence of the band-gap can be well described by the empirical formula 3.1. With the parameter set proposed in [Thu75] the equation can be written in the numerical form

$$E_g(T) = 1.519 - \frac{5.405 \times 10^{-4}\, T^2}{(T + 204)} \qquad \text{eV} \tag{4.1}$$

in the temperature range $0<T<1000$ K yielding a band-gap value of 1.519 eV at 0 K. Equation 4.1 is in perfect agreement with the measurements of [Sel74] or [Stu62].

With applied pressure the lattice constant of GaAs decreases and the direct band-gap increases. This behaviour can be described by a polynomial [Wel75]

$$E_g(P) = 1.45 + 1.26 \times 10^{-2}\, P - 3.77 \times 10^{-5}\, P^2 \qquad \text{eV} \tag{4.2}$$

with P as the hydrostatic pressure [kbar][3] and a standard deviation of 0.02 eV for this fit. The measurements in [Wel75] have been performed at room temperature in a range $0 \leq P \leq 180$ kbar. The second minimum of the lowest conduction band at $[\frac{1}{2}\frac{1}{2}\frac{1}{2}]$ (see fig. 4.2) shifts up with pressure as well as the gap at the Brillouin zone centre, E_g, but the third minimum at [100] decreases [Asp76]. Therefore *GaAs becomes an indirect semiconductor for* $P \gtrsim 35$ *kbar* [Pit70, Wel75, Asp76].

[2]Due to the low As vapour pressure GaAs should not be heated up to temperatures higher than ∼900 K where it would start to evaporate.

[3]1 bar=10^5 Pa

Property	Symbol	Value	Reference
atomic number	Z	31/33	
crystal structure		zincblende	[Sze81]
lattice constant	a	5.653 Å	[Str65, Sze81]
density		5.318 g/cm^3	[Str65]
		5.31 g/cm^3	[Ste84]
atomic density	$N/V = 8/a^3$	4.4279×10^{22} cm^{-3}	[Bla82]
melting point	T_m	1511 K	[Sze81, Str65]
linear thermal expansion	$\alpha = \frac{\Delta a}{a}\Delta T$	6.86×10^{-6} K^{-1}	[Sze81]
coefficient		6.4×10^{-6} K^{-1}	[Str65]
thermal conductivity	κ	0.55 W/cm K	[Bla82]
		0.46 W/cm K	[Sze81]
Debye temperature	θ	360 K	[Bla82]
electron affinity	χ	4.07 V	[Sze81]
dielectric constant	ϵ_s/ϵ_0	12.85	[Bla82]
		13.1	[Sze81]
infrared refractive index	n_∞	3.299	[Bla82]
band-gap	E_g	1.424±0.001 eV	[Sel74]
at 0 K		1.519 eV	[Thu75]
L_6^C minimum		1.707 eV	[Asp76]
X_6^C minimum		1.899 eV	[Asp76]
X_7^C minimum		2.30 eV	[Bla82]
Γ_7^V maximum		-0.341 eV	[Asp76]
electron effective mass			
Γ_6 minimum	m_Γ^*	0.063 m_0	[Asp76]
Γ_6 minimum (0 K)		0.067 m_0	[Asp76]
L_6 minimum	m_L^*	0.55 m_0	[Asp76]
L_6 minimum (0 K)		0.56 m_0	[Asp76]
X_6 minimum	m_X^*	0.85 m_0	[Asp76]
X_6 minimum (0 K)		0.85 m_0	[Asp76]
hole effective mass			
heavy holes maximum	m_{hh}^*	0.50 m_0	[Bla82]
heavy holes maximum (0 K)		0.51 m_0	[Bla82]
light holes maximum	m_{lh}^*	0.088 m_0	[Bla82]
light holes maximum (0 K)		0.082 m_0	[Bla82]
effective density of states			
in the conduction band	N_C	4.21×10^{17} cm^{-3}	[Bla82]
in the valence band	N_V	9.51×10^{18} cm^{-3}	[Bla82]
intrinsic carrier concentration	n_i	2.25×10^6 cm−3	[Bla82]
		1.79×10^6 cm−3	[Sze81]
intrinsic resistivity	ρ_i	>10^8 Ω cm	[Sze81]
intrinsic Fermi level	$E_F - E_V - 1/2E_g$	40 meV	[Bla82]

Table 4.1: *Properties of GaAs (at 300 K unless mentioned otherwise).*

As the discussion on pressure dependence already indicates, the energy band structure of GaAs is far from being simple. Several kinds of band calculations attempted to fit the experimental results which themselves had led sometimes to misinterpretations e.g. in the ordering of the band minima [Bla82]. A widely accepted set of (E-k) dispersion curves along high crystal symmetry directions over a wide energy range is shown in fig. 4.1 and has been calculated following a nonlocal pseudo-potential approach [Che76]. Fig. 4.2 [Bla82] is a zoom into the lower energy part of the band system. The three upper valence bands have all their maxima at the zone centre $\Gamma(000)$. The two uppermost bands are degenerate in point Γ_8 and are called the heavy-hole and light-hole band which refers to the assigned effective mass of the holes. The third valence band is separated by the spin orbit splitting energy, Δ_{so}=341 meV [Asp76] (maximum at Γ_7).
The lowest conduction band of GaAs shows three minima, one at the zone centre (Γ_6) corresponding to the direct band-gap, one at L($\frac{1}{2}\frac{1}{2}\frac{1}{2}$), L_6, and one at X(100)[4], X_6.
Room temperature values in eV for the various band-gaps are specified in fig. 4.2 and have been taken from reference [Asp76] where the parameters for the temperature and pressure dependence (equations 4.1 and 4.2) can be found as well. From the temperature coefficients can be seen that the difference between the L_6 minimum with respect to the Γ_6 minimum decreases with temperature (in contrary to the X_6 minimum). This means that *hot electrons thermalise in the L_6 minimum* with an electron population approaching 80% of the total population near the melting point.

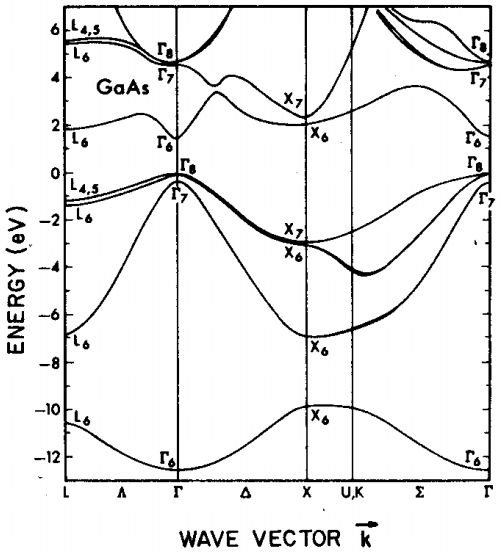

Figure 4.1: *Band structures of GaAs calculated after a nonlocal pseudo-potential scheme [Che76]. The top of the valence band, Γ_8^V, corresponds to an energy of 0 eV.*

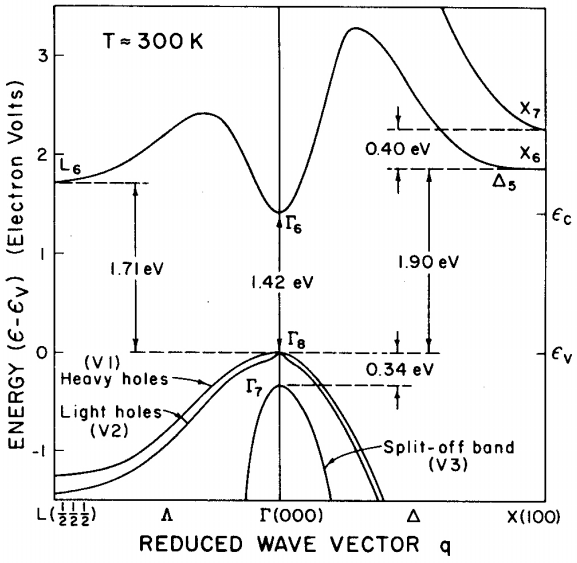

Figure 4.2: *Zoom into fig. 4.1. The uppermost part of the valence band system and the lower most part of the conduction bands is shown with the corresponding energy gaps in eV at room temperature [Bla82].*

[4]It might also be possible [Bla82] that this third minimum is not directly on the zone boundary, but located slightly inside the zone. In this case it would be denoted as Δ_5, but in this thesis X_6 will be used.

If charge carriers are produced in a semiconductor, the periodic crystal potential acts on them. As a result, their interactions can be described assigning them reduced **effective masses** compared to the mass m_0 of a free electron. Different definitions exist for the effective masses of a band leading to the same result for isotropic and parabolic bands [Bla82]. In particular the assumption of parabolicity is not fulfilled e.g. for the highest valence bands and the lowest conduction band. One of the frequently used definitions for the carrier effective mass is the *band curvature effective mass*

$$m^*_{n,p} = \hbar^2 \left(\frac{d^2E}{dk^2} \right)^{-1}$$

The problem of non-parabolicity can be approached by the so-called ($k \cdot p$) perturbation method performing (E-k) expansions about high symmetry locations in the reduced zone. If a band can be described by this method the different effective mass definitions converge towards one effective mass for the band edge ($E \rightarrow E_{edge}, k \rightarrow 0$) which will be used below.
Electrons in the upper valleys of the indirect conduction bands have transverse and longitudinal effective mass components, m_t and m_l. This can be considered for a simple parabolic band writing down

$$(m^*_n)^{3/2} = M_C \; m_t \; m_l^{1/2}$$

with M_C as the number of equivalent minima of the local conduction band minima.
For the Γ_6 conduction band minimum m_t=m_l=0.067 m_0 at low temperatures and M_C=1 (isotropic mass) [Asp76].
The low temperature transverse mass of the L_6 valley, $m_t \simeq 0.0754 m_0$, could be deduced from measurements, the longitudinal mass was scaled from the known longitudinal mass of Ge to $m_l \simeq 1.9 \; m_0$ [Asp76]. This leads to m^*_L, the effective low temperature mass of the four ellipsoid L_6-valley

$$m^*_L = \left[16 m_l \, (m_t)^2 \right]^{1/3} \simeq 0.56 \, m_0$$

For the X_6 valley a three ellipsoid model was proposed with $m_t \simeq 0.19 m_0$ and $m_l \simeq 1.9 m_0$ yielding

$$m^*_X = \left[9 m_l \, (m_t)^2 \right]^{1/3} \simeq 0.85 \, m_0$$

in the low temperature limit. The effective masses of the L_6- and the X_6-conduction band minima are much higher than m_{Γ_6} encouraging the transition of electrons to these minima with rising temperatures[5].
The effective masses for the lowest conduction band valley edges and the two upper most valence band edges are summarised in table 4.1 (the split-off band is not

[5] As the activation energy for the transition to the X_6 minimum is quite high and increasing with temperature, the major fraction of electrons will follow the $\Gamma \rightarrow L$ transition at high temperatures as already mentioned.

mentioned as it contains a negligible fraction of the total hole population). At room temperature, the effective mass of the heavy-hole band is $1/2\, m_0$ whereas the light holes have an effective mass of $0.076\, m_0$ with a population of only ∼6.9% of the total number of holes at room temperature [Bla82].

For a non-degenerate semiconductor ($E_F<E_C$, $n<N_C$) the **effective density of conduction band states**, N_C, has already been defined in equation 3.2. For the case of GaAs m_n^* has to be substituted by m_Γ^*. Taking into account the non-parabolicity of the lowest conduction band, the magnitude and temperature dependence of N_C can be well approximated for $100<T<1200$ K [Bla82] by

$$N_C \simeq 8.63 \times 10^{13}\, T^{3/2} \left(1 - 1.93 \times 10^{-4}\, T - 4.19 \times 10^{-8}\, T^2\right) \qquad \mathrm{cm}^{-3} \tag{4.3}$$

yielding a room temperature value for N_C of $4.21{\times}10^{17}$ cm^{-3}.
For the calculation of N_V, the effective density of the valence band states, the degeneracy and the anisotropy of the two upper most bands at the zone centre has to be taken into account in the determination of m_{hh} and m_{lh}. In equation 3.3 m_p^*, the density-of-states combined valence band mass, is then given by

$$m_p^* = \left[(m_{lh}^*)^{3/2} + (m_{hh}^*)^{3/2}\right]^{2/3} = 0.524\, m_0 \qquad \text{for } T = 300 \text{ K} \tag{4.4}$$

This results in an effective density of states $N_V{\simeq}9.51{\times}\ 10^{18}$ cm^{-3} for the valence band at room temperature.

With the above values for N_C and N_V the **intrinsic carrier density** n_i can be calculated with the help of equation 3.4 and eventually substituting the value for the band-gap with the parametrisation 4.1. Hence, the intrinsic carrier concentration is $n_i{\sim}2.25{\times}10^6$ cm^{-3} at room temperature which means that the **intrinsic resistivity** of GaAs is $>10^8\ \Omega$cm. Typical values for the resistivity of good Si detectors lie around $10^5\ \Omega$ cm.

For calculations or simulations, it is often necessary to know the **intrinsic Fermi energy**. Its location can be defined either with respect to the valence band or to the conduction band or to the mid-gap energy.

$$\begin{aligned} E_F &= E_V + kT \ln\left(\frac{N_V}{n_i}\right) \\ &= E_C - kT \ln\left(\frac{N_C}{n_i}\right) \\ &= E_V + 1/2\left[E_g + kT \ln\left(\frac{N_V}{N_C}\right)\right] \end{aligned}$$

At room temperature, the intrinsic Fermi level is situated 40 meV above mid-gap [Bla82] and increases with temperature whereas the distance to valence and conduction band

decreases due to the decreasing band-gap with temperature.

It should also be mentioned that doping and impurities change completely most of the above described properties of GaAs. This aspect will be described in more detail later in this chapter.

4.1.1 Electron and hole transport, lifetimes and ionisation energy in GaAs

In section 3.4.2 the carrier transport phenomena were already introduced. Charge carriers experience an acceleration under an applied electric field. The transport behaviour has to be treated separately for high and low electric field conditions.

At low electric field the drift velocity v_d is proportional to the field strength $\mathcal{E}$ with the **mobility** μ as the proportionality factor (equation 3.7). Due to the low effective mass of the electrons in GaAs, this material has the advantage of a very high electron mobility compared to silicon. The mobility is determined by various scattering mechanisms as it is directly proportional to the mean free time between scattering interactions.

At low temperatures, below ∼40 K, conduction electrons are mainly scattered by impurity atoms or lattice defects.
Impurity scattering results when a charge carrier passes beside an ionised impurity centre or other lattice defects. Coulomb interactions will deflect the charge carrier path. The impurity concentration determines the probability of impurity scattering which decreases with temperature (the charge carriers move faster which reduces the interaction time with the ionised scattering centres). The mobility μ_i related to this scattering mechanism shows the following dependence [Con50]

$$\mu_i \sim N_I^{-1} \, (m^*)^{-\frac{1}{2}} \, T^{\frac{3}{2}}$$

where N_I is the ionised impurity density. It has been calculated with the assumption that the motion of the thermal conduction electrons can be considered free and using the Rutherford scattering cross section together with a random distribution of impurity ions.

At higher temperatures scattering due to thermal vibrations of the crystal lattice atoms disturbing the periodic potential of the lattice becomes significant. In ionic crystals, two different types of these thermal vibrations may be distinguished. In the *acoustic mode* the positive and negative ions move in the same direction resulting in little polarisation effect. Very effective electron scattering can arise exciting the second type, the *optical mode* where positive and negative ions move in opposite directions and causing electric polarisation.
The so-called *deformation potential scattering* [Bar50] is related to acoustic phonons.

Conduction electrons of thermal energy have a wavelength which is large compared with the lattice constant. Therefore they interact only with acoustic vibrational modes of comparably long wavelength. The disturbance of the periodic crystal potential by the thermal vibrations can be described by a deformation potential which is determined by the bulk elastic behaviour. The importance of this scattering mechanism increases with temperature and the corresponding mobility μ_d varies as [Bar50]

$$\mu_d \sim (m^*)^{-\frac{5}{2}} T^{-\frac{3}{2}}$$

In polar semiconductors the interaction of carriers with the optical mode of lattice vibrations is known as *polar optical scattering*. This is the mobility limiting scattering mechanism above ∼80 K for GaAs [Sti70] as the energy change of the conduction electrons can be large compared with their initial energy.
Another source of polar scattering is *piezoelectric scattering*[6] which is associated with the acoustic modes of the thermal lattice vibrations leading to a periodic electrical potential. Since there is a 90^o phase difference between the matrix elements for piezoelectric and deformation potential scattering [Har56], these acoustic phonon scattering mechanisms should be considered separately.
An approximation for the mobility dependence arising from *polar scattering*, μ_p, was proposed [Ehr60]:

$$\mu_p \sim (m^*)^{-\frac{3}{2}} T^{-\frac{1}{2}}$$

The calculated temperature dependence of the different mentioned scattering mechanisms is shown in fig. 4.3 [Wol70] and compared to a measurement for a high purity GaAs sample. It can be seen that ionised impurity scattering dominates the low temperature range. Piezoelectric scattering limits the intermediate part, while polar optical scattering is responsible for the drop in mobility above ∼50 K. The deformation potential also shown in the plot was adjusted in the intermediate temperature range to obtain agreement between the calculated and the experimental mobility. In any case, its influence might vary considerably due to its strong energy dependence [Wol70].

In addition other scattering mechanisms of smaller impact on the mobility in GaAs exist like *neutral impurity scattering*[7] where conduction electrons are scattered at a neutral impurity atom or *intra-valley scattering* of electrons within one band minimum involving only long wavelength phonons.

At room temperature the mobility is therefore mainly determined by polar optical scattering and impurity scattering. The mobility as a function of impurity concentration for GaAs and Si at room temperature has already been presented before (fig. 3.5).

[6] GaAs is piezoelectric as it shows no inversion symmetry.

[7] Plays a role at very low temperatures where impurities are neutral due to carrier freeze-out and phonons have disappeared to a large extent.

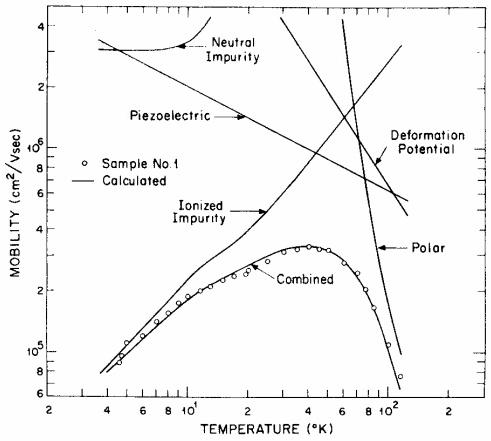

Figure 4.3: *Temperature dependence of the mobility for a high purity GaAs sample. Limitations from different scattering mechanisms are shown. The combined calculated mobility curve is compared to measurements [Wol70].*

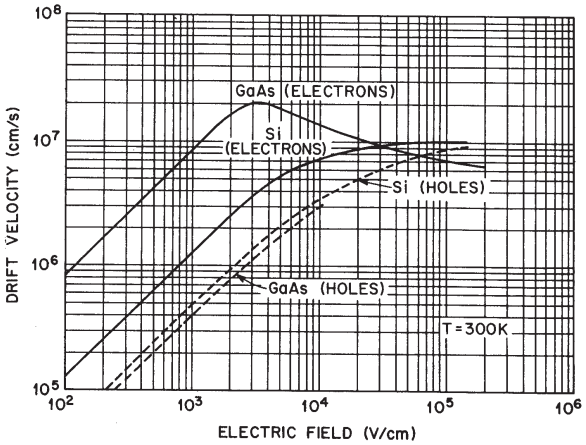

Figure 4.4: *Electron and hole drift velocities as a function of electric field for GaAs and Si at room temperature [Sze85].*

Under high electric field conditions the linear relationship of the drift velocity is no longer valid. The constant mobility part at low electric fields is illustrated in fig. 4.4 [Sze85]. The Si curves indicate that from a certain field strength on an increase in electric field leads to a flattening out of the drift velocity curves until v_d reaches a saturation value. This behaviour can be described considering that the charge carriers acquire energy from the electric field which raises their effective temperature. In thermal equilibrium a steady exchange of phonons takes place, but in the presence of an electric field the carriers emit more phonons than they absorb. The emission of optical phonons gets the most frequent scattering event at high fields yielding finally a saturation value for the drift velocity.

In the case of n-type GaAs the situation is much more complicated. After having reached a maximum drift velocity of about 2×10^7 cm/s at an electric field of $\sim$3.3 kV/cm [Ruc68], the electron drift velocity drops for higher fields. This region is called the region of *negative differential mobility* and is of great interest. Gunn has discovered in 1963 [Gun63] that applying a DC electric field above a certain threshold value across a randomly oriented n-type GaAs sample leads to an oscillating current with frequency in the microwave range (*Gunn effect*). Therefore GaAs can be used as a transferred-electron device [Sze81].
The explanation for the negative differential mobility is related to the band structure of GaAs. In addition to the warming up of the conduction electrons in the electric field they can be transferred to a higher energy band minimum as soon as they gain enough energy. The electrons in the Γ_6 have a very low effective mass (0.063 m_0) and can therefore easily be accelerated into the L_6 minimum which lies about 0.28 eV higher in energy with a much higher density of states. This *inter-valley transfer* mechanism results in an important decrease in mobility due to the difference in effective mass

($\mu(L_6)\sim$2500 cm^2/(Vs) [Bla82] compared to $\mu(\Gamma_6)\sim$8000 cm^2/(Vs) [Bla82]). From about 10 kV/cm on electrons start to significantly populate the X-valleys (X_6 lying $\sim$0.19 eV above L_6; $\mu(X_6)\sim$300 cm^2/(Vs) [Bla82]) while the fraction of electrons continues to decrease in the L-valleys [Wu91a]. Due to this fact and inter-valley phonon scattering the drift velocity tends to saturate at high electric fields.

For still higher fields above a certain value (in the order of $\sim 4\times10^5$ V/cm) the charge carriers gain enough energy to generate themselves electron-hole pairs. This process is called the *avalanche* or *impact ionisation process* [Sze85].

The main transport characteristics of GaAs are summarised in table 4.2.

Property	**Symbol**	**Value**	**Reference**
breakdown field		$\sim 4\times10^5$ V/cm	[Sze81]
max. electron drift velocity (at $\mathcal{E}$ ~3.3 kV/cm)	v_d^{max}	$>2\times10^7$ cm/s	[Ruc68]
saturation drift velocity	v_d^{sat}		
of electrons		$\sim 0.6\times10^7$ cm/s	[Smi80, Sze81]
of holes		$\sim 0.6\times10^7$ cm/s	[Sze81]
electron drift mobility	μ_n	8000 cm^2(Vs)$^{-1}$	[Bla82]
		8500 cm^2(Vs)$^{-1}$	[Sze81]
conductivity mobility at L_6^C	$\mu(L_6)$	$\sim$2500 cm^2(Vs)$^{-1}$	[Bla82]
conductivity mobility at X_6^C	$\mu(X_6)$	$\sim$300 cm^2(Vs)$^{-1}$	[Bla82]
		328$\pm$50 cm^2(Vs)$^{-1}$	[Pit70]
hole drift mobility	μ_p	320 cm^2(Vs)$^{-1}$	[Bla82]
		400 cm^2(Vs)$^{-1}$	[Sze81]
minority carrier lifetimes			
high purity n-type epitaxial GaAs	τ_p	$\sim 4\times10^{-5}$ s	[Rya72]
lowly doped n-type GaAs		$\sim 10^{-8}$ s	[Hwa72]
highly doped n-type GaAs		$< 10^{-9}$ s	[Hwa72]
average ionisation energy			
for alpha particles	ϵ_α	~4.27 eV	[Ebe71]
		~4.35 eV	[Kob72]
for electrons	ϵ_β	~4.57 eV	[Kob72]
Fano factor	F	0.12$\pm$0.01	[Ber97]
radiation length	X_0	~2.3 cm	[Ber90]
most probable specific energy loss	dE/dx	0.56 keV/μm	[Ber90]

Table 4.2: *Charge carrier transport properties and detector resolution parameters of GaAs at 300 K.*

It has to be kept in mind that the mobility is strongly related to the impurity concentration and the compensation (see next section). Mobilities at low electric field, peak velocities and the magnitude of the negative differential mobilities are substantially reduced in compensated GaAs due to compensation-enhanced impurity scattering [Xu88, Wu91b].

Minority carrier lifetimes are determined by the fact of GaAs being a direct band-gap semiconductor. This is a disadvantage as lifetimes in such materials are limited by radiative recombination (section 3.3). Theoretically, however, minority carrier lifetimes should be able to approach 0.1 ms in very pure GaAs crystals [Hal59, Rya72], but this has not yet been achieved experimentally [McG92]. This fact leads to the interpretation that usually the density of traps and recombination centres in GaAs is high. Also in compensated semi-insulating GaAs material trap assisted recombination seems to dominate the radiative recombination process. In practice, minority carrier lifetimes are in the order of only a few nanoseconds [McG94b].

The use of GaAs detectors as radiation spectrometers is related to two further intrinsic material properties, the average ionisation energy ϵ and the Fano factor F. The attraction shown for this material in spectrometry can be explained by the fact that it was one of the first materials which could demonstrate high energy resolution at room temperature [Ebe70]. Good energy resolution signifies small fluctuations in the amount of collected charge. Therefore the ionising particles should be fully absorbed by the material and the number of produced electron-hole pairs should be as big as possible (low average **ionisation energy**). In addition, the variance in the mean number of produced charge carriers has to be small. It has been seen that this variance is smaller than predicted by Poisson statistics indicating that the processes involved in charge carrier generation are not independent from each other. The corresponding correction factor is the **Fano factor** which is ideally as small as possible. The intrinsic energy resolution ΔE of a semiconductor detector at FWHM and particle energy E is therefore described by [Kno89]

$$\Delta E_{FWHM} = 2.35\sqrt{\epsilon F E}$$

The Fano factor was measured for γ-rays with high purity epitaxial GaAs to be 0.12±0.01 [Ber97]. Due to a fitting procedure applied to remove low energy tails this value might even be an overestimation of the Fano factor. Therefore the Fano factor of GaAs is very close to the values measured for Si and Ge[8] [Kno89].
The average ionisation energy decreases with temperature and, contrary to what is generally believed in the case of Si, seems to depend on the nature of the incident radiation. For alpha particles at room temperature it was determined to lie closely around 4.3 eV [Ebe71, Kob72] and for electrons at ∼4.57 eV [Kob72].

After this introduction into the basic material properties of GaAs the following section will mention briefly the material growth process and the doping compensation mechanism.

[8] at cryogenic temperatures

4.2 Semi-insulating GaAs through compensation

4.2.1 GaAs material growth

Various methods exist to grow GaAs material which can be classed in two groups: bulk GaAs growth techniques and epitaxial GaAs growth. The main difference for the end user between these two techniques consists in the higher purity of epitaxial materials, but unfortunately up to now the growth rate and thickness of epitaxial GaAs devices are limited (to about 200 μm) and they are not yet commercially available.

Epitaxy:
There are four main methods of growing **epitaxial GaAs**: LPE (*liquid phase epitaxy*), VPE (*vapour phase epitaxy*), MBE (*molecular beam epitaxy*) and MOCVD (*metal-organic chemical vapour deposition*). The common principle of all epitaxial processes is to grow a very pure single crystal layer[9] at a temperature substantially below the melting point on a substrate wafer acting as a seed crystal. LPE is the oldest method and had provided the first very pure GaAs detectors [Ebe71]. It is a rather simple and fast method consisting of bringing a bulk GaAs substrate into contact with a melt of high purity GaAs. Cooling down of the whole system allows for the growth of a thin film of high purity GaAs material on top of the substrate. It also results in a segregation of impurities into the GaAs melt [McG95]. One of the problems with this technique is the fabrication of larger area devices, but LPE room temperature radiation detectors have been successfully used by different groups [Ebe71, Ale92, Irs96]. The purity of these devices is generally slightly inferior to that obtained with the other epitaxial methods with the purest technique being MOCVD [Smi00].
MBE involves the deposition of atoms or molecules by means of one or more beams on a crystalline surface under ultra high vacuum conditions [Cho83]. Different crucibles for Ga, As and the dopants are used and their temperatures are adjusted in order to attain the desired evaporation rate. To get uniform epitaxial layers the holder with the heated substrate is rotated. Both chemical compositions and doping profiles can be precisely controlled. MBE has the disadvantage of very slow growth rates, but its purity and structural uniformity [Mis92] allows for excellent measurement results [Ber97].
The most popular epitaxial technique to produce high quality radiation detectors at acceptable growth rates is low pressure (LP) VPE. The principle there is similar to LPE replacing the GaAs melt with Ga and As in the vapour phase making use of a chemical reaction [Cam91, Ada97, McG95]. Depending on the molecules used for this reaction different variations of this technique exist, MOCVD being one of them (metal alkyls and arsine as starting materials). Some experimental results obtained with VPE devices can be found in [Bat98, Bat99, Chm99, Rog98b].
A relatively new[10] epitaxial growth technique should also be mentioned which is called CSVT, *close space vapour transport*. It consists in displacing the thermal equilibrium of a chemical reaction between a material which has the same composition as the ma-

[9] Net charge carrier concentrations in the order of 10^{13}-10^{14} cm^{-3} are typically achieved.
[10] in terms of production/application aimed

terial to be grown and a reactant. The reaction between the source material (kept at a certain temperature) and the reactant produces volatile products which are transported over a small distance under a pressure gradient to the substrate. There the inverse reaction takes place, but at a different temperature [Ham99]. High growth rates can be obtained, but the growth rate seems to be proportional to the EL2-concentration (see section 4.2.2) which deteriorates the detector performance.

Bulk growth techniques:
With **bulk GaAs** growth methods large and thick GaAs devices can be provided at the expense of reduced purity[11] and uniformity. The main differences between the various processes lie in the encapsulant used (or not used), details of the heat extraction, in the movement of ingot or furnace and in the type of furnace used.
Most GaAs wafer production is carried out using the *liquid-encapsulated Czochralski* (LEC) growth process. In this method a pure GaAs seed crystal is dipped into a GaAs melt and slowly vertically withdrawn by the rotating crystal puller. The GaAs melt is contained in a pyrolytic (usually boron nitride BN) crucible situated in a furnace. Progressive freezing at the solid-liquid interface between the seed crystal and the melt results in the growth of GaAs single crystals. A liquid encapsulant around the melt in form of molten boron trioxide (B_2O_3) prevents it from decomposition [Sze85]. It provides at the same time a shielding against contamination from various growth system components. Post-growth annealing of the GaAs substrates is usually applied to reduce crystal inhomogeneities associated with dislocations [Miy84]. LEC material is rather susceptible to such micro-inhomogeneities as it is difficult to control the shape of the growth interface and due to rather big temperature gradients during the growth process. There is evidence that these micro-inhomogeneities which are organised in a sort of dislocation network[12] modify the electrical crystal properties and therefore also the free carrier transport behaviour [Vai99, Vai98, Vai97, Rei99, Sie97]. Concerning the impurity concentration of LEC GaAs it mainly depends on the quality of the starting material.
All measurements which will be presented in this thesis stem from LEC grown wafers. Usually, the doping concentrations in the solid seed crystal are different from the ones in the GaAs melt. The *equilibrium segregation coefficient* k_0 is defined as the fraction of these two. During crystal growth, dopants or impurities are constantly being rejected into the melt if $k_0<1$. Depending on the transport rate of the impurities a concentration gradient will develop at the solid-liquid interface leading to an *effective segregation coefficient* k_{eff} valid far away from this interface [Sze85]. This property can either be used to obtain a uniform doping concentration by adjusting pull rate and rotation speed or to get rid of certain unintentional impurities. This principle is common to all bulk GaAs crystal growth processes.

[11] For bulk GaAs the net charge carrier density ranges around 10^{16} cm^{-3}.

[12] The dislocation density is characterised by the *edge pit density* (EPD) given in units of cm^{-2}. LEC grown crystals show quite high values of EPD in the order of 10^4-10^5 cm^{-2} occurring as cellular structures of 100-300 μm diameter. This is a result of high temperature gradients employed during crystal growth to permit good control of the large ingot diameters.

Another bulk GaAs growth variation is the *horizontal Bridgman* (HB) technique. A sealed quartz or boron nitride tube contains on one side a so-called boat with the polycrystalline GaAs and a suitable seed crystal inside and on the other side arsenic. The two sides are kept at different temperatures by a two-zone furnace. As the furnace is slowly moved (horizontally), the GaAs melt cools at one end and a single GaAs crystal is grown. In this process temperature gradients and therefore dislocation densities are low (around 5×10^3 cm^{-2}) and impurity distributions can be guided making again use of the segregation coefficient. The *vertical Bridgman* (VB) process has the advantage that round wafers can be produced from the beginning on and that they can be sliced perpendicular to the growth direction [Kre90].
The *vertical Gradient Freeze* (VGF) method is similar to the HB technique in the sense that it makes also use of a two-zone furnace (here in vertical position) with an As reservoir on one end and the polycrystalline GaAs on the other. Stoichiometry is controlled by regulating the As partial pressure [Fra96]. The growth vessel is rotated and great care is taken to establish a planar liquid-solid interface and to avoid all kinds of thermal stresses in order to minimise dislocations [Gau86]. Thermal stress is a result of radial and axial temperature gradients which can be reduced through optimisation of heater and insulator components and through controlled cooling down. Nowadays, the VGF technique is the most frequently used technique after LEC growth.
A different approach is the *vertical zone melt* (VZM) process. Polycrystalline GaAs is loaded in a sealed crucible with a seed crystal at the bottom and positioned vertically in a furnace. The furnace has a small high temperature zone, a 'spike' zone [Swi89], where the GaAs melts. Vertical movement of the GaAs ingot from the top of the seed crystal downwards results in an upwards movement of the so-called floating zone with GaAs single crystals being formed below this region. The shape of the solid-liquid interface can be adjusted by means of changing the width of the floating zone [Hen91]. Impurities with $k_{eff}<1$ segregate to the final end of the ingot to freeze. A single pass is not as efficient in purifying the crystal as a Czochralski growth, but several passes can easily be employed with the VZM technique [Sze85]. This method is known as *zone refining* and has been shown to segregate Zn and S impurities effectively [Hen96, Moo96]. No evidence could be found of C segregation by zone refining [Moo96]. *Zone levelling* enables to introduce impurities with k_{eff} significantly less than 1 uniformly distributed throughout the crystal. The main interest is to lower the EL2 concentration (see following section) starting growth from a Ga rich melt. Publications confirm a reduction of the EL2 concentration, mainly of the ionised $EL2^+$ defect [Hen96, Moo96, McG96a], but the technique still seems to need some improvements in terms of homogeneity and reproducibility [McG96a, McG96b, Hen96] to be able to provide high mobilities and charge collection efficiencies. It is also possible to combine both zone refining and zone levelling with VZM growth.

The two main goals in GaAs detector material growth are a fast growth rate together with the highest possible purity and homogeneity. Apart from residual impurities in the source material it cannot be avoided that impurities are introduced through chemical reactions between the growth system components such as crucible, reaction

tube, heater elements or involved gases [Mo96]. For instance carbon is the most common unintentional shallow acceptor. Oxygen gives rise to deep donor levels, but can also be used for gettering of silicon [Mar82]. Other frequently found elements which introduce impurity levels (mostly shallow) acting either as donors or acceptors are Si, B, Al, Zn, Pb, Fe or S. Fig. 4.5 [Rog98a] summarises various impurity levels with the corresponding measured ionisation energies. Consequently, it is very important to optimise all the involved system components as well as process parameters like inert gas pressures, temperature, humidity etc. [Sei96, War92].

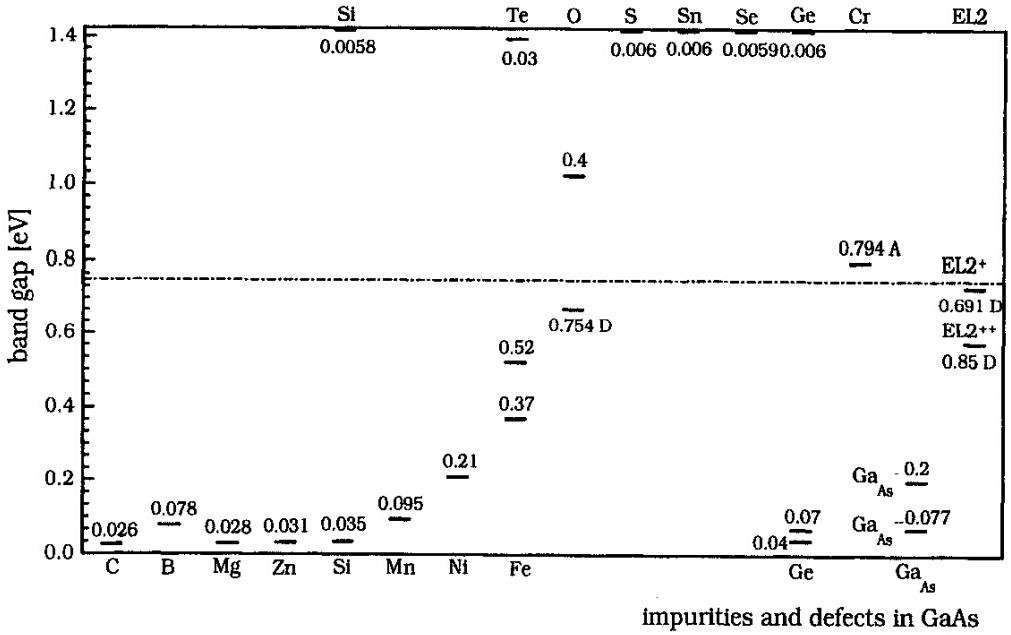

Figure 4.5: *Ionisation energies for various impurities and intrinsic defects in GaAs [Rog98a]. Levels above the Fermi energy level indicate donors (except for acceptor levels marked with 'A'). The energy difference is referring to the bottom of the conduction band. Contrary, values below the Fermi level denote acceptors (except if marked with 'D' for donor) with an energy difference indicated with respect to the top of the valence band.*

4.2.2 Compensation mechanism and defects in semi-insulating GaAs

It is rather difficult to produce very pure and at the same time thick and large GaAs radiation detectors. Nevertheless, it is possible to make very high resistivity material commercially and with good reproducibility. This fact is due to a complex **compensation** mechanism which takes place in GaAs.

In undoped[13] bulk GaAs the concentration of shallow acceptors, N_A, is usually greater than N_D, the shallow donor concentration[14] [Mar80] ($N_A \sim 10^{15}$ cm^{-3} or smaller and $N_A > N_D$; compare also fig. 4.5) and depends on the starting material and the growth process. High resistivity can be achieved as the remaining active shallow acceptors (mainly carbon) are compensated by a deep donor level labelled **EL2** [Mar77], the condition to be fulfilled being $N_{DD} > N_A\text{-}N_D$ with N_{DD} as the deep donor concentration. This balance between shallow donors (Si), shallow acceptors (C) and the EL2 defect is a simple three-model explanation for the compensation mechanism. More complex models exist, but are not further considered here. For detector applications it is of great interest to keep the shallow impurities as low concentrated as possible [War92] as higher compensation means lower free carrier mobility.

The EL2 defect is an electron trap with two active levels located around 0.75 eV below the conduction band edge and another level at about 0.5 eV above the valence band edge [Zai92, McG95, Oml88]. It is a double donor and can therefore exist in three states: neutral when occupied by electrons, plus one having given away one electron (EL^+) and plus two having donated both electrons (EL^{++}). The electrically active level at 0.75 eV belongs to EL^+ and is located almost at mid-gap, whereas EL^{++} corresponds to the level closer to the valence band. The location near the middle of the band-gap pins the Fermi level close to mid-gap resulting in very high resistivity $>10^8\,\Omega$cm. The generally accepted belief is that the EL2 defect is associated with the *As antisite*, As_{Ga}, As atoms taking the positions of Ga atoms in the crystal lattice. There seems to be still some doubt whether it is an isolated antisite or a complex of As_{Ga} with vacancies, with As_i (an As atom occupying an interstitial lattice position) or with something else [Dab89, Bou88, vB85, Lag82]. The different models have to be also consistent with one strange property of the EL2 defect, the existence of a low-temperature persistent metastable state induced by optical excitation [vB85, Del87]. In the metastable state EL2 disappears and renders semi-insulating GaAs p-type (no more compensation of the shallow acceptor surplus). Above 140 K EL2 is again regenerated. Whenever it will be feasible to disentangle the contributions of the various defects and impurities, it might be possible to identify unambiguously the EL2 nature.

It has been shown [Hol82] that the compensation of the GaAs crystal can be controlled through the stoichiometry of the melt. This is consistent with the association of the EL2 defect with an intrinsic defect. The critical atomic fraction of As in the melt is $\sim$0.475. Adding more As atoms increases dramatically the resistivity of the sample to values above 10^8 Ωcm as can be seen in fig. 4.6 [Hol82]. GaAs is conventionally regarded as being **semi-insulating (SI)** if room temperature resistivity is greater than 10^7 Ωcm [Tan89].

[13] Compensation can as well be achieved through doping with suitable atoms like chromium or oxygen introducing levels near mid-gap.

[14] Therefore undoped GaAs is generally p-type.

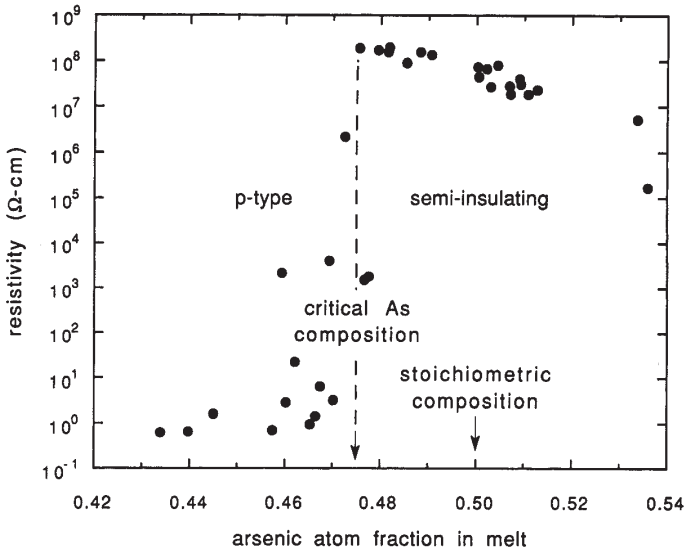

Figure 4.6: *Resistivity of LEC GaAs as a function of the As atom fraction in the melt [Hol82]. The dashed line corresponds to the critical composition above which the material becomes semi-insulating.*

This section shows that varying the stoichiometry of the melt is a nice and powerful method to control resistivity and free carrier concentrations in GaAs. Unfortunately compensation influences decisively detector properties. Mobility is reduced with the level of compensation and it has been shown that especially the $EL2^+$ concentration deteriorates the charge collection efficiency [Rog96, Ber96]. Overall EL2 concentrations in undoped SI GaAs range usually between 1-2$\times 10^{16}$ cm^{-3}, but there is quite some difference between $EL2^+$ concentrations in different GaAs samples. High charge collection efficiencies in SI GaAs detectors are therefore coupled to low $EL2^+$ concentrations which results in high electron lifetimes, but also in high leakage current densities [Rog99]. The conclusion in order to obtain very good GaAs particle detectors is to reduce substantially the total EL2 concentration (together with the impurity concentrations) or to use high purity epitaxial material.

4.3 Electric field distribution in semi-insulating GaAs detectors

To apply an electric field for separation of the electron-hole pairs generated from ionising radiation and to collect the created charge at the same time, at least one rectifying contact has to be utilised. SI GaAs detectors are most commonly fabricated with Schottky contacts on both sides, but configurations with one Schottky and one Ohmic contact or p-i-n detectors exist as well. For maximum charge collection it is necessary that the **active detector region**[15] extends over the complete detector volume. In principle, because of the very high resistivity of GaAs detector material, one would expect to need only a small voltage to collect charge over the entire detector

[15]=Region which is practically without free charge carriers.

volume. This is not the case as affirmed by measurements which make use of different methods[16] (optical, infrared, direct or electron beam probing or pulse height analysis from alpha particles or protons [McG95]) [McG92, McG94b, McG94a, But97, Nav97]. One of these measurements is presented in fig. 4.7 from ref. [McG94a]. The range of alpha particles with a certain energy is relatively well defined (Bragg curve). Therefore the beginning of the plateau in the measured pulse height gives a good indication for the extension of the active layer inside the device volume. In fig. 4.8 [Nav97] the dependence of the active layer width W from the detector bias obtained by OBIC (Optical Beam Induced Current) and SP (Surface Potential) measurements is shown. Only for bias voltages V<20 V the active layer width follows the $\sqrt{V}$ dependence for abrupt junctions (see equation 3.13). For higher voltages the active layer increases approximately linearly[17].

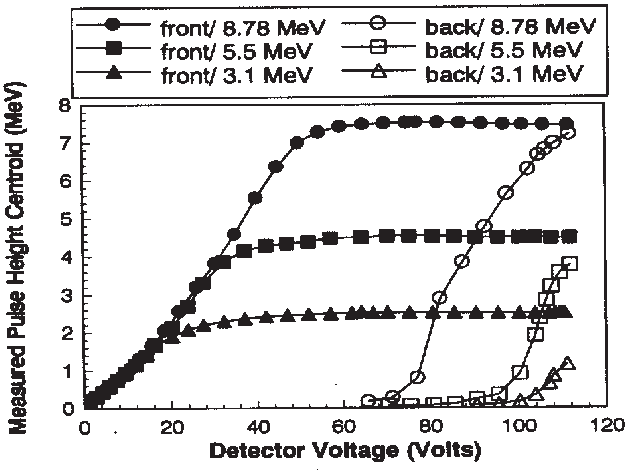

Figure 4.7: *Measured pulse height of alpha particles with 3.1, 5.5 and 8.78 MeV energy as a function of detector bias voltage for a 100 µm thick SI LEC GaAs detector [McG94a]. Filled symbols correspond to front irradiation and empty ones to back irradiation (electric field develops from front side).*

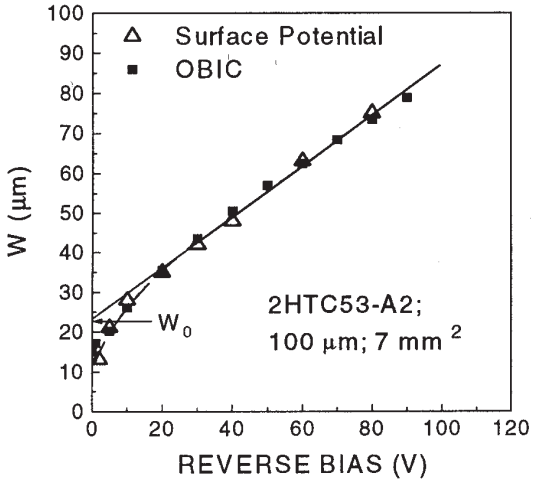

Figure 4.8: *Dependence of the active layer width W from the detector bias for a 100 µm thick SI LEC GaAs detector [Nav97]. SP and OBIC measurements show a linear dependence of W above 20 V.*

All the measurements observe roughly the same behaviour of the electric field applied to GaAs detectors. The detector volume can be divided into a *high and a low field region*. The high field region is almost constant and is followed by an abrupt drop in electric field strength to very low values. As the space charge is proportional to the spatial derivative of the field strength, this corresponds to a *quasi-neutral region* close to the contacts. The space charge distribution in the transition region between the high and the low field region gets wider and moves towards the rear-side contact with

[16]It should be mentioned that C-V measurement which are standard to determine the depletion width of semiconductor detectors can lead to misinterpretations and to overestimations of the active layer width because of the high resistivity of SI material [McG95].

[17]This explains the fact that the term 'depletion layer' should not be used for SI materials.

increasing detector bias [Cas98].

The challenge now is to explain the observed behaviour. Again several models exist, but almost all of them show some discrepancies. One model [Kub94] obtains a linearly decreasing electric field from the Schottky to the Ohmic contact. It solves numerically Poisson and continuity equations taking into account the density of deep levels using quasi-Fermi levels[18]. Although the model seems to describe well the measured CCE of some GaAs diodes, it is not consistent with the observed flat electric field (see figures 4.9 [But97] and 4.10 [Cas98]) close to the Schottky contact.

Another group proposes an electric field model with field enhanced electron cap-

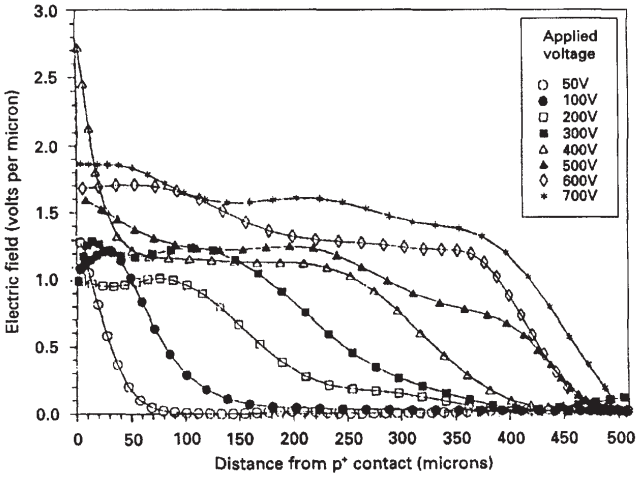

Figure 4.9: *Electric field distribution for a 500 μm thick SI GaAs detector as a function of detector bias measured with a surface probe method [But97].*

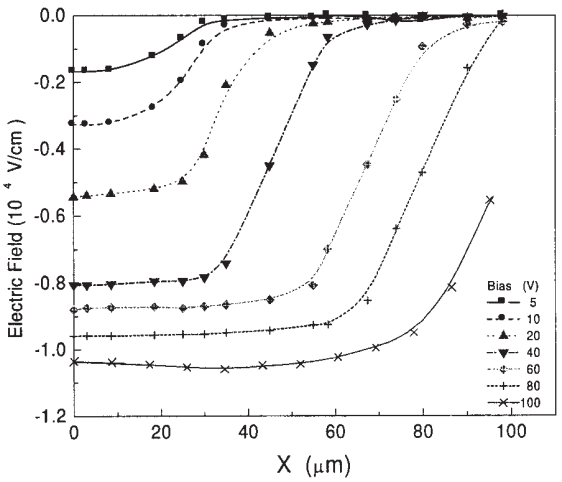

Figure 4.10: *Electric field profiles obtained from surface potential measurements on ∼100 μm thick SI GaAs samples [Cas98].*

ture [McG94a]. In an earlier paper [McG92] they had included the ionisation concentration of the deep donor EL2 in the Poisson equation 3.12. Putting in common values for N_{DD}^{+} and N_{A}^{-}, it can be seen that the deep donors would become completely ionised near the reversed biased Schottky junction leading to a dramatic drop of the electric field near this contact and to a region of positive space charge. This is inconsistent with the observed quasi-neutral space charge region, and the description of the active region width failed as well for this early model.

A solution for these problems was found taking into account the field dependency of the charge carrier emission and capture rates by the deep centres. Without external electric field the deep level capture cross-sections are thermally activated depending exponentially on the activation energy E_B [Pri83]. Measurements at strong electric fields of $\sim 10^4$ V/cm revealed that the capture cross-sections are almost temperature independent, but increase some orders of magnitude with respect to no applied field.

[18]Quasi-Fermi levels have to be used in the Fermi-Dirac function to describe the density of space charges as the thermal equilibrium is disturbed by the current flow resulting from the applied detector bias voltage

The measured capture cross-sections of EL2 for electrons and holes under zero and high electric field are shown in fig. 4.11. The results can be interpreted with a theory of non-radiative multi-phonon capture adding the assumption that high electric fields remove or lower the capture barrier E_B [Pri83].
The thermal emission of an electron from a localised electronic state is described by the Poole-Frenkel effect [Fre38] which is explained by screening of the positive fixed charge of ionised atoms through polarisation of surrounding atoms. The ionisation energy of the level is therefore decreased because of Coulomb potential barrier lowering. A further decrease results from application of an electric field. Nevertheless experimental results showed only a very weak dependence of the EL2 emission rate on the applied electric field [Buc88] which indicates the suppression of the barrier lowering for electron emission.
What follows from this discussion is that under high electric field conditions the electron capture rate of the ionised EL2 centres dominates the emission rate. This results in a decrease of the ionised EL2 concentration close to the reverse biased Schottky contact offering a possible explanation for the quasi-neutral space charge region observed above some critical field value and for the flat electric field [McG94a]. Unfortunately the actual EL2 capture cross-section as a function of electric field is not known which means that only an arbitrary function is used in the model [McG95]. The measurement of this capture cross-section together with the measurement of the filled EL2 defect (the concentration of EL2 in its ground state should clearly increase above a critical electrical field value with field strength) could probably verify the field enhanced electron capture model.

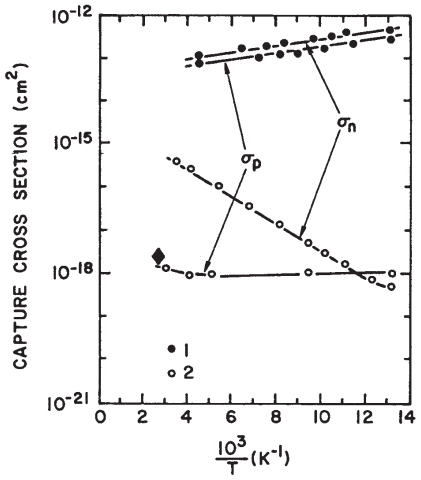

Figure 4.11: *Experimental data for the capture cross-sections of the EL2 level for electrons (σ_n) and holes ($sigma_p$) [Pri83]. Open circles denote measurements at zero electric field and filled circles at high electric fields.*

A very similar model was used by another group [Col97a] integrating electric field dependence of the carrier dynamics (mobility, diffusivity, electron effective mass, thermal velocity are field-dependent). They extended the field dependence of the cap-

ture cross-section which they base on hot carrier dynamics to other deep traps like the EL3 centre. This model also results in a near-flat electric field profile extending from the reverse biased Schottky contact, dropping off rapidly almost to zero value at the border of the active region and increasing in strength with the applied voltage. As the previous model these calculations suffer as well from the unknown field dependence of the capture cross-sections.
A completely different approach to the problem is related to inhomogeneities and dislocations mentioned in section 4.2.1. Thermal quenching effects in inhomogeneous material seem to be one possible explanation for the electric field dependence [Vai98].

Despite the vast quantity of publications about GaAs over the last 40 years there are still a lot of open questions. This concerns also other compound semiconductor materials like $Cd_{1-x}Zn_xTe$, but hopefully all the various effects can be disentangled in the near future.
In connection with the last sections it is perhaps also worth to mention what was stated in one publication [Cas98]: 'It is worth noting that the physics of high resistive materials is substantially different from that of semiconducting materials and the extension of theories and assumptions from semiconductors to semi-insulating materials is not trivial'.

4.4 Summary

This chapter was devoted to an extensive description of semi-insulating gallium arsenide detectors. It seems that the explanation of the spread in published material properties and in measurement results with GaAs detectors lies in its fabrication. The fact that it is a compound could also play a role in this context. GaAs crystal growth results in either very pure epitaxial material or in less pure, but cheaper and thicker bulk material. For optimum X-ray absorption efficiency in the energy range of mammography GaAs detectors have to be at least 200 μm thick. Technically it is not straightforward to obtain epitaxial detectors with this thickness at reasonable cost which explains the use of bulk GaAs material as sensors for the PCC system. The production of high resistivity GaAs relies on a complex compensation mechanism mainly of shallow acceptors with the deep donor level EL2 associated with the As antisite. Although the requirement of high resistivity material for a detector device is fulfilled this mechanism seems to lead to local material inhomogeneities, to a change in the extension of the electric field into the material with respect to the one known for semiconductors and to charge trapping. In practice, this signifies that unexpectedly high bias voltages have to be applied. Special contacts have to be produced to withstand these voltages in order to reduce charge trapping and to obtain good charge collection efficiencies.

After these introductory chapters which were intended to furnish the reader with the fundamental knowledge that is needed to understand all the parts of the PCC sys-

tem the following chapter will proceed to the description of the PCC photon counting chip.

Chapter 5

The Photon Counting Chip (PCC) of the Medipix Collaboration

Contents

The design of a single photon counting chip at CERN, the PCC (**P**hoton **C**ounting **C**hip), became only possible through the availability and maturity of certain technologies and experience gained in high energy physics experiments and related fields. In addition, it needed the enthusiasm of some high energy physics groups to enter the field of medical imaging. The history of this development should help in understanding the choice of this imaging system, its advantages (and disadvantages) and the natural way it emerged from high energy physics. Later in this chapter, a detailed description of the chip will be given and measurement results of the chip performance presented.

5.1 Motivation for pixel detectors in high energy physics

The development of the Photon Counting Chip is strongly related to the development of pixel chip design for high energy physics. In the 80s many groups in the high energy physics community had to face the challenge of planning detectors for the future big colliders, the SSC (**S**uperconducting **S**uper **C**ollider) in Texas (construction

has been cancelled) and the LHC (**L**arge **H**adron **C**ollider) at CERN which is planned to run from the year 2005 on. One of the most critical problems arising from the new colliders was the design of the tracking detectors. In colliders the tracking detectors are the detector elements which are closest to the interaction point of the colliding beams. In this region there is an extremely high density of tracks arising from primary and secondary particles which have been produced after the particle collision. The purpose of tracking detectors is to disentangle the various particle tracks and to assign them to primary or secondary vertices. The very high track density together with a high beam crossing rate and other considerations lead to the following requirements for a good tracking device:

- no dead regions in as large an acceptance as possible
- good spatial resolution in the micrometer range in 3 dimensions
- no ambiguities in the track assignment, capability to resolve clearly high multiplicity events
- short read-out time to cope with high event rates (≈40 MHz bunch crossing rate)
- high radiation tolerance[1] in the order of tens of Mrad
- high signal to noise ratio
- reliability in view of difficult access after starting operation
- low effective mass in order not to disturb particle identification in the outer detectors
- low power consumption (cooling facilities introduce mass)
- data processing and reduction 'in situ'

The systems which were considered in the first half of the 80s were first of all **microstrip detectors** [Hei80]. They consist of thin (usually 300 μm thick), high resistivity silicon sensors segmented on one side into narrow, rectifying, ion-implanted strips with a pitch in the order of 10 μm. The reverse biased diode structures formed between the strips and the rear side of the sensor determine one coordinate of the crossing particles. Different read-out concepts are used, one of the most common being capacitive charge division between strips. In this approach only a fraction of strips is connected via ultrasonic wire bonding to its read-out circuit. Charge from one event is spread between adjacent strips due to drift and diffusion. With analog read-out electronics the centre of the charge distribution can be calculated. It was possible to reach excellent spatial resolutions below 5 μm (see e.g. [Bel83]) and a lot of the above requirements could be fulfilled. Nevertheless, the major problem of unresolvable ambiguities in track assignment arising from multiple hits remained. Even

[1]The two major experiments at LHC, ATLAS [ATL94] and CMS [CMS94], expect a total dose of about 30 Mrad for the inner detectors after 10 years of operation.

double-sided microstrip detectors cannot assign an unambiguous space coordinate to multiple close tracks.

In 1984 **semiconductor drift detectors** were proposed by E. Gatti and P. Rehak [Gat84]. Diodes are put on both sides of the wafer (p^+ implants on n^- substrate) and there is only one collecting electrode (n^+ implant) usually placed somewhere close to the lateral detector edge. Applying a reverse bias from both sides of the detector full depletion can be reached. The negative charge carriers are attracted to the resulting potential well in the middle of the detector and drift towards the n^+ electrode (anode) by means of a graded potential on the implanted strips. Therefore one space coordinate can be obtained measuring the drift time of the electrons. It is possible to obtain the other spatial coordinate by segmenting the n^+ read-out electrode [Reh86]. Spatial resolutions are comparable to strip detectors, but with far less read-out channels.
A strong point of this device is the low noise which is possible thanks to the low output capacitance. The main limitations of drift detectors are related to the generally rather long distances electrons have to drift towards the anode not matching the fast timing requirements in high luminosity colliders[2]. Moreover, as the charge carrier mobilities are temperature dependent the drift times vary considerably with temperature (need for extensive calibrations). They are also dependent on electrical field variations due to material inhomogeneities which makes them not suitable for high radiation environments. Two track resolution is limited due to charge diffusion during the drift time.

CCDs (already described in section 1.5) were also considered as tracking devices. The main disadvantage of CCDs is the read-out time (at best a few ms) which is incompatible with 25 ns bunch crossing at ATLAS and CMS. Moreover, they are sensitive to radiation damage and even well optimised CCD layouts cannot avoid some dead space. Also data reduction on chip is usually not provided.

Another two-dimensional approach was provided by **pad detectors**. They consist of thin semiconductor detectors with segmented electrodes on one side which are connected to their individual signal processing circuits via metal lines on top of the detector. This technique results in pad dimensions in the order of millimetres which is too coarse for the inner tracking systems in many experiments.

In the early 90s Si process technology advanced quickly [Moo65] and 1 μm CMOS[3] technology[4] became standard. The idea of shrinking the size of the pads down to the micrometer scale seemed to become more than a dream [Hei88, Die89, Van89, Sha89, Cam89, Par89] as the limit in realisation was given by the integration of logic close to the detector elements and not by the detector processing itself which was already in an advanced state (planar VLSI technology [Kem80, Kem84]). Such a detector

[2]Drift times are in the order of a few microseconds.

[3]**C**omplementary **M**etal **O**xide **S**emiconductor.

[4]1 μm corresponds to the transistor gate length and is a measure for the component miniaturisation.

system including also information processing functions was proposed to be called a *micropattern detector* [Hei88] as it would provide event selection based on a pattern of the interactions in micrometer scale. Following the nomenclature used for CCDs and optical devices the name active **pixel detector** is more often used instead, each pixel being one tiny electrode. Each detecting element is composed of one diode attached to its read-out electronics. The diode is finely segmented leading to high two-dimensional spatial resolution. The concept of active pixel detectors consists in having the electronics cell equally dimensioned and close to the corresponding pixel. Therefore the capacitance of the collection electrode can remain very small and the signal to noise ratio high. It is also possible to implement some important logical features e.g. for data selection (zero-suppression).
There are several possibilities of realising pixel detectors. Either the sensor and the electronics are processed on the same substrate (monolithic pixel detectors or pixel detectors in SOI) or on two different substrates connecting the sensor and electronics pixellated electrodes together (hybrid pixel detectors).

Monolithic pixel detectors

In monolithic pixel detectors the electronics circuitry is integrated with the detecting elements onto the same substrate. This results in a more robust and thinner device (to reduce energy loss and scattering inside a complex high energy particle detector) compared to the hybrid approach. Different architectures for monolithic pixel detectors are possible [Sno92].
The principle consists of placing the electronic components directly into the high resistivity substrate, usually n-type. To avoid shorts, a p-well has to be implemented to contain the n-MOS transistors. Low leakage currents could be obtained either through gettering of impurities [Hol89] or through careful processing at relatively low processing temperatures [Van89, Van90, Van92]. However, if p-type transistors are placed directly in the substrate, charge losses cannot be completely eliminated if two types of transistors are used.
Therefore the use of a well of the same type as the substrate containing the complete read-out circuitry was proposed [Par89]. In this proposal the p^+ collection electrodes are adjacent to the n-well. The well serves as Faraday cage for the electronics and forms the electric field such that charge created by a particle inside the detector volume will be guided to the collection electrodes. A reverse bias on the diode formed by the collection electrodes and the detector rear side extends the depletion layer into the substrate and underneath the well. Unfortunately, for full depletion and full collection a high well bias is needed or a large collection electrode.
These problems can be solved by using an n-well containing the electronics inside a lowly doped p-type substrate [Ken94, Sno94]. In this approach only p-MOS logic is used inside the active area, and the junction is formed between the n^+ rear side electrode and the collection electrodes (see fig. 5.1 [Sch97]). The substrate is now depleted from the rear side keeping the electric field near the well small. Until full depletion is reached the p-type collection electrodes are shorted. Furthermore, to prevent shorting

the diode from the front side to the rear side while dicing the wafer guard-rings have to be implemented. This is a disadvantage as the wafers have to be processed on both sides which makes the process non-standard and therefore more expensive. Another considerable disadvantage is the restriction in design possibilities. Only p-MOS transistors can be used inside the n-well and therefore no static CMOS logic is possible in the active area.

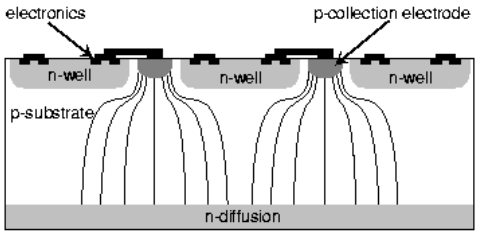

Figure 5.1: *Cross sectional view of a monolithic pixel detector [Sch97]. The field lines guide the charge carriers onto the collecting pixel electrodes.*

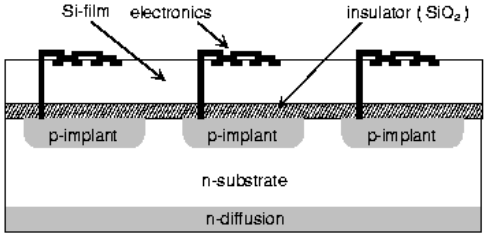

Figure 5.2: *Cross sectional view of a pixel detector in SOI technology [Sch97]. An insulating layer separates the active detector part from the read-out electronics which are embedded in a thin silicon layer.*

Pixel detectors in SOI technology

A different processing technique called SOI (**S**ilicon **O**n **I**nsulator) for electronics circuitry consists in implementing the transistors on a Si film which is grown on an insulating substrate. This reduces the drain and source diode capacitances making the electronics faster for a certain power consumption. Another advantage of SOI is radiation tolerance including the prevention of electronics latch-up[5] provided special precautions are taken at the interface between the oxide and the silicon. Radiation tolerance is the reason why some high energy physics experiments decided to use SOI chip technology[6], but with the sensor bump-bonded to the electronics (hybrid approach). It was proposed [Pen96] to implement a pixel read-out in SOI technology. The high resistivity substrate below the SOI oxide layer could be used as the detection volume. The pixel implants on the sensor should be connected with the electronics using vias through the silicon dioxide (see fig. 5.2). This monolithic detector design requires non-standard processing (double-sided processing, p-implants underneath the oxide layer of the SOI wafer) which can make it very expensive.

Hybrid pixel detectors

[5]Latch-up is when a high current flows between the positive and negative power supplies. It is induced when a parasitic thyristor is turned on between active areas and the substrate for example due to a spike in the power supply. Radiation induced latch-up takes place when a large amount of charge is deposited locally by a particle passing through the device. This may lead to a high current in the circuit or even to its destruction.

[6]Nevertheless, it is also possible to achieve high radiation tolerance by using standard sub-micron CMOS technology which is naturally radiation hard due to tunnelling effects in the very thin gate oxide layer implementing some special design rules for the n-MOS transistors [Sno00, Cam99].

In a hybrid pixel device the read-out chip and the sensor are processed separately. The two parts each have a matching matrix of pixellated electrodes which are connected together mechanically and electrically through small connecting balls (usually made out of solder or indium with diameters as small as ∼20 μm) as represented in fig. 5.3. This procedure is called **flip-chip process** or **bump-bonding process** and offers the possibility of optimising the electronics (flexibility in the choice of the design technology) and the sensor separately. Moreover, the detector material can be chosen for a specific application which makes this method so interesting for medical imaging applications. GaAs, CdTe or $Cd_{1-x}Zn_xTe$ can be used as sensor material instead of silicon which, being a low-Z material, has very low absorption efficiency for X-rays with energies greater than about 20 keV. An important aspect of the technology is the reliability and yield of bump-bonding connections[7].

It is important to note that only the hybrid approach allows the design of the pixel read-out in standard CMOS. This is a major consideration in view of the processing cost.
The PCC, the imaging pixel chip which was used for all the measurements presented in this thesis, has been designed as a hybrid in standard CMOS technology.

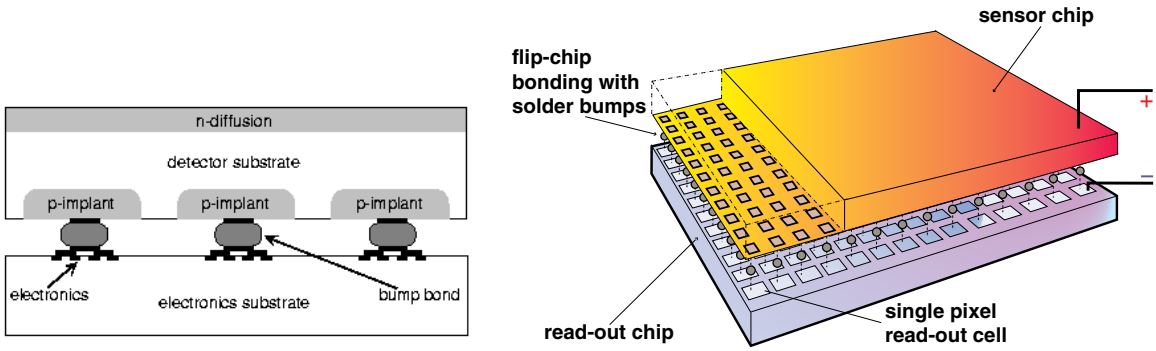

Figure 5.3: *On the left side a cross section through a part of a hybrid pixel detector is shown with the sensor on top and the electronics underneath connected through bump bonds [Sch97]. A different 3-dimensional view (right) gives a good idea of the whole hybrid assembly.*

5.2 A short history of the PCC

To start from the end, the idea of making a single photon counting system for X-ray radiography has been realised by the **Medipix collaboration**. Partners of the collaboration were CERN, the University of Freiburg (Germany), the University of Glasgow (Scotland) and the Universities and INFN of Pisa and Napoli (both Italy). The microelectronics group at CERN and the group from Glasgow were already collaborating in the framework of the RD19 collaboration at CERN [Hei90] which was founded in 1990

[7]Nevertheless all the experiments at LHC except probably LHCb decided to implement hybrid pixel detectors as tracking devices. To reduce the amount of material in the detection system the wafers can be thinned down.

to develop hybrid and monolithic active pixel detectors for the future LHC experiments. The first hybrid pixel detector resulting from that collaboration was assembled to the first chip from the Omega series [Ang91] whose functionality was tested in the WA94 heavy ion experiment in the Omega spectrometer at CERN [Bek93]. Several chips followed [Cam94, Hei96] (for an overview consult [Rop00]) allowing the collaboration to gain a lot of experience in the design and test of hybrid pixel detectors which included steadily more transistors and functions on chip. An important issue has also been the coverage of large area [Cam94] which enabled the collaboration to build a telescope for the WA97 heavy-ion experiment. This telescope consisted of seven compact 5 x 5 cm^2 planes of pixel detectors, each plane comprising 72000 channels [Hei94], resulting in more than half a million of read-out channels. In a following step 13 pixel planes with a total of about 1.1 million channels were successfully used [Man99c].

Although the pixel detector development in RD19 was dedicated to high energy physics experiments, the idea of using the Single Photon Counting principle with hybrid pixel detectors dated back to the late 80s [Hei89] with further enhancements in subsequent years (see e.g. [Hei93a, Hei93b]). Efforts started to demonstrate the advantages of hybrid pixel detectors for applications other than high energy physics like optical, medical or biological imaging [DaV94, DaV95a, DaV97a]. First the feasibility of coupling the silicon pixel detectors to scintillating fibres (for high energy particle tracking) and to scintillating crystals (used as gamma converters in nuclear medicine) was shown [DaV94, DaV95b]. To be able to detect visible and infrared light the aluminium rear side contact had to be replaced by a thinner and concentration enhanced n^+ ion implantation. An image intensifier was used for charge multiplication replacing the photo-diode with the pixel detectors. Images from high energy beam particles as well as from radioactive sources were obtained.

Another group at CERN concentrated on a very interesting imaging application, the use of active pixel devices inside a photo-tube offering the possibility to image single photons in the visible. This idea has been employed for the development of the ISPA tube, the **I**maging **S**ilicon **P**ixel **A**rray tube [Gys95]. The ISPA tube is basically an image intensifier except that the conventional phosphor screen is replaced by a hybrid silicon pixel detector. Photons impinging on the photo-cathode (evaporated on an optical entrance window) release photo-electrons which are accelerated inside the tube vacuum and focused onto the pixel detector anode. Omega pixel chips have been used which contain a discriminator and a binary read-out offering single photon detection [Cam94, Hei96]. They can be triggered with the amplified fast signal from the rear detector side (electron signal) which can also be used to select events in a certain energy window. Originally, the tube has been developed to read out 60 μm scintillating fibres which form a charged particle tracker in a high energy physics experiment [D'A95]. Now the ISPA tube is one proposed option for the read-out of the LHCb Ring Imaging Cherenkov (RICH) counter [LHC98]. Beside this application the aptitude of the tube for auto-radiography [Pue96] and gamma imaging [Pue95, Pue97] has been extensively investigated. The proof of the excellent functioning of the ISPA tube is important for

some imaging applications (like electron microscopy) showing the possibility to use hybrid technology inside vacuum.

Parallel to the RD19 collaboration there was a collaboration at CERN, the RD8 collaboration [RD893], studying the potential of using GaAs detectors for the LHC experiments, especially in view of their predicted radiation tolerance. Material properties in view of detector applications have been extensively studied (see e.g. [Bea94b, Che95, Che96, Bat96, Rog96]). Simple diodes, pad detectors, microstrip detectors, double-sided microstrip detectors as well as pixel detectors from various GaAs materials have been investigated [RD895, Bea94a, Smi96, Bat97]. The Universities of Glasgow and Freiburg participated in RD8 as well as in RD19 combining the pixel effort with GaAs sensors. Moreover, they have their own GaAs detector fabrication facilities on site.

Groups from Italy (mainly Universities/INFN from Pisa, Cagliari, Napoli and Ferrara) also started to be interested in using single photon counting pixel detectors for medical imaging. Different than for the RD19 collaboration, their interest didn't arise from previous work with pixel detectors, but from their experience with double-sided microstrip detectors in high energy physics and in the field of medical imaging. Simulations showing the benefits of double-sided silicon microstrip detectors for radiography have been published beginning of the 90's [Bat90, Ben91]. First images obtained with radioactive X- and gamma-ray sources followed [Alf92]. The 300 μm thick silicon detector consisted of 12 μm wide microstrips on both detector sides with a read-out pitch of 100 μm operating in capacitive charge division mode (floating strips between read-out strips) and has been developed by the Pisa group participating in the ALEPH[8] collaboration at CERN. Extensive tests of the imaging capabilities of the system in view of digital radiography followed, using also a mammographic tube [Alf93]. Soon it became obvious that the silicon sensor should be replaced by a material with much higher absorption efficiency for X-rays in the diagnostic energy range. This lead to an investigation of GaAs detectors [Ben94, Ber95a]. Despite complex coincidence logic applied for the double-sided strip detectors [Con93] efficiency loss due to 'ghost hits' (unresolvable multiple hits) is not negligible with the relatively high photon rate in medical diagnosis (in the order of several 10^5 photons per second and mm^2 for mammography). Therefore the efforts started to focus on pixellated detector geometries [Ber95b]. First images were taken with a matrix of 36 square pixels of 200 x 200 μm^2 area wire-bonded to the (external) read-out circuitry.

In this situation it was only a question of time that the efforts of the different groups working on pixel detectors, GaAs material and medical imaging applications were combined. This led to first common experiments employing GaAs sensors connected to RD19 pixel read-out chips [DaV97b, Ame96, Ame97].

[8]ALEPH is one of the four high energy physics experiments at the LEP, the Large Electron Positron collider at CERN.

The experience of the individual groups finally led to the formation of the Medipix collaboration. On the one hand there was the knowledge and the experience of using GaAs sensors with their good stopping power for low energy X-rays, and on the other hand expertise in designing pixel chips.

5.3 Description of the PCC

The Photon Counting Chip is a prototype electronics chip to read out a semiconductor pixel matrix, aimed at various imaging purposes. It has been designed at CERN [Cam98] taking into account specifications from the Medipix collaboration. The square pixel size is one of the attributes qualifying the chip for imaging applications. The key feature of the chip is that it allows to perform single particle counting in each pixel cell.

The PCC is designed in the SACMOS1 (1 μm **S**elf-**A**ligned Contact **CMOS**) process of FASELEC AG[9], Zürich, whose component density is comparable to a 0.6 μm standard CMOS process. This was the highest density available at the time of the design. The pixel size of $\mathbf{170 \times 170\ \mu m^2}$ could be achieved due to this high density. The whole matrix contains 64 x 64 identical active cells = **4096 pixels** to be bump-bonded to an equally segmented matrix of a semiconductor sensor.

Each pixel cell comprises the following features (compare block diagram shown in fig. 5.4):

– **The analog front-end**

The analog front-end has no switched reset of the preamplifier, but is otherwise identical to the one of the Omega3/LHC1 chip developed by the RD19 collaboration for high energy physics [Hei96]. Charge released by a particle inside the detector drifts in the applied electric field to the detector electrodes and will be transferred via solder bumps ($\approx$24 μm in diameter [Hum97]) to the input of the chip. Only positive signals are accepted.
Pixel cells in an added 65th row at the bottom of the matrix sense the detector leakage current. The sensed current is then reproduced with opposite sign in each of the 64 pixels of the corresponding column to cancel the incoming detector dark current. The compensation current has a practical range of up to 10 nA per pixel for this circuit. The leakage current compensation therefore only works correctly for (column-wise) uniform detector leakage currents.
Subsequently, the signals are amplified by the charge sensitive preamplifier.

– **The comparator**

The height of the amplified signal is compared with a globally set (for the whole

[9]now Philips AG, Binzstr. 44, CH-8045 Zürich.

chip) threshold of the comparator. In addition, the comparator can be trimmed on a pixel-by-pixel basis with a 3 bit DAC[10] which is very important in order to get a uniform distribution of thresholds across the whole pixel chip.
Only when the signal height exceeds the threshold the signal will be further considered. If the cell is not masked (faulty pixels can be masked through 1 mask bit) the width of the now digital pulse is defined through an externally adjustable delay and the comparator will be reset.

– **The counter**

The acquisition time is externally set by a 'shutter' signal. When the shutter is active and the pixel unmasked, the 15 bit pseudo-random counter [Hor80] will count each signal which had passed the comparator threshold. Therefore, the chip is **single photon counting**.
The pseudo-random counter is a finite state machine with $(2^{15} - 1)$ distinctive states. Each clock pulse causes a change of state. The number of counts in each cell will be derived by comparing the pseudo-random number with the contents of a look-up table (LUT). The counter is static and is connected during read-out phase as a shift register to the upper and lower neighbour pixels of the same column enabling a serial read-out of the column. This concept makes the information storage part of the read-out which saves valuable space.

For evaluation of the operation of the chip and its performance an electrical test pulse simulating a particle signal can be applied to each pixel via a test-input capacitance setting one test bit (which means closing the test switch).

The PCC measures ∼12250 μm x ∼14000 μm yielding a total area of ≈1.7 cm^2. About 70% of the total area is sensitive. The insensitive area contains the guard-ring and power supply lines on three sides. The largest insensitive area is at the bottom of the chip. It is due to the already mentioned dummy row for the leakage current sensing plus to a 66th row of bump-bonding contacts used for grounding the guard-ring of the sensor. As well as this there is the peripheral control logic and two rows of wire bonding pads. The total sensitive area is **∼1.18 cm^2**.
Figure 5.5 shows a photograph of the PCC. The matrix of 65 rows and 64 columns of 170 μm square pixels can be distinguished.

Four voltages have to be applied externally to the chip:

1. $\underline{V_{dda}}$: analog power supply: ∼3 V
2. $\underline{V_{dd}}$: digital power supply: ∼3 V
3. $\underline{V_{ss}}$: system ground: 0 V

[10]=Digital-to-Analog Convertor.

4. V_{gnd}: analog reference voltage: ∼1.5 V

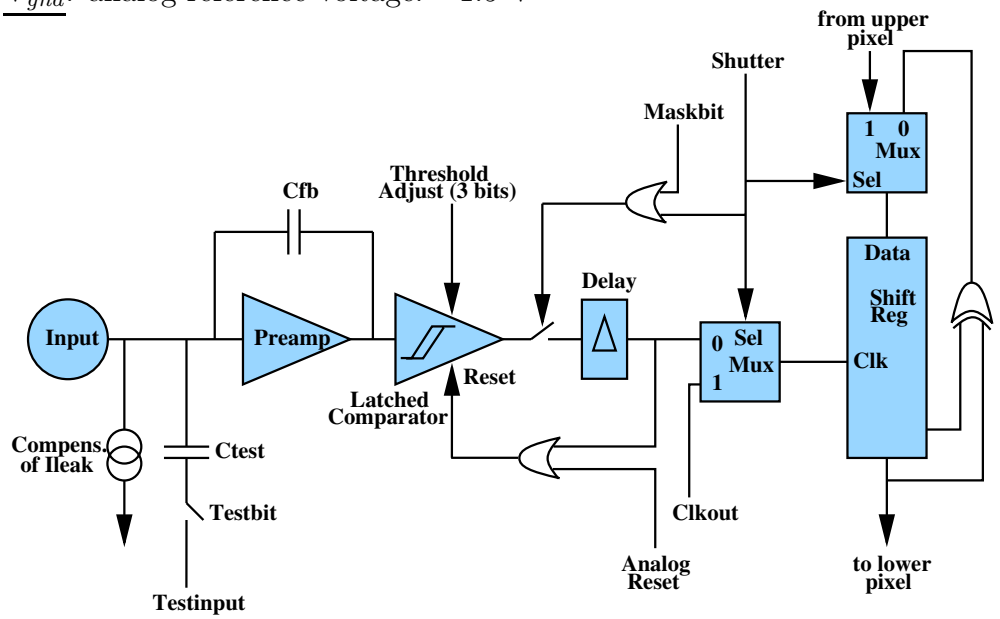

Figure 5.4: *Block diagram of one PCC pixel cell. Main steps: input - charge sensitive preamplifier after leakage current compensation - globally and locally (3 bits) adjustable comparator - delay - 15 bit pseudo-random counter when shutter active, acting also as a shift register during read-out. 1 mask and 1 test bit available.*

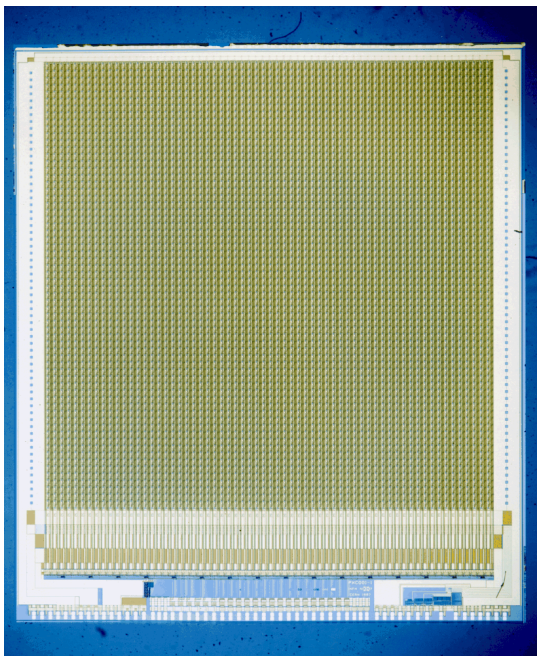

Figure 5.5: *Photograph of the PCC. The matrix comprises 64 x 64 active pixel cells of dimensions 170 x 170 μm^2. A 65th dummy row is added at the bottom for leakage current sensing. Below buffers can be seen and at the edge the double row of pads for wire-bonding and probe-testing the chip.*

The chip operation requires also 5 analog biases whose values have to be optimised in view of the application:

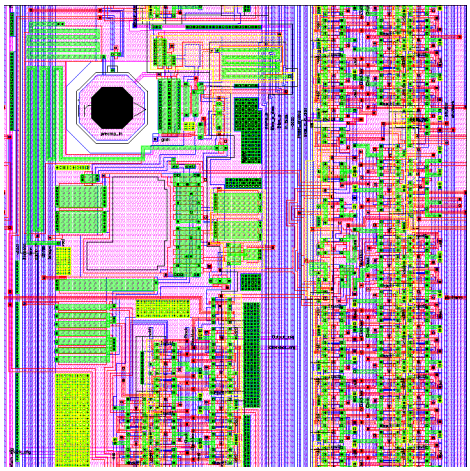

Figure 5.6: *CAD layout of a single pixel cell. In the top left corner the octagonal pad for the bump bond can be recognised. The different shades in the layout correspond to different metal layers (two for the SACMOS1 process) and the polysilicon layer.*

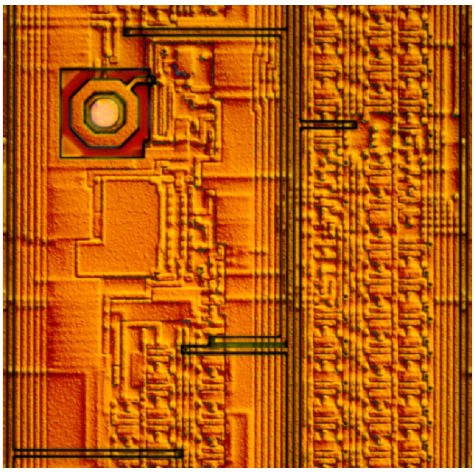

Figure 5.7: *Photograph of the single cell. The left part of the cell contains mostly the digital functions (except the 5 configuration bits - 1 test bit, 1 mask bit and 3 threshold adjustment bits - at the bottom). On the right side the 15 bit counter is located.*

1. V_{bias}: defines the operating point of the preamplifier
2. V_{comp}: controls the return to zero time of the preamplifier and supplies current for the leakage current compensation
3. V_{th}: sets the comparator threshold
4. V_{tha}: current defining the range of the threshold adjustment
5. V_{dl}: delay; defines the length of the pulse at the comparator output

Fig. 5.6 represents the layout of one single pixel cell and fig. 5.7 a photograph of the same. Dimensions correspond to 170 μm on both sides. One cell contains about 400 transistors which results in more than **1.6 M transistors** per chip.

Summary of the main features of the PCC:

- square pixel size of 170 μm x 170 μm
- total active area: $\sim$1.18 cm^2 (64 x 64 pixels)
- a shutter of variable length defining the active time can be applied
- self-triggering when the shutter is on
- leakage current compensation for uniform leakage current
- low threshold ($\sim$2000 e$^-$)

- 3 bit threshold tuning per pixel ⇒ threshold homogeneity
- 15 bit counter ⇒ high dynamic range
- fully static logic ⇒ long data acquisition periods without need for refresh signals possible

5.3.1 Read-out architecture of the PCC and read-out system

The PCC has two read/write shift registers for configuration and data read-out, the control bus and the data bus. The *5 configuration bits* per cell (test, mask and 3 threshold adjust bits) are connected in series column-wise and the clock is multiplexed in sequence to 4 columns. This means that 5 x 64 x 4 = 1280 clock cycles are needed to load the configuration data. Bits are loaded from bottom to top, first the mask, then the test bit followed by the threshold adjust bits. The reading operation is performed from top to bottom (FIFO).

The data bus has to transfer *15 data bits* per cell (15 bit counter), that means 15 x 64 x 4 = 3840 clock cycles are needed to read-out data. Data are downloaded from bottom to top. It is also possible to write a pattern inside the PCC. During this operation only the data line 0 is connected to every 4th column and multiplexed to the following 3 columns. Therefore patterns are repeated after the first four columns. Writing is performed from top to bottom (FIFO); the initialisation of the counters (all combinations in principle possible except all 0's which is a forbidden state for the pseudo-random counter) is done in the same way.

A 16 bit bus is used for the configuration as well as for data transport. The maximum read-out frequency is **10 MHz**. Therefore one complete data frame can be read-out in **384 μs**.

The PCC read-out system (called MRS) has been specially designed by Laben[11] together with INFN Pisa and is based on the VME system. The different hardware components are one (or several) *chip boards* with chips or entire detector assemblies glued onto and wire-bonded to the pad connections of the chip board, a *motherboard* and a *VME board*. Motherboard and chip boards are connected together with a multi-pin connector, the motherboard supporting the chip boards. The motherboard only contains buffers for signal transmission from/to the VME board. Transfer of data and of the digital control signals from/to the VME board is performed via a 100 pin flat cable, the analog biases through multi-core cables. The analog test pulse is also received by the motherboard as well as the detector bias in principle, but in practice the high voltage has been connected directly to the chip board due to noise problems. 5 V, the 5th power supply V_{cc}, has to be supplied to operate the motherboard.
The VME board contains the logic of the read-out system. It generates all digital

[11]Laben S.p.A., S.S. Padana Superiore 290, 20090 Vimodrone (Milano), Italy

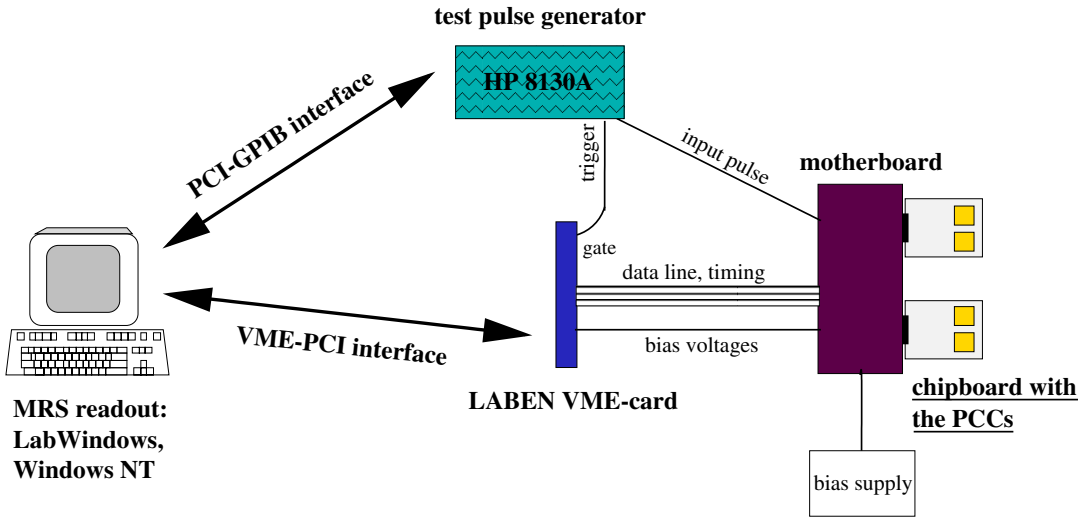

Figure 5.8: *Setup of the PCC system. For the present, 2 detector assemblies can be mounted on a chipboard (right) and 2 chip boards are connected to a motherboard which receives the analog biases either from external bias supplies or from the VME board. Motherboard and chip boards are controlled by the VME card which triggers also the external pulse generator. The VME board itself is controlled by PC. The read-out software is written in C code using LabWindows environment.*

control signals as well as the analog biases[12] for the PCC, the two being separated on the board. A trigger for an external pulse generator can be provided. There are 3 different trigger modes available:

1. *trigger mode 0*: software trigger to use e.g. for radioactive source measurements; the acquisition starts after the trigger plus a selectable delay.

2. *trigger mode 1*: trigger mode for use with an X-ray tube; an external trigger signal enables the gate. The gate signal can be used to start an X-ray tube. The shutter will be low (corresponds to the active acquisition time) after the gate signal and a programmable delay.

3. *trigger mode 2*: a shutter time can be defined during which a programmed number of triggers for an external pulse generator is given. This mode is used during electrical characterisation.

A number of VME boards were purchased from Laben. One board is able to read out an array of up to 18 Photon Counting Chips.

In the beginning the MRS was controlled by a FIC CPU running under OS9. This was changed to a PC setup with a VME/PCI interface. The complete setup containing all the different hardware components is shown schematically in fig. 5.8.

The read-out software has been provided by Napoli, one of the collaborating institutes in the Medipix project. It is written in C and makes use of the graphical environment provided by LabWindows. All the operations are accessible through menus and

[12]We preferred supplying the analog biases through external power supplies and all the measurements which will be presented are done in such a configuration.

buttons and the data can be directly represented. The user is free to include his own custom routines without having to change the program structure. The MRS software runs under Windows NT as well as under Windows 95 or OS9.

5.4 Chip selection through wafer probing

Once the chip design phase is finished the layout file of the chip is sent to the company where it is manufactured. The different processing steps are performed on 6 inch silicon wafers (for the PCC). After processing, these were lapped down to a thickness of $\sim$380 μm (see photograph 5.9). There are 64 PCCs per wafer, but only a certain number will work correctly. In order not to waste money and sensors, good chips have to be selected on wafer prior to sending them to be bump-bonded to the sensors. This testing procedure is called 'selection of Known Good Die'. A specially designed probe card was fabricated which consists of tiny needles to make contact to the wire bonding pads of the chip. (These 58 pads will later be connected through micro-wires with the data and power lines of the chip board.) The probe card is fixed in a wafer probing machine with the electronics wafer sucked with vacuum onto a chuck situated below the probe card. With the help of a microscope and a camera, the contacts are made between a chip and the probe needles. In this way all the bias voltages and control signals can be provided for the chip and data can be read out. After having finished testing one chip, the probe station can be programmed to step automatically to the next one, repeating the procedure. In the end a *wafer map* of the good chips can be generated and sent with the wafer to the bump-bonding firm where only these selected chips will be connected to sensors.

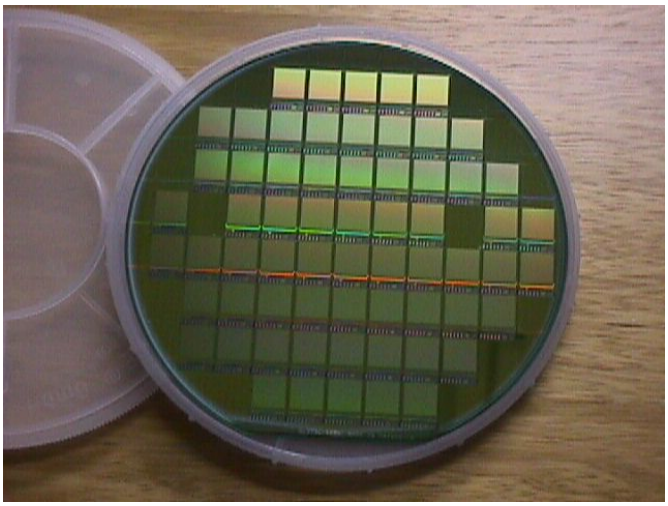

Figure 5.9: *Photograph of a silicon wafer comprising 64 Photon Counting Chips.*

The testing procedure for the PCC consists first of evaluating the digital functions of the chip: writing a pattern inside the chip and reading it out again comparing the

two, testing the threshold adjustment and so on. Because the counter acts during read-out as a shift register for the corresponding column, an error anywhere in the counters results mostly in the loss of the entire column. This has been one of the factors reducing the yield of good chips.
First of all the behaviour of the digital part of the circuit is verified (counters and shift registers, chip configuration). Subsequently, the electrical characterisation of the chips can be done. This is possible thanks to a tiny test-input capacitance. A switch which is controlled by a test flip-flop connects one side of the injection capacitor to the analog input line. When the switch is closed (test bit=1) a step function with amplitude ΔV from an external pulse generator is applied to the analog input line mimicking a particle signal. The equivalent input charge is $Q = C\Delta V$. Normally a train of pulses of fixed amplitude is used. Mean thresholds in mV can be determined as well as threshold variations of the whole pixel matrix and noise values. The threshold is defined being the pulse height where the pixel counts 50% of the pulses. The pixel noise is assumed to be Gaussian. 4 σ of the noise correspond therefore to the region between 2.25% and 97.75% of the threshold curve.

Choosing specific criteria [Bis98] chips can be classified e.g. in bad, good and very good chips and a wafer map created. After having tested a few wafers it was evident that chips located close to the wafer borders showed a much better electrical performance than the ones close to the centre. Chips in the middle had rather high thresholds with large threshold spreads and many pixels not counting properly. There was no immediate, evident explanation for this observation as even a change of the analog biases could not yield the same results as for the outer chips. Therefore it was decided to check the threshold shifts of the input transistors for the analog biases responsible for correct operation of the analog front-end (V_{bias} and V_{comp}). The threshold variations for the V_{bias} input transistor with respect to the chip location on the wafer showed no systematic effect contrary to the one for V_{comp} (see fig. 5.10a)). The chips which had a very satisfying electrical behaviour had also the lowest threshold values for the V_{comp} input transistors and the bad chips located in the wafer centre the highest ones. The reason why only this input transistor showed such strange behaviour is probably related to its large dimensions. It has a W/L of 200/100, a transistor size[13] which is for the new processes even offending the design rules (in the SACMOS1 process there was no limitation given for the maximum transistor size). It was tried to anneal one wafer for 15 minutes at 450^{o}C under controlled gas flow (fig. 5.10b)). As result the transistor V_t threshold spread became smaller, but was still not satisfactory. Therefore the wafer was again annealed, now for one hour at the same temperature and showed afterwards a very good transistor threshold uniformity. This seems to confirm the assumption of radiation damage even though it is not clear at which processing step this could have happened. Moreover, the wafer has been damaged more in the centre than close to the border. One of the steps which could in principle be responsible for such a problem is plasma etching.

[13] W is the width of the transistor gate and L its length usually given in μm. A larger W/L increases the current flowing through the transistor at equal bias.

Despite the better uniformity of the transistor V_t after annealing the chips did not show a big improvement of their electrical behaviour why other wafers were not annealed. The resulting yield of usable chips was therefore in the order of only ∼40%.

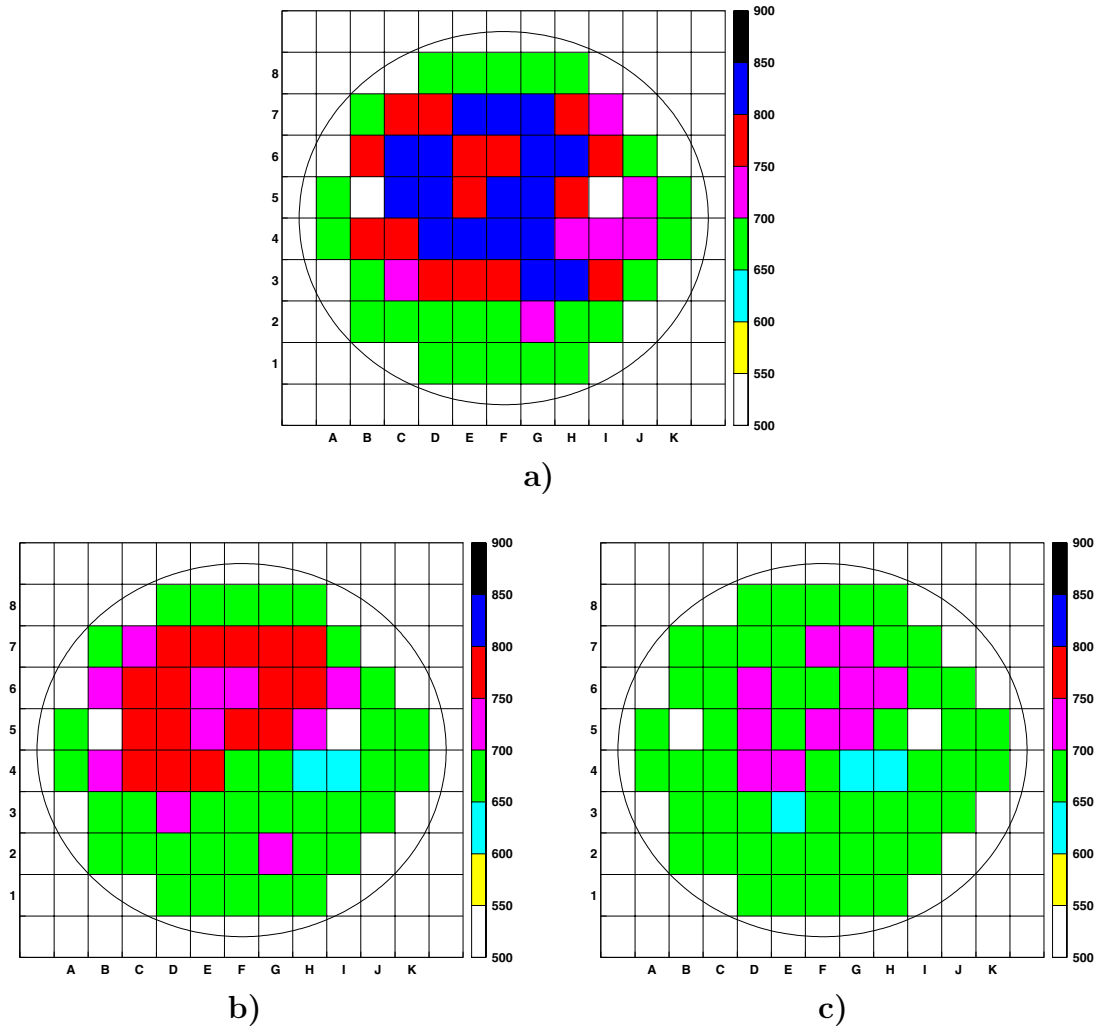

Figure 5.10: *Fig. a) shows the threshold distribution of the input transistor for the analog bias V_{comp} as a function of chip location on the wafer. The values are given in mV and the lowest values for the transistor threshold (lightest shade) correspond to the best chip performances. The same measurement for the same electronics wafer is shown in fig. b), but after 15 minutes of annealing at 450°C. The spatial variations in transistor threshold have almost disappeared after another annealing period of one hour at 450°C (fig. c)).*

5.5 Electrical characterisation of the PCC read-out chip

While a few other wafers were sent to be bump-bonded to sensors, one of the wafers was cut and the chips mounted on small chip boards to be extensively tested. After

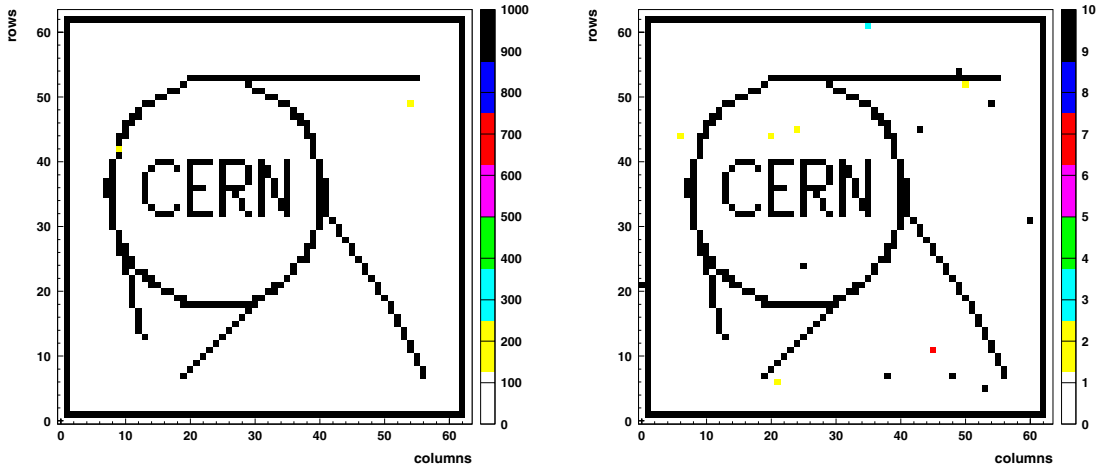

Figure 5.11: *Fig. a) shows the CERN logo acquired by using a test pattern and sending 1000 pulses to the whole matrix. In fig. b) the scale has been changed down to 10 counts maximum showing the extremely low noise level.*

having verified all digital functions one of the first tests consisted in measuring the maximum counting frequency of a single pixel. Therefore the chip has been pulsed with 1000 pulses varying the pulse frequency. The maximum counting rate of the PCC was determined to be **2 MHz**. At that frequency it was still counting correctly all the pulses, whereas at higher frequencies pulses were often counted twice.

Another measurement consisted in estimating the influence of electrical crosstalk between pixels. Crosstalk is the electrical disturbance of a channel by its neighbours. The cause can be capacitive coupling of the channels as well as disturbance of the power supplies. For a counting pixel chip this can result in unwanted signals (not due to a particle crossing). Pulsing single pixels showed no counts in the adjacent pixels. Therefore more and more pixels in the matrix were pulsed at the same time. The test bit was set in a number of selected pixels so that the CERN logo should appear after the test pulses have been coupled in. Around 15% of the matrix was pulsed in this way at the same time with 1000 pulses and all the pixels were unmasked. The shutter time was 500 ms, the average pixel threshold corresponded to ∼3700 e^- (see section 6.1 which explains the calibration of the test input capacitance with a gamma source to establish the conversion mV to number of e^-) with no threshold adjustment applied and the pulse height to ∼ 5400 e^-. The resulting pattern is clear and unsmeared (fig. 5.11a)); there is no deterioration visible due to crosstalk. Fig. 5.11b) is the same plot as a) with only the scale changed to 10 counts which makes the pixels having only a few counts visible. It shows that also the noise in the pixels was negligible.

After that a pattern was created where almost the whole matrix was pulsed (∼3/4) at once except one diagonal cross (the Scottish flag, fig. 5.12). In this case crosstalk is clearly visible resulting in counts registered in non-pulsed pixels. Also the average

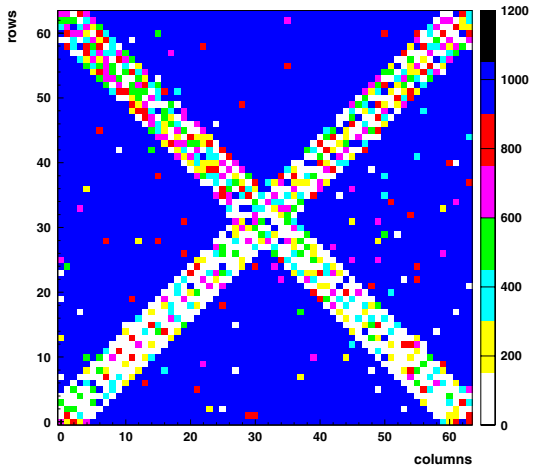

Figure 5.12: *In this test pattern about 3/4 of the pixel matrix was pulsed at the same time with 1000 pulses. The effect of crosstalk is clearly seen in the unpulsed areas.*

threshold had to be put to quite high values (∼14500 e^-) as the chip was very noisy. From these results we can conclude that crosstalk plays a completely negligible role for the PCC as the photon flux for medical imaging applications is relatively low compared to the shaping time of the pixel cells.

One of the important features of the PCC is the 3 bit threshold adjustment per pixel. Its principle can be well explained in figures 5.13a)-c). First of all, a low global threshold without noise is searched changing the analog chip biases. Then the threshold distribution of all the pixels without adjustment is measured (left distribution in fig. 5.13a), ∼500 e^- rms) coupling electrical pulses into the test input. The adjustment current has to be optimised in such a way that ∼1/8 of the threshold distribution measured with maximum threshold adjustment in all pixels (all 3 bits set) is overlapping with the 0 adjustment distribution (right distribution in fig. 5.13a)). Having fixed all the bias currents in this way the threshold distributions for all 8 possible adjustments have to be measured. With this data the read-out program optimises the local threshold adjustments in such a way that the resulting thresholds of each pixel falls inside the overlapping region (central distribution in fig. 5.13a)). As can be seen the tuned distribution gets very narrow (∼120 e^- rms) leading to very homogeneous thresholds in energy well above noise all over the pixel matrix.
After this optimisation the tuned distribution can again be shifted downwards to lower thresholds reducing the global threshold current for all comparators. For this chip the minimum threshold distribution above noise yielded fig. 5.13b) and a minimum average threshold over noise of about 1950 e^-.

The linearity of the threshold adjustment was also measured. The series of the 8 threshold adjustment measurements for one representative pixel is plotted in fig. 5.13c). For pulse heights below the comparator threshold the pixel counts zero (the z-axis corresponds to the number of measured counts). This region is followed by a transition

region[14] where the pixel starts to count until it detects 100% of the signals (the chip was pulsed with 1000 pulses).

In the next chapter various other measurements with the entire detection system consisting of the PCC bump-bonded to a pixellated GaAs sensor are presented.

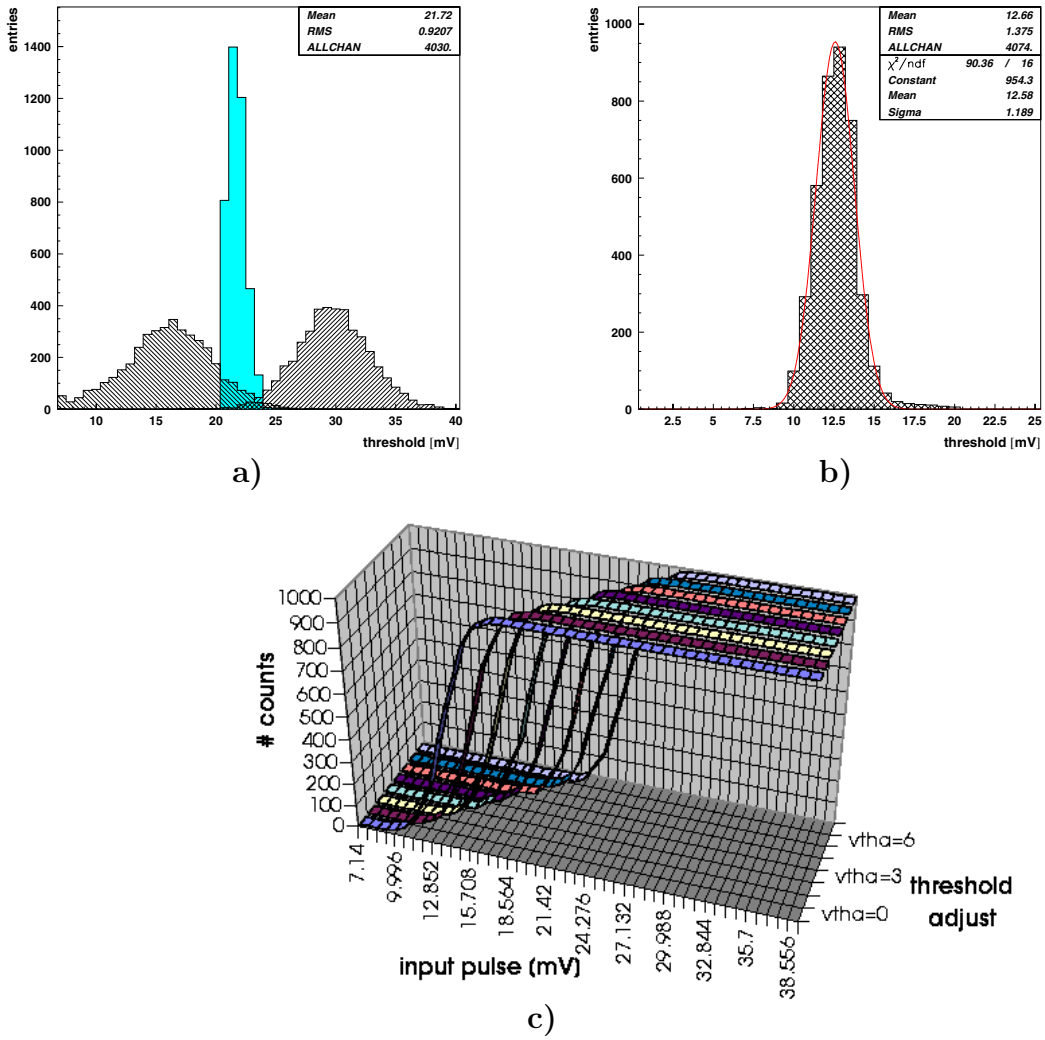

Figure 5.13: *The principle of the 3 bit threshold adjustment can be seen from fig. a). Left the threshold distribution of the 4096 pixels are plotted. All the pixels had 0 local threshold adjustment. With maximum threshold adjustment current (all 3 bits set) it changes to the right distribution. Threshold tuning results in the central narrow threshold distribution which can be shifted downwards to lower thresholds with the global threshold adjustment resulting in fig. b). Fig. c) represents the 8 curves in a single pixel corresponding to the different possibilities of threshold tuning and showing the region where the pixel starts to count.*

[14]This transition region is mainly caused by the noise of the comparator.

5.6 Summary

This chapter introduced the historical development of the PCC. The design of the analog part of the PCC was strongly based on the Omega3/LHC1 chip, a chip developed within the RD19 collaboration for high energy physics experiments. Although requirements for an X-ray imaging and a high energy physics tracking detector differ, the underlying idea of detecting efficiently particles with a good 2-dimensional spatial resolution is the same. The concept of a hybrid CMOS pixel detector is extremely flexible. Different sensor materials can be chosen depending on the application, and functionality in the electronics pixel cell is practically only limited by the pixel size. This is why the Medipix collaboration opted for this technology when looking for an improved detector solution for X-ray projection radiography.
The design characteristics of the prototype photon counting chip were explained in this chapter. The main features of the PCC pixel cell are a pulse shaping front-end, a comparator with a 3 bit threshold tuning, a 15 bit counter and a programmable shutter. The shutter enables a range of acquisition times in the order of milliseconds up to several hours without intermediate read-out cycles. The threshold eliminates noise when no signal is present which results in a true 15 bit dynamic range per pixel. Referring to the terminology in the first chapter, the PCC represents a direct X-ray conversion, digital photon counting system.
The different steps from pixel design to a hybrid system are explained. Chip design is followed by chip production. The resulting electronics wafers have to be tested with the help of a wafer probe station and the good chips selected. Characteristic measurements of the electronics chips were presented. They consist of an evaluation of the digital functions of the chip and applying electrical test pulses to the analog input line of the chip. In this way pixel thresholds can be determined, threshold spreads of the whole pixel array, crosstalk between adjacent pixels in the chip and electronics noise. After this chip selection procedure the electronics chips can be assembled with the sensor chips through flip-chip bonding.

Chapter 6

X-ray Imaging with the PCC Assembled to Semi-Insulating GaAs Detectors

Contents

This chapter is devoted to measurements carried out with the complete photon counting detection system consisting of the PCC bump-bonded to a SI GaAs detector. Electrical measurements are presented as well as imaging results obtained using different radioactive sources. Possible applications other than medical imaging are also mentioned in the last sections.

6.1 Absolute calibration of the PCC

For a full characterisation of the PCC it is necessary to establish a well defined relation between the electrical test signal and electric charge injected into the input of the pixel cell. Electrical signals are used to check the functionality of the chip and parameters like threshold or noise can be extracted (see section 5.5). For these measurements electrical test pulses are injected into the preamplifier input via a tiny test-input capacitance. The value of this capacitance is determined by the layout,

but might vary significantly from one chip processing run to the next due to its small value of a few fF. In a modern CMOS process parasitic capacitances like the test-input capacitance[1] may be 20% different from the design value. The matching within one chip however is much better than this.
It is common practice to use radioactive gamma sources to link pulse heights [mV] to charge [e^-]. For the absolute calibration of the PCC a ^{109}Cd source was selected. It is a pure gamma source emitting X-rays with energies lying close to the energies used for mammography. The two K_α lines (having the highest relative intensities) lie closely around 22 keV and the two K_β lines around 25 keV. At 88 keV there is another gamma emission line with low relative intensity, which will give a small background to the measurement described below.

The principle of the absolute test capacitance calibration measurement is to start from a comparator threshold well below the gamma energies and to move the threshold up in very fine precisely equal steps[2]. As soon as one exceeds the gamma energy there will be a drop in counts, or a peaked distribution after differentiation of the counts versus threshold curve. In the case of a ^{109}Cd source the ideal situation would be if the detector system could separate at least the two peaks at 22 and 25 keV. This was possible in the case of the LHC1/Omega3 chip bump-bonded to a silicon detector [Rop00]. For the PCC the overall noise was too large and prevented separation of the two peaks. Nevertheless, the threshold at which the counts drop almost to zero (except for the few counts originating from the 88 keV line) can be clearly determined. This threshold corresponds with an error caused by the noise to the highest X-ray energy (∼25.6 keV). A photon with this energy deposits about 6000 e^- in GaAs [Ebe71]. It is important to mention that the whole analysis has been performed on a pixel-by-pixel basis. The comparator threshold in each individual pixel marking the end-point of the spectrum is compared with the electrically measured threshold in mV for that pixel at the specific threshold setting. With the assumption of 89% CCE for our detector material (measurement result presented in [Ame98]) it is then straightforward to calculate the value for the test-input capacitance as ∼23.4 fF (see fig. 6.1).

As the system noise always broadens the original gamma line the value of 23.4 fF is a low limit for the test-input capacitance. In order to correct for this broadening effect 250 e^- were subtracted, corresponding to one sigma of our system noise (figure 6.10). This finally results in a value of **∼24.7 fF** for the test-input capacitance. The location of the square in fig. 6.2 corresponds in x to the average threshold voltage setting of the chip where the end-points of the ^{109}Cd spectrum were found and in y to the average pixel thresholds measured with test pulses. The curve itself shows the average value of the thresholds of all 4096 pixels as a function of threshold setting, the error bars in y being the rms of the threshold distribution. It can be seen that

[1]The test-input capacitance is a metal-to-well capacitance and is therefore considered as being 'parasitic'.

[2]The minimum step for setting the comparator threshold is defined for the PCC by a 12 bit DAC working in the range from 0 to 5 V.

the comparator has a limited linear range of about 3000 e^-, the ^{109}Cd calibration point lying already at the upper edge of the linear region. The rms of the threshold distribution is smallest[3] at the threshold setting where the used threshold adjustment mask (compare section 5.5) was created (at 1.35 V). The calibration point lies slightly under the curve as a selection of 230 pixels was taken into account for the analysis. The selected pixels were situated around the centre of the source for statistics reasons and showed a rather low threshold which made it easier to follow the entire spectrum and determine correctly its end-points.

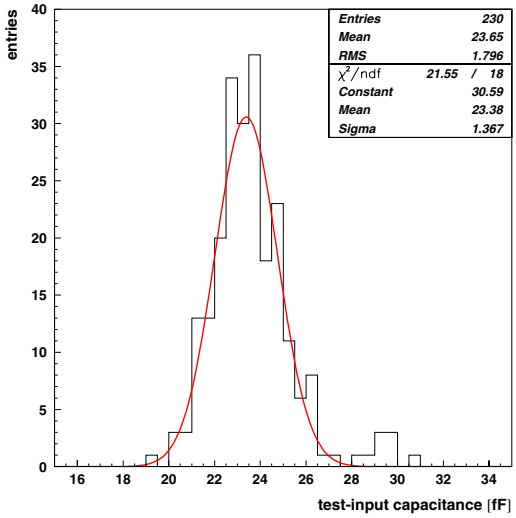

Figure 6.1: *Values for the test-input capacitance evaluated for 230 pixels using the end-points of the ^{109}Cd spectrum and assuming a CCE of 89%. The resulting mean value is a low estimate for the capacitance as the system noise still has to be subtracted.*

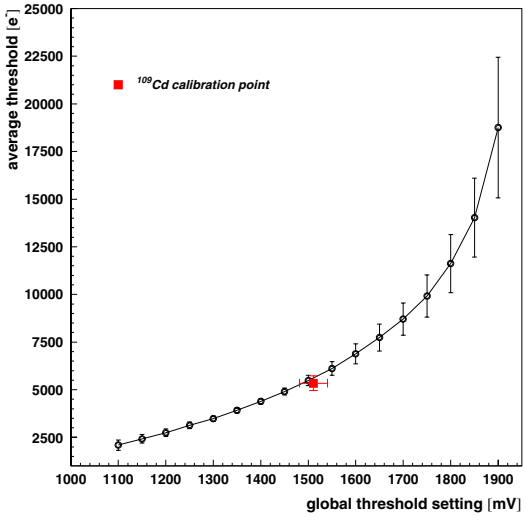

Figure 6.2: *The square in the plot shows the average threshold voltage setting of the chip which corresponds to a threshold of 25.6 keV in GaAs assuming a CCE of 89%. It was calculated with the value of 24.7 fF for the test-input capacitance and for 230 pixels. The curve corresponds to the average threshold in electrons of the whole chip as a function of the global threshold voltage setting, the error bars being the rms of the threshold distributions.*

The calibration result was confirmed by analysing data taken at the Daresbury synchrotron [Wat00]. The same method as described was used, but this time with a (mono-energetic) 14.27 keV synchrotron beam. There the average threshold setting corresponding to the end-points was found at ∼1.25 V and a respective threshold of ∼3000 e^- being in good agreement with the ^{109}Cd calibration.

There are several points to mention concerning the calibration result. Firstly, this calibration was performed with one assembly only; the value for the test-input capacitance might change slightly for others.
Secondly, the result should only be considered as a good approximation due to the fact that the ^{109}Cd peaks could not be resolved.

[3] due to the poor linearity of the comparator

Moreover the value of 89% for the CCE is a very critical factor in the analysis. It has been determined with a shaping time of 1 μs. The PCC has a shaping time of $\sim$150 ns which means that part of the signal could be lost. In that case the value for the test-input capacitance would represent an overestimation and all the absolute values [e^-] given subsequently should be considered as *worst case values*. This assumption would agree better with the design value of 20 fF and the measured value of $\sim$11 fF for the LHC1/Omega3 chip [Rop00]. The Omega3 chip was designed in the same 1 μm SACMOS technology as the PCC with the same design value for its test-input capacitance.
Therefore it will be of great importance to redo the absolute calibration for the PCC, but bump-bonded to silicon detectors. Silicon detectors have a CCE of practically 100% and are very stable in operation. GaAs detectors show local material inhomogeneities with locally fluctuating leakage currents and locally fluctuating CCE. With silicon assemblies it should be possible to resolve the ^{109}Cd peaks. Again it should be stressed that all the measurement results involving electrical test pulses which will be presented in the following sections (minimum reachable threshold, noise,...) could improve as much as a factor of $\sim$2!

6.2 SI GaAs sensor performance

The sensors which were bump-bonded to the PCC consisted of SI GaAs material. This detection material was chosen due to its commercial availability and its high absorption efficiency for X-rays up to $\sim$30 keV, lying in the typical energy range used for medical X-ray diagnostics. Up to a photon energy of $\sim$20 keV even a 200 μm thick GaAs detector shows a detection efficiency of practically 100% compared to only $\sim$27% for a 300 μm thick Si detector (see figure 7.1).
The GaAs raw material originates from Sumitomo and was LEC grown (see section 4.2.1). The contact processing was done by Alenia[4]. The Schottky contact was realised with a Au/Pt/Ti multilayer metallisation. One of the problems with SI GaAs consists of the rear contact fabrication as SI GaAs detectors usually reach breakdown before reaching full CCE. Alenia developed a new rear side contact (non-alloyed ohmic contact NAOC [Ali95]) enabling to bias in a reproducible way 200 μm thick SI GaAs detectors up to a voltage of $\sim$600 V. This non-injecting ohmic contact consists of a shallow implantation of Si^+ ions into the rear surface of the GaAs wafers, a subsequent annealing procedure and special surface treatment at room temperature. Finally the contact is realised depositing a AuGeNi multilayer. The implantation prevents minority carrier injection from the contact and thus shifts breakdown voltages up to very high values.

Fig. 6.3 shows the leakage current dependence as a function of reverse detector bias for a typical 200 μm thick GaAs detector (sensor area $\sim$1.6 cm^2). A saturation region is evident from about 50 V on below which the leakage current increases with reverse

[4]Alenia S.p.A., Via Tiburtina km 12.4, I-00131 Roma.

bias. Around 230 V there is a small 'bump' visible in the IV-curve[5] corresponding to an increase in leakage current of about 1 μA with a subsequent small region of 'negative resistance' which was also observed elsewhere [Rog98a], but whose origin seems to be still not understood. It could well be that this 'bump' region is related to the shallow Si^+ implantation layer. An indication for this is given by the measurement with an alpha source described below.
Above ∼280-300 V a change in slope takes place. The reverse current increases steadily with reverse detector bias, but no abrupt breakdown occurs as would be the case for non-implanted rear contacts. To avoid damage of the PCC assemblies it was decided to work with a current limitation of 20 μA and therefore to reverse bias voltages below ∼400 V.

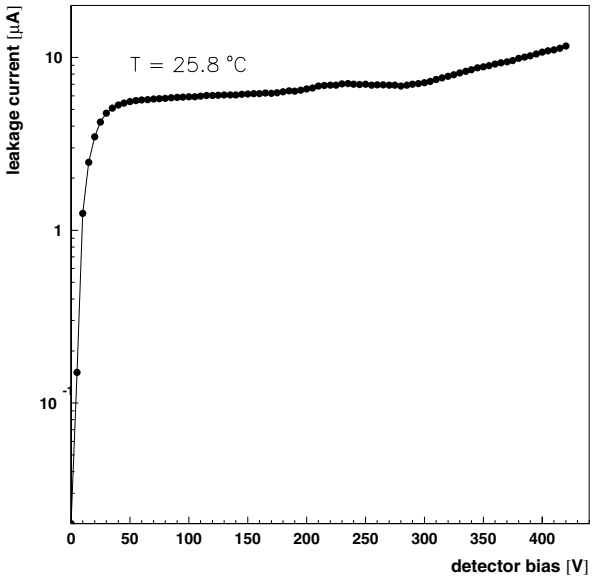

Figure 6.3: *Leakage current as a function of reverse detector bias for one typical GaAs sensor.*

The saturation value for the leakage current amounts to roughly 6 μA which translates to a leakage current density of about 40 nA/mm^2. Most of the used GaAs sensors had values of saturation leakage current density in the range between 25-50 nA/mm^2 at room temperature. A variation of a few degrees in temperature can change this value significantly. It has been shown that the leakage current density is inversely proportional to the substrate resistivity [Rog98a, Irs97]. According to those measurements the observed range of leakage current density would indicate a substrate resistivity of around 10^7 Ωcm. Unfortunately there is no data from the material supplier available for comparison.

To evaluate the detector bias voltage needed to extend the active detection layer to the detector thickness (=200 μm) alpha particles can be used. The detector was

[5]This 'bump' is better visible in linear scale (see [Mik99]), but the logarithmic scale was chosen here to be easier to compare with published IV-curves.

illuminated from the backside with ^{210}Po, a pure and mono-energetic alpha source. The energy of the alpha emission of ^{210}Po is ∼5.4 MeV leading to a penetration depth (end of the Bragg curve) of only ∼20 μm in GaAs [McG94b]. Up to 170 V reverse bias there are practically no counts. The electric field does not reach the charge deposition region of the alphas. The created electron-hole pairs are not separated and they recombine. There is a region of a steep increase in counts from ∼170-260 V. This corresponds to where the electric field reaches the charge deposition region and until it reaches the detector rear side. As can be seen from fig. 6.4 the detector volume starts to be fully active above ∼260 V where a plateau in counting rate is reached. The error bars visualise the rms of the distribution of counts from a circular detector region underneath the alpha source. It is evident that the rms is very large for these transition bias conditions becoming almost constant in the plateau.
The small, but reproducible excess of counts between 260 V and ∼320 V might be due to noise counts caused by charge injection from the rear side contact. An explanation for this could be a nonuniform extension of the electric field inside the sensor volume due to material inhomogeneities. In some regions the electric field might already touch the rear side whereas in others it still needs a few micrometers to extend.
Combining this measurement together with the IV-measurement it is possible to have a valid estimate of the bias voltage needed to fully activate the detector volume. It might be a good guess to define this voltage at the point where the leakage current curve starts to change slope, which is after the 'bump' at about 280 V-300 V. The location of the mentioned 'bump' in the IV-curve of fig. 6.3 is therefore very close to the bias voltage where the electric field reaches the detector rear side. This might demonstrate its relation to the implantation layer.

The same measurement was performed illuminating the GaAs sensor from the rear side with a ^{109}Cd source (see fig. 6.5). The difference between the ^{210}Po and the ^{109}Cd measurement consists in the energy deposition processes of alphas compared to photons. Contrary to the alphas the X-rays and gamma-rays[6] from ^{109}Cd lose their energy throughout the whole detector thickness (although the biggest fraction of the ^{109}Cd X-rays converts in the first tens of micrometers in GaAs; see chapter 7).

In the case of ^{109}Cd some photons are therefore already detectable at 50 V reverse bias. The counts increase linearly up to ∼240 V where the same steep increase in counts can be observed as for the ^{210}Po measurement, only at higher voltages corresponding approximately to the region where the electric field reaches the rear side of the detector. Above 330 V the average number of counts flattens out; at the highest bias measurement point the leakage current was already too high to allow stable detector operation.
No plateau in counts can be observed as for the alphas. This behaviour can be ex-

[6]The difference between X-rays and gamma-rays lies in their origin. Gamma rays are produced either from de-excitation of a nucleus or from annihilation of electrons and positrons. X-rays on the other hand are emitted as bremsstrahlung or are related to the relaxation of orbital electrons to lower energy states.

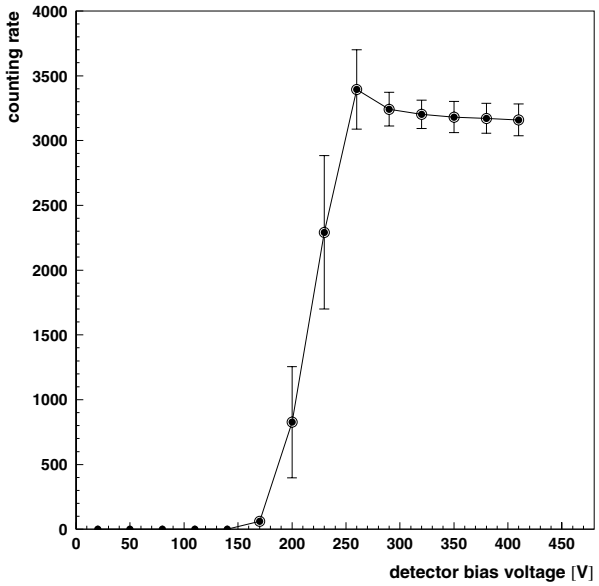

Figure 6.4: *Illumination of one 200 μm thick SI GaAs detector with a ^{210}Po alpha source. Up to a detector bias of ∼170 V there are practically no counts. Going higher with the bias follows a transition region corresponding to the electric field reaching the charge deposition region and then the backplane. A plateau of counts is reached above ∼300 V.*

plained with the comparator threshold. Alpha particles produce so many electron-hole pairs in the GaAs material that they will be counted even when only a small fraction of this charge is collected as the signal is far above threshold[7]. For the ^{109}Cd photons this is not anymore the case as some events with incomplete charge collection may be lost (the comparator threshold for the ^{109}Cd measurement was set to about 3300 e^-). For a ^{109}Cd source the charge collection efficiency of the detector will play a decisive role in the way the curve of the detector bias scan looks.

Fig. 6.6 [Qua96] shows the CCE measured with alpha particles illuminating a 100 μm thick GaAs detector with Alenia NAOC from the front side (squares) as well as from the rear side (circles). In this case the charge was measured with a charge sensitive amplifier (which is a charge *integrating* device). The CCE for alphas from the front side shows a linear increase up to 70 V. For reverse bias voltages above this value up to about 130 V it reaches a plateau which is followed by a steady increase up to the maximum bias. The alphas from the rear side illumination start to be visible from a bias of ∼100 V on and the CCE grows further up to 97% for the highest reverse bias. According to Ramo's theorem [Ram39] the signal from a charge deposition point close to the Schottky contact (front irradiation) is mainly induced by the electron motion (for a positive bias voltage applied on the ohmic side). Inversely the signal for alpha

[7]It should be remembered that in the PCC each particle is counted as one no matter how much charge above threshold is collected.

rear irradiation originates mainly from hole transport. From the comparison of the two curves together with an analysis of the output signal forms many conclusions can be drawn. Firstly, the authors determined the voltage to fully activate the detector volume to be ∼100 V. Above this voltage a slow component (in the range of a couple of μs) in the electron signal disappears completely. This slow component seems to be the charge diffusion term and is governed by the inactive detector volume. Above this voltage (marked V_d in the plot) the CCE is to a large extent determined by trapping and detrapping. In GaAs trapping of electrons is more efficient than hole trapping (section 4.2.2) which explains the lower CCE for front irradiation. Trapping still seems to be active even at highest reverse bias values as the CCE does not reach full height. Nevertheless, high electric fields are responsible for the steady increase of CCE as they shorten the hole transit time[8] and reduce the charge detrapping time.

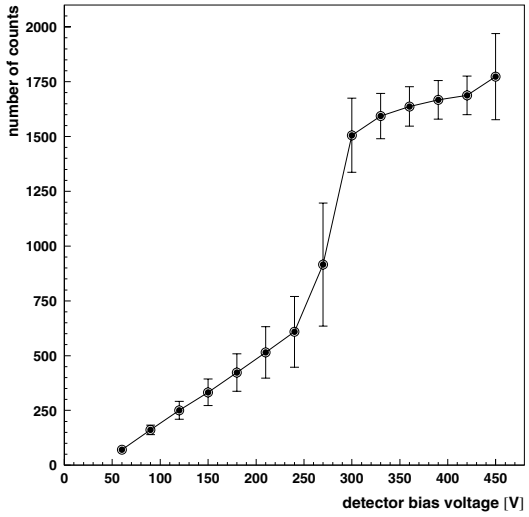

Figure 6.5: *Average number of counts as a function of reverse detector bias for a back irradiation (on the ohmic contact side) with a ^{109}Cd source.*

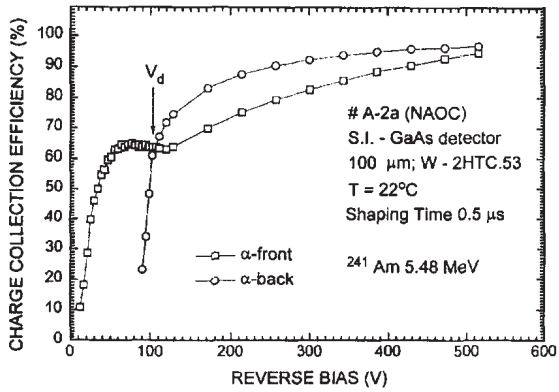

Figure 6.6: *Charge collection efficiency of a 100 μm thick SI GaAs detector for front (Schottky contact) and rear (NAOC) irradiation with alpha particles as a function of reverse bias at room temperature [Qua96].*

Following the argumentation above most of the measurements which will be presented were performed with reverse detector bias of 340 V. This meets the need for maximum detection efficiency for low energy photons together with low detector leakage current.

6.3 Electrical characterisation of the PCC system

For the distinction of low-contrast objects it is very important that all pixels in the chip matrix have a homogeneous threshold. For this purpose the threshold can be

[8] due to an increase in the drift velocity of the holes above ∼300 V for a 100 μm thick GaAs detector (fig. 4.4).

tuned with 3 bits. Moreover, for medical X-ray diagnostics low energy X-rays are used which produce only small signals (down to ∼3000 e-h-pairs) imposing the necessity to reach low thresholds.
Minimum thresholds which can be achieved with the PCC system without biasing the detector lie around **2000 e$^-$** (fig. 6.7). With a detector bias of 320 V the minimum threshold moves slightly up to about 2400 e$^-$ (fig. 6.8) which corresponds to an energy deposition of an ionising particle with **∼10.2 keV** energy in GaAs. These results concern the whole pixel matrix. For single pixels it is possible to go much lower in threshold before they become noisy (which means that they count more than 1000 pulses which is the number of pulses injected). Again it will be important to check the measurements with a silicon sensor connected to the PCC as the high leakage current of the GaAs sensor might influence the results. There is a leakage current compensation present in the PCC (see section 5.3), but as it works only column-wise compensating for the leakage current which is sensed in one dummy pixel at the bottom of the column, it does not account for local variations in the leakage current which are present in GaAs detectors.

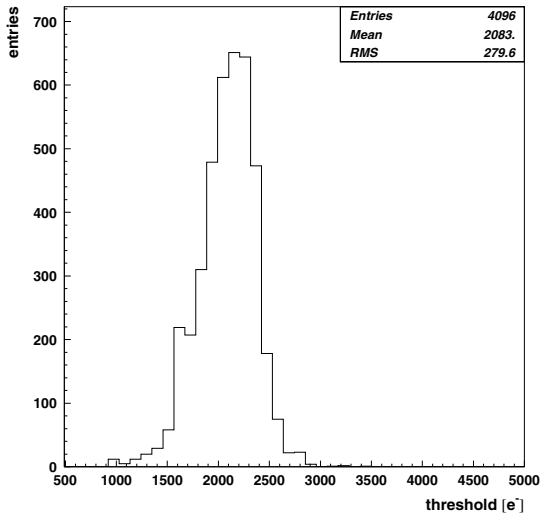

Figure 6.7: *Minimum threshold above noise without detector bias, but with a SI GaAs sensor connected.*

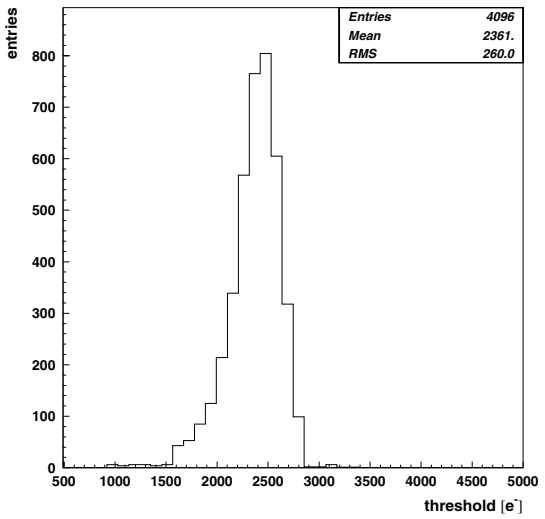

Figure 6.8: *Minimum threshold above noise with a reverse detector bias of 320 V.*

After fine-tuning of the single pixel thresholds with the available 3 adjustment bits the rms of the threshold distribution can be as low as **∼100 e$^-$** as shown for a typical good assembly in fig. 6.9 and almost does not deteriorate with applied bias [Mik99]. Without adjustment the spread is in the order of 500 e$^-$. This value of 100 e$^-$ has to be compared with the system noise (fig. 6.10) which lies around 250 e$^-$. The noise is therefore more significant than the threshold variation in the pixel array after tuning. Its value of 250 e$^-$ is a little higher than for LHC1/Omega3 pixel assemblies (where a mean value of ∼220 e$^-$ was determined [Rop00]) and increases slightly with threshold adjustment.

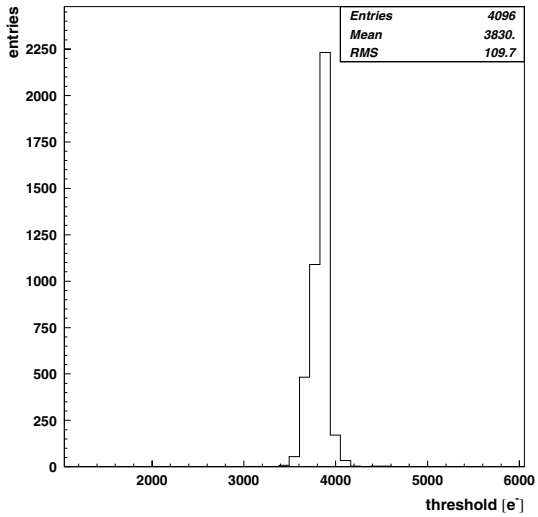

Figure 6.9: *Threshold distribution of an assembly after threshold tuning with an rms of 110 e^-.*

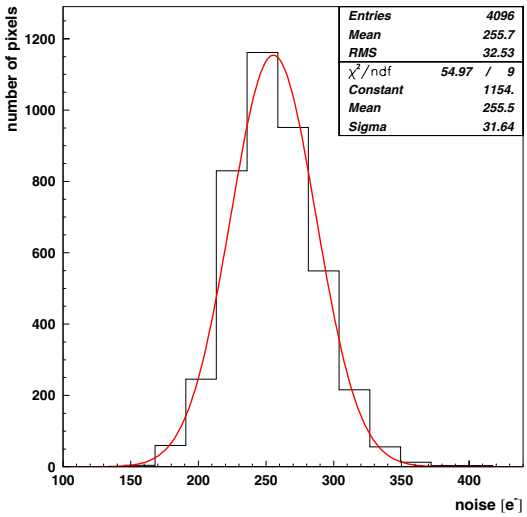

Figure 6.10: *The system noise is in the order of 250 e^-.*

6.4 Imaging with the PCC system

After selection of good electronic chips on wafer and a complete characterisation of the bump-bonded assemblies (including an optimisation of all bias currents and the threshold tuning) images can finally be taken. A requirement is a good electrical contact between the electronics pixels and the sensor pixels through bump bonds. To verify these interconnections source measurements with a ^{90}Sr source were carried out. Missing connections with no counts and noisy pixels (which can result from bad contacts) can easily be identified. One example for a good assembly in terms of bump-bonding connection is presented in fig. 6.11. The assembly was uniformly irradiated with a ^{90}Sr source. Except four pixels which have been masked because they were noisy each pixel shows counts. Moreover, the variation in counts around the average number of counts is very small.
An example for some bump-bonding problem is shown in fig. 6.12. Here the bottom left corner of the detector lifts off from the electronics chip. There are missing connections and a region with big variations in counts. Many pixels count much less than the average and some are noisy. A comparison with an acquisition performed with electrical test pulses proves that the problem is not related to the electronics chip, but to the chip-detector interconnections.

During the period of investigation of these devices several problems related to bump-bonding were encountered. This meant that many of the measurements presented in this thesis had to be carried out using devices which were only partially sensitive. It seems that the attempt to go directly to GaAs detectors without first trying with Si was detrimental to progress. The bump-bonding procedure was rather unreliable and

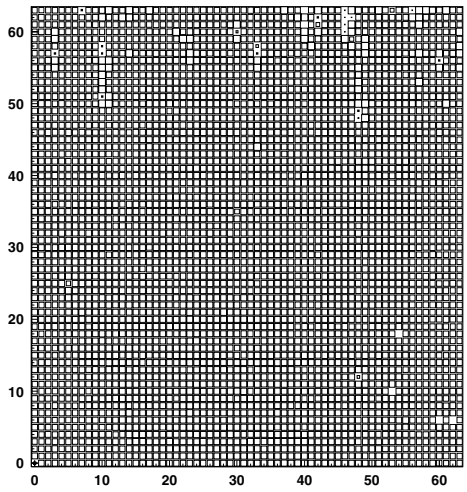

Figure 6.11: *An assembly with good bump-bonding connections shows a uniform distribution of counts all over the matrix arising from ^{90}Sr illumination.*

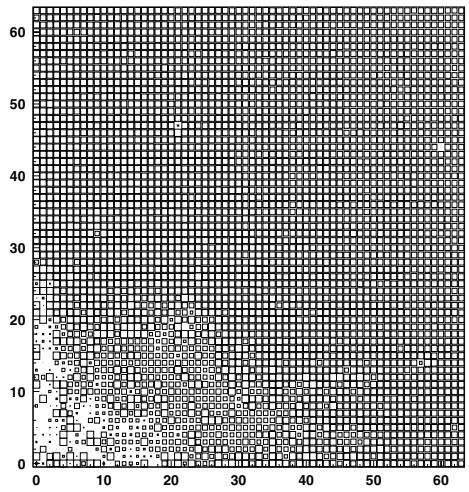

Figure 6.12: *In the case of this assembly the GaAs sensor starts to lift off on the bottom left corner from the electronics chip.*

unfortunately some well assembled devices suffered from reliability problems due to the detector itself. Very recently some Si devices have been delivered and these appear to be functioning correctly (latest results will be reported briefly in section 6.5). Besides there are also some GaAs devices from a different bump-bonding supplier which appear to be well assembled. A major effort is now underway to provide the LHC experiments with reliable assemblies. Further developments of the Medipix concept should benefit from this effort.

6.4.1 Imaging with X-rays, gamma rays and electrons

In traditional medical X-ray diagnosis the photons are supplied by X-ray tubes. Depending on the part of the body to be probed different targets, filters and acceleration voltages are used inside the tubes to vary the photon spectrum. Mammography is an example for an application with rather low energetic photons in order to be able to detect tumours which differ only slightly in density and therefore contrast from the surrounding breast tissue. A molybdenum target with characteristic K_α and K_β lines of 17.5 and 19.6 keV together with a molybdenum filter which cuts off most of the photons with energies higher than 20 keV (K-absorption edge of Mo) is used. To evaluate the performance of the PCC detectors in this energy range a very useful X-ray source is ^{109}Cd with characteristic lines around 22 and 25 keV. ^{241}Am sources can be employed for tests with higher energetic photons[9]. Dental X-ray diagnosis uses for example tube acceleration voltages between 60 and 70 kV together with a tungsten

[9] ^{241}Am has several X-ray emission lines up to 21 keV and three gamma emission lines at 26.3, 33.2 and 59.5 keV from which the 59.5 keV line is by far the most intensive one [Reu83] (although

anode which results in a photon energy spectrum peaking around 30 keV.

One of the first images of a 500 μm thick tungsten wire with the shape of an 'M' was taken with a ^{90}Sr beta source (fig. 6.13). All the pixels were active and no image correction was performed. Around the very clean image of the 'M' one can distinguish rings which correspond to levels of decreasing number of counts as the source was placed close to the centre of the detector. In the bottom left corner there is a region with less counts arising from the tiny wire which is glued onto the GaAs detector rear side to supply the reverse detector bias voltage.
The same tungsten wire was used to produce an image with a ^{109}Cd source (fig. 6.14). Again the image is extremely clean although only raw data is presented. The GaAs detector was biased at 350 V and the bias wire can be seen here as well. Few noisy pixels are visible (black spots) showing either local regions of high detector leakage current or bump connections which start to deteriorate as these regions got worse with time (measurements of the chip alone with test pulses did not present these spots).

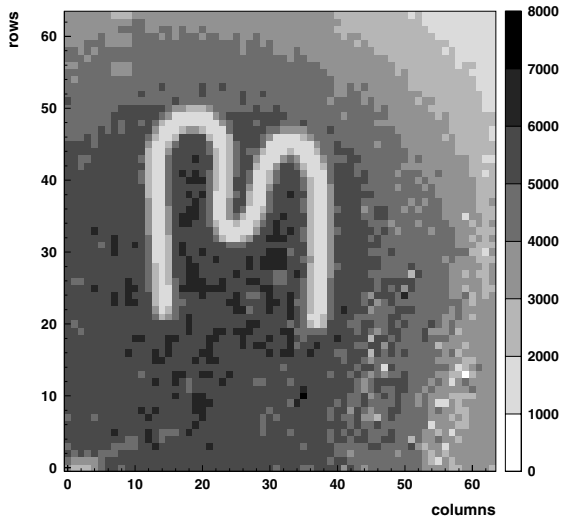

Figure 6.13: *Image of a 500 μm thick tungsten wire with a ^{90}Sr source.*

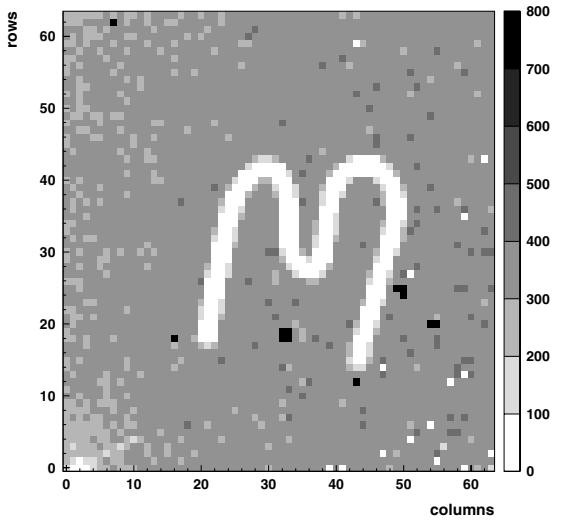

Figure 6.14: *Image of a 500 μm thick tungsten wire with a ^{109}Cd source.*

For the next image a 300 μm thick copper mask was prepared with 300 μm wide letters 'MEDI-PIX' etched out. The mask was fixed very close to the detector rear side and illuminated with a ^{109}Cd source. The resulting image is presented in fig. 6.15 which includes also some noisy detector regions. The letter width of 300 μm corresponds to $\sim$2 pixels which is in agreement with the measurement (the straight part of the letters seems to be centred mostly in-between two pixels).
The capability of the PCC system to distinguish low differences in material thickness is apparent from fig. 6.16 [Bis98]. Unfortunately, a rather bad detector had to be used with an ^{241}Am source to image a steel object with thickness varying between 300

it has to be kept in mind that the absorption efficiency of a 200 μm thick GaAs detector decreases strongly with photon energy; see fig. 7.1).

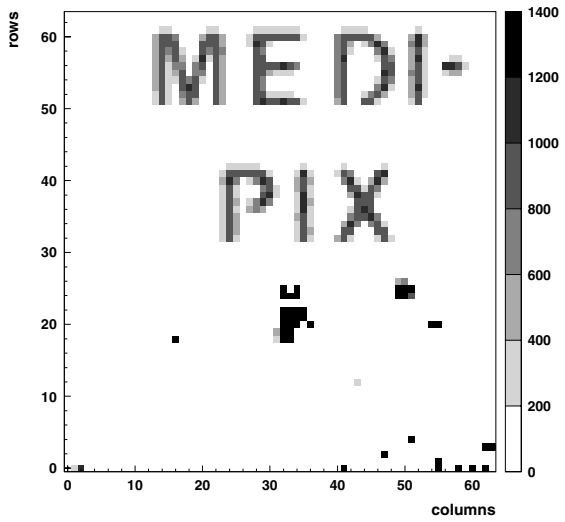

Figure 6.15: *Image of the name 'MEDI-PIX' with a ^{109}Cd source. The opening in the mask which defines the letters is 300 μm wide and was etched out from a 300 μm thick copper mask.*

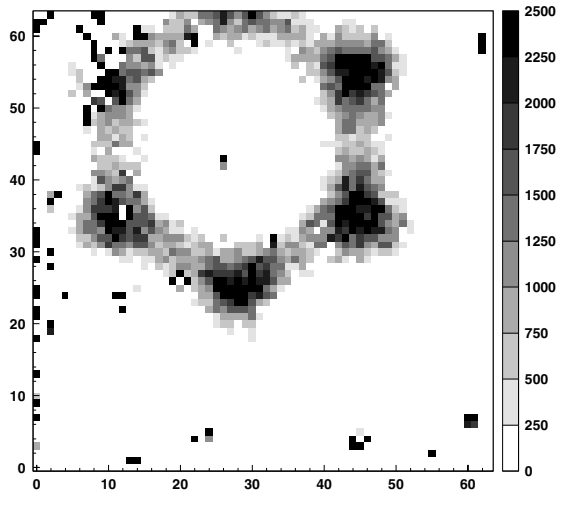

Figure 6.16: *Illumination with an ^{241}Am source of a steel object showing thickness variations between 300 and 500 μm [Bis98]. The background was subtracted.*

and 500 μm. To attenuate the detector non-uniformities, a background image was subtracted.

Finally two images of an M2 steel screw will be presented. For these images an interpolation method was used to enhance some small details. First, an image was taken with an ^{241}Am source placing the screw on a thin plastic foil on top of the GaAs detector (biased at 250 V). A second image with the same acquisition time and source position was made removing the screw. Fig. 6.17 shows the interpolated image of the screw having subtracted the flood image[10] before. The thread with its 500 μm spacing and the 1 mm slit can be clearly distinguished.
The same principle of interpolated subtraction image was used to produce fig. 6.18. This time the 10 mm long M2 screw was irradiated at a distance of 20 cm with a dental X-ray tube at 60 kV operating voltage for 50 ms (which corresponds almost to the minimum tube settings) [Sch99]. The thread is also visible in the middle of the screw.

It is common practice to measure the spatial resolution of an imaging system with a line pair mask. The commercial mask which was used for this measurement consists of a lead sheet of 50 μm thickness where groups of lines are cut out. The lines have a certain width and are placed at a pitch of 2 times the line width. The narrower the lines are, the smaller the pitch and the more difficult it is to separate them.
The spatial resolution of the PCC is limited simply by the pixel size. The theoretical spatial resolution is therefore 340 μm. This was measured with a line pair mask and a

[10] A flood image is an image obtained after a uniform exposure of the detector area.

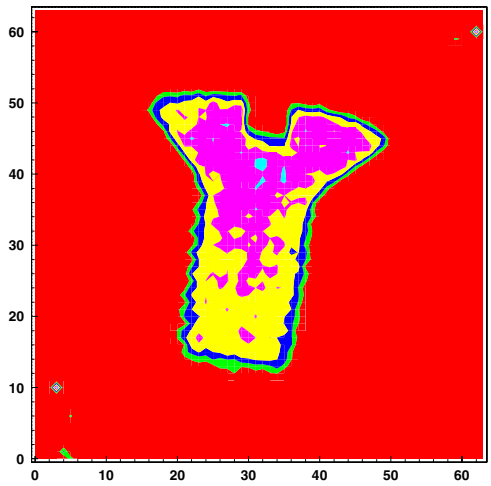

Figure 6.17: *Interpolated image of an M2 screw taken with an ^{241}Am source. A flood image was subtracted.*

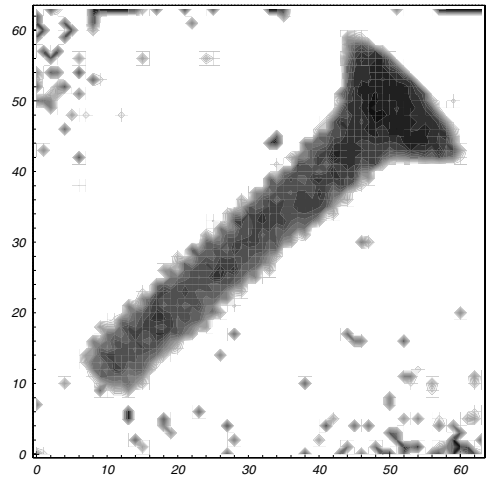

Figure 6.18: *Interpolated X-ray image of an M2 screw [Sch99]. A flood image was subtracted.*

^{109}Cd source (fig. 6.19). In a pattern of 4 lp/mm (line pairs per mm) the lines cannot be distinguished (lower group of lines), but for 3.6 lp/mm the lines start to be separable (upper group of lines). This corresponds to a spatial resolution of ∼278 μm. The part on the bottom of the image is due to bad bump-bonding.

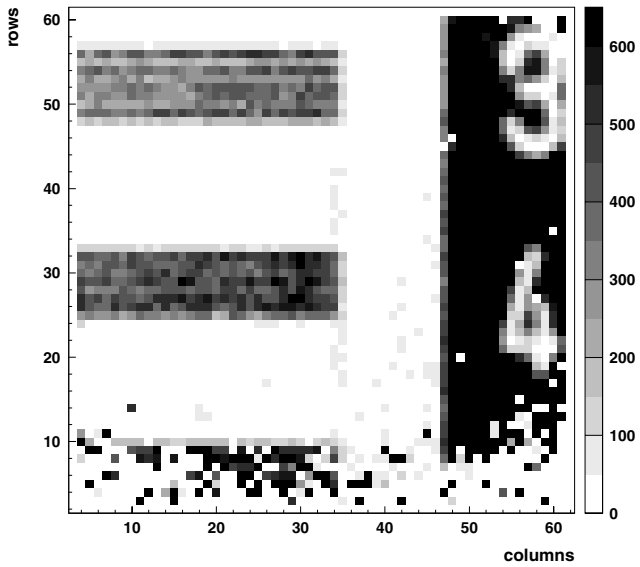

Figure 6.19: *Image of a line pair mask with ^{109}Cd. 3.6 lp/mm (top) can be resolved.*

A first comparison between the performance of an integrating system and the PCC photon counting system was carried out. A tooth was imaged with a conventional X-ray tube (Trophy type 708, long cone, 8 mA, 70 kV, 0.2 s acquisition time) and

a CCD detection system. Fig. 6.20 shows the scanned image[11] with a screw getting thinner the deeper it sits inside the tooth. A good dental detection system should be able to image the screw until its end.
As a comparison two images (one of the top and the other of the bottom part of the tooth due to the relatively small detection area) were made with the PCC (fig. 6.21) using ^{109}Cd as X-ray source. The spatial resolution is clearly poorer than that of the CCD system because of the pixel size, but nevertheless the screw can be clearly distinguished from the surrounding tooth material. Moreover, the differences in tooth thickness are much more clearly visible. The two dark regions on the right side of the image parallel to the screw and the outer edges of the tooth are cracks in the tooth.

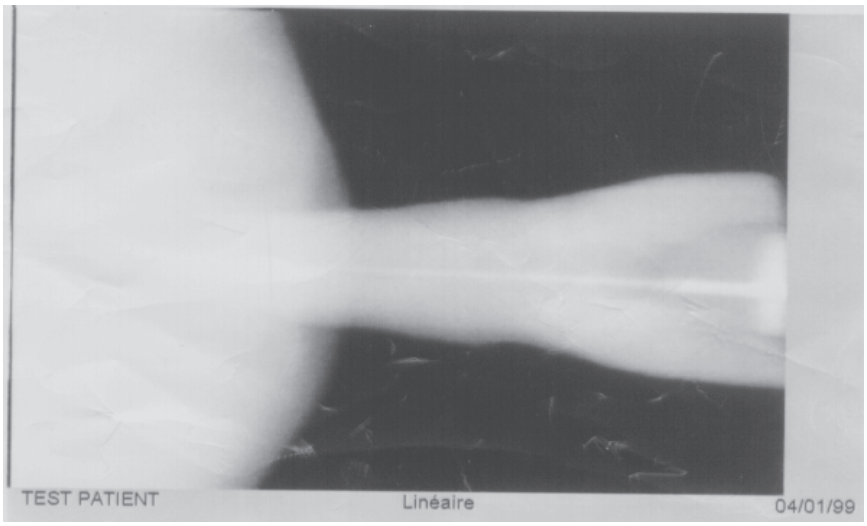

Figure 6.20: *Scanned image of a human tooth with a thin screw inside using a conventional dental X-ray tube and a CCD detection system.*

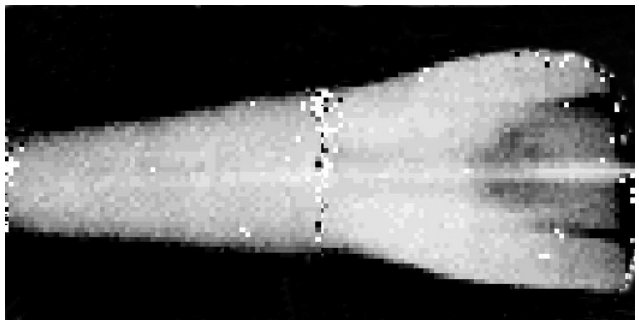

Figure 6.21: *This image of the same tooth as in fig. 6.20 was taken with a ^{109}Cd source and the PCC system and is composed of two images. Differences in tooth density are clearly visible.*

In reference [Gla95] the exposure [μGy] as a function of exposure time for the above mentioned setup used to obtain image 6.20 had been reported (tube A in [Gla95]). The acquisition time of 0.2 s yields therefore an exposure of $\sim$980 μGy.

[11] The original image on screen had slightly higher quality.

For the image acquired with the PCC the exposure was calculated. A calculation of the directional dose equivalent, H'(0.07), using the Γ-factor[12] for ^{109}Cd [RPO] yields a value of ∼33 μSv. With a correction factor which is very small for ^{109}Cd energies [Alb94] the exposure for fig. 6.21 could be determined to be ∼34 μGy lying almost 30 times below the dose used for the image with the CCD system. Conventional X-ray equipment cannot even deliver such low doses.

The measurements presented in these sections confirm that the concept of the PCC, a photon counting chip together with a highly efficient photon detector, is very promising in terms of contrast enhancement and reduced dose in the case of medical imaging applications. As soon as some well bump-bonded assemblies will be available, the missing measurements to fully characterise the imaging system can be completed.

6.4.2 Other imaging applications

The concept of hybrid semiconductor pixel detectors together with the photon counting method may not only be advantageous in medical diagnosis, but for various other applications aimed at a high dynamic range, low noise and good spatial resolution. Fields of possible applications might be as widely spread as nuclear decommissioning, biology, gamma cameras for material control or synchrotron studies. Two of these will be described in the next sections, X-ray powder diffraction and nuclear decommissioning.

6.4.2.1 X-ray powder diffraction

The symmetries of nature have intrigued men for centuries. Starting with philosophical essays the symmetries of space, time and matter (as well as symmetry breaking mechanisms) are nowadays more and more measurement quantities, but they still fascinate with their beauty. One example of this is fractals, another is crystals.
Already hundreds of years ago it was evident that crystals contain a regular arrangement of different planes, the crystal faces. During the crystal growth process, a unit structure is repeated leading to specific crystal symmetries. The study of these symmetries was advanced in 1912 with the suggestion of **M. von Laue** that X-rays could eventually produce diffraction patterns of crystal structures. In the same year the first crystal diffraction patterns were obtained by **W. Friedrich** and **P. Knipping** who sent a beam of X-rays through a crystal plate. The resulting diffraction patterns proved the wave behaviour of X-rays and led subsequently to first estimations of the wavelength range of X-rays. Nowadays X-ray crystallography is an important part of solid state physics using various experimental and analysis methods to enable the reconstruction of the crystal structure. One of the most frequently used experimental methods is X-ray powder diffraction which will be shortly described below; a good introduction and overview of the field of X-ray crystallography can be found

[12]Corresponds to the parameter $h_{0.07}$=5 (mSv/h)/GBq at 10 cm distance in [RPO].

in [Phi60, Gui57].

For structure studies the ideal case would be to investigate single crystals, but these are often not available. In spite of this it is possible to determine the different crystal planes and their relative distances (for not too complex structures) with the **powder diffraction** method. In this case the sample is a very fine crystal powder contained in or attached to a thin capillary tube (see schematic drawing 6.22). If the powder is sufficiently fine the number of tiny crystals is so large that the assumption can be made that all possible orientations of the crystal plane are represented. This technique is called **Debye-Scherrer** method. In practice, the capillary tube is also rotated to achieve a completely random orientation of the crystal planes. If a monochromatic X-ray beam is pointed at the sample a diffraction pattern will occur with diffracted X-rays lying on a series of cones coaxial with the path of the incident beam and opening angles of 4θ. The diffraction condition for a plane {hkl} is given by the **Bragg equation**,

$$n\lambda = 2d_{hkl} \sin \theta_{hkl} \tag{6.1}$$

n denoting the diffraction order, λ the wavelength of the beam and d_{hkl} the distance between the {hkl}-planes. Therefore an exact measurement of the Bragg angles enables to determine the Bragg spacings between crystal planes. To avoid uncertainties it is important also to have the information of higher order diffraction rings together with a *high brilliance beam* as the beam size is related to the width of the diffraction rings. Knowing the beam intensity a measurement of the ring intensities leads to the *scattering amplitudes*[13] of the corresponding crystal planes which are needed (besides the phases) to reconstruct the crystal structure.

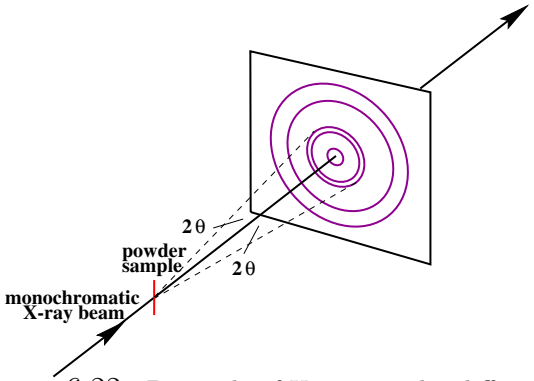

Figure 6.22: *Principle of X-ray powder diffraction.*

To prove that hybrid photon counting pixel detectors might be well suited for some synchrotron applications a powder diffraction test-beam experiment at the Daresbury synchrotron radiation facility (UK) has been set up. A well known substance, potassium niobate ($KNbO_3$), has been chosen as sample showing some close ring structures to be resolved. Fig. 6.23 is a scan over an angular range between 6° and 15° in

[13]=the square-root of the intensity

2θ measured with a scintillator detector at a beam energy of 25.5 keV [Man99b]. The same rings could be resolved with the PCC (fig. 6.24) [Wat00] at 20 keV X-ray energy despite very low statistics as the beam was working in single-bunch mode compared to multi-bunch mode for fig. 6.23. Due to the larger area of the PCC the number of measurement steps could be reduced by a factor of 30 with respect to the scintillator scan. Obviously, a large area detector can reduce significantly the acquisition time.

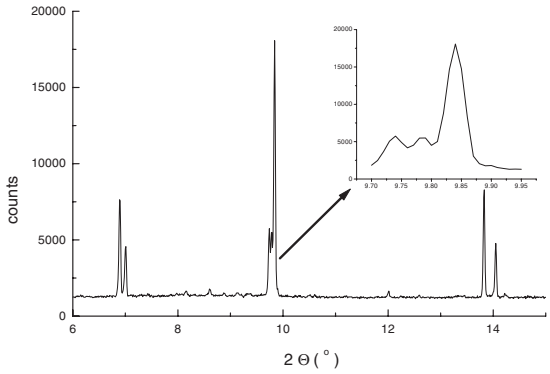

Figure 6.23: *Part of an angular scan of a $KNbO_3$ powder sample measured with a scintillator and a 25.5 keV X-ray multi-bunch beam [Man99b]. The small inserted figure is a zoom of three very close diffraction rings.*

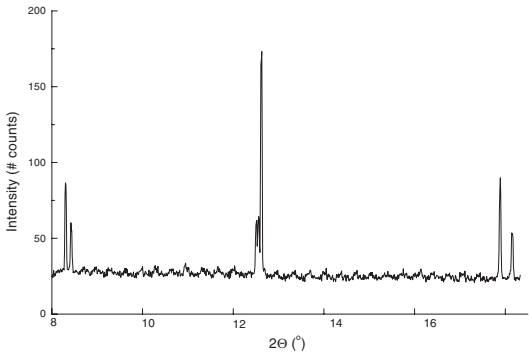

Figure 6.24: *Angular scan of the same $KNbO_3$ sample, but with 20 keV single-bunch beam and the Photon Counting Chip [Wat00].*

The triple peak (zoom in fig. 6.23) has been measured with the PCC at 3 different energies; 14.27, 20 and 25 keV (figures 6.25a)-f)). Corresponding to the Bragg formula 6.1 they were found at different diffraction angles and a distance between the peaks which changes, too. The acquisition time for each image was 10 minutes and the threshold was tuned before and set to about 10.5 keV. The clearest peak separation is given for the lowest beam energy with the highest peak-to-valley ratio. For the 20 keV data a higher background than for the 14.27 keV data is observed. This is most probably due to fluorescence radiation emitted isotropically by the $KNbO_3$ sample. The K-edge for ^{41}Nb lies at $\sim$18.99 keV [Nis] leading to the emission of fluorescence photons with energies of 16.52 and 16.62 keV which are still well above the set threshold of the PCC. Therefore one could have achieved a much better peak-to-valley ratio setting the global threshold e.g. to 18 keV, a possibility which is not given for integrating systems.

To summarise, it was shown that the PCC can be used to image photons at energies of 14.27 keV. The pixel size is probably a little too large for the application, but this should cease to be a problem for the new pixel chip generation. Besides offering high dynamic range, photon counting reduces considerably the noise and might also be useful to cut off unwanted background. Despite much lower statistics the peak-to-valley ratios of the PCC system are comparable to the scintillator system [Wat00]. A large area photon counting system with high dynamic range and highly efficient

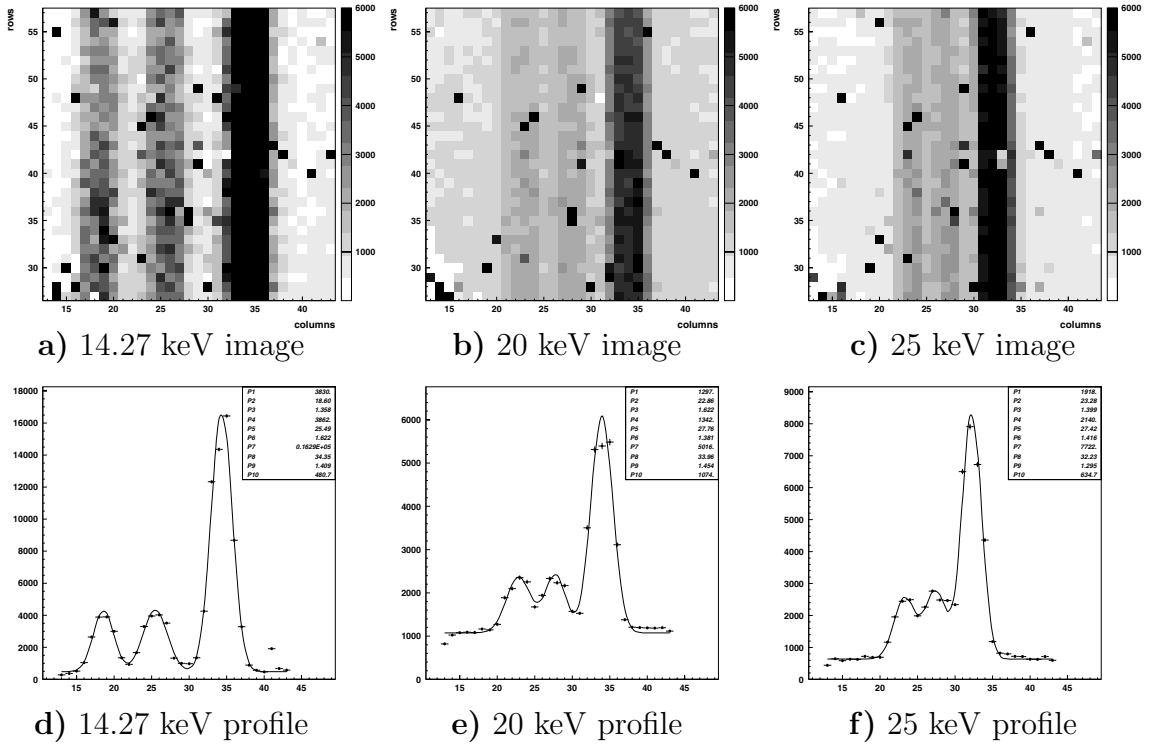

a) 14.27 keV image **b)** 20 keV image **c)** 25 keV image

d) 14.27 keV profile **e)** 20 keV profile **f)** 25 keV profile

Figure 6.25: *Triple peak of a $KNbO_3$ powder sample at three different beam energies. Plots a)-c) show the raw images taken with the PCC, figures d)-f) are the corresponding profile plots.*

detectors like GaAs or $Cd_{1-x}Zn_xTe$ could be an interesting new detector solution for such synchrotron applications.

For the sake of completeness it should be mentioned that nowadays *time resolved powder diffraction* is even more important than conventional powder diffraction. Polymer physicists or other material scientists are attempting to follow fast structural changes arising from perturbations such as sharp changes in temperature which can be deduced from the changes in the X-ray pattern. For biology, fibre diffraction is a very interesting field providing detailed insights into structural mechanisms like the relaxation and straining of muscles. Biological samples pose the problem of being very sensitive to radiation damage. Damage to the structure continues after the beam is stopped because the damage is mainly caused by radiation induced free radicals. Therefore for studying various fast phase transitions the desirable range for the time frames is in the order of hundreds of microseconds combined with a very intense X-ray beam. This goal of fast read-out together with an extremely high dynamic range cannot be achieved for the moment with CCDs. Various types of gas chambers are therefore preferred for high time resolution measurements. If only static images are required, the standard detector systems are image plates or CCD systems.

A summary of the requirements for time resolved X-ray powder diffraction shows that this field has very stringent demands for the detection system:

- time framing capability (with variable frame times) and read-out times in the order of 100 μs
- extremely high dynamic range ($\sim 10^6$) together with a high local saturation level and low noise
- high 2-dimensional spatial resolution in the order of 100 μm
- large 2-dimensional areas for asymmetric samples
- high DQE at an energy range between ~10-30 keV
- possibility of online data reduction
- stability and reliability over long time periods
- simple to use

Connected to a highly efficient sensor material photon counting detectors have the potential in fulfilling the above requirements in combination with deep sub-micron CMOS electronics. If their design would be optimised for these specific applications (especially in view of the deep counter depth needed and the fast read-out) the only remaining problem would be the large area coverage which can be addressed by tiling of the single detector elements. In the future other solutions might also become feasible. One idea is to use the MCM (**M**ulti **C**hip **M**odule) technology approach to provide a fan-in of slightly larger sensor pixels to the chip pixels through metal vias.

6.4.2.2 Gamma camera

Gamma cameras have different fields of application ranging from astrophysics to nuclear medicine for detecting radioactive tracers (like ^{99m}Tc) to the nuclear industry. The experiments presented here were carried out to evaluate the PCC system for applications in decommissioning of nuclear power plants. The aim is to be able to determine the location, the approximate activity and (ideally) the type of radioactive contaminant. The final system should be a small, portable gamma camera combining photon detection with the visible image of the area. Fig. 6.26 shows an example of such a portable gamma camera called CARTOGAM [Mil99] and developed at CEA, Saclay, France. Image 6.27 [Gal00a] of a contaminated rail in a nuclear facility was made with the same camera.
Sometimes the radioactive 'hot spots' have to be localised remotely prior to human intervention through a small opening in the restricted area. The requirements include high dynamic range, low noise, sufficient sensitivity, rough energy resolution, high angular resolution, wide field of vision and low weight.

Typical radioactive sources in nuclear power plants (like ^{60}Co or ^{137}Cs) have energies in the range of a few hundred keV up to MeV, where the detection efficiency of

Figure 6.26: *Photograph of the portable CARTOGAM gamma camera [Mil99].*

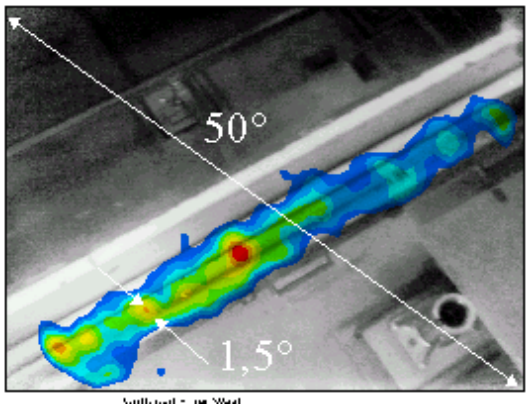

Figure 6.27: *A contaminated rail in a sealing room (CARTOGAM image [Gal00a]).*

a thin GaAs detector is already very small. Moreover, the PCC design is optimised for energy depositions in the range of a few keV to a few tens of keV. Nevertheless with a thicker or/and better absorbing sensor the photon counting principle could improve significantly the performance of conventional gamma cameras mainly because it reduces the background noise to negligible values. Generally, gamma cameras for the nuclear industry are based on a collimator, a scintillator, an image intensifier plus CCD or a position sensitive photomultiplier tube [Mil99].
With a direct detection system like the PCC it would be possible to reduce significantly the length of a standard gamma camera as no scintillator and image intensifying part is used. The reduction in length corresponds also to a major reduction in weight mainly because of the shorter radiation shielding. This would facilitate the manipulation of the camera with robot arms.

The experimental setup to test if the PCC works correctly also for high energy depositions and low dose rates consisted of the PCC bump-bonded to a 200 μm thick SI GaAs sensor. ^{137}Cs was used as the radioactive source (660 keV gamma emission). At the detector location the measured dose rate was $\sim$3 μGy/h. With a detection efficiency of 0.7% each pixel shows in average 1.9 counts per hour. The small thickness of GaAs prevents full energy deposition, however simulations show that more than 5% of events deposit at least 300 keV in one pixel [Gal00b].
A tungsten collimator with a double cone pinhole was used to form an image of the ^{137}Cs source. Because of the low dose rate and the low detection efficiency an acquisition time of 10 hours was chosen. The assembly which was available had a zone of faulty bump-bonding at the borders and especially at the bottom of the matrix. After the 10 hour exposure a general background of $\sim$12 counts/pixel was observed. This should not occur due to the set threshold and measurements of the electronics chip alone show a completely quiet matrix over very long acquisition times. The problem is suspected to be due to the malfunctioning of the detector leakage current compensation circuitry. The dummy cells which sense the leakage current are located on the

bottom of the matrix and were therefore most probably not connected to the detector. Despite these problems a signal-to-noise ratio of 3.9 was obtained (after background subtraction) which made it possible to clearly identify the source position. The smoothed image is shown in fig. 6.28(b). A simulation of the experiment resulted in a very similar image shape (fig. 6.28(a)).

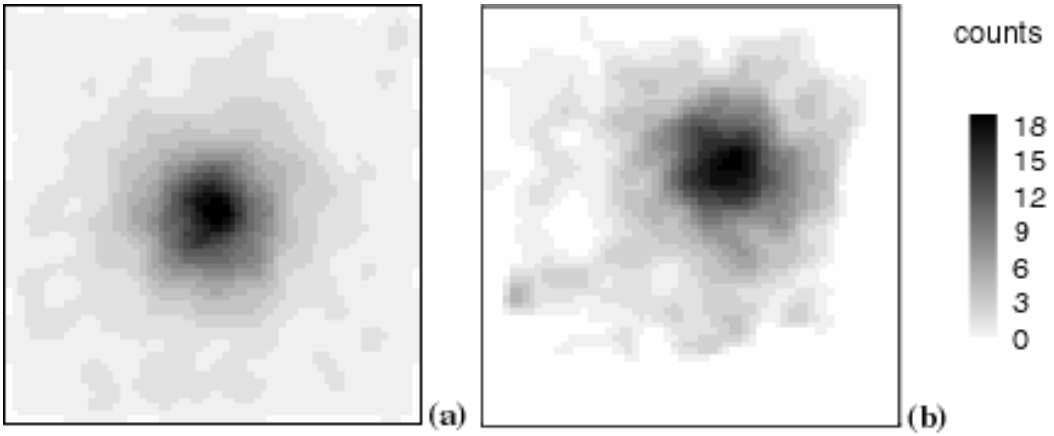

Figure 6.28: *Experimental smoothed image (b) of a collimated ^{137}Cs source with 3 μGy/h dose rate and 10 hours acquisition time (background subtracted). (a) shows the simulated smoothed image of the same setup [Gal00b].*

Individual events were also studied to understand the effect of charge spreading. Therefore the source was placed far away and data was taken during short acquisition times without collimator. A comparison with energy loss simulations resulted in a similar event morphology and cluster size distribution [Gal00b]. This indicates that charge spreading can be attributed mainly to the charge deposition processes and that an extrapolation of the simulations to different sensor materials is valid.
A simulation of the inter-pixel capacitance which resulted in a value of 17 fF [Gal00b] and corresponds to an electric coupling of ∼4% confirmed that electric cross-talk should play no role (the signal in the adjacent pixel should always fall below threshold).

It is evident that for real measurements in a nuclear power plant the acquisition time has to be strongly reduced to a time in the order of 10 minutes. This is equivalent to the requirement of enhanced detection efficiency. To meet this it is foreseen to bump-bond a 1 mm thick CdTe sensor to the next photon counting chip generation[14]. The change of detector material should result in an increase of detection efficiency from 0.7% to 3.5%. Fig. 6.29 shows a simulation of the above experimental setup replacing the GaAs sensor with a 1 mm thick CdTe sensor. In this case the ^{137}Cs source was measured for 10 minutes and had a dose rate of 9 μGy/h. The resulting signal-to-noise ratio was 6.4 which means that the sensitivity limit (SNR≈2) of such a hybrid

[14]Medipix2, the successor of the PCC, will accept positive and negative input charge. The PCC cannot be used with a CdTe sensor as the electronics is only sensitive to positive signals. In CdTe holes have such a low lifetime that only electrons can be used with a good charge collection efficiency.

CdTe - photon counting chip system would be in the order of 1 μGy/h for 10 minutes acquisition time. This is in the order of existing systems [Mil99] and for longer acquisition times there should be a clear advantage in the use of a photon counting system. Moreover, position resolution can be improved with the direct photon detection of a semiconductor system with respect to the conventional indirect detection systems where conversion stages lead to a spatial deterioration of the original photon position. Direct photon detection systems also have a much better potential for spectroscopy which would be very useful to determine the type of radioactive contamination.

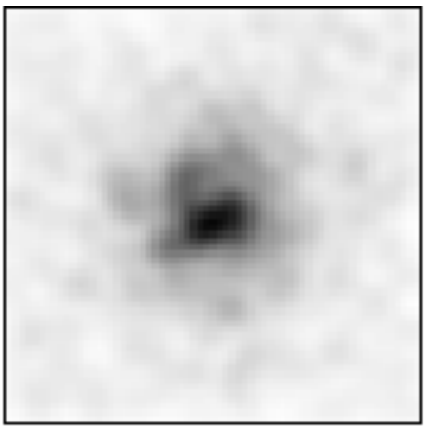

Figure 6.29: *Simulated smoothed image of a collimated ^{137}Cs source with 9 μGy/h dose rate and 10 minutes acquisition time [Gal00b]. The PCC is connected to a 1 mm thick CdTe sensor.*

6.5 Recent results with silicon detectors

Very recently a batch of silicon detectors arrived bump-bonded to the PCC. This will allow for non-ambiguous measurements where a stable and well-known detector performance can be assumed. Detector behaviour can be separated from electronics behaviour which will guarantee a reliable characterisation of the electronics chip (with a repetition of the absolute calibration of the test-input capacitance).

To fix the operating voltage for the 300 μm thick silicon detector a bias scan was made. For this purpose the detector was illuminated uniformly from the rear side with a ^{109}Cd source. As shown in fig. 6.30 the counting rate increases steadily up to $\sim$50 V where it reaches a plateau. The count rate distribution of the pixel matrix below the plateau is characterised by a significant spread in count rate which is represented by the error bars. Above 50 V this spread decreases and reaches a constant value. It was decided to chose 80 V as operating voltage for these detectors.

The PCC is perfectly linear with respect to an increase in exposure (fig. 6.31). The Si assembly was illuminated uniformly with a ^{109}Cd source changing the acquisition time. The linear behaviour of the average count rate with exposure was also confirmed

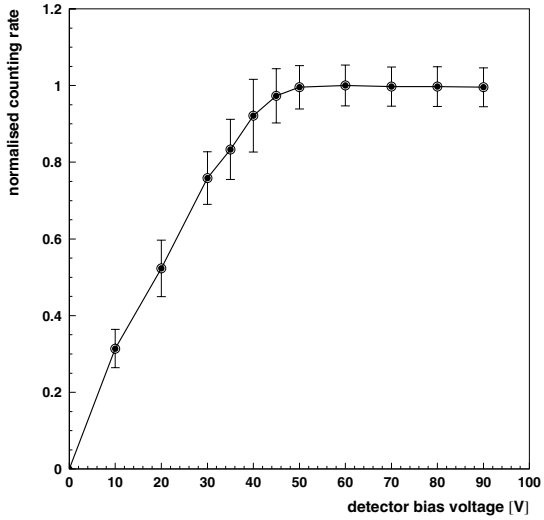

Figure 6.30: *Bias voltage scan of a 300 µm thick silicon sensor. Count rates are normalised to 1 and the error bars represent the standard deviation of a Gaussian fit to the count rate distribution of the pixel matrix. A plateau in count rate is reached above 50 V.*

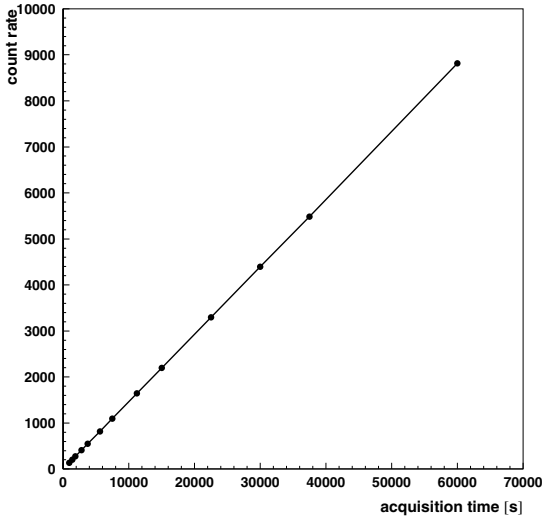

Figure 6.31: *Linearity of the PCC system measured with a uniform ^{109}Cd exposure. Count rate is plotted as a function of exposure time in seconds.*

with a mammographic X-ray tube varying the tube current [Ame00].

The SNR is one important parameter in image quality assessment (compare chapter 1.1.2). In digital radiology it can be determined through evaluation of a flood image [Man99a]. The signal is given by the average count rate N of the uniformly illuminated pixel matrix, and the noise corresponds to the standard deviation σ of the count distribution. The dotted curve of fig. 6.32 shows the measured SNR=N/σ as a function of exposure time in seconds (again a ^{109}Cd source was used to provide the X-rays). Already after an average count rate of ∼2000 counts/pixel[15] (at 15000 s exposure time) the SNR reaches a plateau with a SNR of ∼20. This behaviour is identical to the one published in [Man99a]. The SNR is limited by the non-uniformities in the pixel matrix and any non-uniformity of the source profile.
A dramatic increase of the SNR can be observed correcting the data with an *efficiency map*. The efficiency map should be created with highest possible statistics. An *efficiency factor* can be attributed to each pixel given by $\frac{\text{average count rate}}{\text{individual count rate}}$. Subsequently, the resulting matrix of each acquisition can be multiplied with the efficiency map. This corrects for all kinds of reasons that yield different counting rates like detector non-uniformities, electronics mismatching or also for non-flat source profiles. The dependence of the SNR with exposure time applying this correction method is represented by the solid line in fig. 6.32. The improvement is enormous; a SNR of **65** is reached for the longest exposure (with ∼8800 average count rate). This corresponds to ∼70% of the theoretical limit $N/\sqrt{N}$ of a quantum limited device. Very promising

[15] which corresponds to ∼1/16 of the counter depth.

is the fact that there is no plateau in the SNR which means that it will be possible to still improve it with higher statistics.

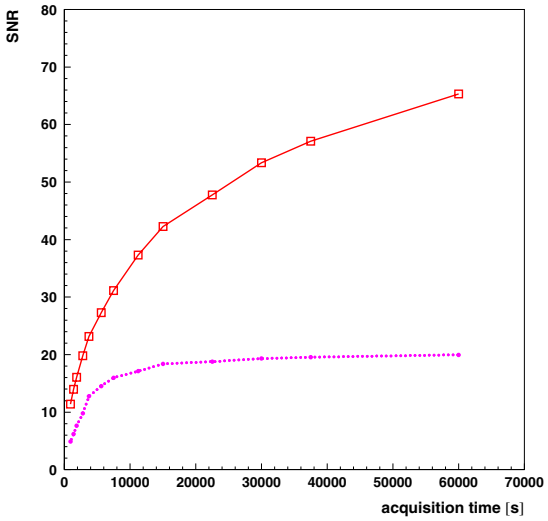

Figure 6.32: *SNR of a silicon assembly as a function of exposure time. The dotted curve plots the raw data; these raw data are multiplied with an efficiency map to yield the solid curve.*

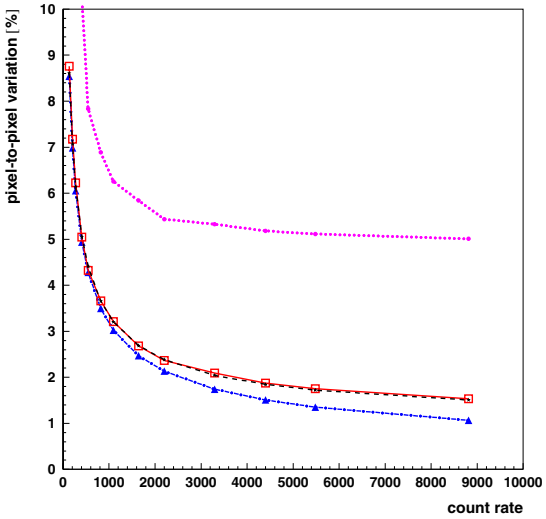

Figure 6.33: *Percentage of noise over average count rate as a function of average count rate. The dotted curve represents the raw data from a flood image and the solid curve the same data multiplied with an efficiency map. The dashed-dotted curve is the Poissonian limit of* $1/\sqrt{N}$ *and the dashed curve the same limit corrected for the statistics of the used efficiency map.*

Fig. 6.33 is a representation of the non-uniformity of the flood image depending on the statistics. Along the x-axis the average count rate measured with different acquisition times is shown. The curve with triangles is the noise normalised with the average signal $\sqrt{N}/N = 1/\sqrt{N}$ in percent in the theoretical limit of Poisson statistics. Therefore for 8800 counts the lowest pixel-to-pixel variation which could be reached amounts to 1%. An increase in statistics will yield an improvement of the image uniformity.
The uppermost dotted curve shows σ/N [%] for the same raw data as in fig. 6.32. It lies far above the theoretical limit with a pixel-to-pixel variation of 5% for the measurement with highest statistics. As the curve is almost flat one cannot hope for much improvement with increasing exposure.
Multiplying the raw data with the efficiency map as just described results in the solid curve with the open squares. The difference for an average count rate of 8800 is only 0.5% compared to the Poissonian limit.
The solid curve with open squares almost overlaps with the dashed curve which is again the Poissonian limit, but this time corrected for the use of an efficiency map. It is calculated using error propagation and is given by $\sqrt{(1/N) + (1/C)}$ [%], where C is the average count rate used for the determination of the efficiency map. The PCC system follows this theoretical curve. It can be expected that if the measurements

would be corrected with an efficiency map of increased statistics[16] the curve should approach the limit of $1/\sqrt{N}$.

6.6 Summary

This chapter presented a selection of measurements with the PCC assembled to GaAs sensors. First of all, the absolute calibration of the test-input capacitance of the chip with a ^{109}Cd X-ray source was explained. The test-input capacitance enables the injection of test-pulses which mimic particle signals to perform all kinds of electrical tests. The determination of its exact value enables the conversion from pulse height [mV] to amount of collected charge. There were some problems associated with this measurement which prohibited a separation of the two main gamma lines of ^{109}Cd around 22 and 25 keV. Moreover, the CCE of the GaAs sensor represents a crucial factor in the calculation. It was determined at a different shaping time than the one of the PCC and should therefore be re-measured. Nevertheless, an upper limit of the test-input capacitance could be given. The resulting value of the input capacitance and hence the numbers for minimum threshold, threshold spread or noise are therefore a worst case estimate. A new measurement of the test-input capacitance with Si sensors assembled to the PCC is in preparation.
Characteristic measurements of the GaAs sensors were performed. A discussion of the resulting IV-curves together with alpha source irradiation from the rear side of the sensor enabled to determine a detector bias voltage which should assure a maximum charge collection at still reasonable detector leakage currents.
A selection of images with different radioactive sources demonstrates that small differences in exposure or material thickness are clearly visible in the projection image. Most images plot the raw data to show the pure system performance. The application of image correction algorithms contains therefore the potential to still improve the images. The spatial resolution of the system was measured with a line pair mask and corresponds to the theoretical one defined by the pixel size. The pixel size of 170×170 μm^2 might be too large for some medical imaging applications, but the next generation CMOS pixel chip, the Medipix2 chip, will overcome this limitation.
A comparison of a tooth image with one made with a dental screen/CCD system indicates that it should be possible to achieve a significant dose reduction.
Very recent measurements with a 300 μm thick silicon detector bump-bonded to the PCC indicate that the system could reach the quantum limited SNR expected from Poisson statistics.

The last sections of this chapter describe the evaluation of two potential imaging applications of the PCC system outside of medical X-ray projection imaging. The first consists of X-ray powder diffraction. The steady increase in performance of synchrotrons and the attractiveness of new time resolved measurement methods result in a lack of suitable detectors. Measurements with the PCC system at a synchrotron test

[16]The applied efficiency map had an average count rate of ∼8800 counts per pixel.

beam were encouraging. A slight modification of the PCC design could offer a detector solution for most of these applications.
The second application concerns the use of a PCC-like system as detector in gamma cameras. Gamma cameras are used in nuclear medicine, astronomy, for material control or in nuclear industry. In particular, the photon counting concept could provide great advantages for imaging of weak radioactive sources due to its noise eliminating property. Probably it would be better to exchange the GaAs sensor with a $Cd_{1-x}Zn_xTe$ sensor for a higher gamma absorption efficiency in the used energy range.

The results of this chapter indicate that the concept of direct photon detection in a high-Z semiconductor sensor together with the capability of processing individual photons offers a clear improvement for various imaging applications in the future.

Chapter 7

Simulations of Energy Loss of Photons and Charge Spread in Semiconductor Pixel Detectors

Contents

Besides the problem of large area coverage spatial resolution of active pixel detectors is still not competitive with film or CCDs. However, CMOS chip technology is improving with an enormous speed driven by the economics of the semiconductor industry, leading to steadily increasing miniaturisation. *Deep sub-micron technologies* are already commercially available (0.25 μm processes) and will be used for designing a new version of the PCC, the **Medipix2 chip**. This will lead to a much reduced pixel cell size and to an improved spatial resolution.

As already explained in chapter 1.4 there are two possible approaches to digital X-ray imaging: charge integration and photon counting. For the photon counting solution studied by the Medipix collaboration one has to face the challenge of **charge sharing** between pixels which has to be properly taken into account while designing an imaging system in photon counting mode. This is related to the comparator threshold. As soon as the charge collected on one pixel falls below the threshold the

hit will be ignored. Thus in practice the threshold would have to be set low enough to still count the pixel with the bigger fraction of collected charge without counting the event more than once. Consequently one would lose one advantage of a very precise threshold setting close to the incident photon energy, the advantage of discriminating strongly Compton scattered events. The other possibility[1] of simply accepting the lower detection efficiency would imply an increased dose to patients and is therefore undesirable.

This problem was the motivation of studying in detail the mechanisms that could lead to charge sharing between neighbouring pixels and of estimating their relative importance. The simulations are divided up in two parts:
The first part (section 7.1) considers the *energy loss processes* inside the detector analysing the resulting spread of deposited charge without electric field.
The second part (section 7.2) concerns simulations of the *charge transport* towards the pixel electrodes under detector bias. It will be shown that diffusion may result in a considerable loss of detection efficiency in photon counting systems for small pixel sizes.

7.1 Simulations of energy loss of photons in semiconductor materials

The dominant energy loss processes for photons in the energy range used in medical X-ray diagnosis (<100 keV) are the *Compton effect* and mainly the *photo-electric effect*. For the simulations the photons enter the detector material along the z-axis and charge spreading occurs in the xy-plane perpendicular to z. Lateral charge spreading in xy due to the photo-electric effect is caused by the energy loss path of the emitted photo-electrons (see fig. 2.2) and Auger electrons as well as by the conversion of the fluorescence photons. Part of the incoming photons are scattered by the Compton and Rayleigh effects prior to photo-electric conversion.
The photo-electric cross-section is highly dependent on the atomic number of the detector material and the binding energy especially of the inner shell electrons. Fig. 7.1 plotted after data from [Nis] shows the total absorption efficiency of photons for Si, GaAs and CdTe. It is clear that due to the higher atomic number CdTe is more efficient than GaAs for photon conversion at energies above ∼20 keV, for example dental diagnosis, but for mammographic energies (around 18 keV) 200 μm of GaAs are still almost 100% efficient. Contributions of the different processes to the photon attenuation coefficient in GaAs and CdTe have already been presented (see figures 2.5 and 2.6. Until about 100 keV the total attenuation coefficient is dominated by the photo-electric effect with the L- and K-edges of the different elements clearly visible

[1]The mentioned solutions concern the current architecture of the PCC. It is for sure possible to find different design solutions like multiple counters or logic recognising simultaneous hits in adjacent pixels, but for their implementation a trade-off in pixel size has to be made. Moreover, the use of a spectrum of different X-ray energies rather than mono-energetic X-rays complicates the situation.

as sharp local increases in the photon attenuation.

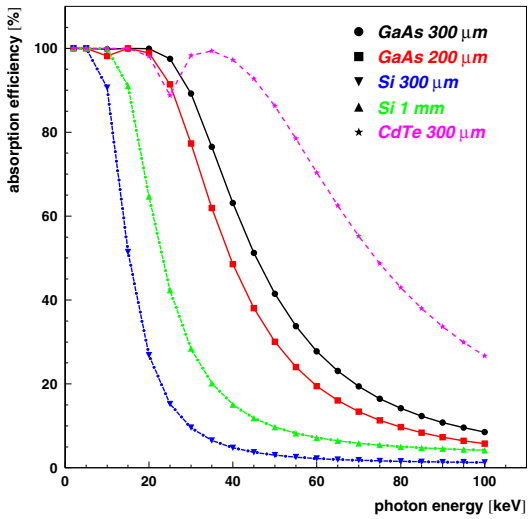

Figure 7.1: *Absorption efficiency for GaAs (200 and 300 µm thick), Si (300 µm and 1 mm) and CdTe (300 µm) as a function of the photon energy ranging from 5 keV to 100 keV (data from [Nis]).*

All of the mentioned energy loss and scattering processes with the corresponding angular distributions of the emitted secondary particles are very well described by a simulation program called **Fluka** (**Flu**ctuating **Ka**skad) [Flu, Aar93] which has been developed at CERN and in related institutes. The electro-magnetic part of Fluka originated in the EGS4 code [EGS85], but has been much further improved. The low energy transport limit of the code is 1 keV for electrons and photons. It is also possible to follow on an event-by-event basis the history of each beam particle.

7.1.1 Energy loss of 20 keV photons in GaAs, CdTe and Si

A first simulation was made to estimate the magnitude of lateral charge spread arising from energy loss processes for mammography in different semiconductor materials. Therefore a point-like beam of 100000 photons with an energy of 20 keV each entering a 300 μm thick GaAs detector at (0,0,0) was simulated with Fluka. The energy loss distribution of the photons travelling in z-direction (corresponding to the detector depth) is presented in fig. 7.2. The x- and y-axis have been divided up in very fine steps (0.2 μm in x and y; 3 μm in z) for maximum accuracy in the directions of interest.

Fig. 7.3 shows the same simulation in a 2-dimensional plot with the attenuation function (equation 2.4) as a solid line. Firstly this plot enables to check the difference between the attenuation coefficient given in literature (μ/ρ=42.58 cm^2/g for 20 keV photons in GaAs [Nis], which corresponds to a mean free path of ~44 μm) and the one resulting from a fit to the simulated data, μ/ρ=41.64 cm^2/g. Secondly it shows us a discrepancy in the comparison more or less in the first 10 μm. This 'missing energy loss' amounts to 3.6% of the total beam energy. It can be shown by switching

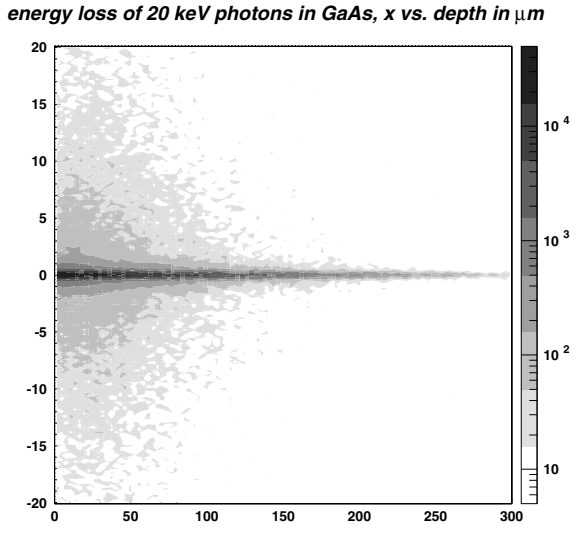

Figure 7.2: *Visualisation of the energy loss of 20 keV photons in GaAs. 100000 events have been simulated. The x-axis corresponds to the detector depth, z [μm], the y-axis to the x-position [μm] and the grey levels represent the integrated energy loss [keV] in logarithmic scale.*

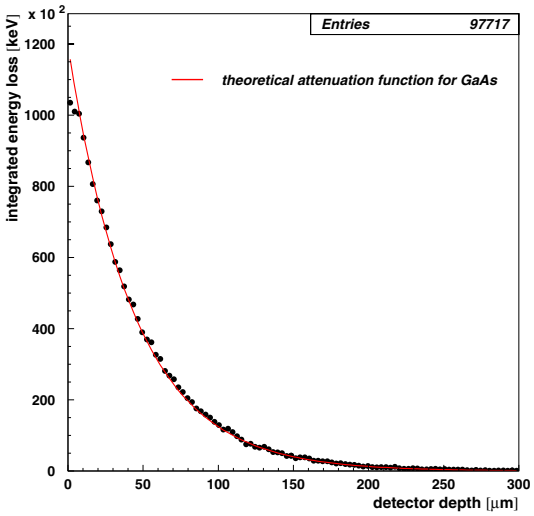

Figure 7.3: *Integrated energy loss [keV] in GaAs of 100000 photons each impinging with an energy of 20 keV as a function of detector depth, z [μm]. The solid line represents the attenuation function.*

off fluorescence (optional card in Fluka) and comparing the simulation results that 3.3% are due to fluorescence radiation (fig. 7.4). Fluorescence radiation[2] is isotropically distributed and escapes backwards from the detector. The remaining 0.3% are backscattered photons or particles escaping the detector volume.

To check the capability of Fluka in treating correctly the atomic binding structures the energy of the photon beam was lowered below the K-edges of Ga (∼10.37 keV) and As (∼11.87 keV) to 9 keV (fig. 7.5). Comparison with fig. 7.2 indicates that the halo of small integrated energy losses around the main energy loss path is due to fluorescence photons as this halo is not any longer present in figures 7.4 and 7.5.

Due to their higher Z and therefore higher photon attenuation coefficients, CdTe and $Cd_{1-x}Zn_xTe$ are also very promising semiconductor materials for radiology. To compare the performance in terms of lateral distribution of energy deposition points with GaAs, the same simulations as described above have been made for a 300 μm thick CdTe sample (fig. 7.6). The energy loss distribution is wider than for GaAs because of the lower photon attenuation coefficient of CdTe around 20 keV photon energy. Therefore the photons travel further in the lateral as well as in the incident photon beam direction.

[2]The energy of α-fluorescence photons in Ga is ∼9.2 keV and in As ∼10.5 keV (compare table 2.1).

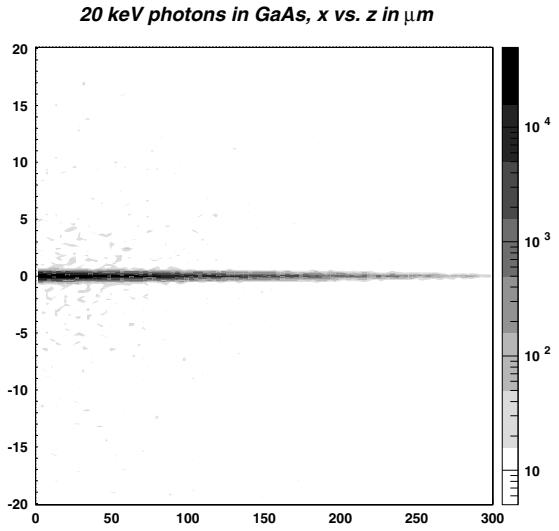

Figure 7.4: *Energy loss distribution as in fig. 7.2, but with the fluorescence option switched off.*

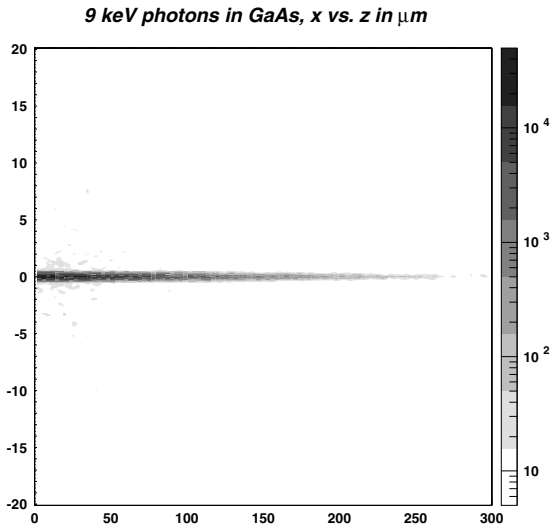

Figure 7.5: *Energy loss distribution as in fig. 7.2, but for 9 keV photons (below the K-edges of Ga and As).*

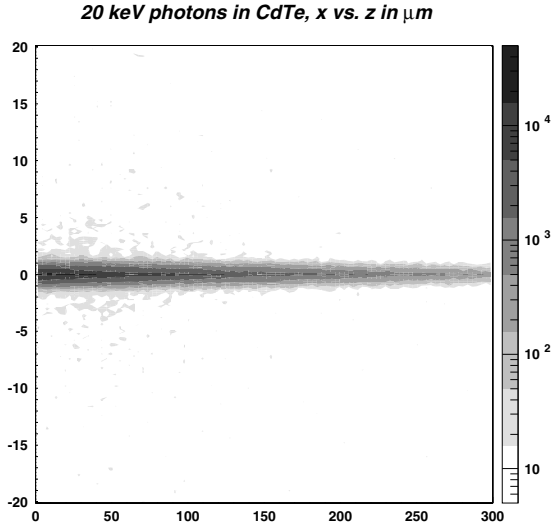

Figure 7.6: *Energy loss distribution as in fig. 7.2, but for CdTe.*

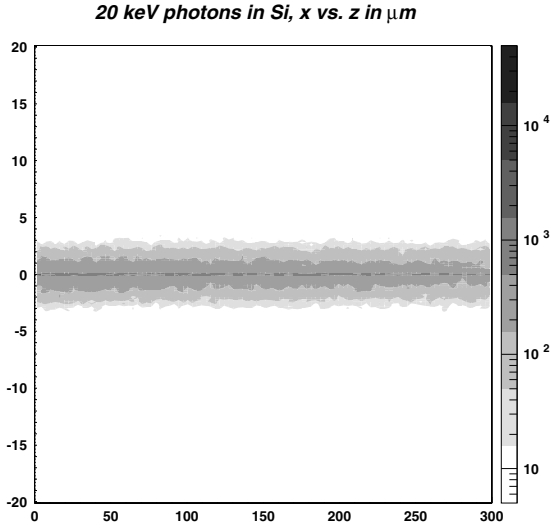

Figure 7.7: *Energy loss distribution as in fig. 7.2, but for silicon.*

Silicon has also been checked in the same way (fig. 7.7). In a 300 μm thick silicon detector 75.5% of the total photon beam energy escapes the detector as the mean free path for photons in Si is $\sim$0.96 mm [Nis]. Therefore silicon is clearly a relatively poor candidate for radiology at energies above $\sim$20 keV.

One difference between CdTe and GaAs as detector material for mammography is that the used X-ray energy range lies above the K-edge of GaAs, but still below the K-edge of CdTe (K-edge of Cd $\sim$26.71 keV and of Te $\sim$31.81 keV, see table 2.1). This is

the reason why there is no halo of isotropic low integrated energy loss from fluorescence photons visible in fig. 7.6 compared to fig. 7.2. Therefore, although CdTe has a lower attenuation coefficient than GaAs for this energy range (μ/ρ=21.44 cm^2/g for 20 keV photons [Nis]), it absorbs more energy (∼2.6% of the total energy escapes the CdTe detector which is 1% less than for the GaAs detector). This conclusion has implications in a photon counting system if the discriminator threshold were to be set near to the incoming photon energy. The discrepancy between recorded energy loss with GaAs compared to CdTe in such a system would be even greater than the mentioned 1% valid for integrating systems. This is due to the energy loss of the photo-electrons and Auger electrons which were produced together with the fluorescence photons that escape the detector backwards. These electrons are stopped much faster than the photons. Hence, their energy will stay mostly within the detector volume, but will be for a large fraction below the threshold of the photon counting device and therefore ignored.

7.1.2 Energy loss of 60 keV photons in GaAs and CdTe

Simulations of the process of energy deposition were also performed for 60 keV photons. At this energy 75% of the total energy escapes from a 300 μm thick GaAs detector, whereas it is only 36% for CdTe of the same thickness (figures 7.8 and 7.9).

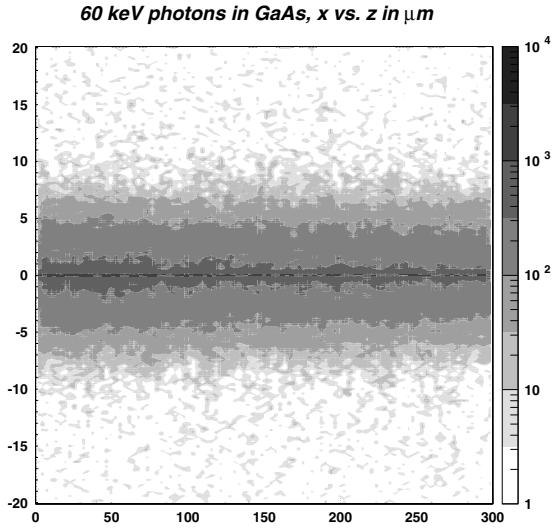

Figure 7.8: *Energy loss distribution as in fig. 7.2, but for a 60 keV photon beam.*

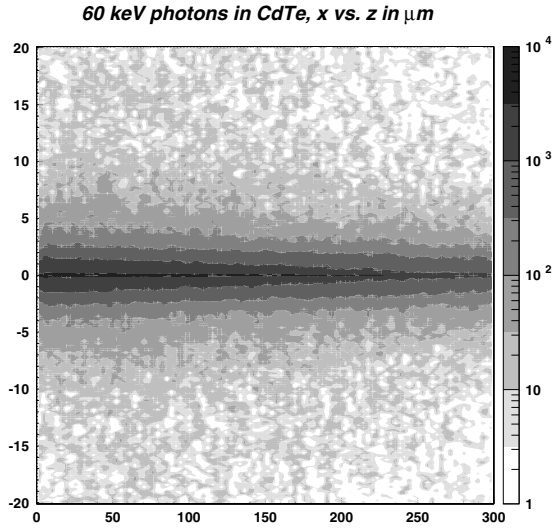

Figure 7.9: *Energy loss distribution as in fig. 7.8, but for CdTe.*

As this work was done to find out the importance of lateral charge spread due to the energy deposition the RMS values from the cross-sections in x (or y) of the energy loss distributions are summarised in table 7.1. It can be seen that for photon energies around 20 keV the charge spreading in x and y is negligible for GaAs and CdTe whilst for Si and for higher photon energies it may be worth being taken into account.

semiconductor	20 keV photons	60 keV photons
GaAs	0.85 μm	3.35 μm
CdTe	0.52 μm	1.46 μm
Si	1.13 μm	

Table 7.1: *RMS values from the cross-sections of the simulated spatial distributions of the deposited energy of a 20 and 60 keV photon beam impinging on 300 μm of GaAs, CdTe and Si.*

7.2 Charge transport simulations in a GaAs pixel detector

Once the energy loss processes of the X-rays in the semiconductor material have been evaluated with regard to lateral charge spreading, the influence of the collection process of the created e-h-pairs has to be studied in detail.
In order to use a semiconductor material as a particle detector a bias has to be applied to produce a region of very low space charge, the active detector volume. In the active region e-h-pairs which are produced by the passage (ionising particles) or the conversion (photons) of the particle do not recombine and will *drift* under the influence of the electric field towards the corresponding collection electrodes. Superimposed on this drift motion is the isotropic *diffusion* of the carriers which causes the charge to spread out (see chapter 3.4).
Charge collection is a complicated process depending on a lot of parameters such as carrier mobility and lifetime, material structure, detector geometry, doping and impurity concentrations, electric field strength and distribution, contacts, temperature, trapping and others. In order to simulate charge collection following X-ray conversion in pixel detectors the 3-dimensional semiconductor device simulation tool **Davinci** [Dav] was used.
Davinci makes use of the six basic partial differential equations to describe the bulk behaviour of semiconductor devices:

- Poisson's equation (3.12) for the electrostatic potential
- Current continuity equations for electrons and holes to describe the carrier concentrations (equations 3.10 and 3.11)
- Carrier energy balance equations for electrons and holes to define stability conditions
- Lattice heat equation which governs the lattice temperature

Apart from the 3D capability the major advantage of Davinci is that it solves the differential equations in a *coupled* way. To do so they are discretised before in a simulation grid (max. number of nodes available: 60000 [Dav]) that has a non-uniform, arbitrary prismatic structure. As the resulting coupled solutions are non-linear, solutions must be obtained by a non-linear iteration method, starting from an initial guess.

A disadvantage of the program is the enormous amount of CPU time necessary to calculate the collection of even one single event; also sometimes its complexity makes it difficult to choose the appropriate model for a given situation out of a palette of available physical models and options.

7.2.1 Simulated geometry and starting conditions

Although Davinci is dedicated to simulate small semiconductor devices it can be used for semiconductor detectors as well. Because of their greater dimensions the definition of the semiconductor grid (corresponding to the detector geometry) is limited by the number of nodes available. The use of symmetric boundary conditions made it possible to restrict the simulations to only 4 pixel quarters. The defined geometry consisted of a pixel detector with square pixels of 50 μm pitch with a gap of 10 μm between the collection electrodes. The accuracy of the simulation grid was chosen to be 4 μm in x and y (in the plane parallel to the detector surface) except in the inter-pixel gaps where a finer gridding of 1 μm was used (most critical volume for charge sharing). The detector thickness was 200 μm and was defined by a gridding of 5 μm (fig. 7.10).

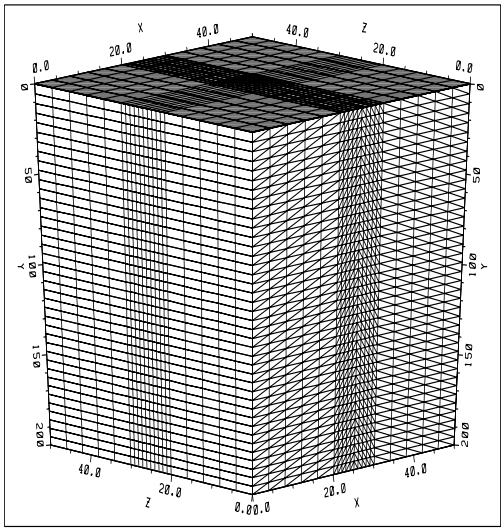

Figure 7.10: *Simulation grid enabling higher calculation accuracy in the 10 μm gap between the pixel quarters. The pixel pitch is 50 μm and the thickness of the GaAs detector 200 μm.*

It was very difficult to fix all the material parameters for compensated SI GaAs as they vary considerably from manufacturer to manufacturer and between different bulk GaAs growth methods. The assumed values for the chosen material parameters are summarised in table 7.2. They should be considered as very rough approximations. The electric field was assumed to be constant over the active detector depth with a field strength of 1 V/μm [Cas98, But97]. The values for the charge carrier mobilities were related to this electric field strength (compare section 4.1.1).

The effect of a connected electronics circuit was roughly accounted for by attaching a lumped resistance and capacitance to the pixel electrodes.

material	compensated SI GaAs
detector thickness	200 μm
pixel size	50 μm square pixels
impurity concentration	10^{15} atoms/cm^3 of both carrier types
detector bias voltage	200 V
electric field $\mathcal{E}$	1 V/μm field strength, constant over detector depth
fixed electron mobility	1000 cm^2/(Vs) (@ $\mathcal{E}$=10^4 V/cm)
fixed hole mobility	350 cm^2/(Vs) (@ $\mathcal{E}$=10^4 V/cm)
electron lifetime	3 ns
hole lifetime	5 ns
charge trapping	not yet considered

Table 7.2: *Parameters used for the Davinci charge transport simulations in a SI GaAs detector.*

7.2.2 Davinci simulation results

The collection of 10000 e-h-pairs[3] generated at different positions in the xy-plane parallel to the detector surface and at different detector depths was simulated. Carrier-carrier scattering for such high local carrier concentrations was included in the simulation. A bias of 200 V was applied at the detector rear side with the pixel electrodes lying at 0 V potential (hole collection). The development in time of the hole charge cloud and its collection on the pixel electrodes is represented in figs. 7.11 a)-e), the same for the electron charge cloud in figs. 7.12 a)-e). One can clearly distinguish the drift motion of the carriers and the expansion of the charge cloud due to diffusion. From figs. 7.11 c)-e) it is also evident that charge is shared between the neighbouring pixels. This is due to the location of the charge generation which was chosen to be in the centre of the gap between two pixels and at a detector depth of 25 μm.

Comparison with a charge deposition point at 175 μm (close to the detector rear plane) shows the difference in collection time between holes and electrons due to the different mobilities. This is also clear studying the signal shape on the collecting electrode (fig. 7.13). For charge generated by a photon at 150 μm depth from the pixel plane the signal resulting from the electron collection arrives much faster than 1 ns whereas the holes are collected about 4 ns later. In this case the signal is mostly due to hole collection as the holes have to travel over a much longer distance [Ram39]. Moving with the charge deposition point closer to the pixel plane the peak of the signal part arising from hole collection moves to shorter collection times. On the other hand the electrons are collected later; at a charge deposition depth of 50 μm the peak of the electron collection is located at about 1 ns after charge deposition.

[3]Corresponds to the energy deposition from a photon of ∼43 keV.

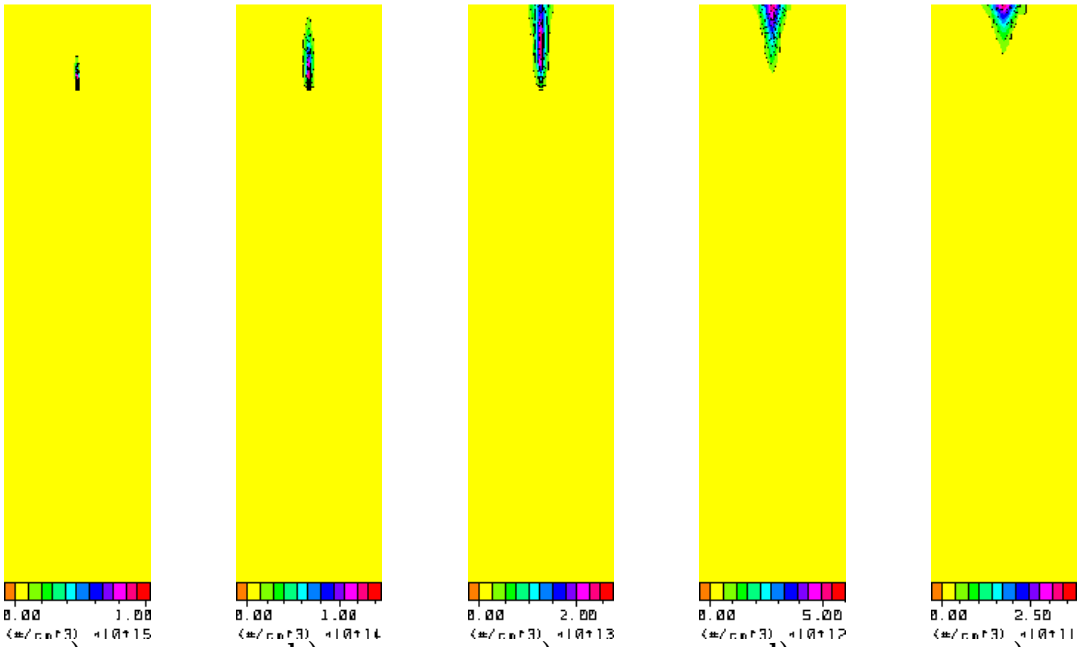

Figure 7.11: *5 time frames showing the holes drifting towards the pixellated detector surface. Charge was deposited at a detector depth of 25 µm in the centre between 2 pixels. From pictures a) to e) the charge carrier concentration inside the bulk is plotted logarithmically with scales* 10^{15}, 10^{14}, 10^{13}, 10^{12} *and* 10^{11} *holes per* cm^3 *and at times of 31, 219, 710, 1900 and 4400 ps after charge deposition respectively.*

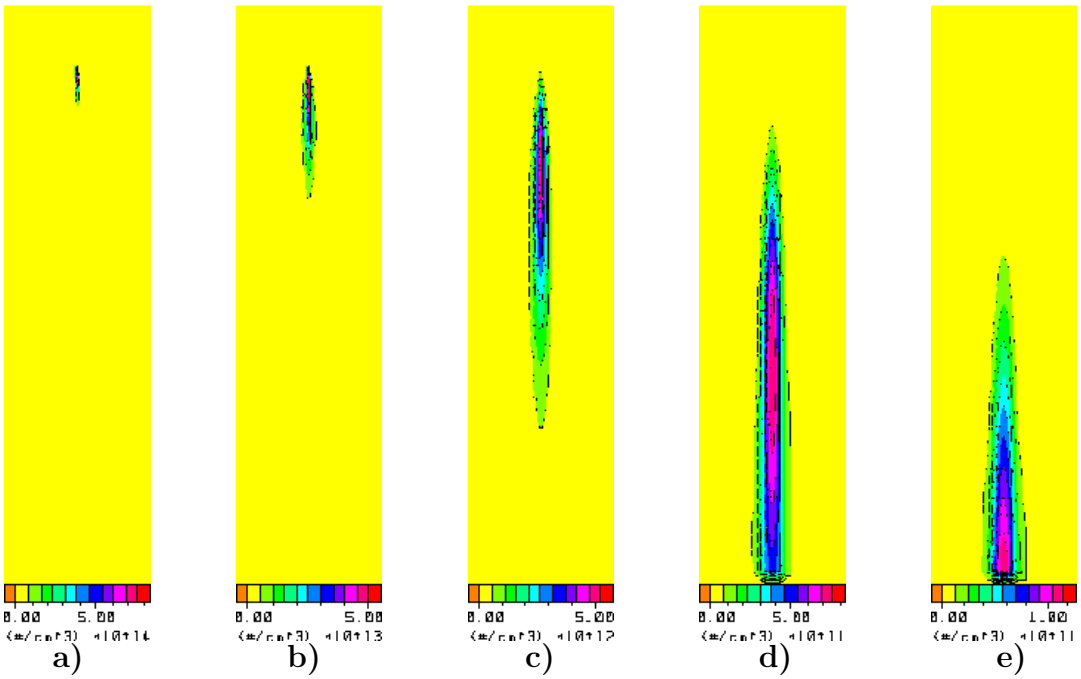

Figure 7.12: *5 time frames showing the electrons drifting towards the detector rear plane. Charge was deposited at a detector depth of 25 µm in the centre between 2 pixels. From pictures a) to e) the charge carrier concentration inside the bulk is plotted logarithmically with scales* 10^{14}, 10^{13}, 10^{12}, 10^{11} *and again* 10^{11} *electrons per* cm^3 *and at times of 31, 219, 710, 1900 and 4400 ps after charge deposition respectively.*

It was observed that the charge carrier lifetimes do not represent a critical factor in the simulations. This seems to be due to the lack of free charge to recombine because of the compensation and the high resistivity of the material.

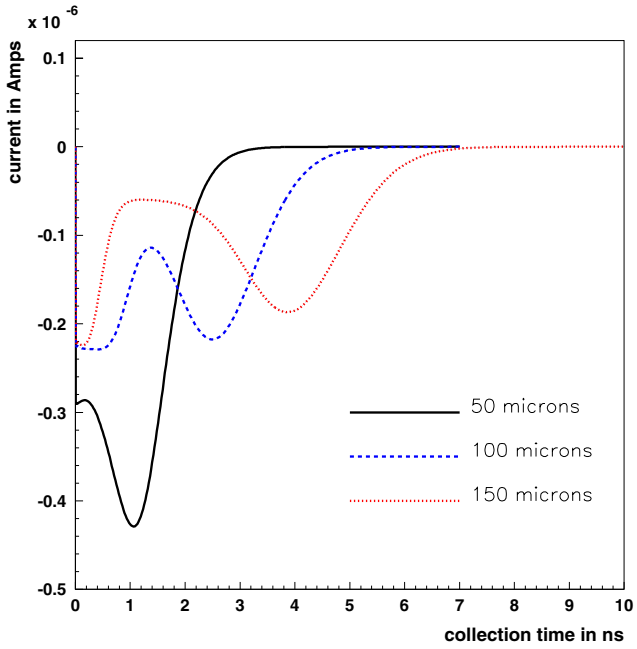

Figure 7.13: *Shown is the current on the collecting pixel electrode [A] as a function of the collection time [ns] for charge deposition depths at 50, 100 and 150 μm from the pixel plane.*

The drift motion of the charges induces also a signal on the neighbouring pixels which has the shape of a differentiation of the 'real' signal (due to capacitive coupling between the pixels) with an integral of 0 after full collection. It is necessary to use extremely fine time integration steps in order to get reasonable quantitative results for the charge collection.

Finally, the implications of charge sharing due to the charge collection process for photon counting systems setting a threshold in each pixel were studied. The results are shown in figs. 7.14 a)-d). Although the results should be considered to be rather qualitative[4] the importance of considering charge sharing when going to very small pixel sizes for photon counting systems is obvious. At a threshold of 90% of the total deposited charge the efficiency of the system would drop to only ∼65% (fig. 7.14 d)) and one would lose in the simulated detector configuration the whole volume of the inter-pixel gaps for charge deposition. Without trapping this effect is mainly due to diffusion. Transverse diffusion in an electric field is independent of the type of charge carrier as the diffusion constant is proportional to and the drift time inversely proportional to the mobility. A possible solution to limit diffusion could be working in

[4]A finer simulation mesh and finer integration steps in time should be used.

over-depletion[5]. A different solution would be to include special logic in the electronics design to deal with multiple hits.

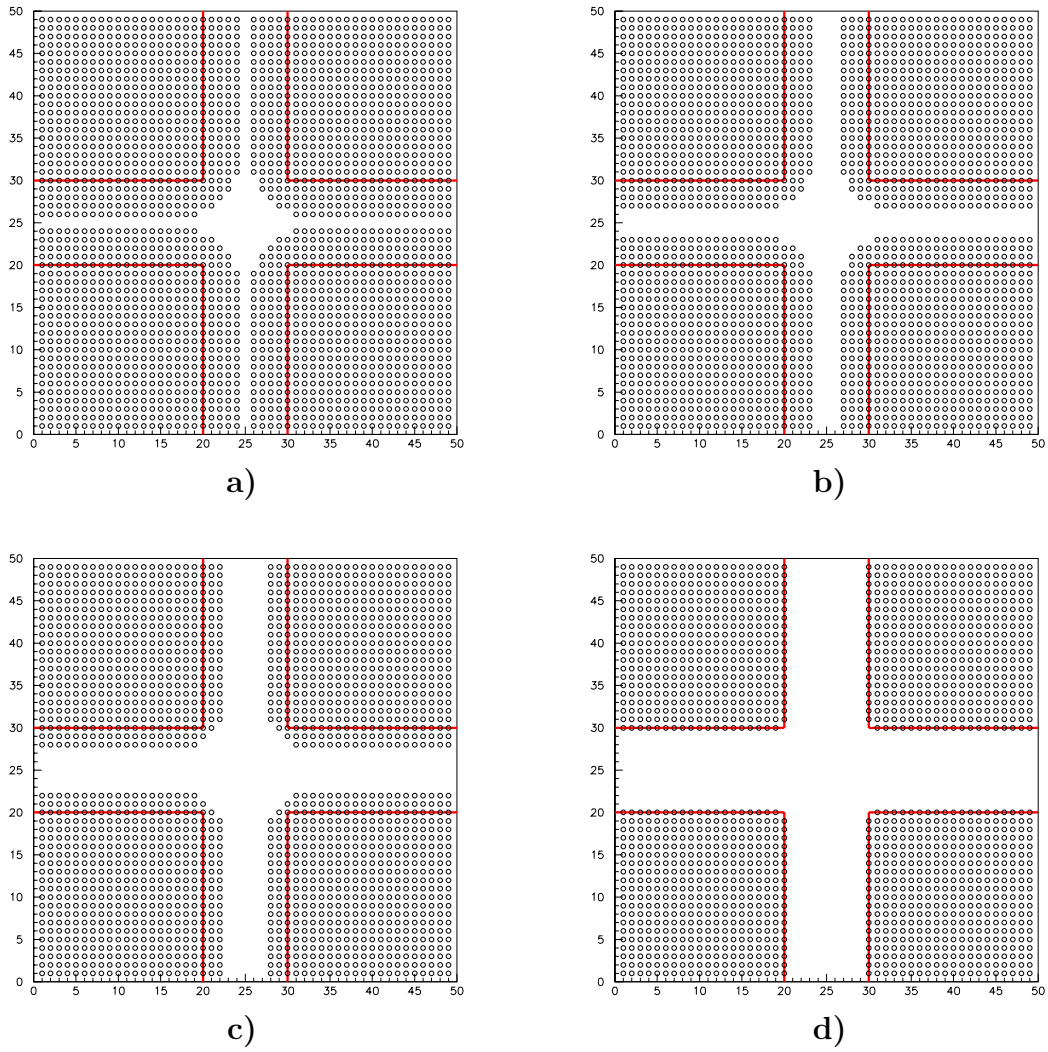

Figure 7.14: *Black circles in the four figures represent the area where hits are detected. The solid lines stand for pixel boundaries. The white areas represent areas of undetected hits. In a) the threshold was set at 60% of the total deposited charge which yielded a detection efficiency of 90%. In b) the threshold was set at 70% of the total deposited charge and a detection efficiency of 83% was simulated. In c) the threshold was set at 80% and resulted in a detection efficiency of 76%. In d) the threshold was set at 90% of the total deposited charge which yielded a detection efficiency of 64%.*

It should be noted that charge trapping effects have not been included yet in the simulations. For SI bulk GaAs this will be absolutely necessary in order to match also quantitatively with experiments. The charge transport simulations presented do not pretend to describe reality, but they can help to understand the charge transport

[5]On the other hand higher electric fields might cause problems concerning field enhanced trapping effects in GaAs. Moreover, it is not easy to over-deplete a GaAs detector without special contact fabrication.

behaviour and the problems which arise with pixel detectors. In the future, all the parameters have to be optimised for the detector material which is decided to be used. Valid trapping models with defined trapping levels, capture cross sections, emission rates and detrapping times have to be implemented.

The final idea is to combine the Fluka charge deposition simulations with the Davinci charge transport simulations. The Fluka output has to be modified in order to be used as input for Davinci. Perhaps a weighted charge deposition distribution for different detector depths can be used to realise this within a tolerable CPU time.

7.3 Summary

The PCC is a first generation photon counting chip whose design was mainly intended to evaluate the advantages of the counting technique compared to the charge integrating method. Various measurements yielded very encouraging results, but also ideas for possible improvements. One of these improvements concerns the pixel pitch which is still too coarse for some applications like mammography. In future versions the pixel pitch will be reduced to $\sim$50 μm. In photon counting mode attention has to be paid to very small pitches due to charge sharing between adjacent pixels. If a photon enters the detector for example close to a pixel border and charge sharing takes place between the hit pixel and its neighbour, the photon will either be counted once (on the hit pixel which is correct), twice (once on both pixels) or not at all depending on the pixel thresholds. The latter will be the case when the pixel thresholds are set close to the incident photon beam energy which is foreseen to be the general setup. This would signify a decrease in photon detection efficiency and wasted patient dose. Therefore charge sharing effects should be investigated for photon counting pixel detectors with small pixel sizes.
Charge sharing simulations were performed and were divided up in two parts. The first part treats the energy deposition of photons and was simulated with the Fluka Monte Carlo code. The different photon conversion processes (photo-electric and Compton process) result in a certain angular distribution of secondary particles which deposit energy in the detector. If this energy deposition were too much spread out in the directions parallel to the detector surface, the generated charge in the semiconductor would be shared between several pixels. The simulations showed that the contribution to charge sharing from energy deposition processes is negligible in GaAs and CdTe for photon energies of 20 keV, but for 60 keV it is already a notable effect. In fact a 300 μm thick GaAs detector is slightly less efficient concerning the energy deposition of 20 keV photons than CdTe. This is in spite of GaAs having a higher photon attenuation coefficient at this energy. The reason is that 20 keV is just above the K-edge of GaAs, but still below the one of CdTe. The location of the K-edge of GaAs just below the energy of the photon beam results in an isotropical emission of many fluorescence photons yielding a wider lateral spread in the charge deposition distribution. Moreover, a significant fraction of these photons escapes backwards from the detector

which might result in the non-detectability of the primary photon due to the threshold in collected charge.
After the conversion of the X-rays into detectable charge this charge has to be separated and transported to the corresponding electrodes with the help of an electric field. A 3-dimensional semiconductor device simulation program called Davinci was used to simulate the charge transport in a 200 μm thick GaAs pixel detector with 50 μm pitch. The results of these simulations are surely not quantitative results as charge trapping, which is an important parameter in this material, could not be included yet. Nevertheless, it could be shown that charge sharing due to diffusion can result in a significant loss in efficiency of photon counting pixel detectors with small pixel size depending on the pixel threshold. For future photon counting pixel chips the question of how to deal with charge sharing represents certainly a challenge.

Conclusions and Outlook

This thesis describes the behaviour of a photon counting X-ray imaging system based on a CMOS pixel read-out chip which has been bump-bonded to a GaAs detector.

The first chapter introduces the fundamental parameters of medical imaging and gives a brief outline of the state of the art in imaging systems for X-ray projection radiology. Key parameters are total patient dose, signal-to-noise ratio, detective quantum efficiency and spatial resolution which can be expressed in terms of a modulation transfer function. A suitable system should be able to image at the same time low contrast and low size objects. It should provide images with high contrast, large dynamic range and high spatial resolution taken at the lowest possible dose.
Technical progress is leading industry slowly away from film-based systems to systems which use electronic devices to capture the image. Most existing systems still use a scintillating material as a means of converting the X-ray photons to light resulting in some image blurring. Major benefits are to be expected from the improved dynamic range of recent imaging devices and the possibility of storing the data in digital format. In some of these recent devices the X-rays are converted into electrical charge directly in a semiconductor material, and this charge is integrated on a capacitor. This direct conversion should lead to an improvement in image resolution.
The approach of the Medipix collaboration with the design of the PCC photon counting pixel chip is then described. It implies the direct X-ray detection concept in a semiconductor detector with high stopping power. Each pixel of the image array has an energy threshold; every photon whose collected charge signal exceeds this threshold is counted as one. This eliminates background noise from the image resulting in an improved signal-to-noise ratio and provides an essentially infinite dynamic range. Moreover, all photons regardless of their energy are given the same weight in the image formation. This approach should lead to a reduction in the number of photons necessary to image an object clearly providing a reduction in the dose given to patients.

The second chapter describes the physical interaction of low energy photons with matter. For X-ray photons in the diagnostic range ($\sim$15-70 keV) the photo-electric effect is dominant in high-Z materials, but also Compton and Rayleigh scattering play a role. Photon attenuation coefficients as a function of X-ray energy indicate the suitability of a material to convert X-rays efficiently to assure a high detective quantum

efficiency.

Following from this the third chapter is devoted to a basic introduction to semiconductor devices and detectors. Most semiconductor detectors are formed from a reverse biased p-n or Schottky diode made of high resistivity material. It is clear from this chapter that as well as a high stopping power for X-rays a good detector material should have a high enough band gap to have low leakage current at room temperature but low enough to provide a sufficient number of electron-hole pairs. Moreover it is important that the material be homogeneous and the free charge carrier lifetime be high enough so that all of the charge can be detected. Semi-insulating GaAs possesses many of these properties.

Chapter 4 presents the basic properties of GaAs material. The range in published parameter values is large and therefore an extensive literature study was necessary to summarise the characteristics of the material. For the reasons mentioned above a very pure GaAs material would be preferred. Unfortunately the growth techniques for such a material are slow, technically challenging and subsequently rather expensive. Also these materials are not commercially available. Most of the work on GaAs detectors has concentrated on using semi-insulating bulk material which has been produced by compensating impurities with the native EL2-defect associated with the As antisite. As such rather thick layers of high resistivity material can be produced. It is evident however, that these EL2 levels represent charge traps which in turn degrade charge collection. This degradation may be attenuated by applying high bias voltages with the help of special contacts. Another limitation in such a material is the homogeneity, a property which is of vital importance in imaging applications. The use of pure epitaxial GaAs could yield a large improvement in detector performance.

Chapter 5 describes the architecture and the behaviour of the PCC. The author was heavily involved in the electrical characterisation of the chip. Electrical tests consist of the determination of the minimum threshold over noise, the threshold spread between the pixels in the matrix, noise measurements and the pixel-wise fine tuning of the threshold. These tests are performed sending trains of test pulses into the chip which mimic a charge signal. This is possible thanks to a test-input capacitance which can be connected with a switch to the analog input line of the pixel cell.
Another important task was to establish a protocol for the selection of Known Good Die from electronics wafer tests in order to provide a map of working chips for bump-bonding. Chips were divided up into three categories. The criteria followed for the classification were based on functionality, minimum threshold and threshold dispersion considerations. The first batch of wafers exhibited systematic input transistor threshold variations across the wafer (transistor thresholds being higher in the centre than at the sides) which seemed to be correlated to chip yield. It was possible to reduce the transistor thresholds of devices in the middle of the wafer with a supplementary annealing step. This did not however result in a large improvement in chip yield.

Working assemblies of the PCC bump-bonded to 200 μm thick semi-insulating GaAs devices were produced. The behaviour of these devices was studied. The GaAs sensors had a special non-alloyed ohmic contact on the rear side which allowed to impose high bias voltages (up to ∼400 V). I-V scans yielded a plateau above ∼50 V with ∼40 nA/mm^2 leakage current density. However, measurements with an alpha source revealed that the active detection volume reached the detector rear side only after ∼250 V. As well as this the number of counts recorded in the pixels using a ^{109}Cd source flattened out only after ∼350 V applied bias voltage without showing a clear plateau.
Although an estimate of the injection capacitance of the test-input is provided by the CMOS manufacturer an absolute calibration of the threshold of the electronics could only be carried out using radioactive gamma or X-ray sources with known photon emission lines and scanning the bias current which controls the threshold. The author undertook this task and was able to make an estimate of the threshold of the electronics based on certain assumptions about the charge collection efficiency of the GaAs detector. Subsequently, it was possible to provide characteristic measurement results in units of charge. Minimum thresholds of ∼2400 e$^-$ can be reached with the biased assemblies. The threshold spread without adjustment is in the order of 500 e$^-$, a value which can be reduced to ∼100 e$^-$ with the 3-bit threshold tuning. The noise of the electronics chain amounts to ∼250 e$^-$. It has to be stressed that all these values represent worst case values due to the assumptions made about charge collection in the GaAs material for the absolute calibration of the test-input capacitance. Tests with recent assemblies of silicon sensors bump-bonded to the PCC indicate a significantly better performance of the chip. Very preliminary measurements have been made [Vis00] using an X-ray gun with a chromium target and an accelerating voltage of 6.5 kV. Hits were observed in the PCC-Si-assembly indicating a threshold of well below 2400 e$^-$. A new absolute calibration measurement with silicon assemblies is in preparation.
A perfectly linear behaviour of the PCC could be shown with Si assemblies. Very recent results indicate that correcting the pixel-to-pixel variation with an efficiency map obtained from a flood image it should be possible to reach the Poissonian noise limit when sufficiently large statistics is used for the efficiency map. With this correction a SNR of a flood image of 65 was achieved (preliminary result).

Returning to the GaAs material, several images were made of different objects using a ^{90}Sr beta source, a ^{109}Cd and an ^{241}Am X- and gamma-ray source. Small differences in photon attenuation of such samples could be clearly imaged. A spatial resolution of 3.6 lp/mm was determined corresponding to the theoretical value.
A comparative measurement of a tooth was made using the PCC with a ^{109}Cd source and a dental X-ray imaging system based on a screen+CCD detector under standard settings. It was possible to image the same tooth with an improvement of ∼30 times in dose.

The author also participated in measurements to assess the PCC device for synchrotron radiation and gamma camera applications. The author shows arguments that in both cases the capability of processing single photons should lead to an improvement in performance compared to existing systems. For synchrotron radiation it will be necessary to solve the problem of large area coverage. Moreover, dynamic range should even be enlarged which is just a question of counter depth. For an implementation in gamma cameras the sensor material should be exchanged or at least made thicker to yield higher stopping power. The noise suppression characteristics of the PCC approach should yield an improved sensitivity to weak radioactive sources compared to existing systems.

A study of charge sharing was also undertaken with a view to future developments where the pixel dimensions will be reduced to $\sim$50 μm. Simulations of energy loss in various semiconductor materials were carried out in order to estimate the charge spreading which follows the X-ray conversion processes. It was concluded that lateral charge spreading at low energies around 20 keV is not significant for GaAs and CdTe, but might be worth taken into account for higher energies. One interesting outcome of these studies is that highest absorption efficiency is not exclusively determined by the photon attenuation coefficient of the considered material. Care has to be taken for photon energy regions just above the absorption edges (K-, L-edges) as the isotropic generation of fluorescence radiation can result in a significant percentage of energy which escapes the detector. This is of even greater concern for photon counting systems as the part of the energy loss which remains inside the detector might be below the threshold and therefore the photon would not be detected.
As well as the simulations of energy deposition, simulations concerning the transport of electrons and holes to the detector electrodes under the influence of an electric field were combined with a very simple simulation of the electronics. Here, charge might be shared between pixels due to lateral diffusion and crosstalk. The conclusions of these simulations are that charge sharing may be a strong limiting factor in photon counting pixel systems of small pitch unless the electronics is designed with this clearly in view. The author hopes that this work provides an important stimulus for discussions on future pixel designs.

Outlook

This thesis was devoted to the study of the PCC prototype photon counting pixel chip connected to GaAs sensors. During this work a number of limitations of the present system have been identified and a number of important lessons have been learned.

Epitaxial GaAs material should be bump-bonded to the PCC for trials. As well as this new materials such as CdTe or $Cd_{1-x}Zn_xTe$ might open new possible applications in case of a low density of material inhomogeneities. Such materials which rely on an

electron collection could be bump-bonded to a future chip.

It is clear from recent measurement results (section 6.5) that assembling the PCC to silicon has many advantages. High resistivity silicon is much more homogeneous than GaAs and provides a known quantity of input charge enabling a thorough characterisation of the electronics. It would be advisable in future to make this step early in the characterisation process.

Medipix2	**PCC** (Medipix1)
pixel size ∼55 x 55 μm^2	pixel size 170 x 170 μm^2
0.25 μm CMOS design technology	1 μm SACMOS technology
256 x 256 pixels per chip	64 x 64 pixels per chip
variable shutter	variable shutter
sensitive to positive and negative input charge	sensitive to positive input charge only
preamplifier - 2 comparators - delay logic - counter	preamplifier - shaper - comparator - delay - counter
∼150 ns peaking time of the preamplifier	∼150 ns peaking time of the shaper
leakage current compensation pixel-wise (up to ∼ +10 nA and ∼ −4 nA per pixel)	leakage current compensation column-wise (up to ∼ +10 nA per pixel) sensing through a dummy pixel row
window discriminator	single discriminator
3 bit threshold tuning per comparator	3 bit threshold tuning
large linear range of the comparator (between ∼ ±80000 e$^-$after simulations)	limited linear comparator range
13 bit counter	15 bit counter
overflow bit for the counter	no overflow bit
read-out time for a 100 MHz serial bus: 9.2 ms	read-out time at 10 MHz with a 16-bit parallel bus: 384 μs
matrix of 3×3 pixels with analog output	
3-side buttable	not buttable

Table 7.3: *Specifications for the new Medipix2 chip in comparison with the PCC.*

The PCC is limited in spatial resolution. Fortunately the micro-electronics industry provides greater and greater component density each year. As a result of this a new collaboration has been founded called *Medipix2* which is developing a chip similar to the PCC but with a pixel pitch of 55 μm. A comparison of the specifications of the PCC and the new chip, called **Medipix2**, is shown in table 7.3. Important new features include the possibility to collect both electrons and holes and a new

detector leakage current compensation circuit which compensates each pixel independently (taking care of possible leakage current inhomogeneities). An increased linear comparator range will help to keep the same threshold adjustment mask for different working conditions. As well as this a window discriminator has been added which should allow the selection of a range of photon energies and offer many possibilities to improve conventional imaging techniques. The number of transistors in the cell is similar than for the PCC, but the area of the cell has been reduced by a factor of $\sim$10. The chip is 3-side buttable which should permit the development of larger area arrays. However no effort has been made to deal with charge sharing issues as yet.

Photon counting pixel detector technology is a relatively recent and exciting development. The initial motivation for the work is described in this thesis and was focused on medical imaging. This work shows the potential of the technology for such applications, but many challenges remain. Larger areas should be covered and specific application areas in medical imaging should be identified. Closer contacts need to be established between the design team and the end users. It may be that such devices, while proving useful for medical applications, find markets faster in other fields.

List of Figures

List of Tables

Bibliography

[Aar93] P. A. Aarnio et al., *Electron-Photon Transport: Always so Good as we Think? Experience with Fluka*, CERN/TIS-RP **93-10** (1993). 7.1

[Ada97] R. L. Adams, *Growth of High Purity GaAs Using Low-Pressure Vapour-Phase Epitaxy*, Nucl. Instr. and Meth. A **395** (1997) 125–128. 63

[Alb94] W. G. Alberts et al., *Neue Dosis-Meßgrößen im Strahlenschutz*, Physikalisch-Technische Bundesanstalt Braunschweig, PTB-Dos-23, Juli 1994 (1994). 98

[Ale92] D. Alexiev and K. S. A. Butcher, *High Purity Liquid Phase Epitaxial Gallium Arsenide Nuclear Radiation Detector*, Nucl. Instr. and Meth. A **317** (1992) 111–115. 63

[Alf92] B. Alfano et al., *First X-ray Images with a Double-sided Microstrips Silicon Crystal. A Novel Detector for Digital Radiography?*, Phys. Med. Biol. **37 (5)** (1992) 1167–1170. 5.2

[Alf93] B. Alfano et al., *Digital Imaging in Radiology: Preliminary Results Obtained with a High Spatial Resolution 2D Silicon Detector*, IEEE Trans. Nucl. Sci. **40 (4)** (1993) 987–991. 80

[Ali95] M. Alietti et al., *Performance of a New Ohmic Contact for GaAs Particle Detectors*, Nucl. Instr. and Meth. A **362** (1995) 344–348. 90

[Ame96] S. R. Amendolia et al., *Use of Silicon and GaAs Pixel Detectors for Digital Autoradiography*, Nucl. Instr. and Meth. A **380** (1996) 410–413. 80

[Ame97] S. R. Amendolia et al., *Use of Silicon and GaAs Pixel Detectors for Digital Autoradiography*, IEEE Trans. Nucl. Sci. **44 (3)** (1997) 929–933. 80

[Ame98] S. R. Amendolia et al., *Charge Collection Properties of GaAs Detectors for Digital Radiography*, Physica Medica **XIV, Suppl. 2** (1998) 17–19. 88

[Ame00] S. R. Amendolia et al., *Test of a GaAs-Based Pixel Device for Digital Mammography*, Presented at the 1st International Workshop on Radiation Imaging Detectors, Sundsvall, Sweden, June 13-17 1999, submitted for publication in Nucl. Instr. and Meth. A (2000). 6.5

[Ang91] F. Anghinolfi et al., *A 1006 Element Hybrid Silicon Pixel Detector with Strobed Binary Output*, CERN/ECP **91-26** (1991). 5.2

[Arf96] F. Arfelli et al., *Digital Mammography at the Trieste Synchrotron Light Source*, IEEE Trans. Nucl. Sci. **43 (3)** (1996) 2061–2067. 21

[Asp76] D. E. Aspnes, *GaAs Lower Conduction-Band Minima: Ordering and Properties*, Physical Review B **14 (12)** (1976) 5331–5343. 57, 57, 58, 58

[ATL94] ATLAS collaboration, *ATLAS Technical Proposal for a General-Purpose pp Experiment at the Large Hadron Collider at CERN,* (1994), CERN/LHCC/**94-43**. 1

[Bar50] J. Bardeen and W. Shockley, *Deformation Potentials and Mobilities in Non-Polar Crystals*, Physical Review **80 (1)** (1950) 72–80. 4.1.1

[Bat90] G. Batignani et al., *A Detailed Monte Carlo Study of the Performance of a Silicon Crystal for X-ray Detection in the Diagnostic Energy Range*, Physica Medica **6** (1990) 39–44. 5.2

[Bat96] R. Bates et al., *Model of Charge Transport in Semi-Insulating Undoped GaAs Microstrip Detectors*, In P. G. Pelfer, J. Ludwig, K. Runge, and H. S. Rupprecht, editors, *Proc. of the 3rd International Workshop on Gallium Arsenide and Related Compounds, San Miniato, Italy, March 1995,* pages 92–104, World Scientific, (1996). 5.2

[Bat97] R. L. Bates et al., *Recent Results on GaAs Detectors*, Nucl. Instr. and Meth. A **392** (1997) 269–273. 5.2

[Bat98] R. L. Bates et al., *Characterisation of Low-Pressure VPE GaAs Diodes Before and After 24 GeV/c Proton Irradiation*, Nucl. Instr. and Meth. A **410** (1998) 46–53. 63

[Bat99] R. L. Bates et al., *Development of Low-Pressure Vapour-Phase Epitaxial GaAs for Medical Imaging*, Nucl. Instr. and Meth. A **434** (1999) 1–13. 63

[Bea94a] S. P. Beaumont et al., *First Results from GaAs Double-Sided Detectors*, Nucl. Instr. and Meth. A **348** (1994) 514–517. 5.2

[Bea94b] S. P. Beaumont et al., *Gallium Arsenide Charged Particle Detectors; Trapping Effects*, Nucl. Instr. and Meth. A **342** (1994) 83–89. 5.2

[Bek93] H. Beker et al., *A Hybrid Silicon Pixel Telescope Tested in a Heavy-Ion Experiment*, Nucl. Instr. and Meth. A **332** (1993) 188–201. 5.2

[Bel83] E. Belau et al., *Silicon Detectors with 5 μm Spatial Resolution for High Energy Particles*, Nucl. Instr. and Meth. A **217** (1983) 224–228. 5.1

[Ben91] W. Bencivelli et al., *Use of EGS4 for the Evaluation of the Performance of a Silicon Detector for X-ray Digital Radiography*, Nucl. Instr. and Meth. A **305** (1991) 574–580. 5.2

[Ben94] W. Bencivelli et al., *Comparison of Different GaAs Detectors for X-Ray Digital Radiography*, Nucl. Instr. and Meth. A **338** (1994) 549–555. 80

[Ber61] R. J. Berger, *The X- or Gamma-Ray Energy Absorption or Transfer Coefficient: Tabulations and Discussion*, Radiation Research **15** (1961) 1–29. 28

[Ber90] R. Bertin et al., *A Preliminary Study of GaAs Solid-State Detectors for High-Energy Physics*, Nucl. Instr. and Meth. A **294** (1990) 211–218. 61

[Ber95a] E. Bertolucci et al., *Electrical Characterization and Detection Performances of Various Semi-Insulating GaAs Crystals for Low Energy Gamma-Rays*, IEEE Trans. Nucl. Sci. **42 (4)** (1995) 254–257. 80

[Ber95b] E. Bertolucci et al., *X-Ray Imaging Using a Pixel GaAs Detector*, Nucl. Instr. and Meth. A **362** (1995) 547–550. 80

[Ber96] K. Berwick et al., *Correlation of the Charge Collection Efficiency of GaAs Particle Detectors with Material Properties*, Nucl. Instr. and Meth. A **380** (1996) 46–49. 68

[Ber97] G. Bertuccio, A. Pullia, J. Lauter, A. Förster, and H. Luth, *Pixel X-Ray Detectors in Epitaxial Gallium Arsenide with High-Energy Resolution Capabilities (Fano Factor Experimental Determination)*, IEEE Trans. Nucl. Sci. **44 (1)** (1997) 1–5. 61, 61, 63

[Beu98] E. Beuville et al., *An Application Specific Integrated Circuit and Data Acquisition System for Digital X-Ray Imaging*, Nucl. Instr. and Meth. A **406** (1998) 337–342. 21

[Bis98] M. G. Bisogni et al., *Performance of a 4096 Pixel Photon Counting Chip*, CERN-EP **98-162** (1998). 5.4, 95, 6.16, 7.3

[Bla82] J. S. Blakemore, *Semiconducting and Other Major Properties of Gallium Arsenide*, J. Appl. Phys. **53 (10)** (1982) R123–R180. 57, 57, 4.2, 4, 58, 59, 59, 61, 7.3

[Boo96] J. M. Boone and A. E. Chavez, *Comparison of X-ray Cross Sections for Diagnostic and Therapeutic Medical Physics*, Med. Phys. **23** (1996) 1997–2005. 2.1, 2.3, 2.1, 26, 2.5, 2.6, 7.3, 7.3

[Bou88] J. C. Bourgoin, H. J. von Bardeleben, and D. Stiévenard, *Native Defects in Gallium Arsenide*, J. Appl. Phys. **64 (9)** (1988) R65–R91. 68

[Bro99] C. Broennimann et al., *A Pixel Detector for the Protein Crystallography Beamline at the SLS*, Proceedings of the 5^{th} International Conference on Position-Sensitive Detectors, University College London, 13-17 September 1999, to appear in Nucl. Instr. and Meth. A (1999). 21

[Buc88] W. R. Buchwald and N. M. Johnson, *Revised Role for the Poole-Frenkel Effect in Deep-Level Characterization*, J. Appl. Phys. **64 (2)** (1988) 958–961. 72

[Bur95] E. Burattini et al., *Mammography with Synchrotron Radiation*, Radiology **195** (1995) 239–244. 5

[But97] C. M. Buttar, *GaAs Detectors - A Review*, Nucl. Instr. and Meth. A **395** (1997) 1–8. 70, 72, 4.9, 7.2.1, 7.3

[Cam89] M. Campbell et al., *A 10 MHz Micro Power CMOS Front-End for Direct Readout of Pixel Detectors*, CERN/EF **89-21** (1989). 1.5.7, 76

[Cam91] J. Camassel et al., *Investigation of Residual Impurity Content in GaAs Layers Grown by VPE Under Very Low Pressure Conditions*, J. of Electr. Materials **20 (1)** (1991) 79–90. 63

[Cam94] M. Campbell et al., *Development of a Pixel Read-Out Chip Compatible with Large Area Coverage*, Nucl. Instr. and Meth. A **342** (1994) 52–58. 5.2

[Cam98] M. Campbell, E. H. M. Heijne, G. Meddeler, E. Pernigotti, and W. Snoeys, *Readout for a 64 x 64 Pixel Matrix with 15-bit Single Photon Counting*, IEEE Trans. Nucl. Sci. **45 (3)** (1998) 751–753. 5.3

[Cam99] M. Campbell et al., *A Pixel Readout Chip for 10-30 MRad in Standard 0.25μm CMOS*, IEEE Trans. Nucl. Sci. **46 (3)** (1999) 156–160. 6

[Cas98] A. Castaldini, A. Cavallini, L. Polenta, C. Canali, and F. Nava, *Analysis of the Active Layer in SI GaAs Schottky Diodes*, Nucl. Instr. and Meth. A **410** (1998) 79–84. 71, 72, 4.10, 72, 7.2.1, 7.3

[Che76] J. R. Chelikowsky and M. L. Cohen, *Nonlocal Pseudopotential Calculations for the Electronic Structure of Eleven Diamond and Zinc-Blende Semiconductors*, Physical Review B **14 (2)** (1976) 556–582. 3.1, 57, 4.1, 7.3

[Che95] J. W. Chen et al., *Evaluation of Active Layer Properties and Charge Collection Efficiency of GaAs Particle Detectors*, Nucl. Instr. and Meth. A **365** (1995) 273–284. 5.2

[Che96] J. W. Chen et al., *Characterization of Interface States and Deep Levels by Impedance Measurements in Undoped Semi-Insultating GaAs*, In P. G. Pelfer, J. Ludwig, K. Runge, and H. S. Rupprecht, editors, *Proc. of the 3rd International Workshop on Gallium Arsenide and Related Compounds, San Miniato, Italy, March 1995,* pages 84–91, World Scientific, (1996). 5.2

[Chm99] V. Chmill et al., *Investigation of Epitaxial GaAs Charged Particle Detectors*, Nucl. Instr. and Meth. A **438** (1999) 362–367. 63

[Cho83] A. Y. Cho, *Growth of III-V Semiconductors by Molecular Beam Epitaxy and their Properties*, Thin Solid Films **100** (1983) 291–317. 63

[CMS] CMS Outreach Office, http://cmsdoc.cern.ch/cms/TRIDAS/html/cmsdoc.html. 1, 7.3

[CMS94] CMS collaboration, *CMS Technical Proposal,* (1994), CERN/LHCC/**94-38**. 1

[Col97a] A. Cola, L. Reggiani, and L. Vasanelli, *Field-Assisted Capture of Electrons in Semi-Insulating GaAs*, J. Appl. Phys. **81 (2)** (1997) 997–999. 72

[Col97b] C. Colledani et al., *Castor 1.0, a VLSI Analog-Digital Circuit for Pixel Imaging Applications*, Nucl. Instr. and Meth. A **395** (1997) 435–442. 21

[Con50] E. Conwell and V. F. Weisskopf, *Theory of Impurity Scattering in Semiconductors*, Physical Review **77 (3)** (1950) 388–390. 4.1.1

[Con93] M. Conti et al., *A Transputer-Based 'List mode' Parallel System for Digital Radiography with 2D Silicon Detectors*, IEEE Trans. Nucl. Sci. **40 (4)** (1993) 996–1000. 80

[Cow97] A. R. Cowen, G. J. S. Parkin, and P. Hawkridge, *Direct Digital Mammography Image Acquisition*, Eur.Radiol. **7** (1997) 918–930. 20, 1.5.6.2, 13

[D'A95] C. D'Ambrosio, T. Gys, H. Leutz, D. Piedigrossi, and D. Puertolas, *First Beam Exposures of a Scintillating Fibre Tracker Read out by an ISPA-Tube*, Nucl. Instr. and Meth. A **359** (1995) 618–621. 5.2

[Dab89] J. Dabrowski and M. Scheffler, *Isolated Arsenic-Antisite Defect in GaAs and the Properties of EL2*, Physical Review B **40 (15)** (1989) 10391–10401. 68

[Dan81] D. R. Dance and R. Davis, *Simulation of Mammography by Monte Carlo Calculation - The Dependence of Radiation Dose, Scatter and Noise on Photon Energy*, In G. Drexler, H. Eriskat, and H. Schibilla, editors, *Patient Exposure to Radiation in Medical X-Ray Diagnosis,* pages 227–243, EUR7438, (1981). 7, 1.2, 17, 7.3

[Dav] *Davinci 1998.4.1*, Avant! Corporation, California; http://www.avanticorp.com/. 7.2

[DaV94] C. DaVia', M. Campbell, E. H. M. Heijne, P. Middelkamp, and G. Stefanini, *A Hybrid Pixel Detector for Readout of Scintillating Fibres*, CERN/ECP **94-10** (1994), Presented at the 27th International Conference on High Energy Physics, Glasgow, Scotland, 20-27 July 1994. 5.2

[DaV95a] C. DaVia', M. Campbell, E. H. M. Heijne, P. Middelkamp, and G. Stefanini, *Experimental Results Using a Hybrid Silicon Pixel Detector for Scintillating Fibre Readout and X-Ray Imaging*, IEEE Trans. Nucl. Sci. **42 (4)** (1995) 409–412. 5.2

[DaV95b] C. DaVia', M. Campbell, E. H. M. Heijne, and G. Stefanini, *Imaging of Visible Photons Using Hybrid Silicon Pixel Detectors*, Nucl. Instr. and Meth. A **355** (1995) 414–419. 5.2

[DaV97a] C. DaVia', *Semiconductor Pixel Detectors for Imaging Applications*, Doctoral Thesis at the Department of Physics and Astronomy of the University of Glasgow, Scotland (1997). 5.2

[DaV97b] C. DaVia' et al., *Gallium Arsenide Pixel Detectors for Medical Imaging*, Nucl. Instr. and Meth. A **395** (1997) 148–151. 80

[Del87] C. Delerue, M. Lannoo, D. Stiévenard, H. J. von Bardeleben, and J. C. Bourgoin, *Metastable State of EL2 in GaAs*, Phys. Rev. Lett. **59 (25)** (1987) 2875–2878. 68

[Die89] B. Dierickx, *XYW Detector: A Smart Two-Dimensional Particle Sensor*, Nucl. Instr. and Meth. A **275** (1989) 542–544. 76

[Dob95] J. T. Dobbins, *Effects of Undersampling on the Proper Interpretation of Modulation Transfer Function, Noise Power Spectra, and Noise Equivalent Quanta of Digital Imaging Systems*, Med. Phys. **22 (2)** (1995) 171–181. 11, 1.1.5

[Ebe70] J. E. Eberhardt, R. D. Ryan, and A. J. Tavendale, *High-Resolution Nuclear Radiation Detectors from Epitaxial n-GaAs*, Appl. Phys. Lett. **17 (10)** (1970) 427–429. 61

[Ebe71] J. E. Eberhardt, R. D. Ryan, and A. J. Tavendale, *Evaluation of Epitaxial n-GaAs for Nuclear Radiation Detection*, Nucl. Instr. and Meth. **94** (1971) 463–476. 61, 62, 63, 88

[Ebi] G. Williams, *Electron Binding Energies*, http://xray.uu.se/hypertext/-EBindEnergies.html. 2.1, 7.3

[EGS85] W. R. Nelson, H. Hirayama, and D. W. O. Rogers, *The EGS4 code system,* (1985), SLAC-**265**. 7.1

[Ehr60] H. Ehrenreich, *Band Structure and Electron Transport of GaAs*, Physical Review **120 (6)** (1960) 1951–1963. 60

[Eva55] R. D. Evans, *The Atomic Nucleus*, McGraw-Hill, New York (1955). 2.1, 2.1, 7.3

[Eva58] R. D. Evans, *Compton Effect*, In S. Flügge, editor, *Handbuch der Physik,* volume 34, pages 218–298, Springer-Verlag (1958). 23, 23

[Far95] A. R. Faruqi, H. N. Andrews, and R. Henderson, *A High Sensitivity Imaging Detector for Electron Microscopy*, Nucl. Instr. and Meth. A **367** (1995) 408–412. 1.5.3

[Far00] A. R. Faruqi and S. Subramaniam, *CCD Detectors in High Resolution Biological Electron Microscopy*, to be published in Quart.Rev.Biophys. (2000). 1.5.3

[Fis99] P. Fischer et al., *A Counting Pixel Chip and Sensor System for X-ray Imaging*, IEEE Trans. Nucl. Sci. **46 (4)** (1999) 1070–1074. 21

[Flu] A. Fassò, A. Ferrari, P. Sala, J. Ranft, et al., http://AliSoft.cern.ch/offline/. 7.1

[Fos97] E. R. Fossum, *CMOS Image Sensors: Electronic Camera-On-A-Chip*, IEEE Trans. on Electron Devices **44 (10)** (1997) 1689–1698. 1.5.7

[Fra96] C. Frank, K. Hein, C. Hannig, and G. Gärtner, *Growth of GaAs Crystals by VGF at Different As Source Temperatures*, Cryst. Res. Technol. **31 (6)** (1996) 753–761. 66

[Fre38] J. Frenkel, *On Pre-Breakdown Phenomena in Insulators and Electronic Semi-Conductors*, Physical Review **54** (1938) 647–648. 72

[Fre97] R. Freifelder and J. S. Karp, *Dedicated PET Scanners for Breast Imaging*, Phys. Med. Biol. **42** (1997) 2463–2480. 5

[Fro98] C. Froejdh and P. Nelvig, *Performance Criteria for X-Ray Imaging Sensors*, Physica Medica **XIV** (1998) 10–12, (Suppl. 2). 1.1.2, 10, 11

[Ful76] E. G. Fuller and E. Hayward, *Photonuclear Reactions*, Dowden, Hutchinson & Ross, Stroudsburg, Pennsylvania (1976). 22

[Gal00a] O. Gal et al., *CARTOGAM - A Portable Gamma Camera for Remote Localisation of Radioactive Sources in Nuclear Facilities*, Presented at the 1st International Workshop on Radiation Imaging Detectors, Sundsvall, Sweden, June 13-17 1999, submitted for publication in Nucl. Instr. and Meth. A (2000). 6.4.2.2, 6.27, 7.3

[Gal00b] O. Gal, B. Mikulec, and M. Million, *Experimental Tests of a Hybrid Pixellated Detector for Gamma Imaging*, Presented at the 1st International Workshop on Radiation Imaging Detectors, Sundsvall, Sweden, June 13-17 1999, submitted for publication in Nucl. Instr. and Meth. A (2000). 6.4.2.2, 6.28, 6.4.2.2, 6.29, 7.3

[Gam95] M. Gambaccini, A. Taibi, A. D. Guerra, F. Frontera, and M. Marziani, *Narrow Energy Band X-Rays via Mosaic Crystal for Mammography Application*, Nucl. Instr. and Meth. A **365** (1995) 248–254. 2

[Gat84] E. Gatti and P. Rehak, *Semiconductor Drift Chamber - an Application of a Novel Charge Transport Scheme*, Nucl. Instr. and Meth. A **225** (1984) 608–614. 5.1

[Gau86] W. A. Gault, E. M. Monberg, and J. E. Clemans, *A Novel Application of the Vertical Gradient Freeze Method to the Growth of High Quality III-V Crystals*, J. of Crystal Growth **74** (1986) 491–506. 66

[Gep98] R. Geppert, *Pixelsysteme für die Röntgendiagnostik*, Doctoral Thesis at the Albert-Ludwigs-Universität, Freiburg i. Brsg., Germany (1998). 11, 1.4

[Gla95] F. Glasser et al., *Preliminary Characterizations of a New Hybrid CdTe Structure for X-Ray Dental Imaging*, In R. L. VanMetter and J. Beutel, editors, *SPIE Proceedings, Medical Imaging, San Diego, California, 26-27 February 1995, Vol. 2432,* pages 442–453 (1995). 97

[Gui57] A. Guinier et al., *Strukturforschung*, In S. Flügge, editor, *Handbuch der Physik,* volume 32, Springer-Verlag (1957). 6.4.2.1

[Gun63] J. B. Gunn, *Microwave Oscillations of Current in III-V Semiconductors*, Solid State Commun. **1** (1963) 88–91. 61

[Gys95] T. Gys, C. D'Ambrosio, H. Leutz, D. Piedigrossi, and D. Puertolas, *A New Position-Sensitive Photon Detector Based on an Imaging Silicon Pixel Array (ISPA-tube)*, Nucl. Instr. and Meth. A **355** (1995) 386–389. 5.2

[Hal59] R. N. Hall, *Recombination Processes in Semiconductors*, Proc. IEE **106B** (1959) 923–931, (Suppl. 17). 61

[Ham99] M. Hammadi, J. C. Bourgoin, and H. Samic, *Mechanism of GaAs Transport by Water Reaction Application to the Growth of Thick Epitaxial Layers*, J. of Materials Science: Materials in Electronics **10** (1999) 1–4. 64

[han] http://www.resonance-pub.com/wroentgen.htm. 1.1, 7.3

[Har56] W. A. Harrison, *Mobility in Zinc Blende and Indium Antimonide*, Physical Review **101** (1956) 903. 60

[Har88] R. M. Harrison, *Digital Radiography*, Phys. Med. Biol. **33 (7)** (1988) 751–784. 1.5.4

[Hei80] E. H. M. Heijne et al., *A Silicon Surface Barrier Microstrip Detector Designed for High Energy Physics*, Nucl. Instr. and Meth. **178** (1980) 331–343. 5.1

[Hei83] E. H. M. Heijne, *Muon Flux Measurement with Silicon Detectors in the CERN Neutrino Beams*, CERN Yellow Report **83-06** (1983). 54

[Hei88] E. H. M. Heijne, P. Jarron, A. Olsen, and N. Redaelli, *The Silicon Micropattern Detector: a Dream?*, Nucl. Instr. and Meth. A **273** (1988) 615–619. 76

[Hei89] E. H. M. Heijne and P. Jarron, *Development of Silicon Pixel Detectors: an Introduction*, Nucl. Instr. and Meth. A **275** (1989) 467–471, also published in CERN/EF **88-14** (1988). 5.2

[Hei90] E. H. M. Heijne et al., *Development of Hybrid and Monolithic Silicon Micro-Pattern Detectors*, CERN DRDC **90-81** (1990), R&D Proposal. 5.2

[Hei93a] E. H. M. Heijne, *Imaging with 2D and 3D Integrated Semiconductor Detectors Using VLSI Technology*, Physica Medica **IX (2-3)** (1993) 109–114, also published in CERN/ECP **92-25** (1992). 5.2

[Hei93b] E. H. M. Heijne et al., *RD19: Status Report and Addendum; Development of Hybrid and Monolithic Silicon Micropattern Detectors*, CERN DRDC **93-6** (1993). 5.2

[Hei94] E. H. M. Heijne et al., *First Operation of a 72k Element Hybrid Silicon Micropattern Pixel Detector Array*, Nucl. Instr. and Meth. A **349** (1994) 138–155. 5.2

[Hei96] E. H. M. Heijne et al., *LHC1: A Semiconductor Pixel Detector Readout Chip with Internal, Tunable Delay Providing a Binary Pattern of Selected Events*, Nucl. Instr. and Meth. A **383** (1996) 55–63. 5.2, 81

[Hen91] R. L. Henry, P. E. R. Nordquist, R. J. Gorman, and S. B. Qadri, *Growth of (100) GaAs by Vertical Zone Melting*, J. of Crystal Growth **109** (1991) 228–233. 66

[Hen96] R. L. Henry, P. E. R. Nordquist, R. J. Gorman, J. S. Blakemore, and W. J. Moore, *Zone Melt Growth of GaAs for Gamma Ray Detector Applications*, Nucl. Instr. and Meth. A **380** (1996) 30–35. 66

[Hol82] D. E. Holmes, R. T. Chen, K. R. Elliott, and C. G. Kirkpatrick, *Stoichiometry-Controlled Compensation in Liquid Encapsulated Czochralski GaAs*, Appl. Phys. Lett. **40 (1)** (1982) 46–48. 68, 4.6, 7.3

[Hol89] S. Holland, *Fabrication of Detectors and Transistors on High-Resistivity Silicon*, Nucl. Instr. and Meth. A **275** (1989) 537–541. 76

[Hor80] P. Horowitz and W. Hill, *The Art of Electronics*, pages 437–440, Cambridge University Press, (1980). 82

[Hub79] J. H. Hubbell and I. Øverbø, *Relativistic Atomic Form Factors and Photon Coherent Scattering Cross Sections*, J. Phys. Chem. Ref. Data **8 (1)** (1979) 69–105. 2.3

[Hum97] G. Humpston and A. P. Needham, *Advanced Flip-Chip Soder Bonding*, Nucl. Instr. and Meth. A **395** (1997) 375–378. 81

[Hwa72] C. J. Hwang, *Quantum Efficiency and Radiative Lifetime of the Band-to-Band Recombination in Heavily Doped n-Type GaAs*, Physical Review B **6 (4)** (1972) 1355–1359. 61

[Irs96] R. Irsigler et al., *LPE-GaAs Radiation Detectors*, In P. G. Pelfer, J. Ludwig, K. Runge, and H. S. Rupprecht, editors, *Proc. of the 3rd International Workshop on Gallium Arsenide and Related Compounds, San Miniato, Italy, March 1995,* pages 10–16, World Scientific, (1996). 63

[Irs97] R. Irsigler et al., *Influence of Contacts and Substrate on Semi-Insulating GaAs Detectors*, Nucl. Instr. and Meth. A **395** (1997) 71–75. 91

[Jon82] C. H. Jones, *Methods of Breast Imaging*, Phys. Med. Biol. **27 (4)** (1982) 463–499. 17

[Kem80] J. Kemmer, *Fabrication of Low Noise Silicon Radiation Detectors by the Planar Process*, Nucl. Instr. and Meth. A **169** (1980) 499–502. 76

[Kem84] J. Kemmer, *Improvement of Detector Fabrication by the Planar Process*, Nucl. Instr. and Meth. A **226** (1984) 89–93. 76

[Ken94] C. Kenney et al., *A Prototype Monolithic Pixel Detector*, Nucl. Instr. and Meth. A **342** (1994) 59–77. 76

[Kle29] O. Klein and Y. Nishina, *Über die Streuung von Strahlung durch freie Elektronen nach der neuen relativistischen Quantendynamik von Dirac*, ZS. f. Physik **52** (1929) 853–868. 23

[Kno89] G. F. Knoll, *Radiation Detection and Measurement*, John Wiley & Sons, second edition (1989). 61, 62

[Kob72] T. Kobayashi, T. Sugita, M. Koyama, and S. Takayanagi, *Performance of GaAs Surface-Barrier Detectors Made from High-Purity Gallium Arsenide*, IEEE Trans. Nucl. Sci. **19 (3)** (1972) 324–333. 61, 62

[Kra93] W. Krampla, G. Oberhauser, H. Mosser, and W. Hruby, *Klinische Erfahrungen im digitalen Röntgeninstitut*, Österreichische Krankenhaus-Zeitung - Sonderfolge Radiologie **34** (1993) 7–9. 1.3

[Kre90] R. E. Kremer, D. Francomano, G. H. Beckhart, and K. M. Burke, *Low Dislocation Density GaAs Grown by the Vertical Bridgman Technique*, J. Mater. Res. **5 (7)** (1990) 1468–1474. 66

[Kub94] T. Kubicki et al., *Calculation of the Electric Field in GaAs Particle Detectors*, Nucl. Instr. and Meth. A **345** (1994) 468–473. 71

[Lag82] J. Lagowski et al., *Origin of the 0.82-eV Electron Trap in GaAs and its Annihilation by Shallow Donors*, Appl. Phys. Lett. **40 (4)** (1982) 342–344. 68

[Leo87] W. R. Leo, *Techniques for Nuclear and Particle Physics Experiments*, Springer-Verlag (1987). 2.1, 30, 9, 31, 32

[Lew97] R. Lewis, *Medical Applications of Synchrotron Radiation X-Rays*, Phys. Med. Biol. **42** (1997) 1213–1243. 13, 8

[LHC98] LHCb collaboration, *LHCb Technical Proposal,* (1998), CERN LHCC 98-4. 5.2

[Mal00] T. Mali, V. Cindro, and M. Mikuž, *Silicon Microstrip Detectors for Digital Mammography - Evaluation and Spatial Resolution Study*, Presented at the 1st International Workshop on Radiation Imaging Detectors, Sundsvall, Sweden, June 13-17 1999, submitted for publication in Nucl. Instr. and Meth. A (2000). 21

[Man99a] S. Manolopoulos et al., *X-ray Imaging with Photon Counting Hybrid Semiconductor Pixel Detectors*, Nucl. Instr. and Meth. A **434** (1999) 38–43. 6.5, 101

[Man99b] S. Manolopoulos et al., *X-ray Powder Diffraction with Hybrid Semiconductor Pixel Detectors*, J. Synchrotron Rad. **6** (1999) 112–115. 99, 6.23, 7.3

[Man99c] V. Manzari et al., *Silicon Pixel Detectors for Tracking in NA57*, Nuclear Physics A **661** (1999) 716c–720c. 5.2

[Mar77] G. M. Martin, A. Mitonneau, and A. Mircea, *Electron Traps in Bulk and Epitaxial GaAs Crystals*, Electronics Letters **13 (7)** (1977) 191–193. 68

[Mar80] G. M. Martin, J. P. Farges, G. Jacob, J. P. Hallais, and G. Poiblaud, *Compensation Mechanisms in GaAs*, J. Appl. Phys. **51 (5)** (1980) 2840–2852. 68

[Mar82] G. M. Martin et al., *Oxygen-Related Gettering of Silicon During Growth of Bulk GaAs Bridgman Crystals*, J. Phys. C: Solid State Phys. **15** (1982) 1841–1856. 66

[McG92] D. S. McGregor, G. F. Knoll, Y. Eisen, and R. Brake, *Development of Bulk GaAs Room Temperature Radiation Detectors*, IEEE Trans. Nucl. Sci. **39 (5)** (1992) 1226–1236. 61, 70, 72

[McG94a] D. S. McGregor, *Evidence for Field Enhanced Electron Capture by EL2 Centers in Semi-Insulating GaAs and the Effect on GaAs Radiation Detectors*, J. Appl. Phys. **75 (12)** (1994) 7910–7915. 70, 4.7, 72, 7.3

[McG94b] D. S. McGregor et al., *Present Status of Undoped Semi-Insulating LEC bulk GaAs as a Radiation Spectrometer*, Nucl. Instr. and Meth. A **343** (1994) 527–538. 61, 70, 91

[McG95] D. S. McGregor and J. E. Kammeraad, *Gallium Arsenide Radiation Detectors and Spectrometers*, In T. E. Schlesinger and R. B. James, editors, *Semiconductors for Room Temperature Nuclear Detector Applications,* volume 43, pages 383–442, Academic Press (1995). 4, 63, 68, 70, 16, 72

[McG96a] D. S. McGregor et al., *Comparison of Vertical Gradient Freeze Bulk GaAs and Custom Grown Vertical Zone Melt Bulk GaAs as Radiation Spectrometers*, Nucl. Instr. and Meth. A **380** (1996) 165–168. 66

[McG96b] D. S. McGregor et al., *Material Analysis and Characterization on Zone Refined and Zone Leveled Vertical Zone Melt GaAs for Radiation Spectrometers*, Nucl. Instr. and Meth. A **380** (1996) 84–87. 66

[Mei99] D. Meier, *CVD Diamond Sensors for Particle Detection and Tracking*, Doctoral Thesis at the Ruprecht-Karls-Universität Heidelberg, Germany (1999). 3.1, 7.3

[Mik99] B. Mikulec, M. Campbell, G. Dipasquale, C. Schwarz, and J. Watt, *Characterisation of a Single Photon Counting Pixel System for Imaging of Low-Contrast Objects*, CERN-EP **99-167** (1999), Presented at the 11th International Workshop on Room Temperature Semiconductor X- and Gamma-Ray Detectors and Associated Electronics, Vienna, Austria, 11-15 October 1999, accepted for publication in NIM A. 5, 6.3

[Mil99] M. Million, *Conception d'un Détecteur Gamma Haute Énergie en Semi-Conducteur pour Cartographie Gamma*, Doctoral Thesis at the Université Paris 7, Paris, France (1999). 6.4.2.2, 6.26, 6.4.2.2, 100, 7.3

[Mis92] M. Missous, *Uniformity of Improved High-Quality GaAs and AlGaAs Epilayers and Schottky Barriers Prepared by Molecular Beam Epitaxy*, Semicond. Sci. Technol. **7** (1992) A249–A254. 63

[Miy84] S. Miyazawa, T. Honda, Y. Ishii, and S. Ishida, *Improvement of Crystal Homogeneities in Liquid-Encapsulated Czochralski Grown, Semi-Insulating GaAs by Heat Treatment*, Appl. Phys. Lett. **44 (4)** (1984) 410–412. 65

[Mo96] L. Mo, K. S. A. Butcher, and D. Alexiev, *Effect of Crucible Materials on Impurities in LPE GaAs*, J. of Crystal Growth **158** (1996) 403–408. 66

[Moo65] G. E. Moore, *Cramming More Components onto Integrated Circuits*, Electronics **38 (8)** (1965) 114–117. 74

[Moo96] W. J. Moore, R. L. Henry, and P. E. R. Nordquist, *Properties of Gallium Arsenide Purified by Zone Refining and Zone Levelling*, Nucl. Instr. and Meth. A **380** (1996) 102–106. 66

[Nav97] F. Nava et al., *Improved performance of GaAs Radiation Detectors with Low Temperature Ohmic Contacts*, IEEE Trans. Nucl. Sci. **44 (3)** (1997) 943–949. 70, 4.8, 7.3

[Nis] J. H. Hubbell and S. M. Seltzer, *Tables of X-Ray Mass Attenuation Coefficients and Mass Energy-Absorption Coefficients*, http://physics.nist.gov/PhysRefData/XrayMassCoef/-cover.html. 13, 99, 7.1, 7.1, 7.1.1, 104, 7.3

[Oml88] P. Omling, P. Silverberg, and L. Samuelson, *Identification of a Second Energy Level of EL2 in n-Type GaAs*, Physical Review B **38 (5)** (1988) 3606–3609. 68

[Ove69] R. Van Overstraeten and F. Van de Wiele, *Introduction to Quantum Physics of Electronics, Part II* (1969), L. Wouters, Leuven. 45

[Par89] S. Parker, *A Proposed VLSI Pixel Device for Particle Detection*, Nucl. Instr. and Meth. A **275** (1989) 494–516. 76

[Pat93] E. M. Paterok, H. Rosenthal, S. Richter, and M. Säbel, *Occult Calcified Breast Lesions*, Eur. Radiol. **3** (1993) 138–144. 5, 7

[Ped97] F. Pedersen, C. Rönnqvist, K. Fransson, L. Gustafsson, and S. Kullander, *Energy Discrimination with an X-Ray Pixel Detector - a Monte-Carlo Simulation*, Nucl. Instr. and Meth. A **395** (1997) 443–447. 17

[Pen96] F. X. Pengg, *Monolithic Silicon Pixel Detectors in SOI Technology*, Doctoral Thesis at the Institute for Semiconductor Physics of the Johannes Kepler Universität Linz, Austria (1996). 78

[Phi60] F. C. Phillips, *An Introduction to Crystallography*, Longmans (1960). 6.4.2.1

[Pit70] G. D. Pitt and J. Lees, *Electrical Properties of the GaAs X_{1C} Minima at Low Electric Fields from a High-Pressure Experiment*, Physical Review B **2 (10)** (1970) 4144–4160. 57, 61

[Piz93] R. J. Pizzutiello and J. E. Cullinan, *Medical Radiographic Imaging*, Eastman Kodak Company (1993). 18, 1.5, 7.3

[Pri83] V. Y. Prinz and S. N. Rechkunov, *Influence of a Strong Electric Field on the Carrier Capture by Nonradiative Deep-Level Centers in GaAs*, phys. stat. sol. (b) **118** (1983) 159–166. 72, 4.11, 7.3

[Pue95] D. Puertolas et al., *An ISPA-Camera for Gamma Rays*, IEEE Trans. Nucl. Sci. **42 (6)** (1995) 2221–2228. 5.2

[Pue96] D. Puertolas, D. Piedigrossi, H. Leutz, T. Gys, and C. D'Ambrosio, *An ISPA Camera for Beta Radiography*, IEEE Trans. Nucl. Sci. **43 (5)** (1996) 2477–2487. 5.2

[Pue97] D. Puertolas et al., *Biomedical Applications of an Imaging Silicon Pixel Array (ISPA) tube*, Nucl. Instr. and Meth. A **387** (1997) 134–136. 5.2

[Qua96] A. A. Quaranta et al., *Analysis of the Output Signal Waveform and Performances of Semi-Insulating GaAs Particle Detectors*, Nucl. Instr. and Meth. A **380** (1996) 201–204. 93, 6.6, 7.3

[Rah99] J. T. Rahn et al., *High Resolution X-Ray Imaging Using Amorphous Silicon Flat-Panel Arrays*, IEEE Trans. Nucl. Sci. **46 (3)** (1999) 457–461. 20

[Ram39] S. Ramo, *Currents Induced by Electron Motion*, Proc. I.R.E. **27** (1939) 584–585. 93, 105

[RD893] *Status Report of the RD-8 Collaboration,* (1993), CERN/DRDC 93-37. 5.2

[RD895] *Status Report of the RD-8 Collaboration,* (1995), CERN/LHCC 95-57. 5.2

[Reh86] P. Rehak et al., *Progress in Semiconductor Drift Detectors*, Nucl. Instr. and Meth. A **248** (1986) 367–378. 5.1

[Rei99] C. Reichel, W. Siegel, and G. Kühnel, *Spatial Variation of Activation Energy in Undoped High-Resistivity Bulk GaAs*, J. Appl. Phys. **85 (2)** (1999) 912–915. 66

[Reu83] U. Reus and W. Westmeier, *Catalog of Gamma-Rays from Radioactive Decays*, Atomic Data and Nuclear Data Tables **29 (2)** (1983) 398. 9

[Roe95] W. C. Röntgen, *Über eine neue Art von Strahlen* (1895), Aus den Sitzungsberichten der Würzburger Physik.-medic. Gesellschaft, vorläufige Mittheilung vom 28.12.1895. 1

[Roe96] C. Roennqvist et al., *A 64-Channel Pixel Readout Chip for Dynamic X-Ray Imaging*, Presented at the 1996 IEEE Nuclear Science Symposium and Medical Imaging Conference, Anaheim, CA, 1996 (1996). 21

[Rog96] M. Rogalla et al., *Characterization of Semi-Insulating GaAs for Detector Application*, Nucl. Instr. and Meth. A **380** (1996) 14–17. 68, 5.2

[Rog98a] M. Rogalla, *Systematic Investigation of Gallium Arsenide Radiation Detectors for High Energy Physics Experiments*, Doctoral Thesis, Shaker Verlag (1998). 66, 4.5, 91, 91, 7.3

[Rog98b] M. Rogalla et al., *The Impact of Deep Acceptors on the Performance of VPE-GaAs X-Ray Detectors*, Nucl. Instr. and Meth. A **410** (1998) 92–95. 63

[Rog99] M. Rogalla and K. Runge, *Formation of a Quasi-Neutral Region in Schottky Diodes Based on Semi-Insulating GaAs and the Influence of the Compensation Mechanism on the Particle Detector Performance*, Nucl. Instr. and Meth. A **434** (1999) 44–56. 68

[Rop00] I. Ropotar, *An Investigation of Silicon Pixel Tracking Detectors and their Application in a Prototype Vertex Telescope in the CERN NA50 Heavy-Ion Experiment*, Doctoral Thesis at the Bergischen Universität Gesamthochschule Wuppertal, Germany, WUB-DIS 99-20, http://www.uni-wuppertal.de/FB8/groups/Drees/doktor/ (2000). 5.2, 88, 89, 6.3

[RPO] *Radiological Protection Ordinance*, The Swiss Federal Council, Annex 3, 22 June 1994. 98, 12

[Rub84] E. Rubenstein, *Medical Imaging with Synchrotron Radiation*, Nucl. Instr. and Meth. **222** (1984) 302–307. 13

[Rub95] E. Rubenstein, J. C. Giacomini, H. J. Gordon, J. A. L. Rubenstein, and G. Brown, *Xenon K-Edge Dichromographic Bronchography: Synchrotron Radiation Based Medical Imaging*, Nucl. Instr. and Meth. A **364** (1995) 360–361. 14

[Ruc68] J. G. Ruch and G. S. Kino, *Transport Properties of GaAs*, Physical Review **174 (3)** (1968) 921–931. 61

[Rya72] R. D. Ryan and J. E. Eberhardt, *Hole Diffusion Length in High Purity n-GaAs*, Solid-State Electronics **15** (1972) 865–868. 61, 61

[Sae96] M. Saebel and H. Aichinger, *Recent Developments in Breast Imaging*, Phys. Med. Biol. **41** (1996) 315–368. 17

[San92] M. Sandborg and G. Alm Carlsson, *Influence of X-ray Energy Spectrum, Contrasting Detail and Detector on the Signal-to-Noise Ratio (SNR) and Detective Quantum Efficiency (DQE) in Projection Radiography*, Phys. Med. Biol. **37 (6)** (1992) 1245–1263. 9

[Sch39] W. Schottky, *Zur Halbleitertheorie der Sperrschicht- und Spitzengleichrichter*, ZS. f. Physik **113** (1939) 367–414. 3.5.2

[Sch97] L. H. H. Scharfetter, *Active Pixel Detectors for the Large Hadron Collider*, Doctoral Thesis at the Institute of Experimental Physics of the Leopold Franzens Universität Innsbruck, Austria (1997). 76, 5.1, 5.2, 5.3, 7.3

[Sch99] C. Schwarz et al., *X-ray Imaging Using a Hybrid Photon Counting GaAs Pixel Detector*, Nucl. Phys. B (Proc. Suppl.) **78** (1999) 491–496. 96, 6.18, 7.3

[Seg77] E. Segrè, *Nuclei and Particles*, Addison-Wesley Publishing Company, Inc., second edition (1977). 2.1, 9

[Sei96] M. Seifert et al., *Studies on Correlation Between the Quality of GaAs LEC Crystals and the Inert Gas Pressure*, J. of Crystal Growth **158** (1996) 409–417. 66

[Sel74] D. D. Sell, H. C. Casey Jr., and K. W. Wecht, *Concentration Dependence of the Refractive Index for n- and p-type GaAs between 1.2 and 1.8 eV*, J. Appl. Phys. **45 (6)** (1974) 2650–2657. 56, 56, 57

[Sel99] P. Seller et al., *Two Approaches to Hybrid X-Ray Pixel Array Readout*, In G. W. Fraser, E. M. Westbrook, and G. E. Derbyshire, editors, *Detectors for Crystallography and Diffraction Studies at Synchrotron Sources,* volume 3774, pages 30–37, Proc. SPIE (1999). 21

[Sha89] S. L. Shapiro, W. M. Dunwoodie, J. F. Arens, J. G. Jernigan, and S. Gaalema, *Silicon PIN Diode Array Hybrids for Charged Particle Detection*, Nucl. Instr. and Meth. A **275** (1989) 580–586. 76

[Sho52] W. Shockley and J. W. T. Read, *Statistics of the Recombinations of Holes and Electrons*, Physical Review **87** (1952) 835–842. 41

[Sie97] W. Siegel, S. Schulte, G. Kühnel, and J. Monecke, *Hall Mobility Lowering in Undoped n-Type Bulk GaAs Due to Cellular-Structure Related Nonuniformities*, J. Appl. Phys. **81 (7)** (1997) 3155–3159. 66

[Smi80] P. M. Smith, M. Inoue, and J. Frey, *Electron Velocity in Si and GaAs at Very High Electric Fields*, Appl. Phys. Lett. **37 (9)** (1980) 797–798. 61

[Smi96] K. M. Smith, *GaAs Detector Status*, Nucl. Instr. and Meth. A **383** (1996) 75–80. 5.2

[Smi00] K. M. Smith, private communication, (2000). 63

[Sno92] W. Snoeys, *A New Integrated Pixel Detector for High Energy Physics*, Doctoral Thesis at Stanford University, California (1992). 76

[Sno94] W. Snoeys, J. D. Plummer, S. Parker, and C. Kenney, *PIN Detector Arrays and Integrated Readout Circuitry on High-Resistivity Float-Zone Silicon*, IEEE Trans. on Electron Devices **41 (6)** (1994) 903–912. 76

[Sno00] W. Snoeys et al., *Layout Techniques to Enhance the Radiation Tolerance of Standard CMOS Technologies Demonstrated on a Pixel Detector Readout Chip*, Nucl. Instr. and Meth. A **439** (2000) 349–360. 6

[Squ95] M. R. Squillante and K. S. Shah, *Other Materials: Status and Prospects*, In T. E. Schlesinger and R. B. James, editors, *Semiconductors for Room Temperature Nuclear Detector Applications,* volume 43, pages 465–491, Academic Press (1995). 14

[Sta71] C. V. Starodubtsev, ВЗАИМОДЕЙСТВИЕ ГАММА-ИЗЛУЧЕНИЯ С ВЕЩЕСТВОМ, АКАДЕМИЯ НАУК УЗБЕКСКОЙ ССР, ТАШКЕНТ (1971). 2.1

[Ste84] R. M. Sternheimer, M. J. Berger, and S. M. Seltzer, *Density Effect for the Ionization Loss of Charged Particles in Various Substances*, Atomic Data and Nuclear Data Tables **30** (1984) 261–271. 31, 3.1, 57, 7.3

[Sti70] G. E. Stillman, C. M. Wolfe, and J. O. Dimmock, *Hall Coefficient Factor for Polar Mode Scattering in n-Type GaAs*, J. Phys. Chem. Solids **31** (1970) 1199–1204. 4.1.1

[Str65] M. E. Straumanis and C. D. Kim, *Phase Extent of Gallium Arsenide Determined by the Lattice Constant and Density Method*, Acta Cryst. **19** (1965) 256–259. 55, 57

[Stu62] M. D. Sturge, *Optical Absorption of Gallium Arsenide between 0.6 and 2.75 eV*, Physical Review **127 (3)** (1962) 768–773. 56

[Swi89] E. M. Swiggard, *Liquid Encapsulated Vertical Zone Melt (VZM) Growth of GaAs Crystals*, J. of Crystal Growth **94** (1989) 556–558. 66

[Sze81] S. M. Sze, *Physics of Semiconductor Devices*, John Wiley & Sons, second edition (1981). 3.1, 3.1, 3.2, 3.2, 54, 56, 57, 61, 7.3, 7.3

[Sze85] S. M. Sze, *Semiconductor Devices, Physics and Technology*, John Wiley & Sons (1985). 37, 37, 45, 3.5, 3.4.3, 51, 54, 4.4, 61, 65, 66, 7.3

[Tan89] R.-S. Tang, J. S. Blakemore, R. E. Kremer, and K. M. Burke, *Undoped Semi-Insulating GaAs Grown by a Vertical Bridgman Method: Electrical Property Analysis Using a Simple Ambipolar Correction*, J. Appl. Phys. **66 (11)** (1989) 5428–5434. 68

[Thu75] C. D. Thurmond, *The Standard Thermodynamic Functions for the Formation of Electrons and Holes in Ge, Si, GaAs and GaP*, J. Electrochem. Soc. **122 (8)** (1975) 1133–1141. 35, 3.2, 56, 57, 7.3

[Vai97] J. Vaitkus et al., *Traps in GaAs Detectors (Before and After Irradiation) and Electric Field Redistribution in Excited SI-GaAs*, Nucl. Instr. and Meth. A **395** (1997) 94–97. 66

[Vai98] J. Vaitkus et al., *Defects and Radiation Damage in Semi-Insulating GaAs Radiation Detectors*, Nucl. Instr. and Meth. A **410** (1998) 61–67. 66, 72

[Vai99] J. Vaitkus et al., *Analysis of Trap Spectra in LEC and Epitaxial GaAs*, Nucl. Instr. and Meth. A **434** (1999) 61–66. 66

[Van89] G. Vanstraelen, I. Debusschere, C. Claeys, and G. Declerck, *Fully Integrated CMOS Pixel Detector for High Energy Particles*, Nucl. Instr. and Meth. A **275** (1989) 574–579. 76

[Van90] G. Vanstraelen, *Monolithic Integration of Solid-State Particle Detectors and their Read-out Electronics on High Resistivity Silicon*, Doctoral Thesis at the Katholieke Universiteit Leuven, Belgium (1990). 76

[Van92] G. Vanstraelen, E. Simoen, C. Claeys, and G. J. Declerck, *Short-Channel pMOST's in a High-Resistivity Silicon Substrate - I and II*, IEEE Trans. on Electron Devices **39 (10)** (1992) 2268–2283. 76

[Var67] Y. P. Varshni, *Temperature Dependence of the Energy Gap in Semiconductors*, Physica **34** (1967) 149–154. 35, 36, 3.2, 7.3

[vB85] H. J. von Bardeleben, D. Stiévenard, J. C. Bourgoin, and A. Huber, *Identification of EL2 in GaAs*, Appl. Phys. Lett. **47 (9)** (1985) 970–972. 68

[Vis00] J. Visschers, private communication, (2000). 7.3

[War92] R. M. Ware, P. J. Doering, B. Freidenreich, R. T. Koegl, and T. Collins, *Improved Uniformity of GaAs by Carbon Control*, Semicond. Sci. Technol. **7** (1992) A224–A228. 66, 68

[Wat00] J. Watt et al., *Applications of Pixellated GaAs X-ray Detectors in a Synchrotron Radiation Beam*, Presented at the 1st International Workshop on Radiation Imaging Detectors, Sundsvall, Sweden, June 13-17 1999, submitted for publication in Nucl. Instr. and Meth. A (2000). 89, 99, 6.24, 99, 7.3

[Web98] S. Webb, *The Physics of Medical Imaging*, Institute of Physics Publishing (1998). 7, 1.3, 7, 1.4, 1.1.1, 1.1.2, 1.2, 13, 1.5.1, 18, 1.5.2, 1.5.5, 1.5.6.2, 7.3

[Wel75] B. Welber, M. Cardona, C. K. Kim, and S. Rodriguez, *Dependence of the Direct Energy Gap of GaAs on Hydrostatic Pressure*, Physical Review B **12 (12)** (1975) 5729–5738. 56, 57

[Wel94] U. Welander et al., *Resolution as Defined by Line Spread and Modulation Transfer Functions for Four Digital Intraoral Radiographic Systems*, Oral and Maxillofacial Radiology; Oral Surg Oral Med Oral Path **78 (1)** (1994) 109–115. 10, 11

[Wel95] U. Welander et al., *Absolute Measures of Image Quality for the Sens-A-Ray Direct Digital Intraoral Radiography System*, Oral and Maxillofacial Radiology; Oral Surg Oral Med Oral Path Oral Radiol **80 (3)** (1995) 345–350. 9

[Wol70] C. M. Wolfe, G. E. Stillman, and W. T. Lindley, *Electron Mobility in High-Purity GaAs*, J. Appl. Phys. **41 (7)** (1970) 3088–3091. 60, 4.3, 7.3

[Wor97] A. Workman and D. S. Brettle, *Physical Performance Measures of Radiographic Imaging Systems*, Dentomaxillofacial Radiology **26** (1997) 139–146. 1.1.1, 1.1.2, 9, 1.1.4, 1.1.5

[Wu91a] E. Y. Wu, *Intervalley-Scattering Effect on the Double-Peak Velocity Behavior of Electrons in Compensated GaAs*, Physical Review B **44 (7)** (1991) 3316–3319. 61

[Wu91b] E. Y. Wu and B. H. Yu, *High Field Electron Transport in Compensated GaAs*, Appl. Phys. Lett. **58 (14)** (1991) 1503–1505. 61

[Xmu] R. Nowotny, *Program XmuDat; IAEA-NDS-195*, http://www-nds.iaea.org/reports/nds-195.htm. 2.3, 2.5, 2.6, 7.3

[Xu88] J. Xu and M. Shur, *Temperature Dependence of Electron Mobility and Peak Velocity in Compensated GaAs*, Appl. Phys. Lett. **52 (11)** (1988) 922–923. 61

[Yaf97] M. J. Yaffe and J. A. Rowlands, *X-ray Detectors for Digital Radiography*, Phys. Med. Biol. **42** (1997) 1–39. 18, 1.5.3, 1.5.4, 1.5.5, 1.5.6.2

[Zai92] M. A. Zaidi, H. Maaref, and J. C. Bourgoin, *Minority Carrier Capture Cross Section of the EL2 Defect in GaAs*, Appl. Phys. Lett. **61 (20)** (1992) 2452–2454. 68

Acknowledgements

In May 1997 I started my doctoral studentship at CERN in the micro-electronics group. I would like to thank everybody who offered me this possibility which might have determined my future.
My very special thanks go to Erik Heijne, who was my CERN supervisor during these three years. There is no doubt that I could still profit highly from his great experience in silicon strip and pixel detector development. I was extremely lucky that Walter Kutschera accepted to be my home supervisor. I enjoyed very much some inspiring discussions with him and I would like to thank him for enabling me to participate in interesting training courses.
CERN also offered me the possibility of training and of attending two conferences which provided very important impulses for my work. I thank Mike Letheren and Pierre Jarron for their kind reception in the MIC group.

When I arrived in the group I was immediately integrated and encouraged by everybody. I am still very grateful for all the help, useful advice and also constructive criticism I received during this period. I think this group is one of the most friendly groups to be found in the working environment!
I did not forget the discussions with Cinzia Da Via' who shares the same passion for medical applications and who was able to strengthen my self-confidence when I arrived. Walter Snoeys did his best to make me familiar with electronics and electronics simulations. Paul Aspell is not only a fantastic colleague, he also knows how to play the bass guitar! Eugenio Cantatore was very patient in explaining to me the secrets of the Omega3 chip. On this occasion thanks to Didier Puertolas for helping me with some special experiments with this chip. Ken Wyllie is so kind as to always remind me that I still have to practice a lot to improve my English. Bert van Koningsveld always saves me from the most critical situations with PCs and workstations. My homesickness was immediately attenuated after a chat with Harry Beker, the specialist of VME, OS9 and so on. Last but not least I greatly enjoy the kindness and humour of Jean-Claude Santiard. Let me thank Federico Faccio as well for his way of listening to people. There are many other kind and special colleagues related to the MIC group like Gerrit Meddeler or Ernst-Jan Buis, but I hope they will forgive me if I didn't mention them by name. In any case it was surely not on purpose and I hope that the lack of time to finish my thesis serves as a valid excuse.
I do not forget to thank Jean-Paul Avondo and Françoise Cossey for their prompt help with technical problems.
I would also like to mention the small, but great Austrian community at CERN. I always enjoyed the parties and occasional chats. Thanks to Petra Riedler, Christoph Posch, Edda Gschwendtner, Michael Hoch and all the others.

Even though they are far away I still feel very close to my best friends Doris Brunner and Guenter Dinhobl.

I return the special thanks to my room mate Iztok Ropotar who preferred to change to banking than to continue in physics. I don't know anybody else who expresses himself clearer than he does. This might sometimes be difficult to swallow, but often his remarks were correct and his advice very valuable. I think everybody will somehow miss him here.

In the Medipix project at CERN it was Elena Pernigotti who worked for the project when I started. We shared quite some efforts, but we also had much fun together. I appreciated a lot her reliability and activity at work, but even more I appreciated her as a person.
All my best wishes to the next doctoral student in the line of the Medipix project, Xavier Llopart. He has all the requirements to become a very successful successor, professionally as well as personally.

I acknowledge also my colleagues in the Medipix collaboration. All of the groups are doing their best to convince other people of the benefits the PCC-approach could bring. Special thanks to Maurizio Conti and Marino Maiorino who are doing a great job in providing the software for the collaboration. It was a pleasure for me to work with Giusy Bisogni, Giovanna Dipasquale, Christoph Schwarz and John Watt.

Mokhtar Chmeissani is one of the persons you never forget once you meet him. He is always full of ideas and tries to realise them with maximum energy. I hope he was as pleased as me about our common effort to get the simulations always closer and closer to reality. With Thierry Gys I had to solve some interesting simulation problems as well. I am especially indebted to Marc Million from whom I learned a lot about simulation principles. A big part of that I still had no chance to apply.

The Glasgow group deserves a special mention. Richard Bates, Val O'Shea, John Watt, Keith Mathieson, Steven Passmore, Steven Divine and Mahfuzur Rahman are a great team. Very special thanks to Kenway Smith who is one of the kindest professors I know.

Also proud of being Scottish is Michael Campbell to whom I owe a lot. He took care that my working progress advanced during these three years. We shared all the ups and downs of the project and he put all his efforts in trying to make me always think positively. Moreover, he is a very good friend.

Finally I would like to express my gratitude to everybody who had the heavy task of reading parts of my thesis, Michael Campbell, Walter Snoeys, Marc Million, Mahfuzur Rahman and Wasi Faruqi.

All my love goes to my family, in particular to Ivan, Livia and Julia and to my parents, my sister and my grand-parents. My parents and also my grand-parents always supported me in my studies. I received steady encouragement from my mother who was always there in all possible and impossible situations. It happened sometimes that she and my sister had to be engaged as emergency babysitters. I hope I can return all that later somehow.
Without the teamwork of Ivan this thesis wouldn't have been possible. I thank him for his love even when I was stressed and nervous, in particular during the last weeks. Livia and Julia were also extremely patient with me. I am incredibly lucky to have such wonderful daughters who always manage to help me balance my priorities.